

TECTONO-STRATIGRAPHIC EVOLUTION OF THE CONTINENTAL MIOCENE
BASINS IN SOUTHWEST ANATOLIA

A THESIS SUBMITTED TO
THE GRADUATE SCHOOL OF NATURAL AND APPLIED SCIENCES
OF
MIDDLE EAST TECHNICAL UNIVERSITY

BY
AYTEN KOÇ

IN PARTIAL FULFILLMENT OF THE REQUIREMENTS
FOR
THE DEGREE OF DOCTOR OF PHILOSOPHY
IN
GEOLOGICAL ENGINEERING

SEPTEMBER 2013

Approval of the thesis:

**TECTONO-STRATIGRAPHIC EVOLUTION OF THE CONTINENTAL
MIOCENE BASINS IN SOUTHWEST ANATOLIA**

submitted by **AYTEN KOÇ** in partial fulfillment of the requirements for the degree of
**Doctor of Philosophy in Geological Engineering Department, Middle East
Technical University** by,

Prof. Dr. Canan Özgen

Dean, Graduate School of **Natural and Applied Sciences**

Prof. Dr. Erdin Bozkurt

Head of Department, **Geological Engineering**

Prof. Dr. Nuretdin Kaymakcı

Supervisor, **Geological Engineering Dept., METU**

Assoc. Prof. Douwe J.J. van Hinsbergen

Co-Supervisor, **Dept. of Earth Sciences, Utrecht University**

Examining Committee Members:

Prof. Dr. Kadir Dirik

Geological Engineering Dept., HÜ

Prof. Dr. Nuretdin Kaymakcı

Supervisor, Geological Engineering Dept., METU

Prof. Dr. Erdin Bozkurt

Geological Engineering Dept., METU

Assoc. Prof. Dr. Bora Rojay

Geological Engineering Dept., METU

Assist. Prof. Dr. Arda Özacar

Geological Engineering Dept., METU

Date: 04.09.2013

I hereby declare that all information in this document has been obtained and presented in accordance with academic rules and ethical conduct. I also declare that, as required by these rules and conduct, I have fully cited and referenced all material and results that are not original to this work.

Name, Surname: Ayten KOÇ

Signature:

ABSTRACT

TECTONO-STRATIGRAPHIC EVOLUTION OF THE CONTINENTAL MIOCENE BASINS IN SOUTHWEST ANATOLIA

KOÇ, Ayten

Ph.D., Department of Geological Engineering

Supervisor: Prof. Dr. Nuretdin Kaymakçı

Co-Supervisor: Assoc. Prof. Douwe J.J. van Hinsbergen

September 2013, 185 pages

The Tauride range in southern Turkey is flanked and overlain by Neogene sedimentary basins. To the south and on top of the high range, these basins are mainly marine, whereas poorly studied intra-montane basins dominated by continental deposits are exposed to the north. In this study, the stratigraphy and structure of these continental basins which includes Altınapa, Yalvaç and Ilgın Basins are studied. Their stratigraphy of these basins displays poorly expressed fining upwards sequences of fluvio-lacustrine sediments, deposition of which interrupted by regionally correlateable unconformities; they might also have similar hiatuses in each basin. The most prominent unconformity surface occurred during the Middle Miocene and corresponds to a volcanic activity in the region. $^{40}\text{Ar}/^{39}\text{Ar}$ dating of the volcanoclastic samples from the Altınapa and Ilgın basins yielded 11.8–11.6 Ma ages. The main basin forming phase was extensional and occurred just before or during the Middle Miocene. The extension directions obtained from paleostress inversion techniques indicate multiple extension directions which are consistent with recent seismic activity and available focal mechanism solutions. The Middle Miocene and onwards extensional history of these basins are consistent with the regional tectonics associated with the Cyprus subduction zone. This suggests that the Cyprus subduction zone has been retreated relative to central Anatolia since, at least, the Middle Miocene time. In addition to extensional history of the region, these continental basins contain evidences for the post-Late Miocene differential uplift of the Taurides in southern Anatolia. These continental basins were very close to sea level during the Middle and Late Miocene and are now lying at an elevation of 1 km. On the other hand, the upper Miocene marine deposits just south of the study area currently lie at an elevation of ~2 km which are elevated ~1 km with respect to these continental basins. We conclude that the current high elevation of the Taurides is related to late Neogene extension and vertical differential uplift possibly due to slab edge processes along the Cyprian Subduction and related mantle processes.

Keywords: uniaxial stress, paleostress, Isparta Angle, post-Late Miocene uplifts

ÖZ

GÜNEYBATI ANADOLU'DA BULUNAN KARASAL MİYOSEN HAVZALARININ TEKTONO-STRATİGRAFİK GELİŞİMİ

KOÇ, Ayten

Doktora, Jeoloji Mühendisliği Bölümü

Tez Danışmanı: Prof.Dr. Nuretdin Kaymakçı

Yardımcı Tez Danışmanı: Doç. Dr. Douwe J.J. van Hinsbergen

September 2012, 185 sayfa

Türkiye'nin güneyinde bulunan Toros kuşağı, Neojen yaşlı sedimanter havzalar tarafından örtülmüştür. Güneyde bu kuşak üzerinde genellikle denizel havzalar yerleşirken, kuzeyde ise dağlar arasına sıkışmış karasal havzalar örtmektedir. Bu çalışmada, Altınapa, Ilgın ve Yalvaç karasal havzalarının stratigrafisi ve yapısal unsurları çalışılmıştır. Herbir havzadaki gölsel depolanma yaklaşık aynı dönemlerde kesintiye uğramış ve bölgesel uyumsuzluk düzlemleri ile ilintilidir. En belirgin uyumsuzluk düzlemi Orta Miyosen'de oluşmuştur. Bu dönem aynı zamanda, bölgede volkanik aktivitenin olduğu dönemdir. Altınapa ve Ilgın Havzalarından alınan volkanik örneklerden yapılan $^{40}\text{Ar}/^{39}\text{Ar}$ yaş tayini 11.8-11.6 Ma vermiştir. Ana havza oluşum fazı gerilmeli bir rejimde, Orta Miyosen'den önce yada esnasında oluşmuştur. Paleostres analizlerinden gelen gerilme yönleri ise çok değişkendir ve bu değişkenlik bölgede kaydedilen sismik aktivitelerdeki gerilme yönlerinde de mevcuttur. Orta Miyosen'den bu yana bu havzalarda görülen gerilmeli rejim geçmişi, Kıbrıs dalma batma zonu etkisindeki bölgesel tektonik ile uyumludur. Bu durum, Kıbrıs dalma-batma zonunun orta Anadolu'ya göre geriye doğru hareketinin en azından Orta Miyosen'den beri devam ettiğine işaret etmektedir. Bölgedeki gerilmeli rejim geçmişine ek olarak, bu karasal havzalar Güney Anadolu'da yer alan Toros kuşağının Geç Miyosen sonrası diferansiyel yükselmesine kanıtlar barındırmaktadır. Bu havzalar, Orta ve Geç Miyosen döneminde deniz seviyesine çok yakın iken, bugün deniz seviyesinden ~1 km yüksekte bulunmaktadır. Diğer taraftan, çalışma alanının hemen güneyinde bulunan Geç Miyosen yaşlı denizel birimler, bugün deniz seviyesinden ~2 km yüksekte iken, bu karasal havzalardan ise ~1 km daha yükseklikte bulunmaktadır. Bu çalışma, Torosların bu günkü yükseklikliğinin, Kıbrıs dalma-batma zonu boyunca etkili olan dalan plaka kenar prosesleri ile ilişkili manto proseslerinin neden olduğu geç Neojen dönemine ait gerilmeli rejimin ve düşey diferansiyel yükselmenin etkisinde oluştuğunu göstermiştir.

Anahtar Kelimeler: tek eksenli stres, paleostres, İsparata Açısı, Geç Miyosen sonrası yükselme

To my Mother Huriye, I wasn't ready to let you go,
I really miss you,

To my Father Necmettin, always quietly supported me in my life,

ACKNOWLEDGEMENT

This research was completed with the great helps and supports of many people. I know that the words are not enough to express their contribution and support; nevertheless, I would like to express my sincere gratitude to all of them.

First of all, I owe my deepest gratitude to my research guide, Dr. Nuretdin Kaymakcı, especially for his valuable contributions and detailed review of the thesis. He has always given me great freedom to pursue independent work. I have benefited greatly from his critical thinking and insight to geological problems. My special words of thanks should also go to my co-supervisor Dr. Douwe J.J. van Hinsbergen for his encouragement and motivation in various phases of this research. His clear guidance, valuable discussions and continual support in friendly and kind manner gave me strength to continue my work. His cooperation and positive attitude really deserve an everlasting appreciation.

Special thanks to my Ph.D. committee members, Dr. Kadir Dirik, Dr. Erdin Bozkurt, Dr. Bora Rojay and Dr. Arda Özacar for their support, guidance and helpful suggestions when I needed it. Their enthusiasm and integral view on research for providing high-quality work have made a deep impression on me.

I would like to express my gratitude to METU Geological Engineering Department folks, especially Esin Grunberg who was giving me strength when I was discouraged and depressed. In this regard, I would like to thank Orhan Karaman for his helps during field studies.

The following people are thanked because of their encouragement, moral support and personal helps. I would like to express my heart-felt gratitude to Ayşe Bayrakçeken, Esra Balgalmış, Gözde Yal, Mert Eker, Seda Çiçek, Suna & Kemal Şerbetçi couple, Selim Cambazoğlu and Sevgi Özen. They have always been there for me with their supporting hands whenever I needed it the most. I am thankful to my colleagues in METU, especially Erhan Gülyüz, Kıvanç Yücel, Murat Özkaptan, Mustafa Yücel Kaya and Okay Çimen for their helps during field works.

I would like to gratefully acknowledge the Yüzüncü Yıl University (Van, Turkey) for providing me financial support. And also this research was supported by ÖYP research foundation No: BAP-08-11-DPT.2002K120510

Last and the foremost, I would like to express my special thanks to my family for their understanding, patience and endless support. In this regard, my heart felt regard goes to my brother Kemal, brother-in-law Hasan and Kadri for their helps during field works. Their infallible love and support has always been my strength. I owe my deepest gratitude towards my sisters Fatma, Ayşegül, Aysel and sister-in-law Makbule for their

patience and sacrifice. Without their continual support, encouragement and love, I would not have been able to complete much of what I have done and become who I am. I am thankful to my nephew Onur for giving me happiness during the field studies.

As always it is impossible to mention everybody who had a contribution to this work however there are those whose spiritual support is even more important. I feel a deep sense of gratitude for my mother Huriye and my father Necmettin who formed part of my vision and taught me good things that really matter in life.

*“goodness can never be defied
and
good human beings can never be denied”*

TABLE OF CONTENTS

ABSTRACT	v
ÖZ	vi
ACKNOWLEDGEMENT	viii
TABLE OF CONTENTS	x
LIST OF TABLES	xiii
LIST OF FIGURES	xiv
CHAPTERS	
1. INTRODUCTION	1
1.1 General	1
1.2 Aims of this thesis	3
1.3 Approach taken	4
1.4 Organization of thesis	5
1.5 Study area	5
1.6 Previous studies	8
1.6.1 Studies on Altınapa Basin	8
1.6.2 Studies on Ilgın Basin	8
1.6.3 Studies on Yalvaç Basin	9
2. TECTONO-SEDIMENTARY EVOLUTION AND GEOCHRONOLOGY OF THE MIDDLE MIOCENE ALTINAPA BASIN (KONYA)	11
2.1 Lithostratigraphy	11
2.1.1 Lower Altınapa Group (LAG)	13
2.1.2 Upper Altınapa Group (UAG)	19
2.1.3 Topraklı Formation (TFm)	24
2.2 ⁴⁰ Ar/ ³⁹ Ar Geochronology	25
2.3 Structural Geology	28
2.3.1 Remote Sensing	28
2.3.2 Field Observation	30
2.4 Paleostress Analysis	34
2.4.1 Data and Method	34
2.4.2 Spatial Characteristics	38
2.4.3 Temporal Relationships	40

3. TECTONO-SEDIMENTARY EVOLUTION AND GEOCHRONOLOGY OF THE MIOCENE ILGIN BASIN (TAURIDE BELT, TURKEY)	43
3.1 Lithostratigraphy.....	43
3.1.1 Kumdöken Formation (KDFm)	45
3.1.2 Aşağıçiğil Formation (AÇFm).....	50
3.1.3 Belekler Formation (BLFm)	54
3.1.4 Quaternary Units (Qua).....	59
3.2 ⁴⁰ Ar/ ³⁹ Ar Geochronology	59
3.3 Structural Geology	62
3.3.1 Lineament Analysis from Remotely Sensed Data	62
3.3.2 Field Observation.....	64
3.4 Paleostress Analysis.....	75
3.4.1 Veins	75
3.4.2 Fault Slip Data	82
3.4.3 Spatial Characteristics.....	89
3.4.4 Temporal Relationships	93
4. TECTONO-SEDIMENTARY EVOLUTION AND GEOCHRONOLOGY OF THE MIOCENE YALVAÇ BASIN (ISPARTA).....	97
4.1 Lithostratigraphy.....	97
4.1.1 Bağkonak Formation (BKFm)	100
4.1.2 Yarıkkaya Formation (YKFm).....	105
4.1.3 Göksöğüt Formation (GSFm)	111
4.1.4 Kırkbaş Formation (KBFm).....	113
4.2 Structural Geology	114
4.2.1 Lineament Analysis from Remotely Sensed Data	114
4.2.2 Field Observation.....	116
4.3 Paleostress Analysis.....	129
4.3.1 Veins	129
4.3.2 Fault Slip Analysis.....	131
4.3.3 Spatial Characteristics.....	140
4.3.4 Temporal Characteristics	143
5. SYNTHESIS	145
5.1 Temporal Relationships	145

5.1.1	Altınapa Basin	145
5.1.2	İlgin Basin	146
5.1.3	Yalvaç Basin	147
5.1.4	Regional Implications	148
5.1.5	Regional Relationships: Extend of Continental-Marine Transition	152
5.2	Structural Implications	154
5.2.1	Altınapa Basin	154
5.2.2	İlgin Basin	156
5.2.3	Yalvaç Basin	158
5.2.4	Local Structural Correlation	159
5.2.5	Regional Implications	163
6.	CONCLUSIONS	165
	REFERENCES	169
	APPENDICES	
	A. PUBLISHED RESEARCH PAPER	185
	CURRICULUM VITAE	207

LIST OF TABLES

TABLES

Table 2.1 Summary of $^{40}\text{Ar}/^{39}\text{Ar}$ data. Full data tables are given in the appendix. Errors are reported with 2σ uncertainty and represent analytical error. Full external errors are reported between brackets. MWSD is Mean Square Weighted Deviate. N is the number of analysis included in the weighted mean age, between brackets the number of experiments excluded.....	26
Table 2.2. Locations and paleostress orientations for Altınapa Basin.	37
Table 3.1. Summary of $^{40}\text{Ar}/^{39}\text{Ar}$ data. Full data tables are given in the appendix. Errors are reported with 2σ uncertainty and represent analytical error. Full external errors are reported between brackets. MWSD is Mean Square Weighted Deviate. N is the number of analysis included in the weighted mean age, between brackets the number of experiments excluded.	60
Table 3.2. Locations and paleostress orientations from Ilgın Basin.	86
Table 4.1. Locations and paleostress orientations from Yalvaç Basin.....	136
Table 5.1. Tabulated information introduces the basic features for the each basin (Altınapa, Ilgın and Yalvaç basins).	150

LIST OF FIGURES

FIGURES

Figure 1.1. a) Major tectonic zones of Turkey (modified from Okay et al., (1996) and Kaymakci et al. (2010). b) simplified geological map of southern Turkey overlaid on an SRTM topographic and bathymetric image (geological map is simplified from MTA 1/500.000 map series). c) Profile along the line XX'. Note that altitude of the Tauride range is ~1 km higher than the elevation of central Anatolia..... 2

Figure 1.2. Simplified geological map of the Isparta Angle illustrating locations of the study area and conceptual cross-section along line AB depicting the relationship between marine and continental deposits. Note blow up image indicating small outcrop of marine deposits around Beyşehir. Blue dashed line is the northernmost extend of the paleo-shoreline during the late Miocene. 7

Figure 2.1. Generalized stratigraphic column for the Altınapa Basin..... 12

Figure 2.2. (a) Revised geological map of the study area from the 1/500000 scale geological map produced by MTA. (b) Inset map showing the location of the measured sections for the lower (L-L') and upper (U-U') Altınapa groups. Dashed lines named as A, B, C, D and E indicate the trace of the cross-sections in Figure 17. 13

Figure 2.3. Field views of basal conglomerates from the lower Altınapa group along the Kızılören Fault (a). Poorly bedded basal conglomerate explored along the Konya-Beyşehir road (b). Close-up view of the basal conglomerate with reverse graded beds (c). Note coarse, poorly sorted, sub-angular conglomerates. Matrix-supported basal conglomerate, located close to Dereaşıklar (d). The conglomerate interfingers with clast-supported, polymict conglomerates (e). 14

Figure 2.4. Field view of the basal conglomeratic unit (B and C) at the lower Altınapa Group near Dereaşıklar. Note that the Neogene conglomeratic unit overlies unconformably Mesozoic ophiolitic mélange (A). View towards the East..... 15

Figure 2.5. Field view of the angular unconformity between the lower (B) and upper (C) Altınapa groups. 16

Figure 2.6. Measured section of the lower Altınapa group. 17

Figure 2.7. Field view of typical facies of the lower Altınapa group: a) clast-supported, polymict conglomeratic units b) cross-bedded and bioturbated, fresh-water gastropods-bearing sandstones, c) well bedded fresh water stromatolitic limestone and d) alternation of siltstone, green-blue coal bearing claystone, marls..... 18

Figure 2.8. Field view of facies changes of lower Altınapa group from SW margin towards northeast into the basin center. The white line represents the Kızılören (normal) fault (ticks on the hanging-wall block). Note that coarse, poorly sorted, sub-angular coarse clastics dominate along the SW margin while they rapidly become finer-grained to marl-dominated towards NE (view to NW).....	19
Figure 2.9. Schematic illustration of the lithostratigraphy of the Altınapa Basin. The section number is given on the geological map of the study area. Notice that grain size decreases from west to east. Vertical bars indicate the scales of each column independently.....	20
Figure 2.10. Field view of onlapping lacustrine algal limestones of the upper Altınapa group over the basement (location is 2 km north of Başarakavak, view to NW)	21
Figure 2.11. Field view of the angular unconformity between the upper Altınapa group (UAG) and overlying Topraklı formation (A) near Ulumuhsine. The UAG consists of pinkish/white tuff (B), freshwater limestone (C) (65m) and marl/tuff alternation (D)...	22
Figure 2.12. Measured section of the upper Altınapa group around Ulumuhsine (see Figure 2.3b for location of the section).....	23
Figure 2.13. Tuff facies of upper Altınapa group (UAG). a) The tuff facies at the bottom and b) their close up view. c) block and ash facies at the top of the UAG and d) their close up view.	24
Figure 2.14. Replicate single crystal fusion $^{40}\text{Ar}/^{39}\text{Ar}$ ages are plotted versus the % of $^{39}\text{Ar}/\text{K}$ released in each fusion analysis for the three lava samples from the upper Altınapa group. The width of the bars/steps represents the 2σ analytical error. On top the K/Ca ratio (grey area, width is 2σ error) is displayed. Weighted mean ages are given. The small insets show the inverse isochron diagrams.	27
Figure 2.15. Structural map of the Altınapa Basin, indicating faults and lineaments. Rose diagram (length weighted) indicating orientations of both faults and lineaments.	29
Figure 2.16. Syn-sedimentary normal fault in the tuff units of upper Altınapa group....	30
Figure 2.17. Structural cross-sections constructed from the geological map. Inset map shows the locations of the cross-sections. Different colors for faults correspond to the same fault in the different sections.	32
Figure 2.18. (a) Stereoplot showing all of the collected fault-slip measurements (N=377), (b) bidirectional rose diagram of fault strikes.	35
Figure 2.19. Stereoplots showing constructed paleostress orientations, fault planes and slip lineations (lower hemisphere equal area projection).....	36

Figure 2.20. Density diagrams for principal stress orientations and frequency distributions of Φ values. (a-d) Whole data, (e-h) based on data from upper Altınapa group, (i-l) based on lower Altınapa group. Notice that the σ_1 is dominantly sub-vertical while σ_2 and σ_3 orientations are sub-horizontal with strongly varying directions indicating uniaxial stress conditions. 38

Figure 2.21. Major faults and lineament map of the study area. Arrows indicate horizontal component of the minor principal stress (σ_3) and numbers indicate the paleostress measurement sites which correspond to site numbers in Figure 2.19..... 39

Figure 2.22. Paleostress stratigraphy of the Altınapa Basin from the Middle Miocene to Recent. Arrows represent σ_3 directions. Focal solutions are belong to 11 September 2009 Sille Earthquake (Mw=4.9 ETHZ), 3 February 2002 Sultandağı Earthquake (Ms=6.4, Taymaz et al., 2004) and 15 December 2000 Afyon Earthquake (Ms=5.8, Taymaz et al., 2004). Note that the unconstrained nature of σ_3 directions and variation of extension directions of the earthquakes in the region. 41

Figure 3.1. Revised geological map of the Ilgın Basin from the 1/100000 scale MTA geological map based on the field studies and remotely sensed data. Blue rectangle areas are used to indicate the location of the measured sections of the lithological units. Inset b for Aşağıçiğil formation (AÇFm), Inset c for Kumdöken formation (KDFm) and Inset c for lacustrine part of the Aşağıçiğil formation (AÇFm). Routes of the measured sections are indicated by white solid lines (A-A' for AÇFm, (K-K') for KDFm and (B-B' and C-C') lacustrine part of the AÇFm. 44

Figure 3.2. Generalized stratigraphic column for the Ilgın Basin. Red labels with rectangle outline indicate the horizons of the fauna (mammalian fossils) and flora (spores & pollens). 46

Figure 3.3. Field view of an angular unconformity between the Kumdöken and Aşağıçiğil formations (a). White rectangle indicated as inset b shows the bedding attitude of KDFm in azimuth method (b). Close-up view of the polymict, angular to sub rounded, poorly sorted red conglomeratic unit of the KDFm (c). 47

Figure 3.4. Reference section of the Kumdöken formation. The sequence basically consists of fine grained mudstone unit intercalated with alluvi-fluvial coarse grained deposition. 48

Figure 3.5. Close-up view of pebble imbrication in the conglomeratic unit of the KDFm (a). Scour-and-fill structure formed at the base of the conglomerate (b). Bioturbated mudstone unit (indicated with blue circles) (c). Cross-bedded silty-mudstone (d). 49

Figure 3.6. Field view of the angular unconformity between the Aşağıçiğil and Belekler formations. 51

Figure 3.7. Measured section of the Aşağıçığıl formation. The sequence basically consists alluvi-fluvial facies units interfingering with lacustrine facies units. 52

Figure 3.8. Field views of the typical facies changes of the AÇFm. Basal conglomeratic unit shows matrix (a) and clast (b) supported characteristics. Close up view of the basal conglomerate with normal graded beds (c) and imbricated clasts (d). Conglomerates intercalated with intensely bioturbated coarse sandstone (e) which contains channel structures filled with medium to coarse pebbles (f). Fresh water gastropods (g) bearing siltstone/mudstone and fresh water stromatolitic limestone (h) alternation..... 53

Figure 3.9. Measured section succeeded by fresh water gastropods bearing mudstone, marl alternations (c and d) and intercalations of well-cemented, thick-bedded algal limestone (a and b). Close-up view pumice level (e) from which sample was collected for Ar/Ar dating. 55

Figure 3.10. Field view of the contact relation between the BLFm and AÇFm in the north of the basin. The photo was taken from coal mine in the Çavuşçugöl area. View to West. 56

Figure 3.11. Belekler formation from west to center of the basin. Note that the formation characterizes loosely consolidated angular conglomerates (a) in the west of the basin and it consists of mudstone (b) in the central part of the basin. Cross-section interprets the grain size changes of the Belekler formation..... 57

Figure 3.12. Field view of lateral facies changes of the Belekler formation. Alternation of red mudstone with white marl/claystone along the Ilgın-Beyşehir road. View to west. 58

Figure 3.13. Replicate single crystal fusion $^{40}\text{Ar}/^{39}\text{Ar}$ ages are plotted versus the % of $^{39}\text{Ar}/\text{K}$ released in each fusion analysis for the three pumice samples from the Ilgın Basin. The width of the bars/steps represents the 2σ analytical error. On top the K/Ca ratio (grey area, width is 2σ error) is displayed. Weighted mean ages are given. The lowermost graph shows the inverse isochron diagram. 61

Figure 3.14. Lineament map of the Ilgın Basin. Rose diagram (length weighted) shows orientations of both faults and lineaments. Base image is Digital Elevation Model produced from the 1/25.000 scale topographic maps..... 63

Figure 3.15. Structural cross-sections produced from the geological map given in Figure 3.1. 65

Figure 3.16. Digital Elevation Model (DEM) with 25*25 spatial resolution prepared from 1/25.000 scale topographic maps shows 3D view of the NE dipping Akşehir-Afyon Fault Zone (AAFZ) at the western margin of the Ilgın Basin. Sultandağları contains

several NE-SW trending valleys which are indicated by red dash lines. Flat-iron morphologic structure along the fault zone is characteristic for normal fault activity. 66

Figure 3.17. Cross-section along the Doğanhisar-Fırınılı road shows N20W striking faults of the Akşehir-Afyon Fault Zone. Faults are conjugate and dipping towards and away to basin center. The rectangle areas on the cross-section indicate the location of the photos a and b. 67

Figure 3.18. The fault scarp (a) and stereographic plot of fault-slip data (b) from Ilgın Fault Zone (IFZ). 69

Figure 3.19. Field view of the Argıthanı Segment of ABDFZ along the Argıthanı-Kabaklı road. Note the folds on the hanging wall beds against the fault. View to east. . 71

Figure 3.20. Field view of the Balkı Segment (BS) at the 2 km south of the Eldeş. Note the juxtaposition of basement limestone and Aşağıcığıl formation. View to west. Lower-hemisphere Schmidt projection of fault-slip data and constructed paleostress configurations. Note that large arrows indicate approximately N-S extensional deformation. D and P indicate the dip direction and plunge, respectively. 72

Figure 3.21. Field view of E-W trending fault scarp of the Derbent Segment. Black line indicates the trace of the fault which juxtaposes Belekler formation and recent river deposits. View to south. 73

Figure 3.22. Field view of the normal fault within the Derbent segment along the Ilgın-Derbent road. Red rectangle indicates the close-up view of the (b). Lower-hemisphere Schmidt projection of fault-slip data and constructed paleostress configurations is also given. Blue rectangle is used to indicate the hammer as a scale. View to east. 74

Figure 3.23. Field view of the veins emplaced within the basement limestone unit. Approximately NE-SW striking calcite veins (6 km north of Ilgın, view to SW). a) Different vein occurrences are indicated with color arrows. b) Close-up image of a vein. 77

Figure 3.24. Stereographic plot of the vein measurements within the basement in the vicinity of Çavuşçugöl. a) Cyclographic traces of the veins on the lower hemisphere equal-angle net. Red dots represent the pole of the vein planes. b) Contour diagram of the veins based on their poles and orientation of the best fit plane, and direction of paleostress configurations. MLV: Mean Lineation Vector of the pole of the vein planes and identified by red star, MGC: Mean Great Circle passing through the pole of the vein planes. 78

Figure 3.25. Vein formation with slicken-fiber (a). The orientation of the vein surface with slicken-fibers (b), and theoretical idea (Ramsey and Chester, 2004) behind the

occurrence of the hybrid fractures (c). Blue and red arrows show extension and compression directions, respectively. 79

Figure 3.26. Vein formation in the basement limestone. Approximately N-S striking, syntaxial hydrothermal vein, where crystals grow from the wall rock into the vein (younger in the center, older close to the vein wall). 80

Figure 3.27. Stereographic plot of the vein measurements within the basement located at the vicinity of the Ilgin. a) Cyclographic traces of the veins on the lower hemisphere equal-angle net. Red dots represent the pole of the vein planes. b) Contour diagram of the veins based on their poles and orientation of the best fit plane, and direction of paleostress configurations. MLV: Mean Lineation Vector of the pole of the vein planes and identified by red star, MGC: Mean Great Circle passing through the pole of the vein planes. 80

Figure 3.28. Vein formation in the limestone unit of the Aşağıcıgil formation. Approximately E-W striking calcite veins (a). Blue arrows indicate extension direction. Location of the photo b is showed by yellow rectangle on the photo a. Dash lines show the vein center. 81

Figure 3.29. Stereographic plot of the vein measurements within the limestone at the vicinity of Ilgin. a) Cyclographic traces of the veins on the lower hemisphere equal-angle net. Red dots represent the pole of the vein planes. b) Contour diagram of the veins based on their poles and orientation of the best fit plane, and direction of paleostress configurations. MLV: Mean Lineation Vector of the pole of the vein planes and identified by red star, MGC: Mean Great Circle passing through the pole of the vein planes. 82

Figure 3.30. a) Bidirectional rose diagram shows the strike of the measured fault planes. Note bimodal distribution in N80°-90°E (dominant direction) and N40°-50°E. b) The histogram of the fault dip amounts. 83

Figure 3.31. Stereoplots showing constructed paleostress orientations, fault planes and slip lineations (lower hemisphere equal area projection) for each location. 84

Figure 3.32. Mesoscale conjugate normal faults (white dash line) and strike-slip fault (yellow dash line) in Pre-Neogene basement limestone in site I40 (a). Note that dextral strike-slip is cut by normal faults. Red rectangle indicates the close-up view of the strike slip movement (b) and white rectangle shows the close-up view of slickenlines produced by dip-slip normal movement (c). Note compass (yellow rectangle) for scale. 87

Figure 3.33. Mesoscale syn-sedimentary step like normal faults within the Early Miocene Kumdöken formation in Site 34 (a). Yellow rectangle indicates the close-up view of the slickenlines on the fault surfaces (b). Note that fault orientation is approximately E-W. 88

Figure 3.34. Field view and sketch of the pure strike-slip faults observed within the Early Miocene Kumdöken formation in Site 33. Yellow rectangle indicates the close-up view of the slickenlines on the fault surfaces which is given in inset b. Note that fault orientation is approximately NE-SW. Simplified sketch of the block movement is given in inset c. Blue arrows indicates the relative movement of fault blocks. Red arrows show movement on horizontal plane. 89

Figure 3.35. Density diagrams for principle stress orientations (σ_1 , σ_2 and σ_3 , in a, b and c respectively) and frequency distribution of Φ values for whole data (d). Notice that the σ_1 is significantly (sub-)vertical while σ_2 and σ_3 orientations are horizontal. 90

Figure 3.36. Spatial distribution of the paleostress measurements on the major faults and lineament map of the Ilgın Basin. Arrows indicate horizontal component of the minor principle stress (σ_3). Numbers indicate locations of paleostress measurement which correspond the site numbers in Figure 3.31 and Table 3.2. Blue rectangle areas in the base map show the location of the close-up view of the inset maps which are labeled as b and c. Red rectangle area represents mapped area given in Figure 3.1 92

Figure 3.37. Paleostress stratigraphy of the Ilgın Basin from the Early Miocene to Recent. Arrows represent σ_3 directions. Red, blue and black arrows indicate E-W extension, N-S extension and hybrid paleostress solution, respectively. Black star are used to represent syn-sedimentary fault-slip solution. Focal solutions are belong to 27 July 2011 Ilgın Earthquake (M=4.7 ERD and M=4.6 GFZ) and 3 February 2002 Sultandağ Earthquake (M=6.4 Taymaz et al., 2004). Stratigraphic location of the vein data is also given. Note that nature of σ_3 directions and extension directions of the earthquakes and the vein data in the region. 94

Figure 3.38. Normal faults which indicates coeval N-S and E-W extension direction. White solid lines represents the E-W trending growth fault displacement and solid black line states the trace of the Ilgın Fault which delimits western boundary of the Çavuşçugöl graben. 95

Figure 4.1. Revised geological map of the study area based on the field studies and remotely sensed data. Blue rectangle areas are used to indicate the location of the measured sections of the lithological units. Inset map a for Göksöğüt formation (GSFm), inset map b for Yarıkkaya formation (YKFm) and inset map c for Bağkonak formation (BKFm). Routes of the measured sections are indicated by white solid lines (G-G' for GSFm, (Y-Y') for YKFm and (BK-BK') for BKFm (see Appendix for larger scale of this map). 98

Figure 4.2. Generalized stratigraphic column for the Yalvaç Basin. 99

Figure 4.3. Field view of the angular unconformity between Bağkonak formation and basement limestone. View towards the north. 100

Figure 4.4. General view of the angular unconformity between the Bağkonak formation (BKFm) above and the Pre-Neogene basement limestone units below. Un-interpreted figure is given in (a) and interpreted figure is showed in (b). North east of the Bağkonak and view to north.	101
Figure 4.5. Measured section of the Bağkonak formation.	102
Figure 4.6. Basal conglomerate of the BKFm around the Özgüney (a), cross-bedding in the conglomerates is observed in the lower part of the YKFm around north of the Yarikkaya (b), close up view of the conglomerates with pressure solutions at the edge of the conglomerates (c), mudstone from the YKFm containing trace fossils (d), close up view of the gastropod rich level in the YKFm (e), block-sized, poorly sorted, sub-angular to sub-rounded conglomerates belonging to GSFm (f), black sandstone level in the GSFm (g), buff to brown, banded and porous possibly lacustrine algal limestone in the GSFm (h), red mudstone and conglomerate unit of the KBFm (i, j respectively). .	103
Figure 4.7. General view of the Bağkonak formation. The white dashed-line represents the boundary between formations. Note that coarse, poorly sorted, sub-angular coarse clastics dominate along the NE margin while the unit gradually become finer-grained to marl-dominated towards SW (view to NE).....	104
Figure 4.8. Measured section of the lower part of the Yarikkaya formation (in the footwall block).....	106
Figure 4.9. General view of the nonconformity between Pre-Neogene low metamorphic basement unit and Yarikkaya formation (dashed line) and cross-section along the line AB (solid white line).....	107
Figure 4.10. Measured section of the upper part of the Yarikkaya formation (in the hanging wall block).....	109
Figure 4.11. General view of the unconformity between Yarikkaya formation and Göksöğüt formation (a). White dashed line represents the bed surfaces. Black solid line indicates line of the cross-section which is given in (b).Close-up view of the Göksöğüt formation is given in (c).....	110
Figure 4.12. The measured section of the Göksöğüt formation and the location of the sections over the cross-section.....	112
Figure 4.13. Structural map of the Yalvaç Basin, indicating faults and lineaments. Rose diagram (length weighted) is prepared from both discriminated faults and lineaments. Background image is shaded relief of DEM with 25*25 grid spacing.	115
Figure 4.14. Structural cross-sections produced from the geological map. Inset map shows the locations of the sections.	117

- Figure 4.15. General view of the western segment of the Yarikkaya Fault Zone (view to NE). Vertical red arrows indicate the trace of the fault..... 118
- Figure 4.16. Hanging valleys along the YKFZ (dashed lines) overlaid on DEM (25*25 grid spacing). Red and blue lines with arrows indicate streams and their flow directions. Red lines refer to analyzed profiles. Note sharp change in topography (knick points) on the profiles along the YFZ. 119
- Figure 4.17. a) Fault plane of YKFZ and b) constructed paleostress configuration based on the collected slickensides from the YKFZ (equal area, lower hemisphere projection). White dash lines show the Reidel faults on the fault surface and indicate the movement direction of the hanging-wall block. 120
- Figure 4.18. a) Map view of the Yarikkaya fault segments and relay ramps between them. b) Schematic block diagram of a typical relay ramp between two overstepping segments of a normal fault zone (adopted from the Çiftçi and Bozkurt (2007))...... 121
- Figure 4.19. Çakırçal Fault Zone between Yarikkaya formation and Pre-Neogene basement. Note the change in the thickness of the Yarikkaya formation. 122
- Figure 4.20. General view of the central segment of the Çakırçal Fault Zone (view to NE). Vertical red arrows indicate the trace of the fault..... 123
- Figure 4.21. a) Configuration of reconstructed paleostress orientations (equal area, lower hemisphere projection) b) close-up view of slickensides one of the E-W striking segments of ÇFZ around Sücüllü (view to north). Note low pitch of the slickensides (29°W)..... 124
- Figure 4.22. General view of Sağır Fault Zone (view to west). White dash line indicates the trace of the fault..... 125
- Figure 4.23. a) Fault scarp of the Sağır Fault Zone (SFZ) at the northwest of the Sağır. b) Constructed paleostress configuration based on kinematic indicator collected on the SFZ (equal area, lower hemisphere projection). The white arrow indicates the dip of the fault surface and the movement direction of the hanging-wall block. 126
- Figure 4.24. a) Field view of the northeastern tip of the Kumdanlı Fault Zone (white dashed line). Note colluvial wedge, unconsolidated sediment accumulated at the break of the steep slope. b) KFZ delimits the southeastern boundary of the Plio-Quaternary Hoyran basin. c) Configuration of paleostress orientations based on fault slip data collected from KFZ around Aşağıtirtar (equal area, lower hemisphere projection). 127
- Figure 4.25. Field view of the eastern tip of the Yaka Fault Zone (YAFZ) (a). Well-developed slickenline on the fault surface (b) and stereographic plot of these slip data on the Schmidt's lower hemisphere net (c). 128

Figure 4.26. Vein formation in the Göksöğüt formation. (a) Approximately E-W striking, syntaxial calcite vein, where crystals grow from the wall rock into the vein. (b) Crosscutting relationship between vein sets. Young vein (approximately N-S striking) cuts through and offsets the older vein (approximately E-W striking).	130
Figure 4.27. a) Stereographic projections of veins and b) contour diagrams of poles to the veins (red dots) and orientation of constructed principal stress directions (equal angle, lower hemisphere projection).	131
Figure 4.28. (a) Bidirectional rose diagram of all fault strikes. Note that dominant direction is NE-SW. (b) Graph shows the histogram of the fault dip amounts. (c) Stereographic plots of fault planes, slip-lines and constructed paleostress orientations (equal area lower hemisphere projection).	132
Figure 4.29. a) Close-up view of overprinting slickensides and b) schematic illustration of their order. Numbers indicate the sense of movement (1: dip-slip normal sense, 2: Strike-slip sense)	135
Figure 4.30. a) Syn-sedimentary faults with at the base of the Yarikkaya formation. b) Close up view showing dextral strike-slip slickensides. c) Interpreted image.....	139
Figure 4.31. a) Syn-sedimentary normal faults with at the base of the Yarikkaya formation, b) close up figure showing slickensides indicate normal sense of movement, c) close-up view of the mesoscopic scale syn-sedimentary normal fault which causes vertical displacement of the coal levels, d) rose diagram shows the direction of the all syn-sedimentary faults, notice that orientation of minor stress is variable.	140
Figure 4.32. Density diagrams (a, b and c) for principle stress orientations (σ_1 , σ_2 and σ_3 , respectively) and frequency distribution of Φ values for whole data (d). Notice that the σ_1 is significantly (sub-)vertical while σ_2 and σ_3 orientations are horizontal.....	141
Figure 4.33. Spatial distribution and minor stress (σ_3) orientations (black arrows). Numbers refer to sampling sites. Red arrows indicate strike-slip solutions. Note that minor stresses tend to be orthogonal to nearby major faults.....	142
Figure 4.34. Temporal distribution and minor stress (σ_3) orientations (red and black arrows). Numbers refer to sampling sites. Red and blue arrows are used to indicate roughly E-W and N-S extension direction. Note that extension directions changing from E-W to N-S.	144
Figure 5.1. Correlation of the unconformity bounded lithologic units of each basin. Note that three basic angular unconformity surfaces in each basin are correlated with each other.	151

Figure 5.2. Paleogeographic maps showing the Early and Middle Miocene shorelines and the continental basins in the Isparta Angle (position of the Lycian Nappes adopted from Hayward 1984).	153
Figure 5.3. a) Geological map of the Altınapa Basin with major structures and dominant paleostress orientations (arrows) in its different parts. b) Rose diagram of horizontal component of minor principal stress directions prepared from whole data (σ_3). Note radial geometry of the extension directions where three sets dominate over other orientations.	155
Figure 5.4. a) Geological map of the Ilgın Basin with major structures and dominant extension directions (arrows) b) Rose diagram prepared from horizontal component of minor principal stress orientations. Note radial geometry of the extension directions where three sets dominate over other orientations.	157
Figure 5.5. a) Geological map of the Yalvaç Basin with major structures and dominant directions of horizontal component of minor principal stress. b) Rose diagram prepared from the horizontal component of minor principal stresses obtained in all sampling sites. Note radial geometry of the extension directions where three sets dominate over other orientations.	159
Figure 5.6. The major structures and dominant stress orientation directions and moment tensor solutions of major earthquakes overlaid on shaded relief image and Neogene units of the study area.	160
Figure 5.7. Paleostress stratigraphy of study area. Rose diagrams show horizontal component of the minimum stress (σ_3) for each basins since Early Miocene. Note that although, there is roughly domination of NW-SE and NNE-SSW directed extension, in reality, the horizontal component of the minor stress is not constrained in any particular direction and it is multidirectional over time. This implies uniaxial vertical stress conditions.	162

CHAPTER 1

INTRODUCTION

1.1 General

In the eastern Mediterranean region, convergence between Africa and Europe since the Cretaceous was accommodated by northward subduction of various branches of the Neotethys Ocean (Şengör and Yılmaz, 1981; Barrier and Vrielynck, 2008). As a result, the geology of Turkey includes a number of suture zones that demarcate the former positions of now subducted oceans. The most important of these is the İzmir-Ankara-Erzincan suture zone (Figure 1.1), where the Pontides to the north, belonging to Eurasia since the early Mesozoic (Torsvik and Cocks, 2009), and the Tauride-Anatolide Platform to the south, rifted away from Gondwana in the Triassic, collided after the complete subduction of the northern branch of the Neotethys. The collision of the Tauride-Anatolide Platform with the Pontides started at the end of Cretaceous and may have lasted until the end of the Eocene (Okay and Özgül, 1984; Kaymakci et al., 2009; Meijers et al., 2010; van Hinsbergen et al., 2010; Gülyüz et al., 2012). A second Cretaceous to Paleocene subduction zone existed to the south of the İzmir-Ankara suture zone, between the Kırşehir Block and the Taurides in central Turkey (the Inner Tauride Suture; e.g. Okay et al., 1996; Pourteau et al., 2010) and led to the formation of the Tauride fold-thrust belt in southern Turkey.

To the south of the Taurides, oceanic crust of the southern branch of the Neotethys still subducts today in the Cyprus subduction zone (Khair and Tsokas, 1999; Biryol et al., 2011) (Figure 1.1). In Eastern Turkey, the southern branch has been entirely subducted and is demarcated by the Bitlis suture zone, with the arrest of subduction at the end of the Middle Miocene (Şengör and Yılmaz, 1981; Faccenna et al., 2006; Hüsing et al., 2009). Subduction below the Taurides is in its latest stages, and was probably associated with slab break-off and slab roll-back processes since the Middle Miocene (Faccenna et al., 2006; Gans et al., 2009; van Hinsbergen et al., 2010; Biryol et al., 2011).

The Tauride fold-thrust belt forms a carbonate-dominated mountain range in southern Turkey, and is characterized by dominantly southward thrusting which lasted until late Eocene time (Ricou et al., 1975; Andrew and Robertson, 2002; Özer et al., 2004; Mackintosh and Robertson, 2009; Meijers et al., 2011). Although the belt shows large wavelength folds and thrusts, its high topography today is bounded by normal faults that bound Neogene sedimentary basins. These basins are filled by marine to continental sediments and volcanics, and were formed in the overriding plate of the present-day Cyprus subduction zone. Their development may therefore shed light on the

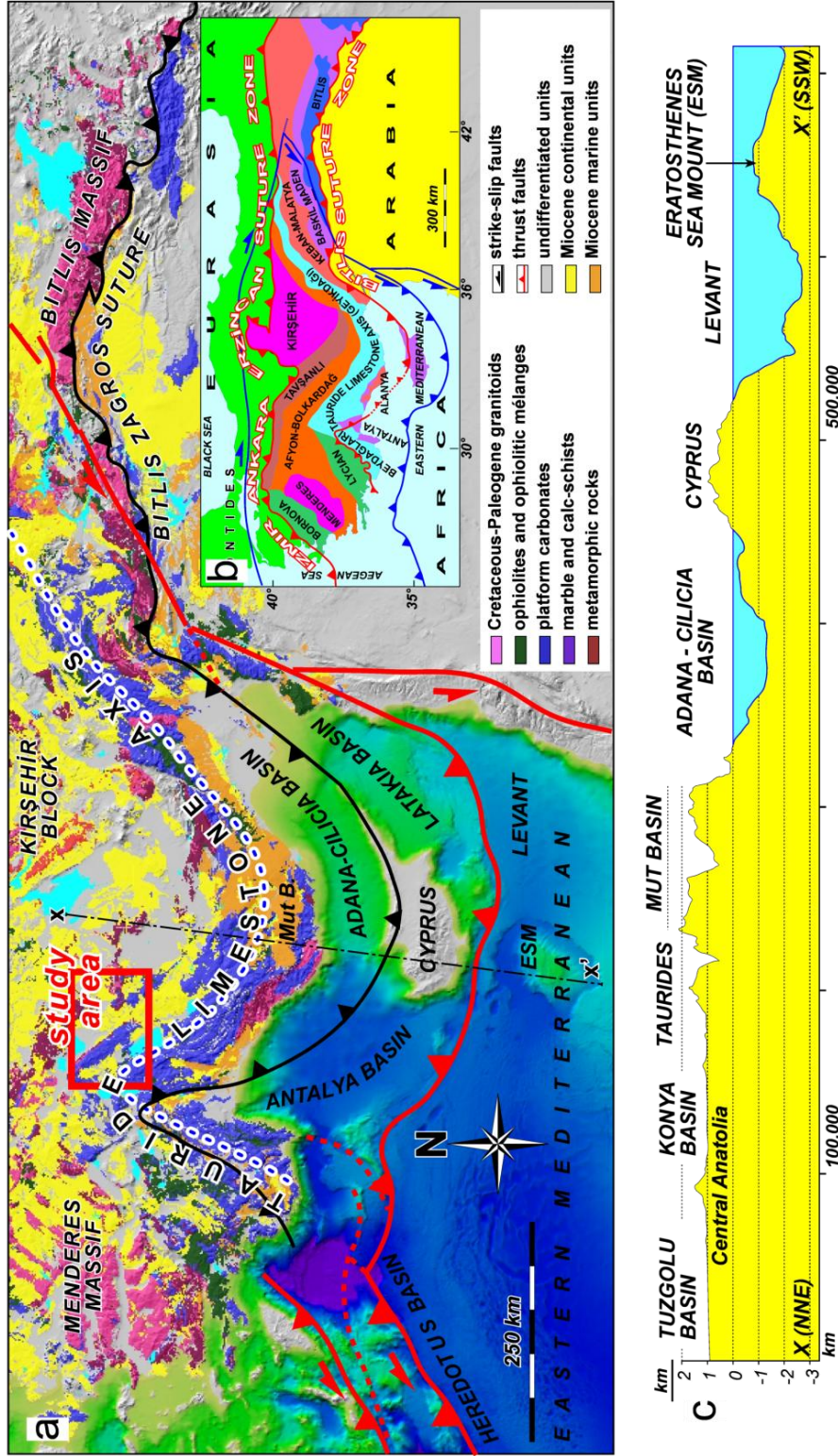


Figure 1.1. a) Major tectonic zones of Turkey (modified from Okay et al., (1996) and Kaymakci et al. (2010). b) simplified geological map of southern Turkey overlaid on an SRTM topographic and bathymetric image (geological map is simplified from MTA 1/500,000 map series). c) Profile along the line XX'. Note that altitude of the Tauride range is ~1 km higher than the elevation of central Anatolia.

geodynamic evolution of the eastern Mediterranean subduction zone since the Miocene. The dominantly marine basins are located mainly in the southern limb of the belt and include the well-described Adana, Mut and Antalya (also comprising the Manavgat, Köprüçay and Aksu) basins (e.g. Yetiş, 1988; Poisson et al., 2003; Bassant et al., 2005; Eriş et al., 2005; Karabıyıkoglu et al., 2005; Derman and Gürbüz, 2007; Gül, 2007; Çiner et al., 2008; Darbaş and Nazik, 2010; Janson et al., 2010; Cosentino et al. 2012; Schildgen et al., 2012). A diachronous marine transgression flooded the southern part of the belt in Cyprus from the late Oligocene onward, and reached the Antalya, Mut and Adana regions in the north during the Early Miocene (Bassant et al., 2005).

To the north of the present-day Taurides, intra-continental basins started to form during an ill-defined time interval in the Neogene. These include the Altınapa, Ilgın and Yalvaç basins (Figure 2), descriptions of which are limited to Turkish language literature (Göğ er and K ıral, 1969;   zcan et al., 1990; Yağmurlu, 1991a, b; Eren, 1993; 1996;   zkan, 1998;   zkan and S  g  t, 1999). Motivated by the poor geological research on these basins, this study aims to improve geological understanding in context of the regional geodynamics and uplift of the Anatolian Plateau during the late Neogene.

1.2 Aims of this thesis

The study area is located in a transition zone between two tectonic domains of East and West Anatolia. Neogene tectonic framework of the East Anatolia is controlled by collision and further northwards convergence of Arabian Plate towards the Eurasian Plate, while Western Anatolia is affected has been experiencing continental extension consequent to combined effect of orogenic collapse, tectonic escape of the Anatolian Block and back-arc extension associated with roll-back of the northwards subducting African Plate. Altınapa, Ilgın and Yalvaç basins are continental and they are located in a zone where these two tectonic regimes interact. On the other hand, the average altitude of these basins is around 1.0 km and the surrounding Taurus Mountains rise as high as 2 km above sea level. Recent studies (  iner et al. 2008, Cosentino et al. 2012, Schildgen et al 2012) in the area about 30km south of the study area indicated that the marine deposits above Taurides are as young as Tortonian and now they are uplifted more than 2 km. This implies that marine continental transition was close to the study area during the Late Miocene. In this regard, sedimentological characteristics of the basins' infill are very crucial: (i) to locate northern limits of paleo-shorelines as a base level during the Miocene, (ii) to provide constraints on the uplift history of southern and Central Anatolia and as well as (iii) to improve geological understanding of the region within the context of west Anatolian extensional and East Anatolian compressional tectonic regimes. In this respect, this thesis is concerned mainly on the tectono-stratigraphical evolution of Altınapa, Ilgın and Yalvaç basins and their bearing on the uplift history of central Anatolia and the Taurides. In order to reach these goals, following specific

questions required have to be answered.

1. What is the stratigraphy of the infill successions within the Altınapa, Ilgın and Yalvaç basins?
2. What are the sedimentological characteristics, depositional environments and paleogeography of their infills?
3. What were the tectonic regimes during their deposition and how it evolved in time?
4. What are the major tectonic structures that controlled and shaped 3D geometry of these basins?
5. What are the temporal and spatial relationships of these structures, their kinematics and basin infill during the Neogene?
6. What is the role and significance of these basins within the geodynamics of Eastern Mediterranean during the Neogene?

1.3 Approach taken

This study integrates several data sets obtained from various geological disciplines in order to provide necessary to fulfill the stated objectives of the thesis. The methods can be classified into three groups as remote sensing, field studies, laboratory and office studies.

Field mapping combined with processing and interpretation of satellite images and aerial photos was performed for each basin. During mapping following steps were taken and detailed studies were carried out: (1) measurement of stratigraphic sections to document stratigraphy and facies characteristics of each stratigraphic unit within each basin and to locate the position of major unconformities and key horizons, (2) determination of major and as well as mesoscopic faults for slip data collection in order to infer the orientations and relative magnitude of principal stresses and their spatial and temporal behavior and (3) analysis and construction of true-to-scale and sketched cross-sections to illustrate the relationships among various lithologic associations and to indicate how deposition and tectonism interacted during basin evolution since Early Miocene.

Following field based studies, collected data and samples were analyzed to determine their petrographic and sedimentological characteristics and isotope study were carried out to determine age of volcanic rocks. Fault-slip data and other structural data were analyzed and elaborated to understand tectonic development and paleostress inversion. Paleostress inversion technique was performed, by using Angelier's software (Angelier, 1994), to resolve the kinematics of the local and regional faults. For other structural data various orthographic and stereographic projection techniques were applied.

Angelier's method was utilized in the reconstruction of the stress ellipsoid, which was used to determine relative magnitudes and orientations of the principle stresses (Angelier 1994). Based on the quality estimator (RUP and ANG) and the value of the stress ratio based on reduced stress tensor (Φ), stress configuration for each sites were constructed and resultant solutions are used for inferring the deformation pattern and kinematics for each of the basins.

All these studies improved the understanding of deformational and depositional mechanism of Altınapa, Ilgın and Yalvaç basins, and also helped to understand temporal and spatial relationships for each basin and among these basins.

1.4 Organization of thesis

The thesis is organized as follows.

The first chapter provides the introduction to the thesis, which basically contains information about region, aim of the thesis, methods, the study area and previous studies.

Chapter 2, 3 and 4 provide the Neogene stratigraphical and structural characteristics of the Altınapa, Ilgın and Yalvaç basins, respectively. Each chapter provides updated stratigraphy of the basin infill calibrated and dated by paleontological data and Ar/Ar techniques. Also, kinematic evolution of each basin and the study area as a whole was, based on fault-slip data, discussed.

Chapter 5 integrates results of present study, and that form the literature and unpublished studies and discusses their tectonic significance in the better understanding of the regional tectonic evolution.

Chapter 6 is devoted to the conclusions of the thesis.

1.5 Study area

Taurides belt constitutes the link between Alpine and Himalayan chain - longest mountain chain - formed due to subduction of Tethys ocean and collision of continental plates that were part of Gondwana into the Eurasian plate since Mesozoic. Morphologically Anatolia is a plateau which rises approximately 1 km above sea level in its central part and its elevation increases eastwards towards Iran as high as 2 km above mean sea level. It is marked by Black Sea Mountains in the north and by the Taurus Mountain chain; both mountain ranges rise more than 2 km average above sea level (Figure 1.1).

Present day tectonics of Anatolia is shaped by northward convergence of Arabian Plate along the Bitlis Zagros Suture, northwards subduction of African Plate under Anatolia along Cyprean and Hellenic trenches, and westwards escape of Anatolia Block along the North and East Anatolian fault zones possibly facilitated by push in the east and pull in the south and the west, possibly due to Arabian collision and roll-back and slab edge processes of the subducting African oceanic crust.

The recent publications related to the first order mechanisms responsible for the high topography of Anatolia and its northern and southern mountain chains that are running approximately parallel to the present shorelines indicated that the mantle lithosphere of Anatolia is either very thin or absent (e.g. Facenna et al., 2006; Gans et al., 2009; Özacar et al., 2010; Biryol et al., 2011). However, little is known about the inception age, extend, and rate of uplift.

The study area is in south-central Anatolia located in a very strategic position within and northern edge of the Tauride Mountains and it has the potential to solve some of the issues related to uplift of the Taurides and the central Anatolia. Because the area is characterized by thick continental deposits and is its close proximity to youngest marine deposits on top of the Taurides; the marine sediments exposed around Beyşehir and Isparta lie an elevation about 1500 m above sea level (Figures 1.1 & 1.2). At present, the study area is located in a zone where east Anatolian compressional-contractional regime is dominated by west Anatolian extensional tectonic regime. In this regard, the study area has the potential to provide new insights into the easternmost extend of west Anatolian extension and tectonic development of the region early Miocene onwards.

The study are comprise three intra-continental basins namely, Altınapa, Ilgın, and Yalvaç basins (Figure 1.2) that contain thick continental deposits spanning from Early Miocene to Recent, with marked regionally correlatable unconformities. Although the marine basins in the region are relatively well studied, the studies on these continental basins are scarce. This is possibly due to difficulty in dating continental deposits as well as geological complexity of these basins.

Tectonically, the Altınapa and Ilgın basins are located at the eastern limb of the Isparta Angle (IA). They are separated by the Akşehir-Afyon Fault Zone (Figure 1.2) from the Yalvaç Basin which is located within the north-central part of the IA.

All these continental basins are located within the Ankara and Konya quadrangles of the 1/500.000 scale geologic map of Turkey prepared by General Directorate of Mineral Research and Exploration (Ankara, Turkey). Additionally, they are located within K25-K28, L25-L29, M25-M29 1/25.000 scale topographic maps which were used during field works.

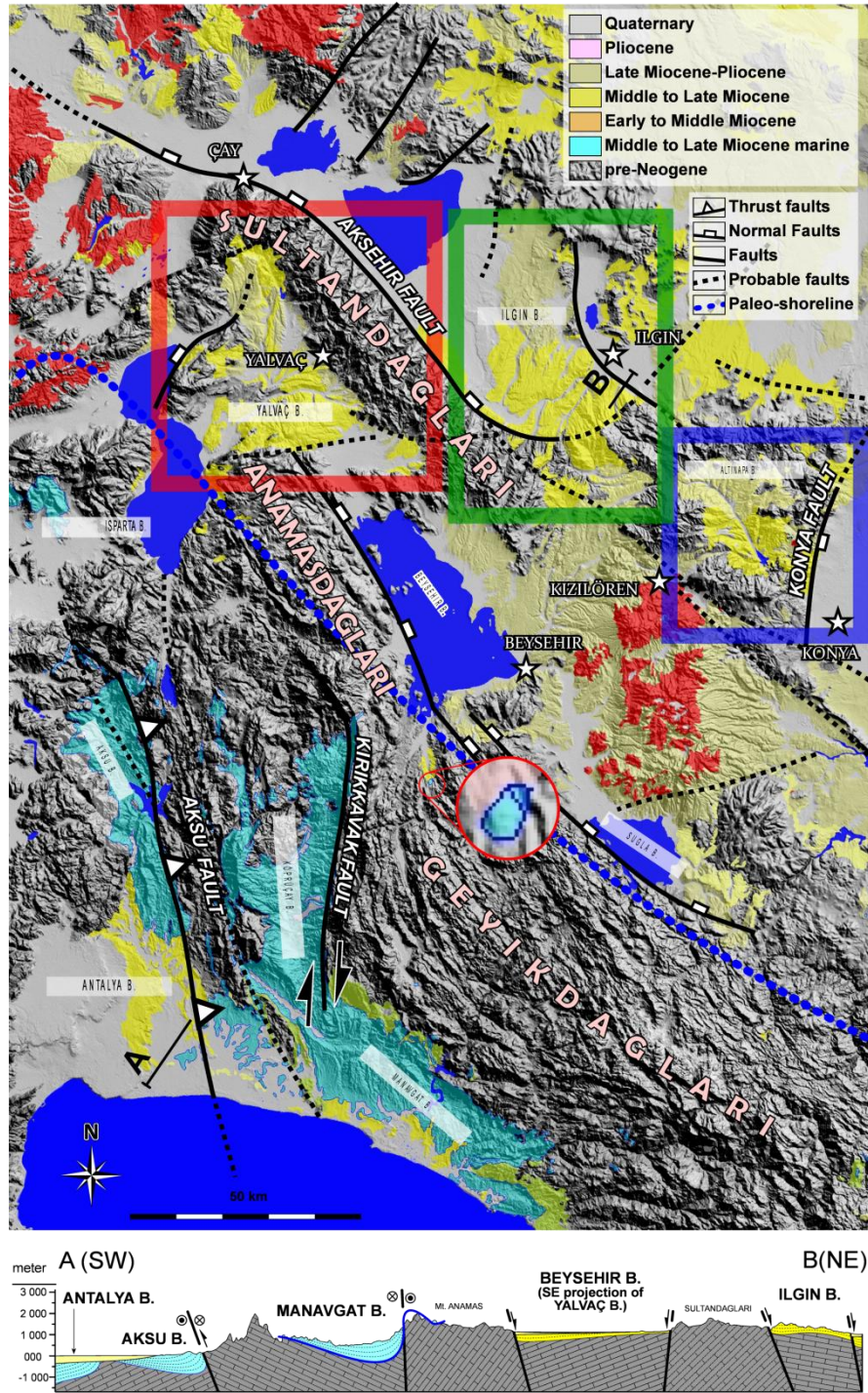


Figure 1.2. Simplified geological map of the Isparta Angle illustrating locations of the study area and conceptual cross-section along line AB depicting the relationship between marine and continental deposits. Note blow up image indicating small outcrop of marine deposits around Beyşehir. Blue dashed line is the northernmost extend of the paleo-shoreline during the late Miocene.

1.6 Previous studies

Previous studies are summarized for each basin separately as Altınapa, Ilgın and Yalvaç basins, respectively.

1.6.1 Studies on Altınapa Basin

Previous studies carried out so far are in regional scale and none of them are directly related to Altınapa Basin. However, considerable studies have been carried out to understand the geology of the surrounding region. Göğ er and K ıral (1969) carried out one of the first comprehensive study where volcanic units around K ız ıl oren (Figure 1.2) and its vicinity were mapped and defined. But, various Neogene units were counted together and were not studied separately.

After this pioneering study, Keller et al. (1977) studied on volcanic rocks in Konya region and introduced the relationships between the volcanic rocks and its surrounding sedimentary rocks. Additionally, the results of K/Ar radiometric ages obtained from Konya volcanics were also presented in the study.

G orm    (1984) and   zcan et al. (1988) studied the pre-Neogene units which constitute the basement rocks of the Altınapa Basin. Unfortunately, Neogene stratigraphy of the basin has been studied by a very limited number of researchers including Eren (1992, 1993, 1996),   zkan (1998),   zkan and S  g  t (1999). A detailed subdivision of the Neogene units into six lithostratigraphic units was made by Eren (1993). Finally,   zkan (1998) and,   zkan and S  g  t (1999) studied small part of the Altınapa Basin. They provided stratigraphic data and introduced a revised stratigraphy where they proposed five formations for the Neogene unit in the region.

There is no any study related to structure, geometry and the kinematics of the structures in the Altınapa Basin.

1.6.2 Studies on Ilgın Basin

Detailed studies on Ilgın Basin were performed in order to evaluate the coal potential and reserves of the basin. Lahn (1945), Wedding (1968), and Bektimuro  lu (1978) focused directly on lignite bearing Neogene units of the region. These (unpublished) studies sponsored by Mineral Research and Exploration Institute (MTA) of Turkey.

Niehoff (1961) carried out a very detailed study on the basement rocks of the basin. In this study, the relationships between various pre-Neogene units were discussed. Additionally, van der Kaaden (1966) performed a study focused on the metamorphic units in the region and then Weisner (1968) defined the age ranges of these metamorphic units.

The study performed by Göğ er and K ıral (1973) addressed the basement rocks of the basin as well as the Neogene units for the first time. However, the authors did not distinguish different Neogene units; instead, they were grouped together and defined as single unit namely “Dilek i formation”.

Umut et al. (1990) studied the basement rocks exposed in an area east of the I ı ın and north of Alt ınapa basins. In this study, Silurian-Devonian limestones forming the basement rock assemblages at the eastern part of the basin were studied. Eren (1992, unpublished) carried out a similar study and established the tectostratigraphy of the basin.

In addition to these geological studies, palyno-flora of the I ı ın Basin is studied by some researchers like  a  lar and Ayhan (1991), Tuno  lu and  elik (1995) and Karayi  it et al. (1999). These studies proposed, based palynological data and ostracod fauna variable ages for the I ı ın lignites

The most recent studies on I ı ın Basin are carried out by the Huseyinca and Ya  ar (2007) and Koopman et al. (2012). Huseyinca and Ya  ar (2007) investigated the northern part of the I ı ın province and studied the stratigraphy and the tectonic history of the  avuş u region. Koopman et al. (2012) linked basin scale observations with the regional structural setting and proposed a kinematic scenario for the evolution of the I ı ın Basin based on fault-slip data and morphological observations.

In addition to all, there are a number of studies on the Sultanda  ları Mountains and Ak  ehir-Afyon Fault zone, which is the most prominent structure in the region and limits the I ı ın Basin in the west. Seismicity and seismotectonics of these structures are studied by Ko  yi  it et al. (2000), Ko  yi  it and   zacar (2003), Ko  yi  it and Deveci (2007).

1.6.3 Studies on Yalva  Basin

First studies on Yalva  Basin were performed by several researchers, such as Lahn, (1940); Wedding, (1954); F  st, (1955); G  ktunal ı, (1957); Pekmezciler, (1958) on behalf of the Mineral Research and Exploration Institute (MTA) of Turkey in order to reveal lignite potential of the basin. These studies were directly related to Yalva  Basin

and mainly concentrated on lignite-bearing Neogene units. However, they unpublished reports in MTA.

The Sultandağları Mountains delimiting the Yalvaç Basin in the north and east is studied by Demirkol et al., (1977), Demirkol, (1982, 1984), Demirkol and Sipahi (1979), Demirkol and Yetiş (1985) and Eren (1990) who carried out considerable studies to understand the geology of the region. These studies are focused on pre-Neogene units which form the basement rocks of the Yalvaç Basin.

After these pioneering studies, the detailed Neogene stratigraphy of the Yalvaç Basin is established by Yağmurlu (1991a) and lithostratigraphy of the Neogene deposits in the basin were divided into five main stratigraphic units. Moreover, Yağmurlu (1991b) studied on tectono-sedimentary characteristics and structural evolution of the Yalvaç Basin. In this study, the tectonic and stratigraphic characteristics of the area were discussed within the regional kinematic context. It is proposed that four different stress regime has been effective over the region since Eocene.

In addition to all, several other studies were also performed in the region and most of them are related mainly to Isparta Angle and its development mechanism (Barka et al., 1995; Yağmurlu et al., 1997; Glover and Robertson, 1998; Koçyiğit et al., 2000 and Poisson et al., 2003).

CHAPTER 2

TECTONO-SEDIMENTARY EVOLUTION AND GEOCHRONOLOGY OF THE MIDDLE MIOCENE ALTINAPA BASIN (KONYA)

In this chapter, stratigraphic units and geologic structures of the Altınapa Basin are described and evaluated in detail.

The Altınapa Basin, located in the eastern limb of the Isparta Angle (Blumenthal, 1963), is one of the best exposed intra-montane continental basin in the region (Figure 1.2). It has a clastic and volcano-sedimentary infill of more than 850 m thick and rests nonconformably on the metamorphosed Mesozoic carbonates of the Tauride Belt, as well as on the high-pressure rocks of the inner-Tauride suture zone (Pourteau et al., 2010). These high-pressure rocks, with Cretaceous to Paleocene metamorphic ages, include Silurian-Permian meta-carbonates, flysch-type metaclastics and meta-magmatic rocks (Karakaya, 1991), and massive Triassic-Cretaceous platform-type meta-carbonates, meta-dolerites and continental meta-clastics (Eren, 1996).

2.1 Lithostratigraphy

The infill of the Altınapa Basin is dominated by continental clastic sediments, lava flows and volcanoclastic deposits. It was first mapped by Göğür and Kırıl (1969), who included the entire Neogene stratigraphy in the Dilekçi formation. After this pioneering study, the researches were concentrated mainly on the Neogene stratigraphy (Eren, 1992, 1993, 1996; Özkan, 1998; Özkan and Söğüt, 1999). Eren (1993) made a detailed subdivision of the Neogene Dilekçi formation into six lithostratigraphic units. Özkan (1998) and Özkan and Söğüt (1999) provided additional stratigraphic data and introduced a revised stratigraphy with five new formations. For the sake of convenience, the lithostratigraphy of the Neogene deposits in the Altınapa Basin is revised and defined three main stratigraphic units, namely the lower and upper Altınapa groups, and the Topraklı formation, separated by unconformities. Below, their lithology, age and contact relationships are described and a first-order interpretation of their depositional environments is provided (Figure 2.1).

AGE	UNITS	LITHOLOGY	DESCRIPTION
Quat.	Alluvium		alluvial plain and alluvial fan sediments (gravel, sand, silt, and mud)
Late Miocene-Pliocene	Topraklı Fm.		partly consolidated, unsorted, matrix supported polygenic red conglomerate, sandstone and mudstone
Middle Miocene	upper Altınapa group (UAG)		ANGULAR UNCONFORMITY pinkish block-and-ash deposits (clasts are derived from ~90% volcanics, and ~10% limestone) white tuff/tuffite
			creamy-white, thick-bedded, well cemented algal limestone
			intercalations of marl and tuffites. Usually maximum bed thickness is 20-30 cm.
			pyroclastic material, volcanic blocks (60-70 cm) and lava flows with andesitic composition
			Ar/Ar age: 11.54 ± 0.02 Ma. unwelded ignimbrite with floating pumice fragments (3-4 cm)
			Ar/Ar age: 11.67 ± 0.05 Ma Ar/Ar age: 11.88 ± 0.26 Ma
Early-Middle Miocene	lower Altınapa group (LAG)		ANGULAR UNCONFORMITY white-creamy thick-bedded, well cemented algal limestone
			variegated siltstone, shale and marl alternation, intercalated with thinly bedded limestone, and organic rich horizons
			yellowish sandstone-bluish shale marl alternation sandstones are bioturbated, occasionally cross-bedded, fossil (fresh water gastropods) rich horizons
			unsorted, grain-supported, polygenetic conglomerates with angular to subangular pebbles (smaller than 10 cm diameter) derived from limestones (80%) and nearby ophiolitic rocks (20%)
Pre-Miocene	Basement		poorly sorted, matrix supported, upwards fining, polygenetic conglomerates with clasts derived from limestones (60%) and nearby ophiolitic rocks (40%)
			NONCONFORMITY Silurian-Permian meta-carbonates, turbiditic meta-clastics and meta-igneous rocks, Triassic-Cretaceous continental meta-clastics, platform type thick meta-carbonates and meta-diabasic dykes

Figure 2.1. Generalized stratigraphic column for the Altınapa Basin.

2.1.1 Lower Altınapa Group (LAG)

The LAG is characterized by conglomerate, sandstone and siltstone at the bottom, grading upwards and basinwards into claystone, marl, sandstone and medium to thick-bedded massive lacustrine limestones. These lithologies were included in the Dilekçi formation by Göğer and Kırıl (1969). Özkan and Söğüt (1999) divided this sequence into three separate formations, where lower conglomeratic unit is named “Sille formation”, intermediate stromatolitic limestone unit, “Yalıtepe formation” and upper limestone/marl unit, “Ulumuhsine formation”. These units are well-exposed along the Kızılören Fault (Figures 2.2 & 2.3a), near Dereaşıklar (Figure 2.4) and north of Küçük Muhsine (Figure 2.5); it is considered as the type locality for the LAG. The group unconformably overlies the Mesozoic basement, and is unconformably overlain by the upper Altınapa group.

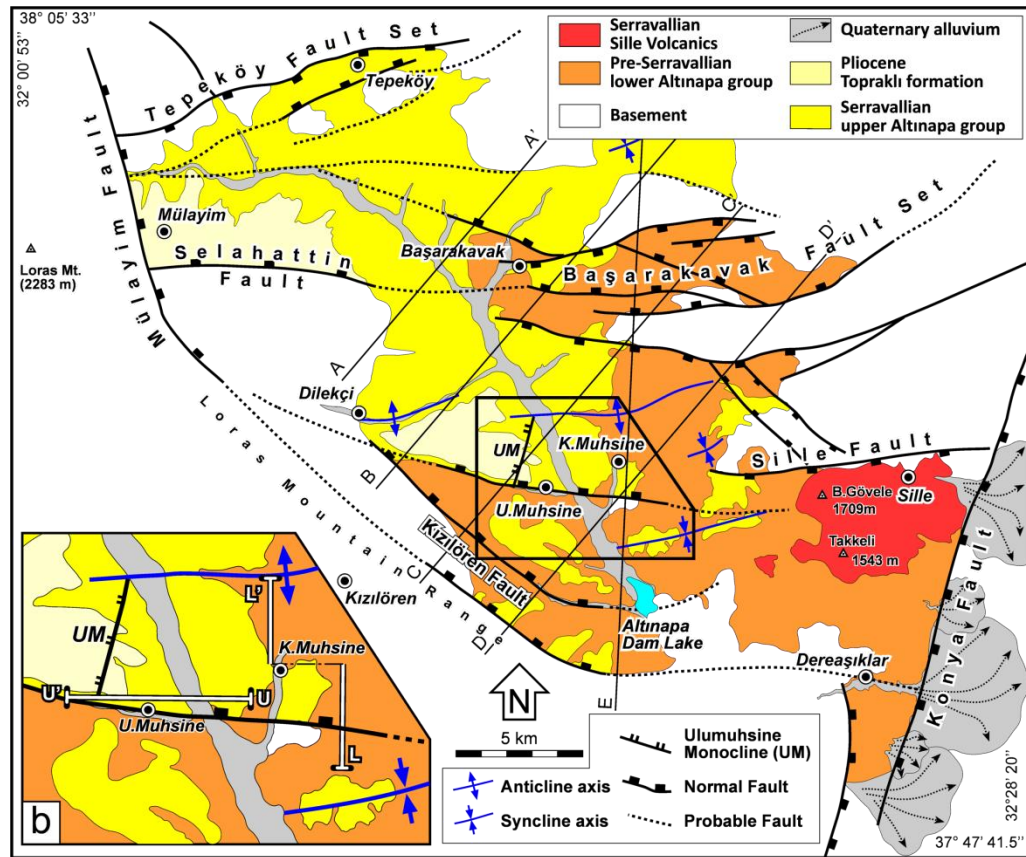


Figure 2.2. (a) Revised geological map of the study area from the 1/500000 scale geological map produced by MTA. (b) Inset map showing the location of the measured sections for the lower (L-L') and upper (U-U') Altınapa groups. Dashed lines named as A, B, C, D and E indicate the trace of the cross-sections in Figure 17.

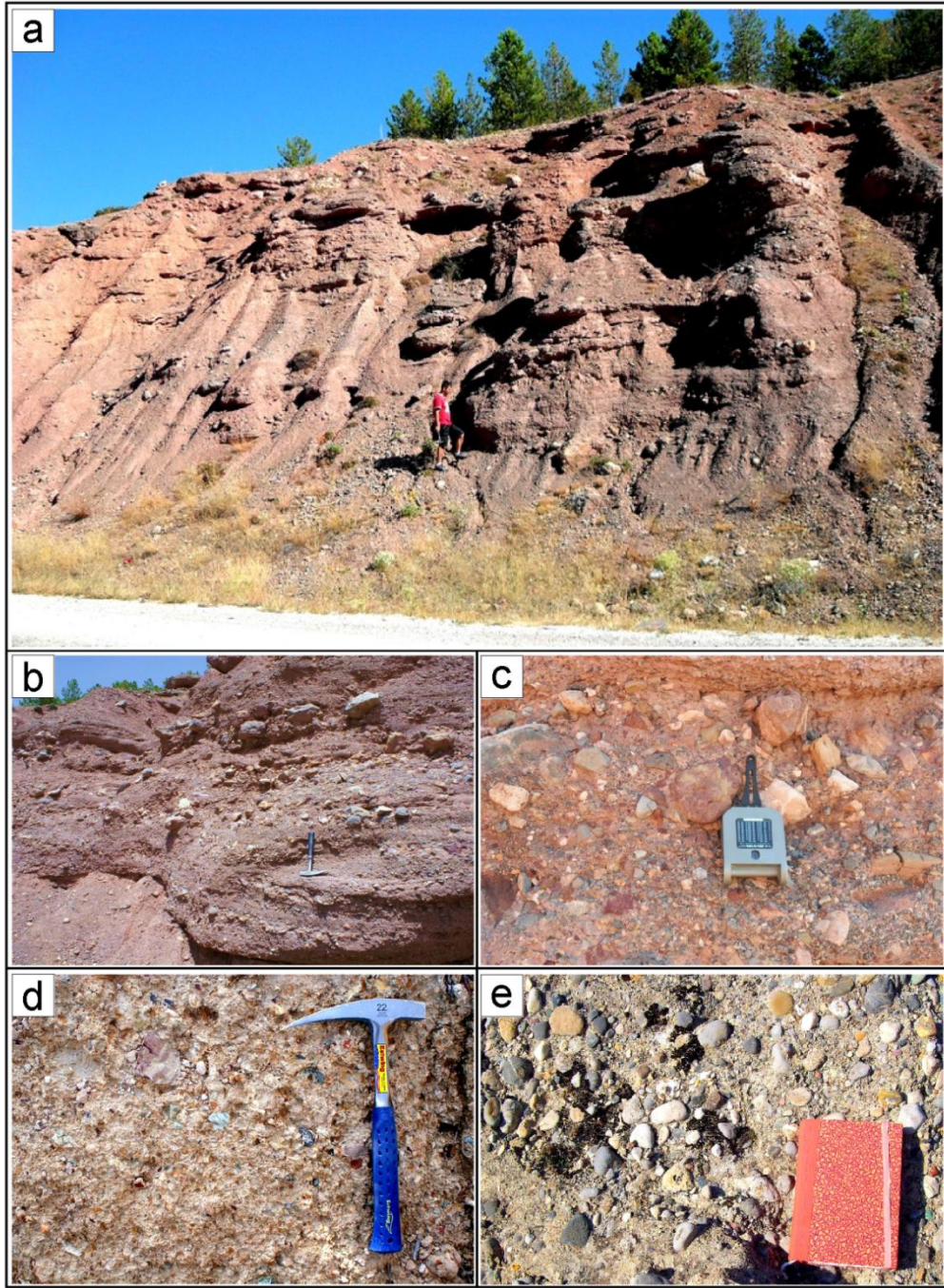


Figure 2.3. Field views of basal conglomerates from the lower Altınapa group along the Kızılören Fault (a). Poorly bedded basal conglomerate explored along the Konya-Beyşehir road (b). Close-up view of the basal conglomerate with reverse graded beds (c). Note coarse, poorly sorted, sub-angular conglomerates. Matrix-supported basal conglomerate, located close to Dereaşıklar (d). The conglomerate interfingers with clast-supported, polymict conglomerates (e).

The sequence starts, at the bottom above the high-relief carbonate basement of the Loras Mountain, with coarse, angular, well-cemented, limestone-dominated breccias that grade upwards into reddish/purple, unsorted and polymict, sub-angular to sub-rounded pebble to boulder-size (occasionally up to 1 m diameter) conglomerates (Figure 2.3b). At stratigraphically higher levels, sedimentary structures such as pebble imbrications and channel deposits are occasionally observed. The large clasts are dispersed in a poorly sorted, finer matrix where conglomerates typically appear as matrix supported. The clasts consist mostly of sub-rounded limestones (60 %) with calcite veins, sub-angular radiolarites, various radiolarian cherts and sub-rounded but ellipsoidal ultramafic rocks (~30%) dominated by serpentinites set in a silty-sandy matrix with ironoxide cement (Figure 2.3c). The clast composition compares well with the regional basement lithology. The maximum observable thickness of this succession is approximately 200 m along the SW margin of the basin.

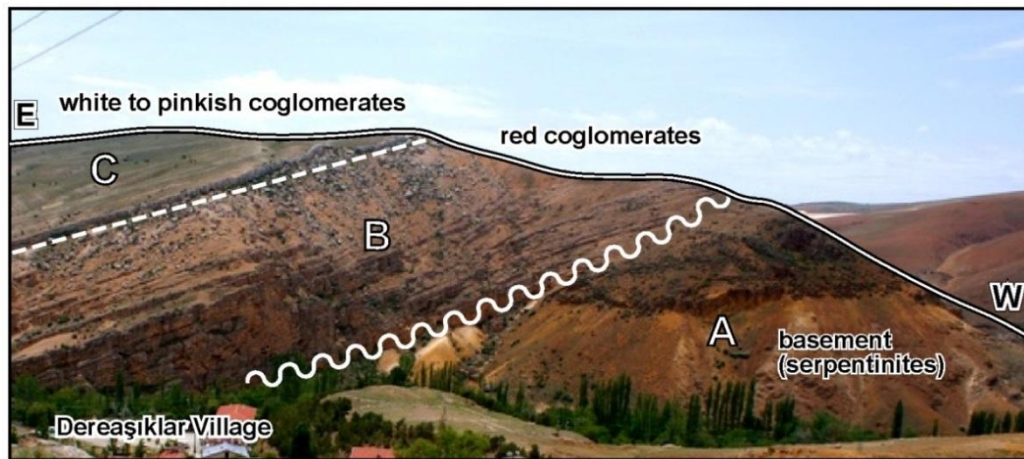


Figure 2.4. Field view of the basal conglomeratic unit (B and C) at the lower Altınapa Group near Dereaşıklar. Note that the Neogene conglomeratic unit overlies unconformably Mesozoic ophiolitic *mélange* (A). View towards the East.

Around Dereaşıklar, the LAG is composed of red, thick-bedded (Figure 2.4), matrix supported (Figure 2.3d) conglomerates, interfingering with dark gray to white, clast-supported, polymictic conglomerates, consisting of dominantly sub-angular to sub-rounded pebbles up to 10 cm diameter, with chert (20%) and limestone (80%) derived directly from the nearby basement (Figure 2.3e). It unconformably overlies the basement of serpentinitized ophiolitic *mélange* (Figure 2.4).

The location of the measured section (Figure 2.6) is chosen at north of Küçük Muhsine where, apart from the red basal conglomeratic unit, the complete sequence is

well-exposed. In the measured section, the sequence begins with conglomerates (Figure 2.7a), which correspond to the dark gray to white, clast-supported, polymict conglomeratic unit in Dereaşıklar. The sequence continues upward with yellowish occasionally cross-bedded and bioturbated, fresh-water gastropod-bearing sandstones (Figure 2.7b). It is succeeded, towards the central and NE parts of the basin, by rhythmic alternations of siltstone, green-blue coal bearing claystone, marls (Figure 2.7d), and medium to thick (15 cm to 5 m) well-bedded fresh water stromatolitic limestone (Figure 2.7c). The LAG has a minimum thickness of 430 m.

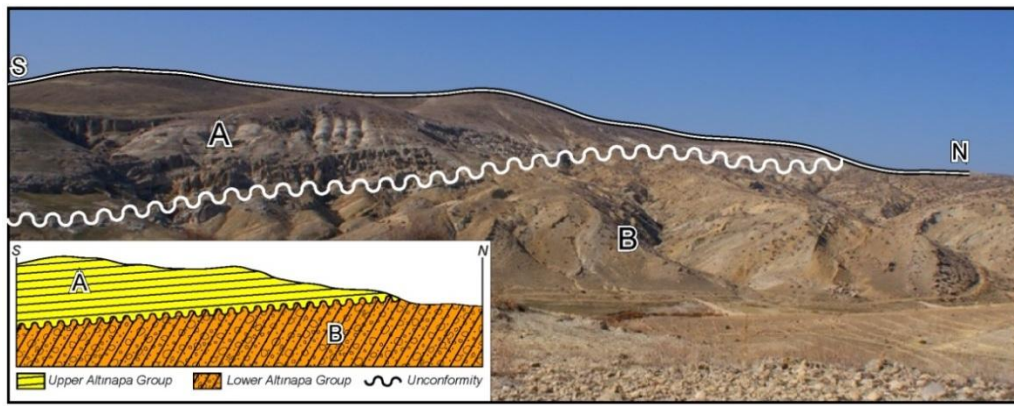


Figure 2.5. Field view of the angular unconformity between the lower (B) and upper (C) Altınapa groups.

From the Loras Mountain in the west to Küçük Mühsine in the east, there is a gradual decrease in grain size from reddish conglomerates to fine-grained yellowish/white marly deposits (Figure 2.8 and Figure 2.9). The unconformity between the LAG and the underlying basement is well exposed in an erosional window to the east of the Altınapa Lake near Küçük Muhsine (Figure 2.2). The LAG in this area consists of clastics much finer than those adjacent to Loras Mountain. Similar grain size distributions are also observed elsewhere in the basin, and suggest that the basin detritus was dominantly shed from the SW margin. The spatial distribution of various lithologies as shown in Figure 2.9 is consistent with inference source area to the southwest.

Any fossils were not observed in the lower conglomeratic unit of the LAG, and previous studies (Eren 1993; Özkan 1998; Özkan and Sögüt, 1999) also did not report any fossil assemblages in this part of the LAG. To the west, however, around Kızılören, well outside the Altınapa Basin, Görmüş (1984) reported vertebrates fossil, including *Protoryx carolinae* Major, *Gazella deperdita* Gaudry, *Sus erymanthius* Roth and Wagner, *Prostrepticerus rothundicordis* Weithofes, *Ovis* sp. and *Hiparion* sp.,

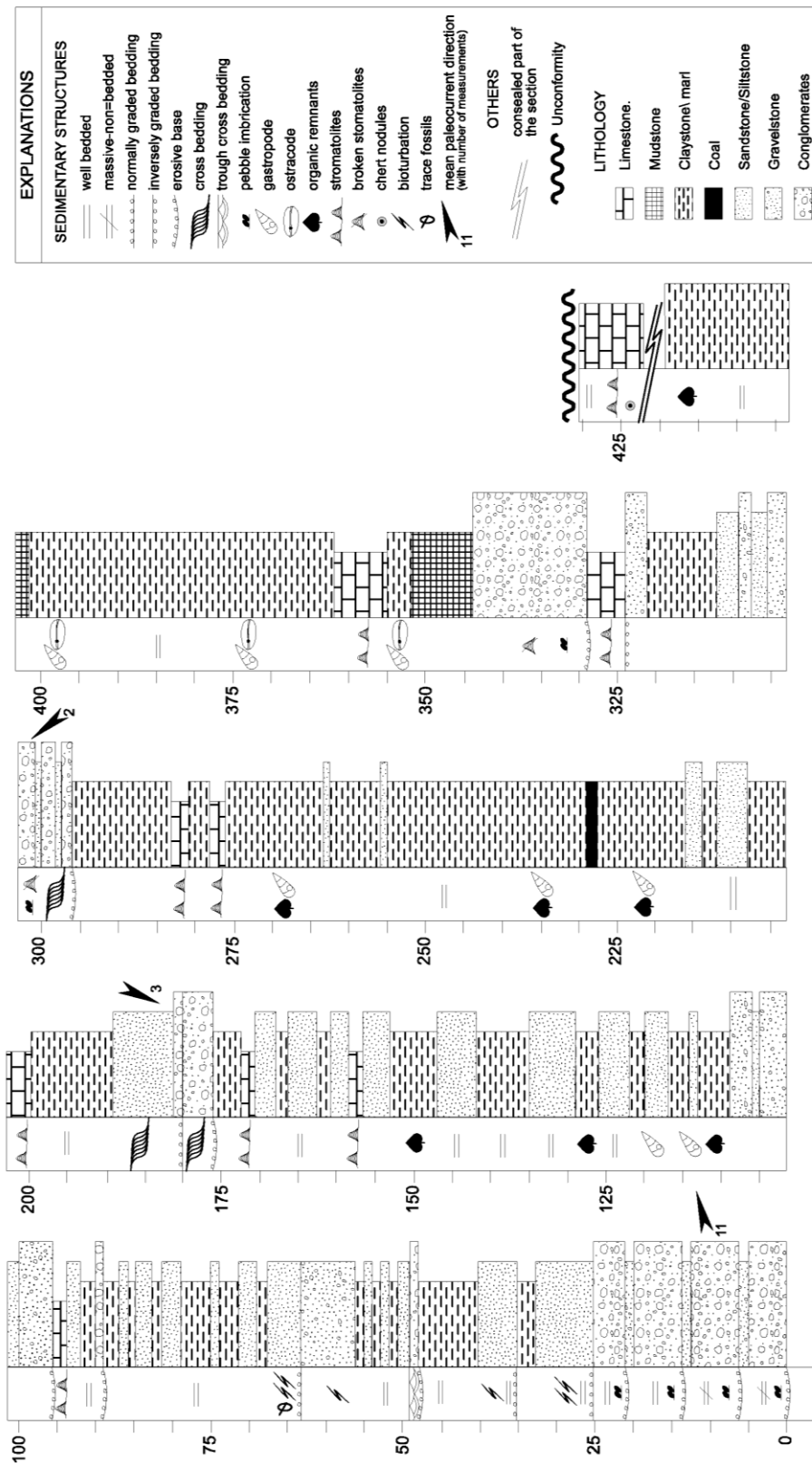


Figure 2.6. Measured section of the lower Altnapa group.

Ictitherium sp. from a red conglomeratic horizon suggesting a Late Miocene-Pliocene age. Given the similar lithology, Özkan and Söğüt (1999) suggested a similar age for the LAG. It was note, however, that the LAG underlies volcanics of the UAG, whereas the Kızılören unit overlies these. The age of the Kızılören unit therefore merely provides a minimum age for the LAG and UAG. On the other hand, Göger and Kırıl (1969) found fresh water fossils including *Unio* sp., *Radix* sp., ostracodes, bivalves and *Chara* sp. in limestones which have a lateral transition with these reddish conglomerates, and they suggested a Pliocene age. Eren (1993) assigned a Late Miocene-Early Pliocene age based on stratigraphic orders together with K/Ar radiometric ages obtained from the Konya volcanics to the east (Keller et al., 1977). Furthermore, Özkan (1998) described *Schizotrix* sp., *Chara* sp., and *Scytonema* sp. from their Yalıtepe formation, which corresponds to the central part of the LAG, and ascribed the formation to the Upper Miocene-Lower Pliocene. However, dating of endemic lacustrine fauna is subject to large uncertainties, and it is showed that the age of the overlying upper Altınapa group is Middle Miocene based on our new $^{40}\text{Ar}/^{39}\text{Ar}$ data in this study.

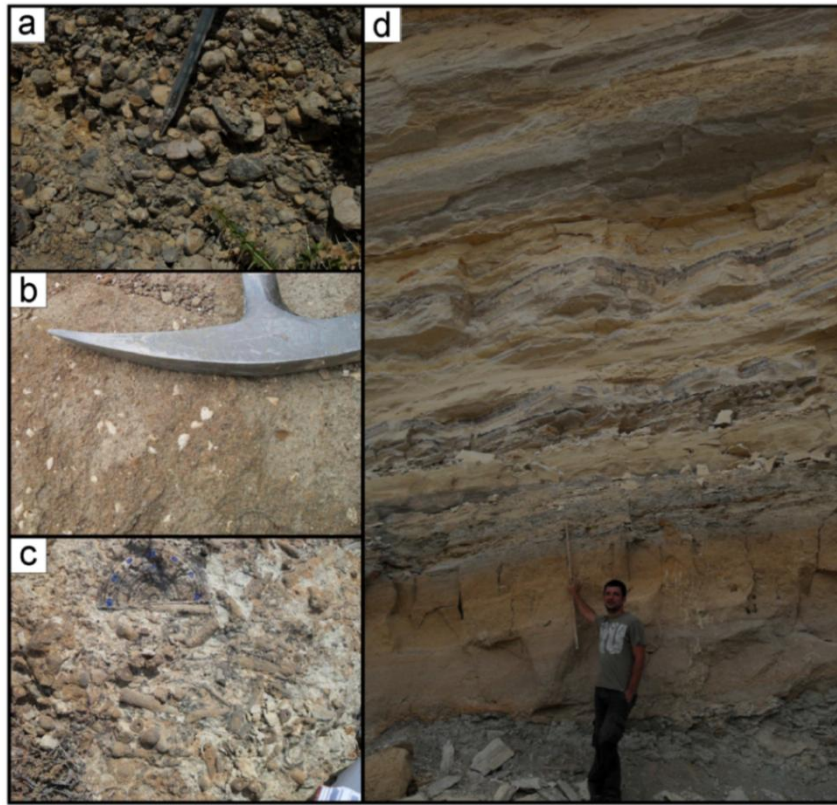


Figure 2.7. Field view of typical facies of the lower Altınapa group: a) clast-supported, polymict conglomeratic units b) cross-bedded and bioturbated, fresh-water gastropods-bearing sandstones, c) well bedded fresh water stromatolitic limestone and d) alternation of siltstone, green-blue coal bearing claystone, marls.

Unsorted, angular, occasionally reversely graded, matrix supported and boulder- to pebble-sized conglomerates indicate that the LAG was probably deposited in colluvial wedges, alluvial fans and terrestrial debris flows. From the SW margin towards the basin center, a gradual decrease occurs in the particles' size (Figures 2.8 and 2.9), indicating a lateral transition from alluvial fans to lacustrine deposition.



Figure 2.8. Field view of facies changes of lower Altınapa group from SW margin towards northeast into the basin center. The white line represents the Kızılören (normal) fault (ticks on the hanging-wall block). Note that coarse, poorly sorted, sub-angular coarse clastics dominate along the SW margin while they rapidly become finer-grained to marl-dominated towards NE (view to NW).

For the upper part of the LAG, lithologic characteristics (clay/siltstone and stromatolitic limestone) and fossil content suggest a shallow lacustrine environment. Hence, the lower Altınapa group comprises facies associations extending from proximal alluvial fans along the basin margin to lacustrine facies in the central parts of the basin.

2.1.2 Upper Altınapa Group (UAG)

The UAG is characterized by limestones and marls interbedded with volcanic and volcanoclastic rocks. The limestone/marl and the volcano-sedimentary parts of the sequence have previously been subdivided into separate formations (Niehoff, 1961; Wiesner, 1968). Göğer and Kırıl (1969) included these rocks in the Dilekçi formation, in which the upper part of the sequence was named the Ulumuhsine limestone member, while the volcano-sedimentary parts were named the Küçük Muhsine Agglomerate Member and Erenkaya Tuff Member. On the other hand, Eren (1993) named the whole sequence, including limestone and volcanic rocks, Küçük Muhsine formation.

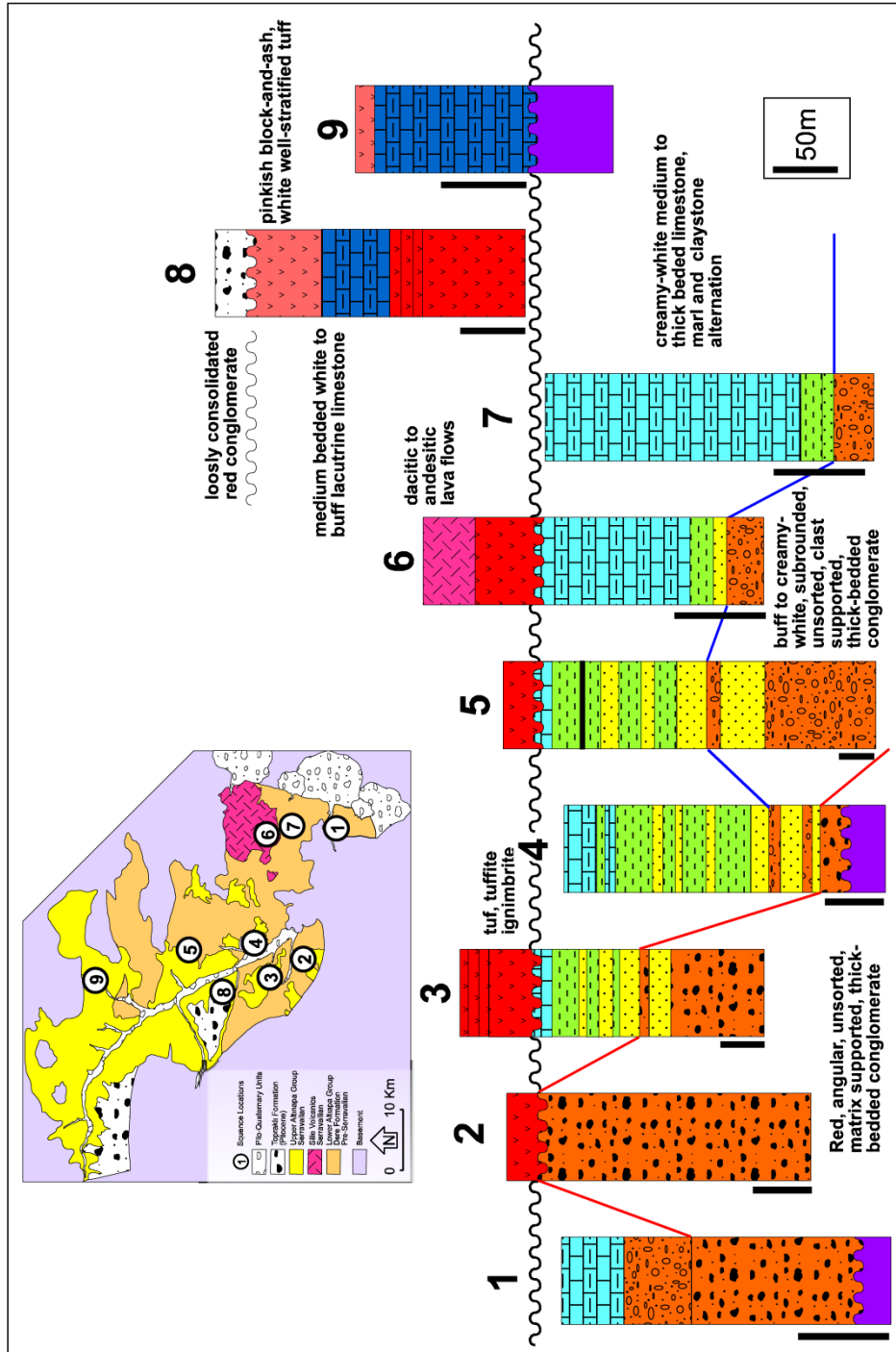


Figure 2.9. Schematic illustration of the lithostratigraphy of the Altunapa Basin. The section number is given on the geological map of the study area. Notice that grain size decreases from west to east. Vertical bars indicate the scales of each column independently.

Around Küçük Muhsine (Figure 2.5 and Figure 2.9), the base of the UAG is defined by a well-exposed angular unconformity with the underlying LAG. To the north of Başarakavak, it onlaps onto basement rocks (Figures 2.9 and 2.10). The UAG is unconformably covered by conglomerates of the Topraklı formation (Figure 2.11).

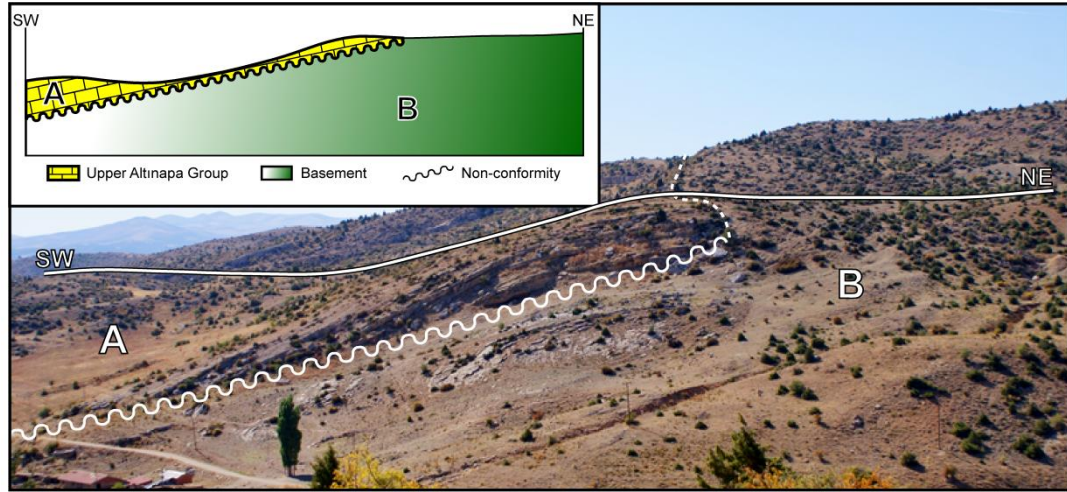


Figure 2.10. Field view of onlapping lacustrine algal limestones of the upper Altınapa group over the basement (location is 2 km north of Başarakavak, view to NW)

Unlike the LAG, the UAG contains intervals of volcanogenic material composed of intercalations of ignimbrites, dark grey to buff tuffs and tuffites, andesitic lava, lapilli/tuff and volcanic breccias (ash and block), intercalated with white to buff lacustrine limestones and creamy/white to greenish marls. These volcanic rocks are calc-alkaline in character and interpreted as belonging to the Miocene volcanic arc associated with the Cyprus subduction zone (Keller et al., 1977; Temel et al., 1998).

The type locality of the UAG starts from Küçükmühsine where the sequence starts with partly consolidated tuffs at the bottom (Figure 2.12) and comprising floats of pumice fragments having diameters as large as 3-4 cm (Figure 2.15a, b). The size and concentration of the pumice fragments increase upwards in each tuff horizon. The sequence continues upwards with a thick layer of volcanic breccia with andesite and dacite blocks with maximum block sizes up to 70 cm diameter. This level is succeeded by well-consolidated, well-bedded tuffite sequences with bed thicknesses up to 1 m and a total thickness of approximately 300 m. Tuffaceous layers generally contain crystals of plagioclase, quartz, biotite, amphibole, and volcanic glass (Eren, 1992). These sequences are succeeded by clay-marl alternations and intercalations of thick-bedded, well-cemented algal limestones. The thickness of the limestones around Ulumuhsine

where they are best exposed, is approximately 65m (Figures 2.11 and 2.12), while they are approximately 90m around NE of Başarakavak located at north-eastern part of the study area. The top of the sequence consists of white tuff and tuffites and pinkish block-and-ash deposits (Figure 2.11 and Figure 2.13c, d). These deposits contain angular, poorly sorted clasts comprising 90% of volcanogenic and 10 % of limestone origin. The sizes of the contained clasts are less than 30 and 10 cm, respectively. The measured stratigraphic thickness of the UAG is 480 m.

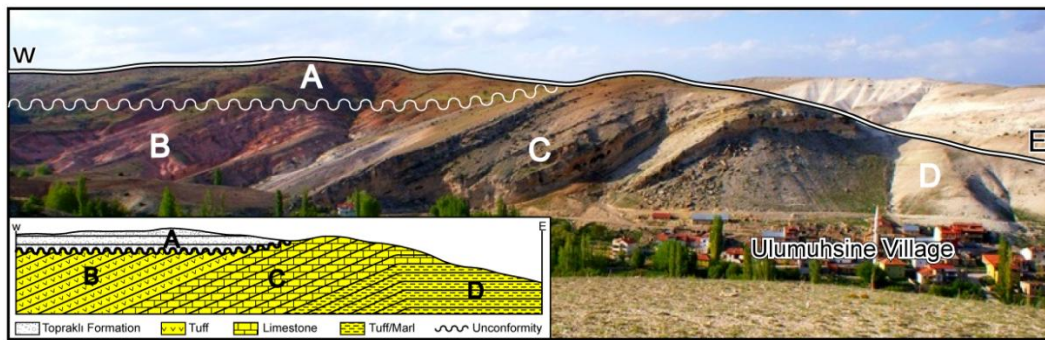


Figure 2.11. Field view of the angular unconformity between the upper Altınapa group (UAG) and overlying Topraklı formation (A) near Ulumuhsine. The UAG consists of pinkish/white tuff (B), freshwater limestone (C) (65m) and marl/tuff alternation (D).

As mentioned above, Göğ r and K ral (1969) reported fresh water fossils in some limestone units, including *Unio sp.*, *Radix sp.*, *Planorbis sp.*, ostracodes, and *Chara sp.* and suggested a Pliocene age for this formation.  zkan and S ğ t (1999) also proposed Late Miocene-early Pliocene age for the unit based on gastropoda fossils such as *Radix sp.*, *Planorbis sp.*, bivalves such as *Unio sp.*, and algae such as *Chara sp.* These ages do not fit in our stratigraphy and radiometric ages. However, Al   ek (2010) observed similar fossil assemblages together with some mammal fossils in SW Turkey which are indicating MN 3-4 Zone, an age range starting in the Burdigalian. Additionally, K-Ar ages of volcanic units in the east of the Altınapa Basin start as old as 11.95 Ma (Besang et al., 1977; Keller et al., 1977), which indicates the age of the volcanic activity in the Altınapa Basin and fits with our observations and age range. Therefore, the ages proposed by G   r and K   r (1969) and   zkan and S    t (1999) need to be revised.

The absence of conglomerates and channeled sandstones, as well as the dominance of clay/siltstone and limestone of the upper Altınapa group, and its fossil content indicate a quiet lacustrine environment with volcanic influx.

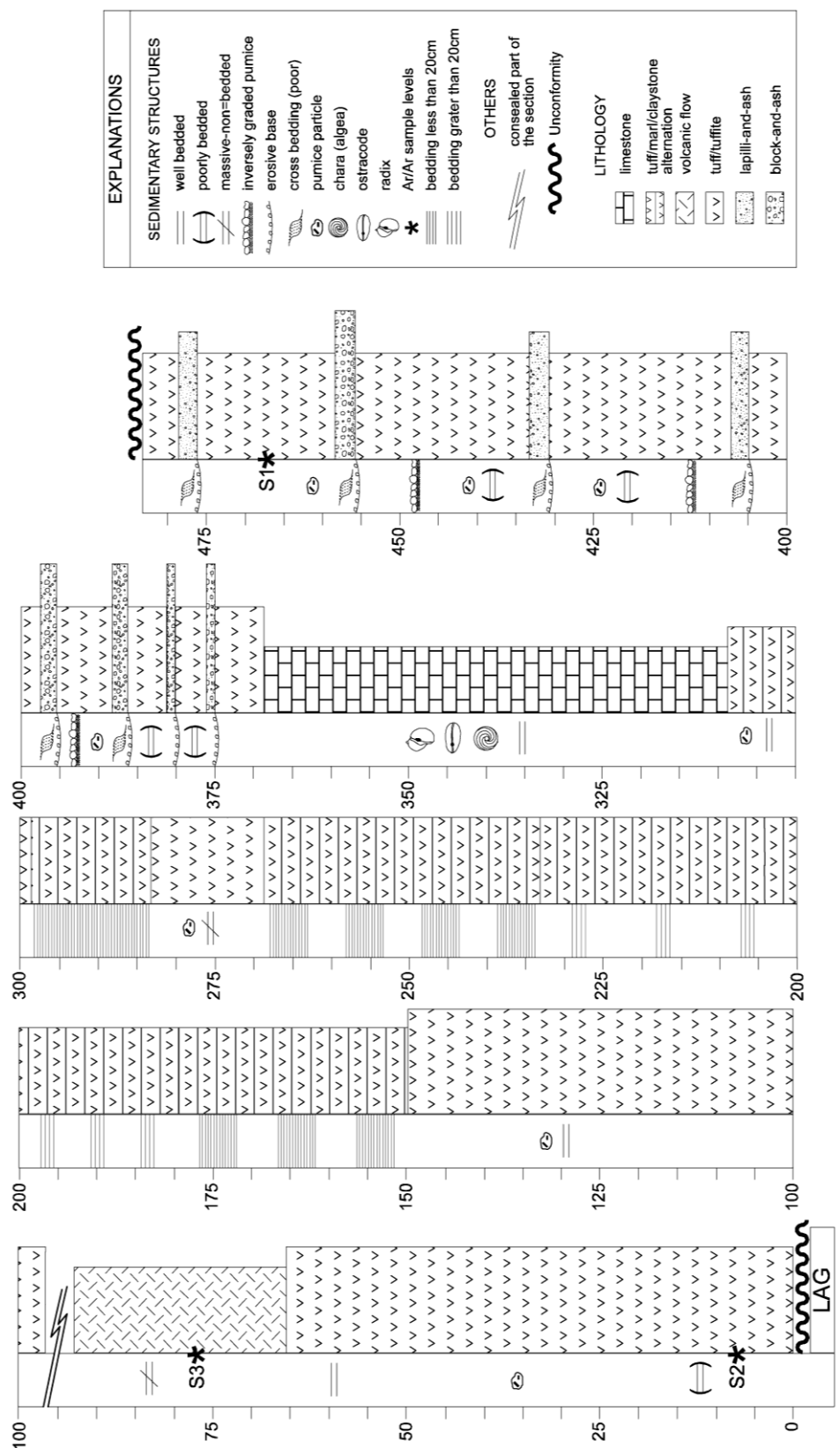


Figure 2.12. Measured section of the upper Altinapa group around Ulumuhsine (see Figure 2.3b for location of the section).

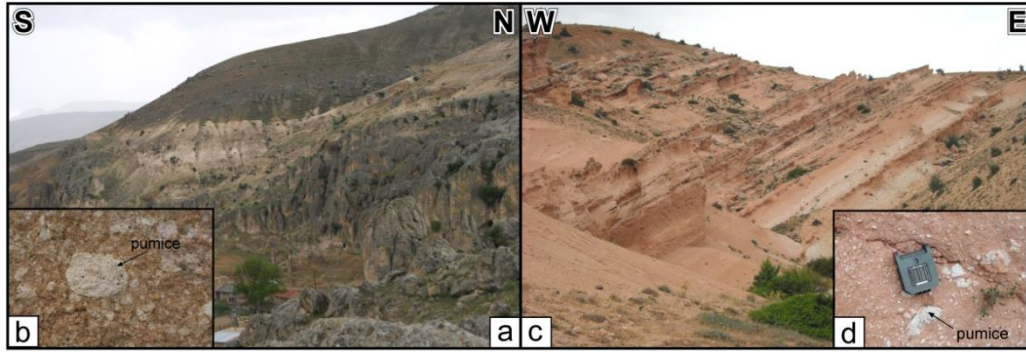


Figure 2.13. Tuff facies of upper Altınapa group (UAG). a) The tuff facies at the bottom and b) their close up view. c) block and ash facies at the top of the UAG and d) their close up view.

2.1.3 Topraklı Formation (TFm)

The Topraklı formation (TFm) unconformably covers the UAG (Figure 2.11) and is characterized by reddish-brownish conglomerate, sandstone and occasional mudstone. It has a limited distribution close to the western boundaries of the basin (Figure 2.9). The rocks were mapped as Topraklı conglomerates and Alluvium by Doğan (1975), and Eren (1993) and Özkan (1998) named the sequence “Topraklı formation”, which is also adopted in this study. The Topraklı formation is well exposed NW of the Ulumuhsine and it unconformably overlies pinkish tuffs and algal limestone belonging to the UAG (Figure 2.9 and Figure 2.11).

NW of Ulumuhsine, the formation is composed of a coarsening upward sequence of loosely cemented, unsorted and polymict, angular, pebble- to boulder-size (occasionally up to 80 cm diameter), matrix-supported conglomerates. Clasts originate from mostly limestones, sandstones, quartzites and cherts, i.e., lithologies that are abundant in the basement of the region. In addition, it reworks lacustrine limestone, dacite and andesite derived from Neogene units. The clasts are floating in a muddy/sandy matrix with iron-oxide cement. In addition, normally graded, polymict, sub-angular clast-supported conglomerates were also observed in some levels. Sedimentary structures such as planar cross-bedding and pebble imbrications are common in these stratigraphic levels. Another common facies within this unit comprises alternations of mudstone and matrix-supported conglomerate. There are also well-developed channels and occasional concretions within the mudstones, both indicating alluvial plain deposition with paleosol horizons.

No fossils have been observed from the unit, so far, and its age can only be constrained by superposition. The Topraklı formation covers all of the Neogene units in the basin and is in turn overlain by Quaternary alluvium.

Unsorted, as well as upward-coarsening, matrix-supported and boulder- to pebble-size conglomerates with angular pebbles suggest deposition in alluvial fans and continental debris flows. Additionally, sub-rounded, normally graded, grain-supported conglomerates showing pebble imbrications and erosional surfaces represent channeled fluvial stages within the alluvial fan deposition. Mudstones were most likely deposited by over concentrated currents, which define the flooding area and the distal part of the alluvial fan deposits. The caliche profiles in the mudstone suggest interruptions of sedimentation in a dry environment.

2.2 $^{40}\text{Ar}/^{39}\text{Ar}$ Geochronology

Because previous age assignments rely on poorly dated endemic lacustrine faunae, it is provide three $^{40}\text{Ar}/^{39}\text{Ar}$ ages from lavas and pumice horizons in the UAG (Figure 2.1). One sample was taken from the lowermost lava we encountered (S3), one sample was taken from a gray tuff halfway the sequence (S2), and the third was collected from the uppermost pinkish tuffs (S1).

Bulk samples were crushed, washed and sieved. Grain size fractions of 1000-2000 μm (S1, S2) or 500-1000 μm (S3) were used for standard magnetic and heavy liquid separations. Final mineral fractions were separated by hand-picking under a microscope. The samples were wrapped in Al-foil packages and loaded in a 9 mm ID quartz vial. Between each set of 4 samples and at top and bottom positions, Fish Canyon Tuff sanidine (FCs) standard was used as neutron fluence monitor. The vial was irradiated for 10 hours in the OSU Triga CLICIT facility, USA. After irradiation, samples and standards were loaded in 2 mm diameter holes of a copper tray and placed in an ultra-high vacuum extraction line. Single crystal $^{40}\text{Ar}/^{39}\text{Ar}$ fusion experiments were performed at the Vrije Universiteit Amsterdam, The Netherlands using a Synrad 48-5 CO_2 laser and custom made beam delivery system. Samples were purified in an in-house designed sample clean up line and analyzed on a MAP215-50 noble gas mass spectrometer fitted with a Balzers SEV217 detector. Mass discrimination was monitored by 3 replicate runs of air pipettes every 12 unknowns and blanks were run every 3 unknowns.

Ages are calculated using the in-house developed ArArCalc software (Koppers, 2002) with Steiger and Jäger (1977) decay constants. Ages are calculated relative to the FCs of 28.198 ± 0.23 Ma (Kuiper et al., 2008); note that this study reports 28.201 Ma using decay constants of Min et al. (2000), which converts to 28.198 Ma using Steiger and Jäger (1977). Correction factors for neutron interference reactions are $(2.64 \pm 0.04) \times 10^{-4}$

Table 2.1 Summary of $^{40}\text{Ar}/^{39}\text{Ar}$ data. Full data tables are given in the appendix. Errors are reported with 2σ uncertainty and represent analytical error. Full external errors are reported between brackets. MSWD is Mean Square Weighted Deviate. N is the number of analysis included in the weighted mean age, between brackets the number of experiments excluded.

Irradiation ID	Location		Material	Weighted Mean Age	MSWD	N	Inverse Isochron	$^{40}\text{Ar}/^{36}\text{Ar}$ Intercept
	Long	Lat						
VU78B-S1	32,24106	37,92545	Sanidine	$11.54 \pm 0.02(0.24)$	1.61	9(1)	$11.53 \pm 0.01(0.24)$	333 ± 25
VU78B-S2	32,28291	37,92859	Glass	No reliable age	0.48	7(3)	$11.88 \pm 0.11(0.26)$	310.6 ± 2.3
VU78B-S3	32,26722	37,92645	Feldspar	$11.67 \pm 0.05(0.24)$	1.14	4(5)	$11.70 \pm 0.03(0.24)$	276 ± 11

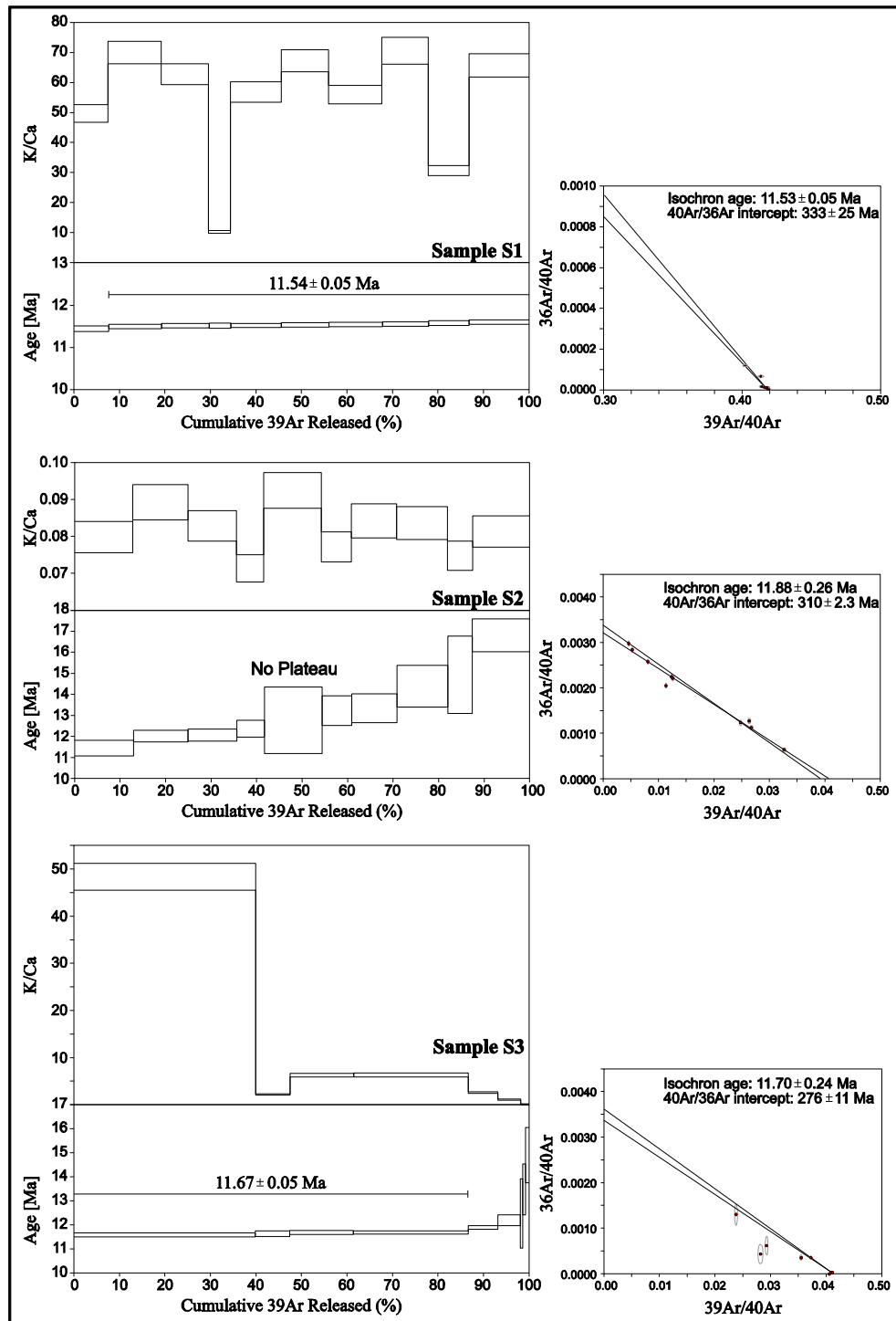


Figure 2.14. Replicate single crystal fusion $^{40}\text{Ar}/^{39}\text{Ar}$ ages are plotted versus the % of $^{39}\text{Ar}/\text{K}$ released in each fusion analysis for the three lava samples from the upper Altnapa group. The width of the bars/steps represents the 2σ analytical error. On top the K/Ca ratio (grey area, width is 2σ error) is displayed. Weighted mean ages are given. The small insets show the inverse isochron diagrams.

for $(^{36}\text{Ar}/^{37}\text{Ar})_{\text{Ca}}$, $(6.73 \pm 0.08) \times 10^{-4}$ for $(^{39}\text{Ar}/^{37}\text{Ar})_{\text{Ca}}$, $(1.211 \pm 0.006) \times 10^{-2}$ for $(^{38}\text{Ar}/^{39}\text{Ar})_{\text{K}}$ and $(8.6 \pm 1.4) \times 10^{-4}$ for $(^{40}\text{Ar}/^{39}\text{Ar})_{\text{K}}$. The $^{40}\text{Ar}/^{36}\text{Ar}$ ratio of 295.5 of Nier (1950) is used in the calculations. Errors are reported at 2 sigma level. Outliers are identified by comparing MSWD with the T-student distributions. The summary of the $^{40}\text{Ar}/^{39}\text{Ar}$ results is given Table 1 and plateaus and isochrones are given in Figure 2.14. Sample S2 is the deepest level in the stratigraphy (Figure 2.1 and 2.12). It does not yield a reliable weighted mean age. The sample is low on potassium and has low radiogenic ^{40}Ar yields. It most likely represents a glass fraction. The inverse isochron shows clear indications of excess argon and the inverse isochron age is 11.88 ± 0.11 Ma (± 0.26 Ma, full external error). K and/or Ar mobility can be an issue in glass fractions (Morgan et al., 2009) and this age is therefore considered to be less reliable. However, its age is consistent with the stratigraphy with samples S3 and S1 being younger and stratigraphically higher in the section. Sample S3 has a mixed population of grains based on K/Ca ratios. The four youngest grains with highest K/Ca ratio yield a weighted mean age of 11.67 ± 0.05 Ma (± 0.24 Ma full external error).

Sanidine of the highest sample S1 yields a weighted mean age of 11.54 ± 0.02 Ma (analytical error); or ± 0.24 Ma (full external error including standard age and decay constant uncertainties). The sample has high radiogenic $^{40}\text{Ar}^*$ contents and therefore data points cluster together on the isochrones. Although the $^{40}\text{Ar}/^{36}\text{Ar}$ atmospheric intercept on the inverse isochron deviates from the atmospheric intercept the weighted mean and isochron ages are similar.

2.3 Structural Geology

The major structures which shaped the Altınapa Basin include large scale normal faults, numerous mesoscopic faults commonly with no more than a few meters offset, and non-systematic open folds. Most of these structures were mapped using remote sensing techniques and subsequently verified in the field. Kinematic data were collected from mesoscopic faults for construction of paleostress configurations.

2.3.1 Remote Sensing

The applied remote sensing techniques include processing and interpretation of satellite images and interpretation of stereographic aerial photographs of 1/40.000 scale, using mirror stereoscopes. The used satellite imagery includes Landsat TM and ETM+ and Terra-ASTER images. In addition, Quickbird images obtained from Google Earth were used for areas where higher resolution was required. All of these images were co-registered using 1/25.000 scale topographical maps and combined in a GIS medium together with previously obtained maps and a field database.

In addition to aerial photos and satellite images, 25*25m resolution digital elevation models (DEM's) prepared from 1/25.000 scale topographical maps were used, together with 90*90m (3 arc seconds) resolution Shuttle Radar Topographical Mission (SRTM) data. These images and DEM's have different spatial resolutions, which is useful for detection and delineation of structures at different scales. In addition, the images were draped on the DEM's for 3D visualization in different directions, enhancing morphological expressions of structures in all directions. After the images were enhanced, lineaments were delineated manually on the images. Lineaments showing appreciable morphological expressions were labeled as faults. A resultant lineament map is shown in Figure 2.15. In addition, a length-weighted rose diagram prepared from the trends of these structures (Figure 2.15) displays two dominant directions (NE-SW and NW-SE) having approximately 60° acute angles.

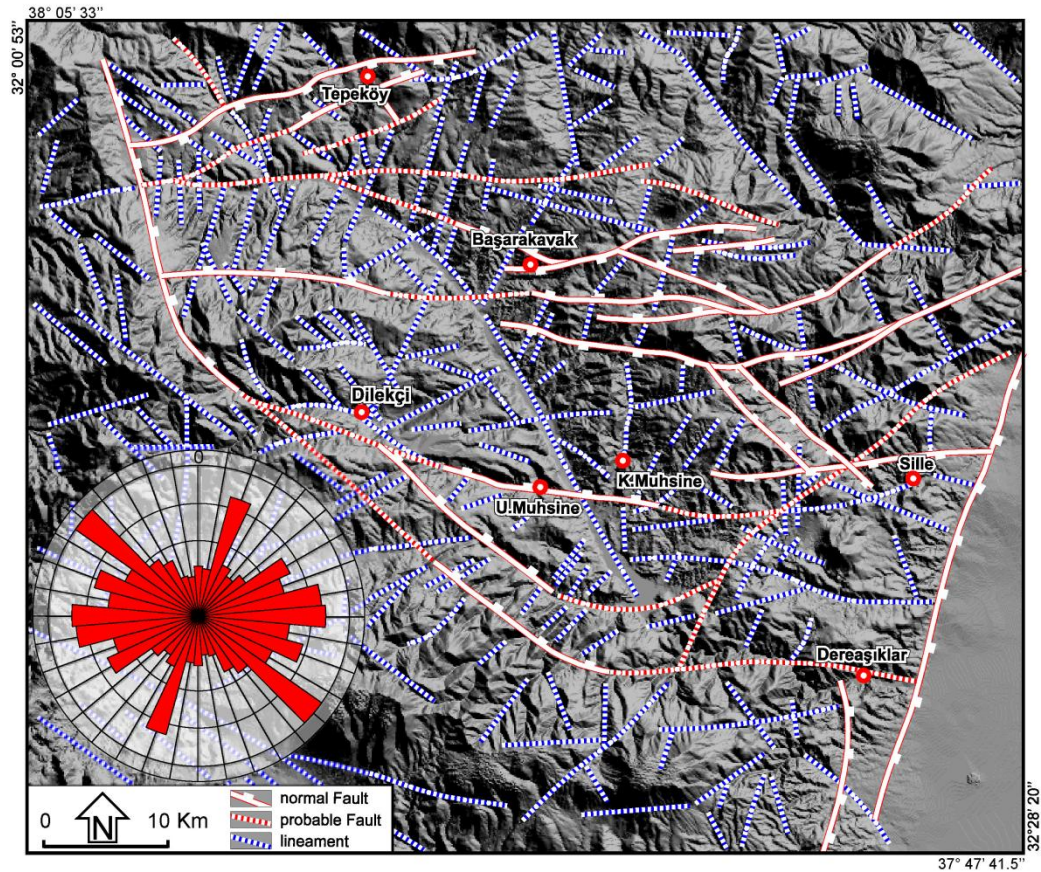


Figure 2.15. Structural map of the Altınapa Basin, indicating faults and lineaments. Rose diagram (length weighted) indicating orientations of both faults and lineaments.

2.3.2 Field Observation

The major structures that shaped the Altınapa Basin are normal faults along at the margins of the basin. The basin stratigraphy is deformed along gentle to open folds and, in one locality, in a conspicuous 100 m scale monocline. In addition, numerous mesoscopic faults, which developed after and during sedimentation (Figure 2.16), have pervasively affected the basin (Figure 2.2).

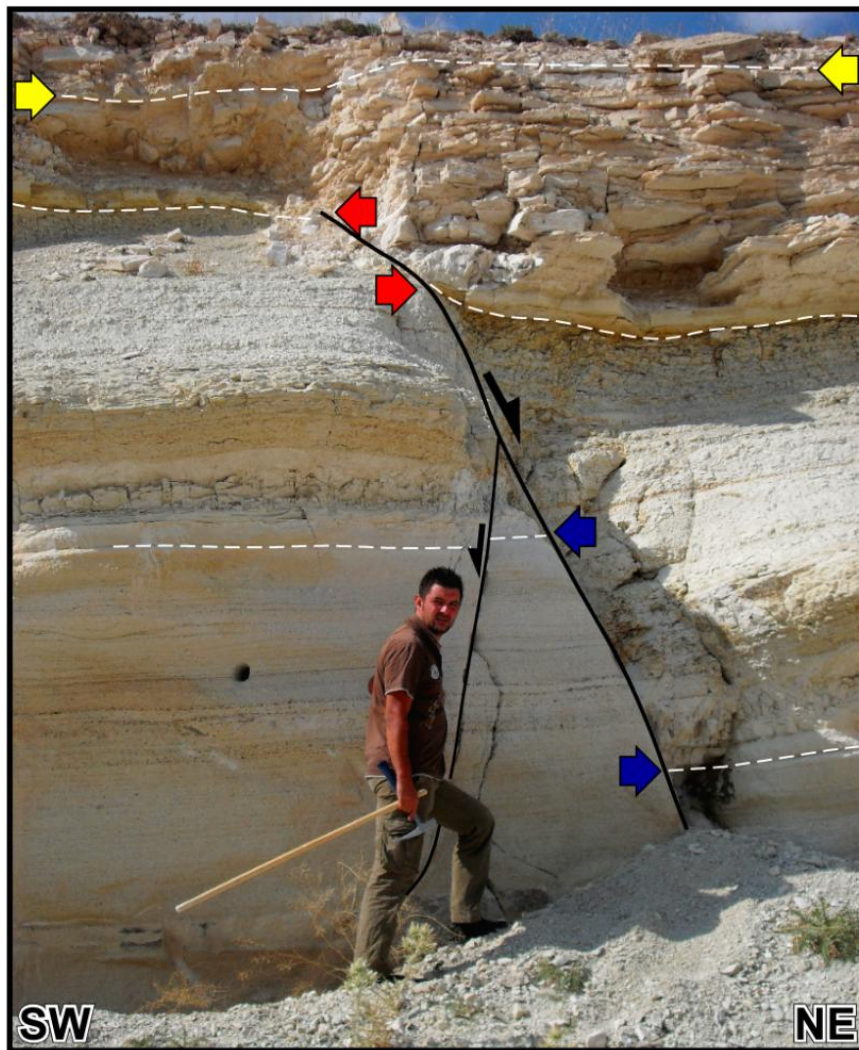


Figure 2.16. Syn-sedimentary normal fault in the tuff units of upper Altınapa group.

Morphologically, the most prominent faults are identified at the margins of the basin (Figure 2.2). Generally they are recognized as linear to curvilinear mountain fronts rising steeply at the contact of the basin fill units and basement rocks. Among these, the Kızılören Fault (KF) is inferred mainly on the basis of a thick accumulation of red clastics abutting against the basement rocks, although the main fault plane was not observed during field studies (Figure 2.2). Nevertheless, the fault zone is characterized by smaller scale syn- and antithetic normal faults exposed along the sediment-basement contact.

The Mülâyim Fault (MF) is oriented NNW-SSE and dips to the NE. It controls the northwestern margin of the basin and separates gently dipping Plio-Quaternary Topraklı sediments from the carbonate basement units (Figure 2.2). Along the fault, the basin fill units are characterized by unsorted, angular to sub-angular, boulder- to pebble-size (up to 1 m) sedimentary breccias and conglomerates. At the vicinity of Mülâyim, adjacent to the fault, the basin fill units are almost horizontal.

The Tepeköy Fault Set (TFS) located at the northern margin of the basin comprises two ENE-WSW oriented conjugate normal faults. The northern branch of the fault set dips southwards while the southern branch dips northwards defining a graben around Tepeköy (Figure 2.2). Both of the branches of the TFS extend beyond the present boundaries of the Altınapa Basin and are delimited in the SW by the Mülâyim Fault, which is almost perpendicular to the TFS. The south-dipping branch of the Tepeköy Fault delimits the northern boundary of the basin. The basement at this part of the basin comprises Paleozoic to Jurassic marbles and quartzites.

The Selahattin Fault (SF) is developed in the NW part of the study area and is oriented parallel to the TFS. It is also delimited by the Mülâyim Fault in the west. Along the SF the Topraklı formation is juxtaposed with the basement units, which are composed mainly of Triassic carbonates. The eastward continuation of the fault within the upper Altınapa group is uncertain. Morphologically, however, the fault can be followed eastward where it seems to link-up with one of the north-dipping branches of Başarakavak Fault Set (BFS) (Figure 2.2).

The Başarakavak Fault Set (BFS) comprises a number of E-W striking faults with horst and graben morphology. Along the major faults of the BFS, basement and basin fill units are juxtaposed. Lateral continuity of the fault set within the basement is morphologically well expressed while within the basin towards the west the BFS is not exposed.

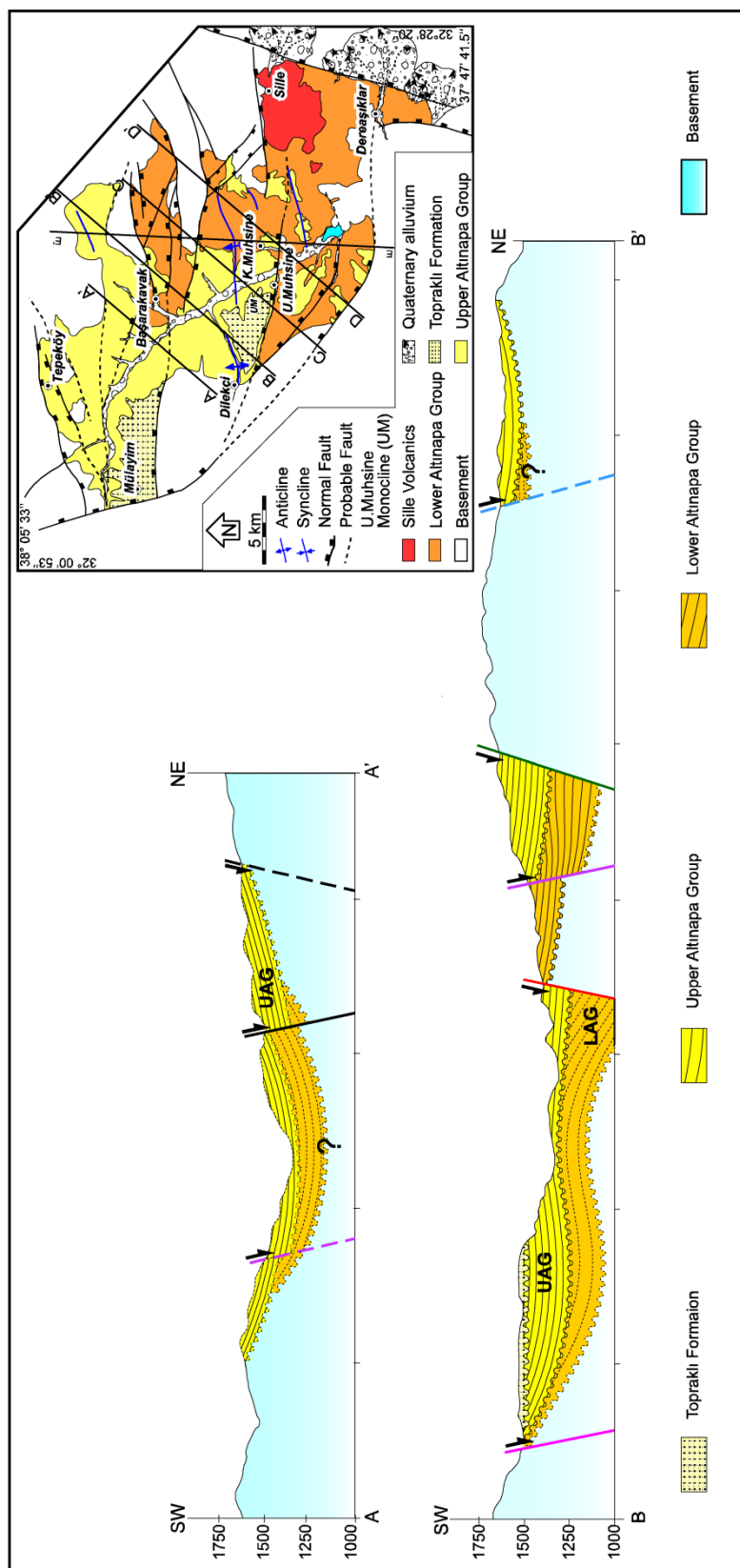


Figure 2.17. Structural cross-sections constructed from the geological map. Inset map shows the locations of the cross-sections. Different colors for faults correspond to the same fault in the different sections.

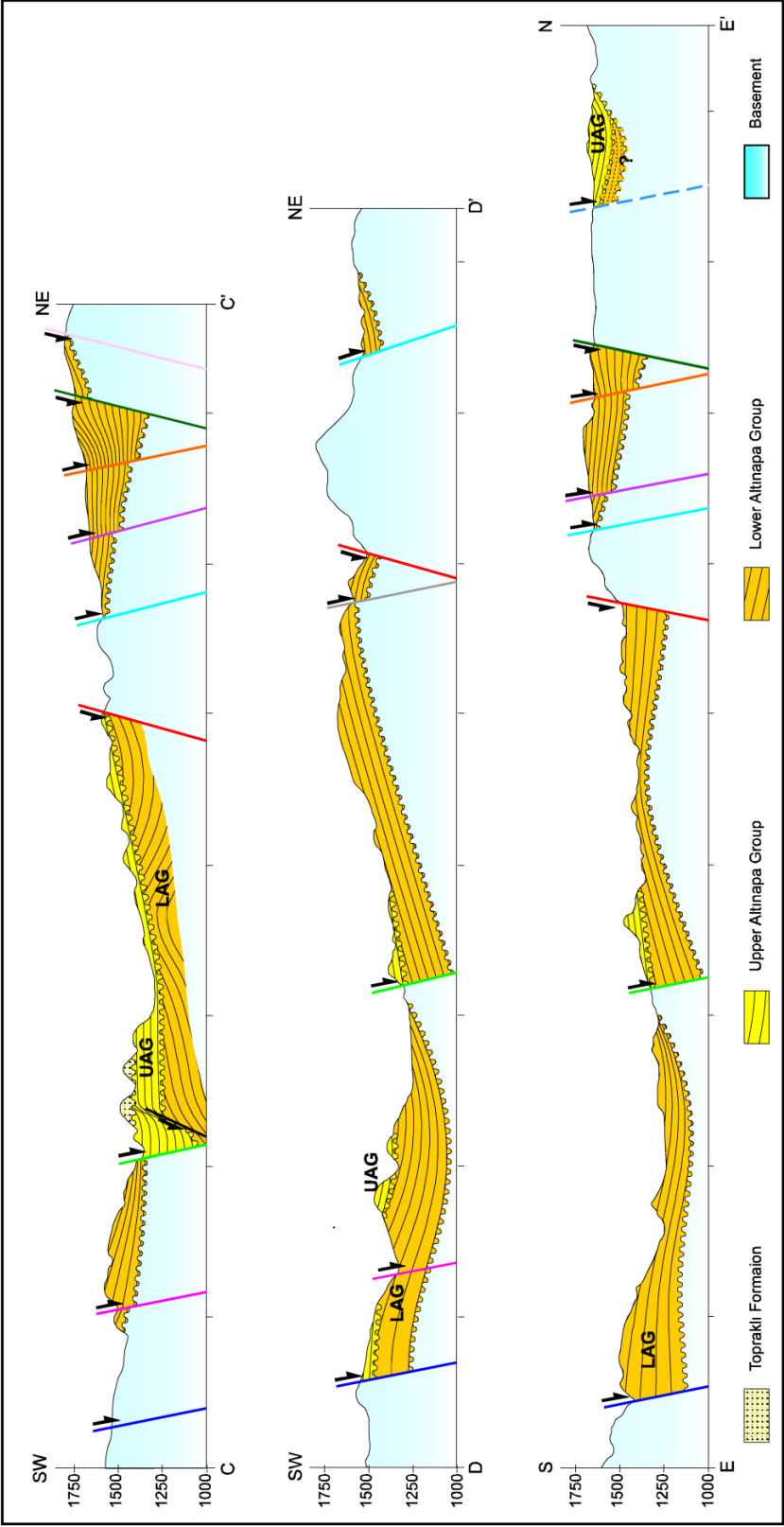


Figure 2.17. Continued.

The southeastern boundary of the basin is delineated by the active (Ögütçü et al., 2011) Konya Fault which controls the northwestern boundary of the vast Konya Plain. The Konya fault is about 45 km long and shows an approximately NNE-SSW trend. It dips SE and separates the Neogene sedimentary fill of the Altınapa Basin in the footwall from the Quaternary alluvial sediments of the Konya Basin in the hanging wall. Well preserved fault planes with slip lines are exposed, and linear coalesced alluvial fan and apron systems developed within the Konya Basin, consistent with its ongoing activity as evident from the 11 September 2009 Sille Earthquake, ($M_w=4.9$) along the fault. Finally, the eastern margin of the basin is characterized by onlap of lacustrine algal limestones of the UAG (Figures 2.10 and 2.17), showing an asymmetric development of the basin.

The mainly E-W trending open folds that deform the stratigraphy of the Altınapa Basin are developed within both the lower and upper Altınapa groups. However, the dips of the limbs of these folds seem more gentle within the upper Altınapa group, with dips not exceeding 30° , whereas they are steeper within the lower Altınapa group, with dips up to 50° (Figure 2.17). All of these folds form a series of anticlines and synclines parallel to the Tepeköy and Başarakavak Faults and almost perpendicular to the NNW-SSE trending basin bounding faults (Kızılören Fault). Their maximum observed wavelength is approximately 10 km and they developed in the hanging-walls of the normal faults. An exception to this general fold trend is formed by the Ulumuhsine Monocline, which strikes $N15^\circ E$, parallel to the Konya Fault and dips $30^\circ W$ (Figure 2.2, 2.11 and 2.17). This monocline, which is consistent with a buried blind normal fault at depth, deforms the UAG, but is unconformably covered by the Topraklı formation.

2.4 Paleostress Analysis

In addition to the large-scale structural analysis, we carried out a detailed kinematic analysis from mesoscopic structures in order to unravel paleostress configurations during the development of the Altınapa Basin.

2.4.1 Data and Method

The paleostress configurations are reconstructed using Angelier's software to analyze fault slip data collected from exposed fault planes. Analysis of fault attitudes and their associated directions and sense of slip are used to infer principal stresses, a procedure also known as paleostress inversion (Carey and Burinier, 1974; Etchecopar et al., 1981; Angelier, 1990; 1994). Two assumptions are fundamental to these methods: 1) the bulk state of stress in a small area is uniform, and 2) the slip direction is parallel to the maximum resolved shear stress on each fault plane. Paleostress analyses determine the

best-fitting reduced stress tensor based on the given fault slip data, identifying the orientations of the three principal stress axes (σ_1 : maximum, σ_2 : intermediate and σ_3 : minimum) and the shape ratio of stress ellipsoid, $\Phi = (\sigma_2 - \sigma_3) / (\sigma_1 - \sigma_3)$ ranging between two extreme values of 0 and 1. The Φ ratio constraints all-possible cases between uniaxial ($\sigma_2 = \sigma_3$; $\Phi = 0$ or $\sigma_1 = \sigma_2$; $\Phi = 1$) to tri-axial stress configurations ($\sigma_1 > \sigma_2 > \sigma_3$; $\Phi = 0.5$) (Angelier, 1994).

From 29 sites (Table 2.2), 377 fault-slip measurements (Figure 2.18a), including direction and sense of relative movements were collected. Most of the data were collected from the infill of the Altınapa Basin, and from faults juxtaposing basement and basin-fill units. Strikes of the mesoscopic fault planes clustering around E-W and NE-SW directions (Figure 2.18b) are consistent with the general trend of the major fault Dips range between 45° to 90° . Inversion of the data was carried out on each site separately and 29 stress configurations are constructed (Figure 2.19 and Table 2.2).

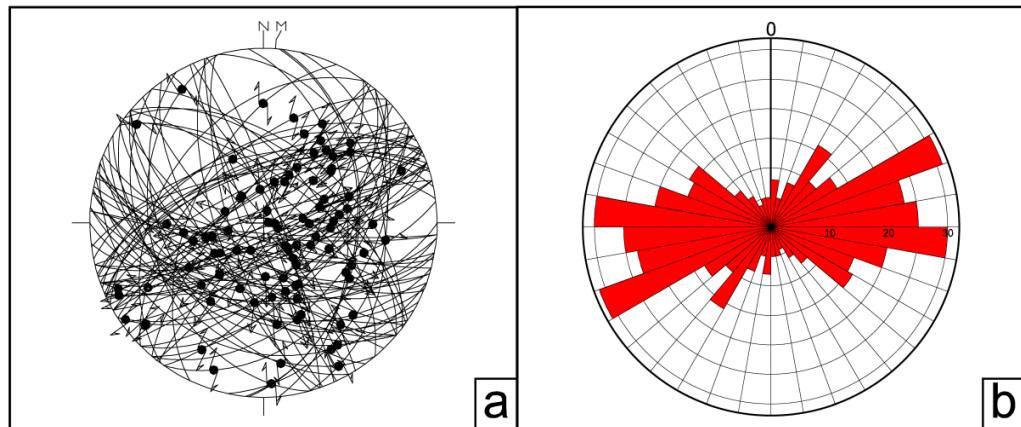


Figure 2.18. (a) Stereoplot showing all of the collected fault-slip measurements (N=377), (b) bidirectional rose diagram of fault strikes.

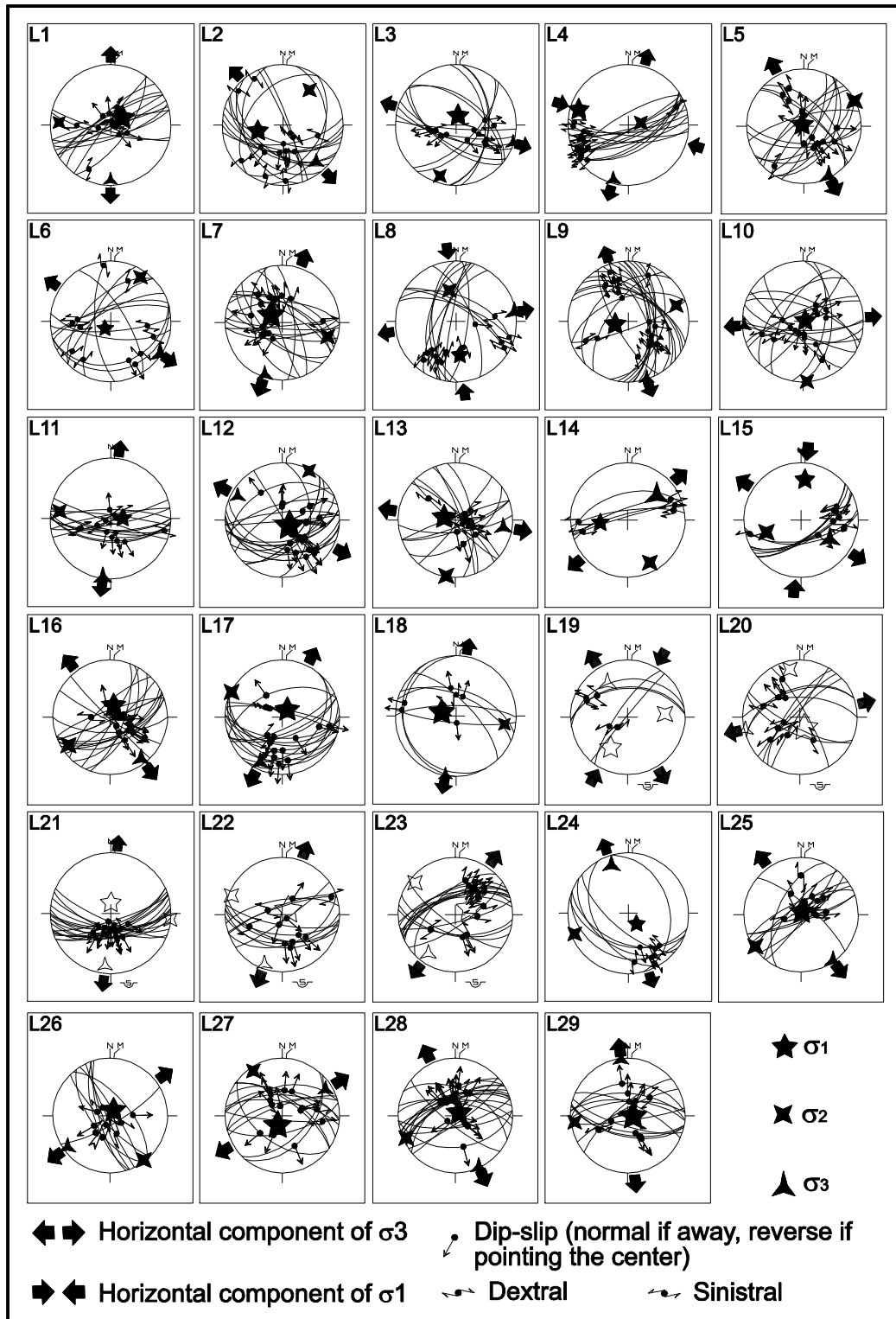


Figure 2.19. Stereoplots showing constructed paleostress orientations, fault planes and slip lineations (lower hemisphere equal area projection).

Table 2.2. Locations and paleostress orientations for Altınapa Basin.

Loc	Long	Lat	$\sigma_1(P^\circ/D^\circ)$	$\sigma_2(P^\circ/D^\circ)$	$\sigma_3(P^\circ/D^\circ)$	Φ	Mean ANG	Mean RUP	N
L1	32.16011	38.06960	71°/059°	16°/273°	10°/180°	0.112	37	73	13
L2	32.16214	38.06511	55°/257°	28°/037°	19°/138°	0.462	28	64	15
L3	32.10005	38.01244	77°/013°	13°/197°	01°/107°	0.276	18	42	13
L4	32.20648	37.95920	12°/287°	77°/081°	05°/195°	0.360	9	24	16
L5	32.31572	37.88673	87°/318°	01°/063°	03°/153°	0.449	18	46	15
L6	32.22815	37.98963	80°/226°	10°/033°	02°/123°	0.607	25	55	12
L7	32.25550	38.03066	71°/303°	18°/107°	05°/199°	0.142	22	46	16
L8	32.25891	38.03231	44°/173°	46°/348°	03°/081°	0.597	18	33	13
L9	32.40211	37.93452	73°/259°	17°/072°	02°/162°	0.330	25	49	20
L10	32.42253	37.87497	87°/066°	01°/176°	03°/266°	0.105	23	59	15
L11	32.38741	37.85167	74°/088°	16°/278°	03°/187°	0.513	25	59	14
L12	32.42282	37.87736	77°/128°	02°/029°	13°/298°	0.094	21	44	19
L13	32.39163	37.90838	74°/284°	02°/189°	16°/099°	0.330	25	51	12
L14	32.40954	37.85433	50°/265°	18°/152°	34°/050°	0.711	45	86	5
L15	32.42488	37.88497	30°/005°	36°/250°	39°/123°	0.734	33	55	8
L16	32.35526	37.95844	73°/017°	14°/236°	10°/143°	0.311	15	37	17
L17	32.33364	37.90951	77°/034°	02°/296°	13°/206°	0.352	16	47	16
L18	32.39194	37.85823	70°/285°	20°/099°	02°/190°	0.027	11	40	7
L19	32.42945	37.99422	39°/209°	35°/085°	31°/329°	0.462	30	62	5
L20	32.38742	37.89012	74°/157°	16°/348°	03°/257°	0.176	25	56	10
L21	32.34830	37.95438	76°/002°	01°/096°	14°/186°	0.264	11	22	18
L22	32.29146	37.89938	79°/053°	06°/291°	09°/200°	0.163	21	47	11
L23	32.28899	37.97180	68°/067°	11°/308°	19°/215°	0.206	13	39	16
L24	32.34778	37.96698	72°/141°	06°/249°	17°/341°	0.580	11	29	7
L25	32.28488	37.93799	86°/019°	03°/235°	03°/145°	0.396	28	69	10
L26	32.26213	38.00526	81°/033°	03°/143°	08°/233°	0.368	30	53	9
L27	32.27441	38.00479	75°/205°	08°/327°	13°/059°	0.192	15	39	14
L28	32.24566	37.92514	83°/053°	07°/246°	01°/155°	0.307	13	42	19
L29	32.34543	37.95603	82°/096°	07°/263°	02°/353°	0.136	16	47	12

σ_1 , σ_2 , σ_3 magnitude ratios of principle stresses; D/P, direction/plunge; Φ stress ratio; ANG, maximum allowed angular divergence RUP, maximum allowed quality value N, number of measurement for each site.

2.4.2 Spatial Characteristics

In order to understand the type of deformation, the constructed paleostress orientations are analyzed for their regional consistency. Figure 2.20 shows that σ_1 is generally oriented (sub-) vertically in all sites, whereas σ_2 and σ_3 do not show a consistent direction. Such distributions are characteristic for uniaxial stress conditions and result in stress permutation in regions where the magnitudes of σ_2 and σ_3 are close to or equal to each other (Homberg et al., 1997). The deformation that affected the Altınapa Basin is clearly extensional, as indicated by the vertical σ_1 , and consistent with normal fault activity along the major faults in the basin. The near equal σ_2 and σ_3 magnitudes should produce Φ values approaching zero in the case of σ_1 magnitudes much greater than that of σ_2 . As seen in Figure 2.20d and Table 2.2, the frequency distribution of Φ values are bimodal and has peak values at 0.15 and 0.35. In other words, in more than 20 sites Φ values are less than 0.5. This indicates that uniaxial stress conditions prevailed in the region.

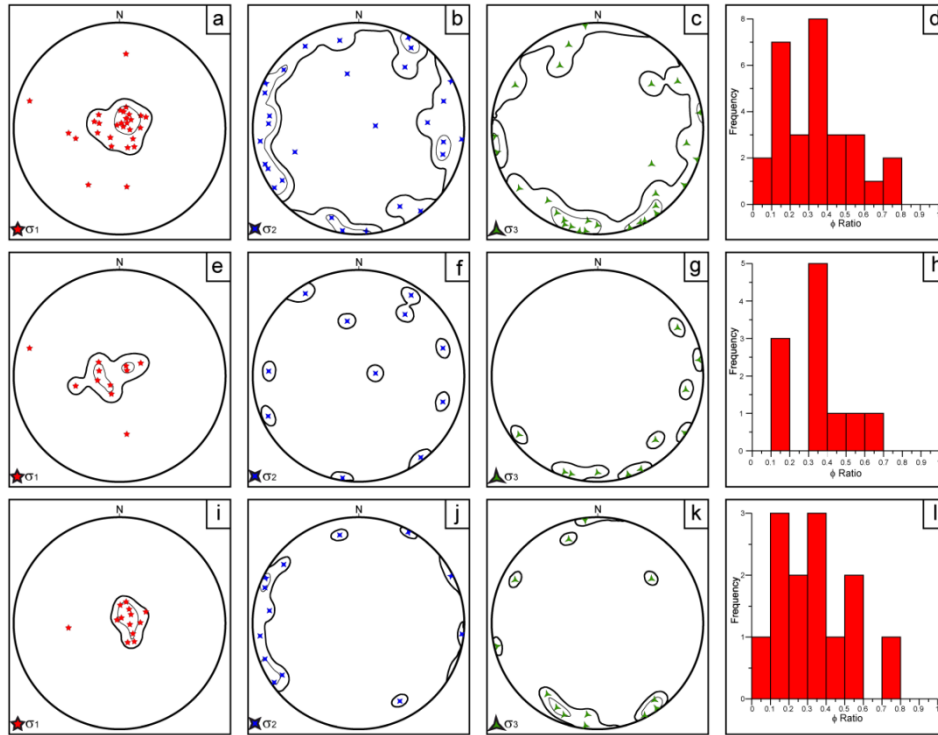


Figure 2.20. Density diagrams for principal stress orientations and frequency distributions of Φ values. (a-d) Whole data, (e-h) based on data from upper Altınapa group, (i-l) based on lower Altınapa group. Notice that the σ_1 is dominantly sub-vertical while σ_2 and σ_3 orientations are sub-horizontal with strongly varying directions indicating uniaxial stress conditions.

The horizontal component of the minor principal stress is plotted on the map of Figure 2.21 to verify the compatibility of the constructed paleostress configurations relative to regional structures. Apart from some strike-slip solutions (sites 4, 8, 15 and 19), most of the σ_3 directions are (near-) orthogonal to the dominant trends of the major structures (except for sites 3 and 6). This pattern implies unconstrained slip (somewhat similar to free fall of hanging-wall blocks along fault planes) along the major normal faults, as expected in uniaxial stress conditions. The sites with strike-slip solutions are indications of transfer faults and/or stress perturbations due to accommodation of local space problems.

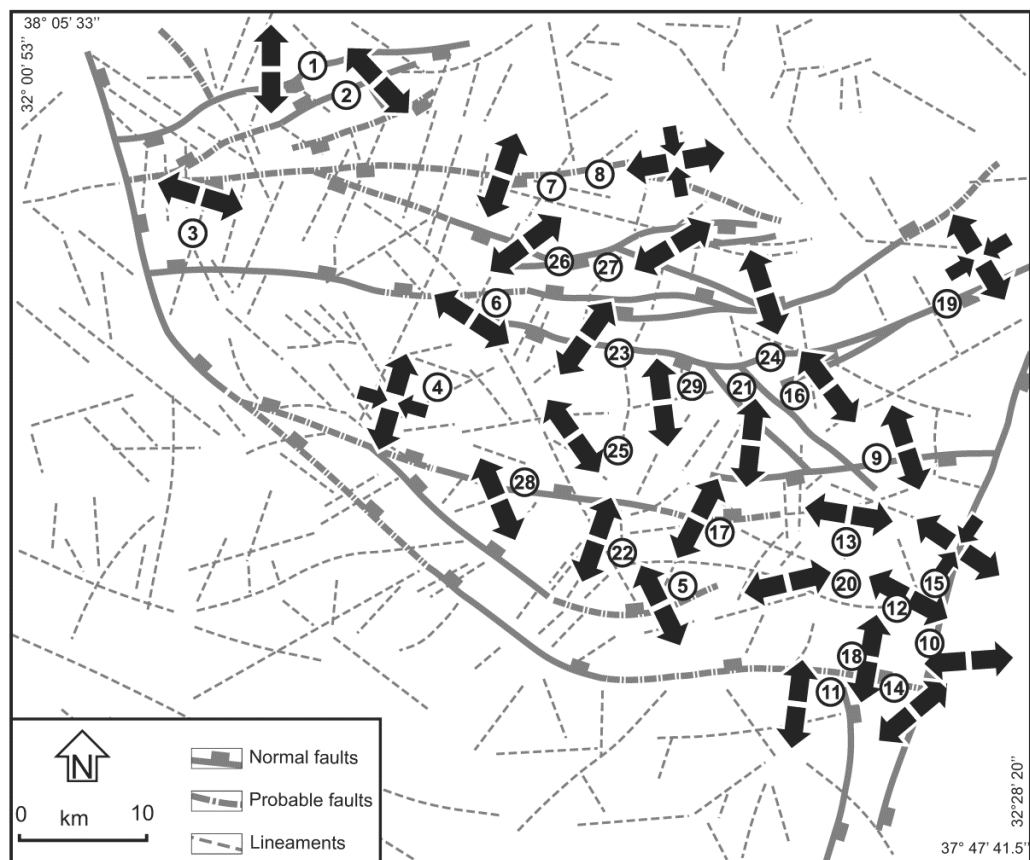


Figure 2.21. Major faults and lineament map of the study area. Arrows indicate horizontal component of the minor principal stress (σ_3) and numbers indicate the paleostress measurement sites which correspond to site numbers in Figure 2.19.

2.4.3 Temporal Relationships

In addition to spatial distribution of the paleostress directions, temporal changes of the paleostress configurations throughout the stratigraphy are very important to unravel any paleostress stratigraphy of the basin. In paleostress stratigraphy, the basement rocks potentially record the entire paleostress history during basin subsidence, whereas basin strata record paleostress tensors that were coeval with sedimentation. Structures developed in the upper most basin fill offer insight into only the youngest tectonism (Kleinspehn et al., 1989). Therefore, the younger events need to be extracted from the older ones, successively from younger to older. Therefore it is ordered our paleostress data according to the age of the rocks from which they were collected (Figure 2.22), and according to cross-cutting relationships. The paleostress directions for the lower and upper Altınapa groups were plotted separately, and the resultant contour diagrams were compared. As seen in Figures 2.20, 2.21 and 2.22, there is no notable difference between the measurements from the lower and upper Altınapa groups.

The youngest, still active extension direction in the Altınapa Basin is reflected by the Konya fault, reflected by paleostress sites 10 and 15. These extension directions trend approximately E-W to NW-SE. This youngest tectonic regime is consistent with focal mechanism solutions of the Sille Earthquake (11 September 2009, Mw=4.9, ETHZ) (Figure 2.22). However, recent earthquakes along the Akşehir-Afyon Graben (AAG) to the north of the Altınapa Basin (Taymaz et al., 2004; Ergin et al., 2009) demonstrate extension directions ranging from N-S to NE-SW (Figure 2.23), attesting to the fact that currently central Turkey has strongly varying σ_3 directions while σ_1 is (sub-)vertical. This is consistent with the paleostress patterns obtained throughout the stratigraphical successions of the Altınapa Basin.

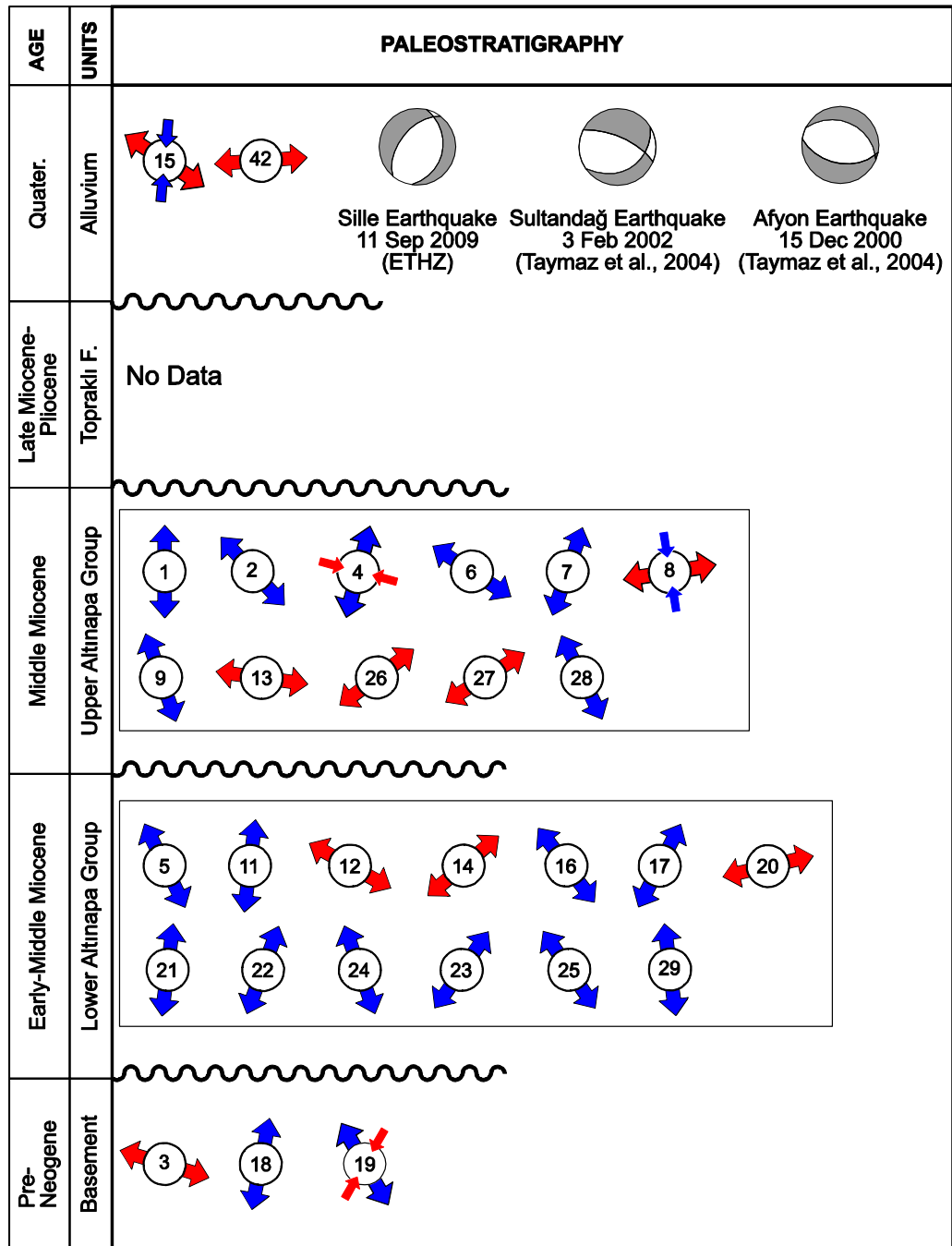


Figure 2.22. Paleostress stratigraphy of the Altınapa Basin from the Middle Miocene to Recent. Arrows represent σ_3 directions. Focal solutions are belong to 11 September 2009 Sille Earthquake ($M_w=4.9$ ETHZ), 3 February 2002 Sultandağı Earthquake ($M_s=6.4$, Taymaz et al., 2004) and 15 December 2000 Afyon Earthquake ($M_s=5.8$, Taymaz et al., 2004). Note that the unconstrained nature of σ_3 directions and variation of extension directions of the earthquakes in the region.

CHAPTER 3

TECTONO-SEDIMENTARY EVOLUTION AND GEOCHRONOLOGY OF THE MIOCENE ILGIN BASIN (TAURIDE BELT, TURKEY)

This chapter describes the lithology and the geological structure of the Ilgin Basin. The stratigraphy of the basin is updated based on newly obtained data. Outcrop scale observations and fault-slip data collection were performed during field studies and analyzed, interpreted and evaluated for their relationships with the major structures in the basin.

The Ilgin Basin is an approximately 27 km wide, 50 km long and NNW-SSE trending intra-montane basin (Figure 3.1). It is located within the outer eastern limb of the Isparta Angle (Blumenthal, 1963).and has a poorly exposed stratigraphy, consisting of Neogene continental clastic sediments unconformably resting on top of a metamorphic rocks and non-metamorphosed Precambrian to Eocene sedimentary rocks assigned to the Anatolide-Tauride Belt (Okay and Tüysüz, 1999). The basin lies adjacent to a major NW-SE trending fault zone known as the Akşehir Fault Zone (AFZ), an oblique-slip normal fault (Koçyiğit et al., 2000) separating Neogene infill at ~1000 m elevation of the Ilgin Basin from the Sultandağları Horst that is elevated to nearly 2000 m.

3.1 Lithostratigraphy

The stratigraphy of the Ilgin Basin consists of continental clastic sediments. Lignite rich levels are the most prominent deposit in the basin. The earliest studies in the basin include Lahn (1945), Wedding (1968), and Bektimuroğlu (1978) were focused mainly on the lignite bearing Neogene units in order to evaluate the lignite potential of the basin. The first study that incorporated the entire the Neogene infill of the basin was performed by Tüfekçi (1987) in the northern part of the Ilgin Basin, which defined Neogene units based on geomorphological criteria, identifying one single formation with three members. After these pioneering studies, the Neogene stratigraphy of the Ilgin Basin was constructed by Koçyiğit et al. (2000), who provided additional age constraints from macro- and micro-mammalian fossils. They divided the Neogene deposits in the basin into three main lithostratigraphic units from older to younger; (1) the Köstere/Gölyaka formation, (2) the Doğançık/Gözpınarı formation and (3) the Taşköprü/Dursunlu formation. Hüseyinca and Eren (2007) provided the most recent study focused on the northern part of the Ilgin province and identified four formations, from older to younger these include; (1) the Harmanyazı formation, (2) the Ulumuhsine formation, (3) the Sebiller formation and (4) the Tekeler formation, which are not compatible with the previous subdivisions. Therefore, the lithostratigraphy of the Ilgin

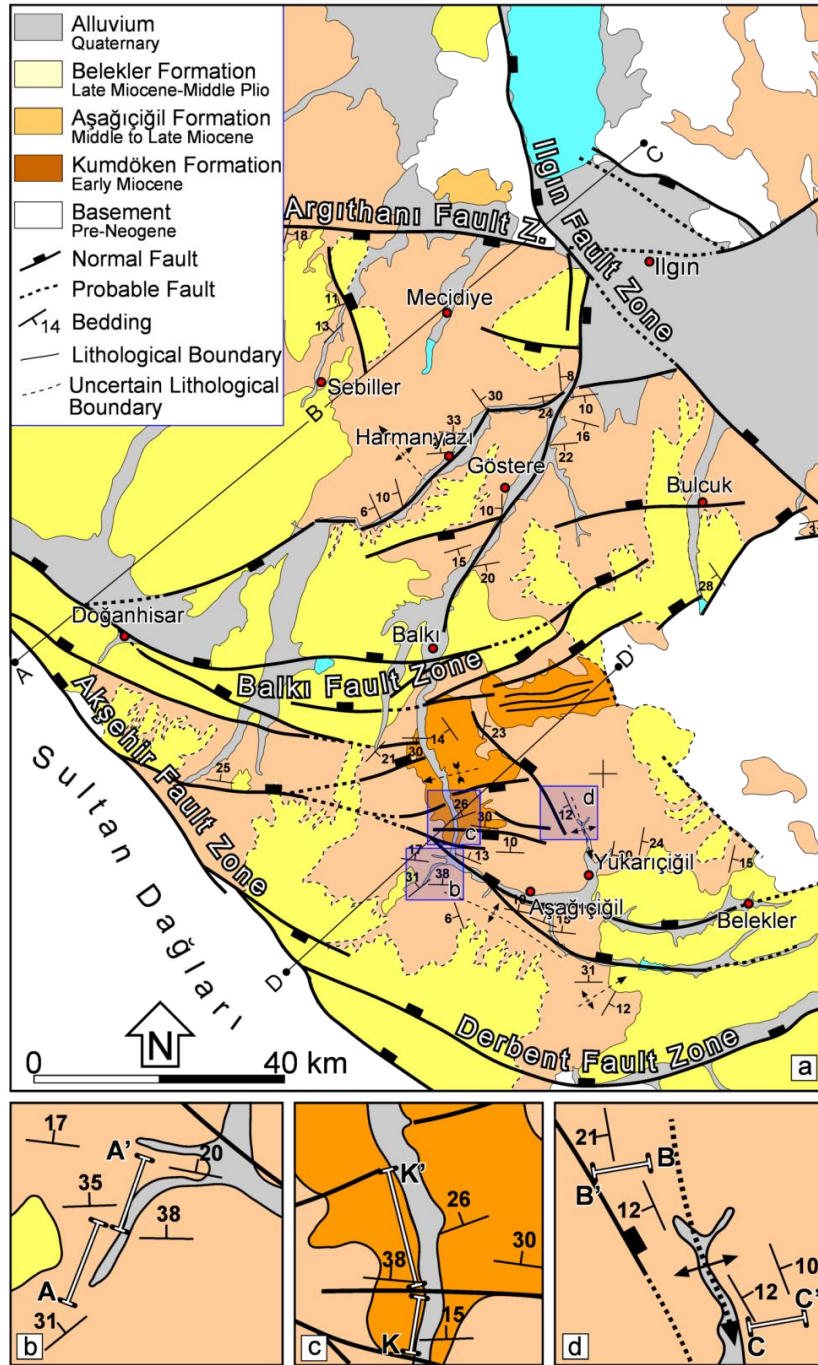


Figure 3.1. Revised geological map of the Iğın Basin from the 1/100000 scale MTA geological map based on the field studies and remotely sensed data. Blue rectangle areas are used to indicate the location of the measured sections of the lithological units. Inset b for Aşağıcığıl formation (AÇFm), Inset c for Kumdöken formation (KDFm) and Inset c for lacustrine part of the Aşağıcığıl formation (AÇFm). Routes of the measured sections are indicated by white solid lines (A-A' for AÇFm, (K-K') for KDFm and (B-B' and C-C') lacustrine part of the AÇFm.

Basin is revised in this study and four main stratigraphic units are proposed, from older to younger including (1) the Kumdöken formation, (2) the Aşağıçiğil formation, and (3) the Belekler formation (Umut et al., 1987). Their lithology, age and contact relationships are described in the following sections and the first order interpretation of their depositional environments is also provided (Figure 3.2).

3.1.1 Kumdöken Formation (KDFm)

The Kumdöken formation (KDFm) which is characterized by alternation of boulder to block sized reddish conglomerates with fine grained reddish/yellowish mudstone is named for the first time in this study. In previous studies, it was regarded as a conglomerate member of the Aşağıçiğil formation (corresponding to Köstere/Gölyaka formation in Koçyiğit et al., (2000), and Harmanyazı formation in Hüseyinca and Eren (2007)) and its stratigraphic position was not correctly defined by Umut et al., (1987). For this reasons, it is redefined and mapped as a separate formation in this study. The base of the Kumdöken formation (KDFm) is mainly represented by conglomerates. Upwards, the conglomerates alternate with coarse to fine sandstone and silty-mudstone. These units are well-exposed along the Ilgın-Beyşehir road (Figure 3.3), near Kumdöken which was selected as the type locality (Figure 3.1a and c). The contact relationship between the KDFm and the basement rocks is not well- exposed, but the KDFm is the oldest observable Neogene rock unit of the basin and the contact relation between the KDFm and the basement rocks is probably nonconformity. This unit is unconformably overlain by the Aşağıçiğil formation (Figure 3.3a).

The oldest part of the sequence starts with generally clast-supported (or matrix supported at some levels), well-cemented and thick-bedded conglomerates (Figure 3.3b and Figure 3.4) that consist mostly of creamy white and dark/light grey recrystallized limestone (90%) and various cherts and ellipsoidal slightly foliated greenish metamorphic rocks and white/pinkish silica (%10) set in a silty-sandy matrix with iron oxide cement (Figure 3.3c). Clasts of the conglomerates are angular to sub-rounded, poorly sorted and ranging from gravel to boulder size (occasionally up to 25 cm of the long axis). A sedimentary structure such as pebble imbrication is occasionally observed at this level of the formation (Figure 3.5a). Bottom bedding surfaces of the conglomerates are remarkably irregular indicating erosional processes such as scour-and-fill structures (Figure 3.5b). The unit is followed upwards by red to yellow sandstone and silty mudstone alternating with conglomerates (Figure 3.3b and Figure 3.4). This thin- to medium-bedded (5-40 cm) silty-mudstone levels contain 2-3 mm coarse sands/granules (very fine gravel) that are floating in muddy matrix. Characteristics of the conglomerates interbedded with mudstones change at some levels and arrangements of the clasts show regular increase in size within one layer (Figure 3.4). The unit is followed upwards by, channel structures consisting of coarse sand and

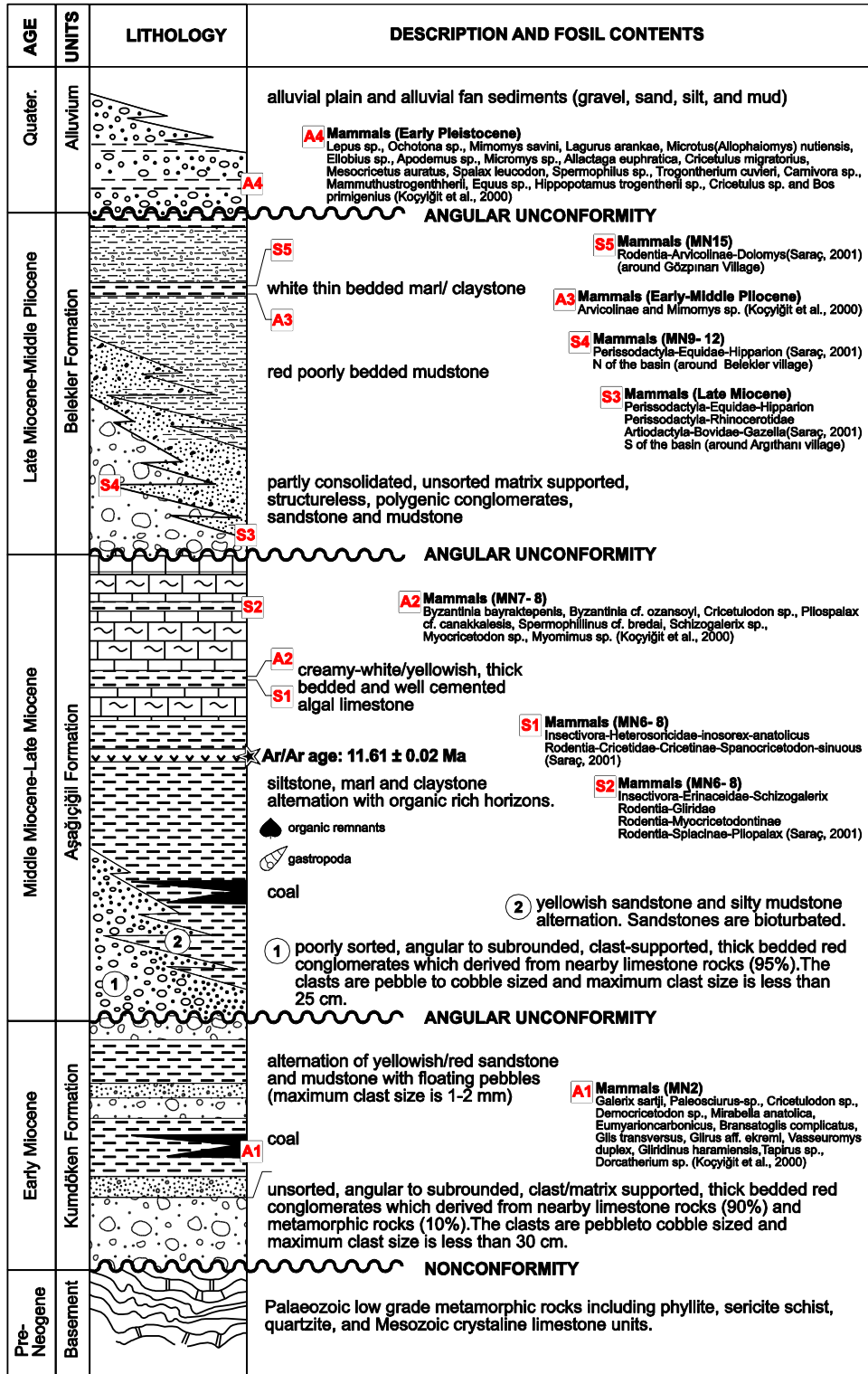


Figure 3.2. Generalized stratigraphic column for the Ilgın Basin. Red labels with rectangle outline indicate the horizons of the fauna (mammalian fossils) and flora (spores & pollens).



Figure 3.3. Field view of an angular unconformity between the Kumdöken and Aşağıçiğil formations (a). White rectangle indicated as inset b shows the bedding attitude of KDFm in azimuth method (b). Close-up view of the polymict, angular to sub rounded, poorly sorted red conglomeratic unit of the KDFm (c).

gravel size clasts within mudstone levels. Additionally intense bioturbation (Figure 3.5c) and cross-bedding structures are noted at higher levels in the sequence (Figure 3.5d). The measured section of the KDFm which is indicated as K-K' in Figure 3.1c has a minimum thickness of 375 m (Figure 3.4).

Koçyiğit et al. (2000) reported micro-mammal fauna from different stratigraphic horizons of alluvi-fluvial as well as lacustrine deposits (Figure 3.2). They determined the following fauna from Gölyaka, north of Ilgın; *Galerix sartji*, *Paleosciurus sp.*, *Cricetulodon sp.*, *Democricetodon sp.*, *Mirabella anatolica*, *Eumyarioncarbonicus*, *Bransatoglis complicatus*, *Glis transversus*, *Glirus aff. ekremi*, *Vasseuromys duplex*, *Gliridinus haramiensis*, *Tapirus sp.*, *Dorcatherium sp.*, all characterizing mammal stage

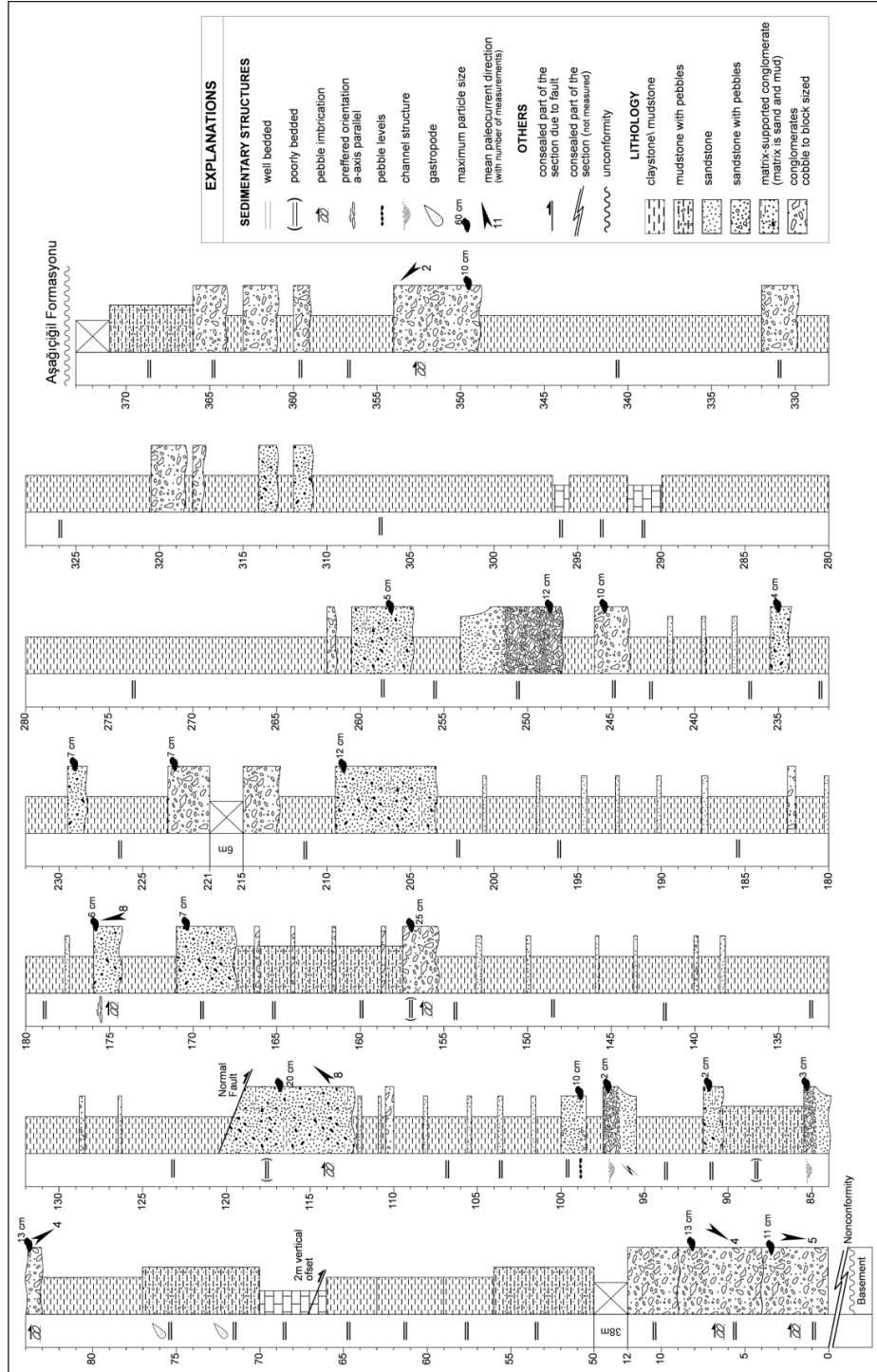


Figure 3.4. Reference section of the Kumdöken formation. The sequence basically consists of fine grained mudstone unit intercalated with alluvi-fluvial coarse grained deposition.

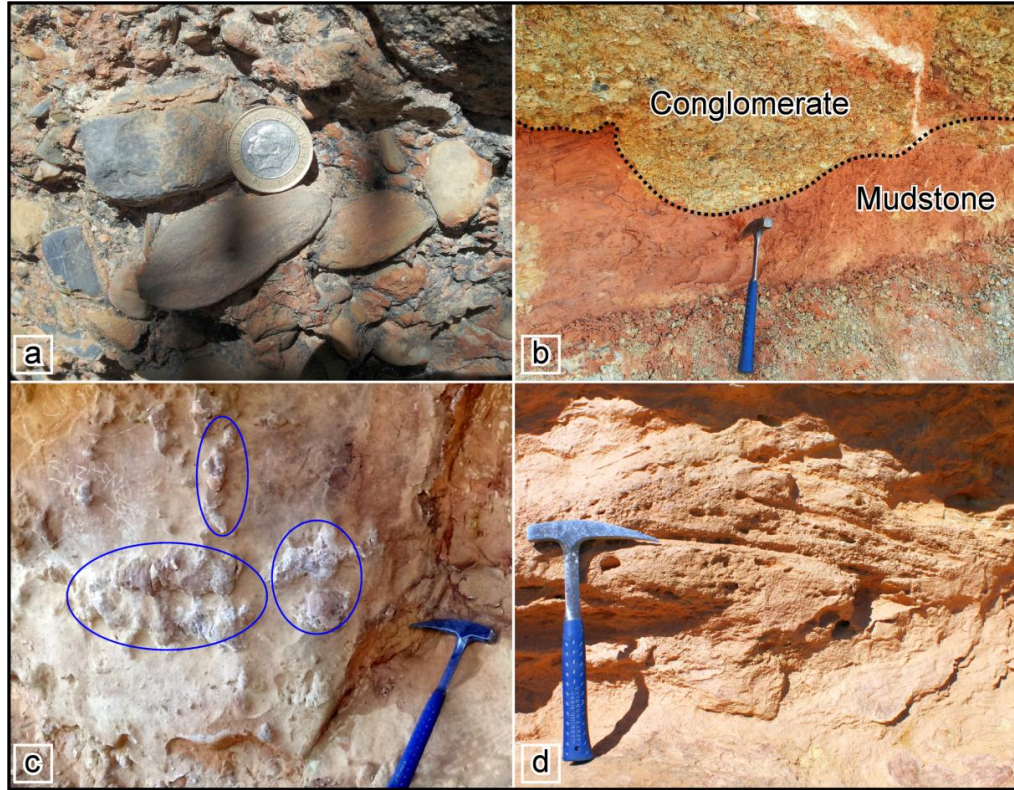


Figure 3.5. Close-up view of pebble imbrication in the conglomeratic unit of the KDFm (a). Scour-and-fill structure formed at the base of the conglomerate (b). Bioturbated mudstone unit (indicated with blue circles) (c). Cross-bedded silty-mudstone (d).

MN2 (A1 in Figure 3.1) zone (Steininger, 1999; Mein, 1999). They named these units as Gölyaka formation and claimed that they are lateral equivalent of their Köstere formation which contains rodent fossils indicating Middle to Late Miocene age (MN 6-8 Zones). In our stratigraphy, basal conglomeratic member of the Gölyaka formation of Koçyiğit et al. (2000) corresponds to Kumdöken formation and the MN 6-8 micro-mammal localities belongs to Aşağıçiğil formation. Based on this information, the age of Kumdöken formation ought to be Early Miocene.

Unsorted, angular and boulder sized reddish conglomerates in the lower level of the unit indicates very close proximity to the source area. Sandy matrix -supported conglomerates indicates aqueous (fluvial) transport, but at lower flow regime in which sand and finer gravel particles were deposited together. Intermittently, the clast-supported conglomeratic levels participate in the system, referring energetic aqueous transport that deposited gravel beds, while sand is still carried in suspension (Colby 1963). The erosional base of the conglomerate units also demonstrates a high energy

environment. In the measured section of the KDFm, inversely graded conglomerates are also observed at some levels of the sequence. This type of grading is relatively uncommon, but is characteristic of debris flow deposits common in alluvial fan environments (Mial and Smith 1989, Mial 1996). The fine grained red mudstones form the quiet water depositional environment. Red coloration of the mudstone reflects deposition in an oxidizing environment. This is generally achieved in continental environments due to oxidation (Walker 1967). Therefore, the mudstones may be deposited in river floodplains, in downstream parts of the fluvial environment, or in distal parts of alluvial fans. The KDFm comprises facies associations ranging from alluvial fans to proximal fluvial systems of both axial deposition and tributaries entering the system laterally.

3.1.2 Aşağıçığıl Formation (AÇFm)

The Aşağıçığıl formation (AÇFm) was named by Umut et al. (1987) and is characterized by alternation of white/yellowish and gray limestone, sandstone, tuff, marl and claystone. Alternative names were provided by Koçyiğit et al., (2000) who termed this the Köstere formation, who depicted a syn-tectonic fan to flood plain depositional setting. Additionally, Hüseyinca and Eren (2007) defined it as the Harmanyazı formation characterized by claystone as a basic lithology intercalated with marl and limestone. The Aşağıçığıl formation is well exposed along the Balkı-Aşağıçığıl main road, and two sections were measured to characterize the unit, close to the Aşağıçığıl (Figure 3.1b and d). AÇFm unconformably overlies KDFm in the south of the basin (Figure 3.3). It is delimited by the Akşehir-Afyon Fault zone in the west, whereas lacustrine algal limestones of the AÇFm onlap over basement rocks in the east, around Çavuşçugöl (Figure 3.1). The Belekler formation unconformably delimits the upper boundary of the formation in the south and the north of the basin (Figure 3.6).

The lithology and facies characteristics of the unit are gradually changing from west which defines the tectonically active boundary of the basin to east which defines the central part of the basin. Based on the basin geometry, first measured section (SC1) (A-A' line in Figure 3.1a) was recorded along the Kireşen Stream, a branch of the Balkı River, close to the western edge of the basin. The sequence (Figure 3.7) starts at the bottom with angular, poorly rounded, unsorted, both matrix (Figure 3.8a) and locally clast-supported (Figure 3.8b) gray/yellowish conglomerates. Clasts of the conglomerates ranging from pebble to cobble size (occasionally up to 25 cm), are polymict, and consist of 85% variable type and color (dark/light gray and creamy white) limestone, white quartz and greenish metamorphic rocks with slight foliation, and other rock fragments (15%) (Figure 3.8b). At these levels stratification is poor and the unit is crudely bedded. The sequence continues upwards with sub-rounded, graded, clast-supported dark gray conglomerates (Figure 4.8c) alternating with yellowish, highly bioturbated (Figure 3.8e)

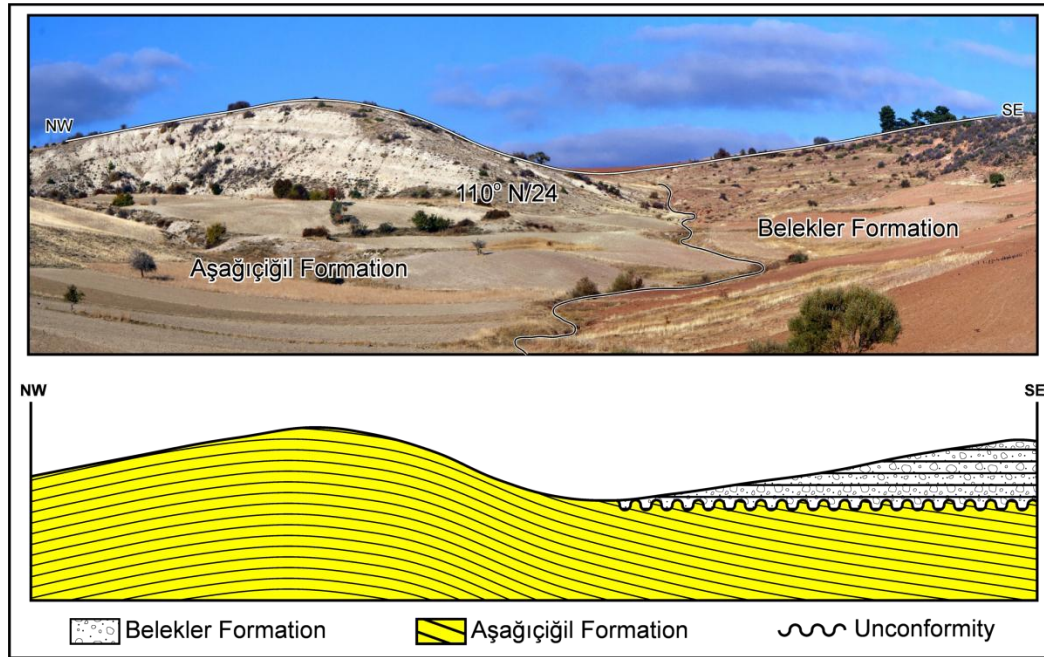


Figure 3.6. Field view of the angular unconformity between the Aşağıcığıl and Belekler formations.

and fresh water gastropod bearing (Figure 3.8g) pebbly sandstones. Pebble imbrication is occasionally observed at these conglomeratic levels (Figure 3.8d). Channel lag deposits in this coarse sandstone are clast-supported and composed of coarse to medium size gravel (Figure 3.8f). The coarse grained sandstone is gradually replaced upwards by silty sandstone. At the stratigraphically higher levels, the section shows alternation of marl, siltstone and organic-rich blue claystone, and finally medium to thick bedded algal limestone (Figure 3.7h). The AÇFm has a minimum thickness of 357 m in this section (SC1).

From the Sultandağları Mountain in the west towards the center of the basin, the second section was recorded, which is given as B-B' in Figure 3.1d. The section (Figure 3.9) is located 2 km north of the Yukarıcığıl and it is characterized by lateral decrease in grain size and the facies changes into fine grained gray mudstone/white marl (Figure 3.9c and Figure 3.9d) and algal limestone (Figure 3.8a and b). The oldest part of the section starts with dark grey mudstone unit with thin pumice bearing levels (Figure 3.9e). From this level, a pumice sample was collected for $^{40}\text{Ar}/^{39}\text{Ar}$ dating. Aside from pumice levels, organic-rich horizons with 10-15 cm thick also intercalate in mudstone/claystone units. At the base of the SC2, the AÇFm is separated by a fault from the KDFm. The upper boundary of the AÇFm is clearly observed in the field, 2 km east of Yukarıcığıl, where the Belekler formation unconformably overlies the AÇFm (Figure 3.6). The 63 m thick SC2

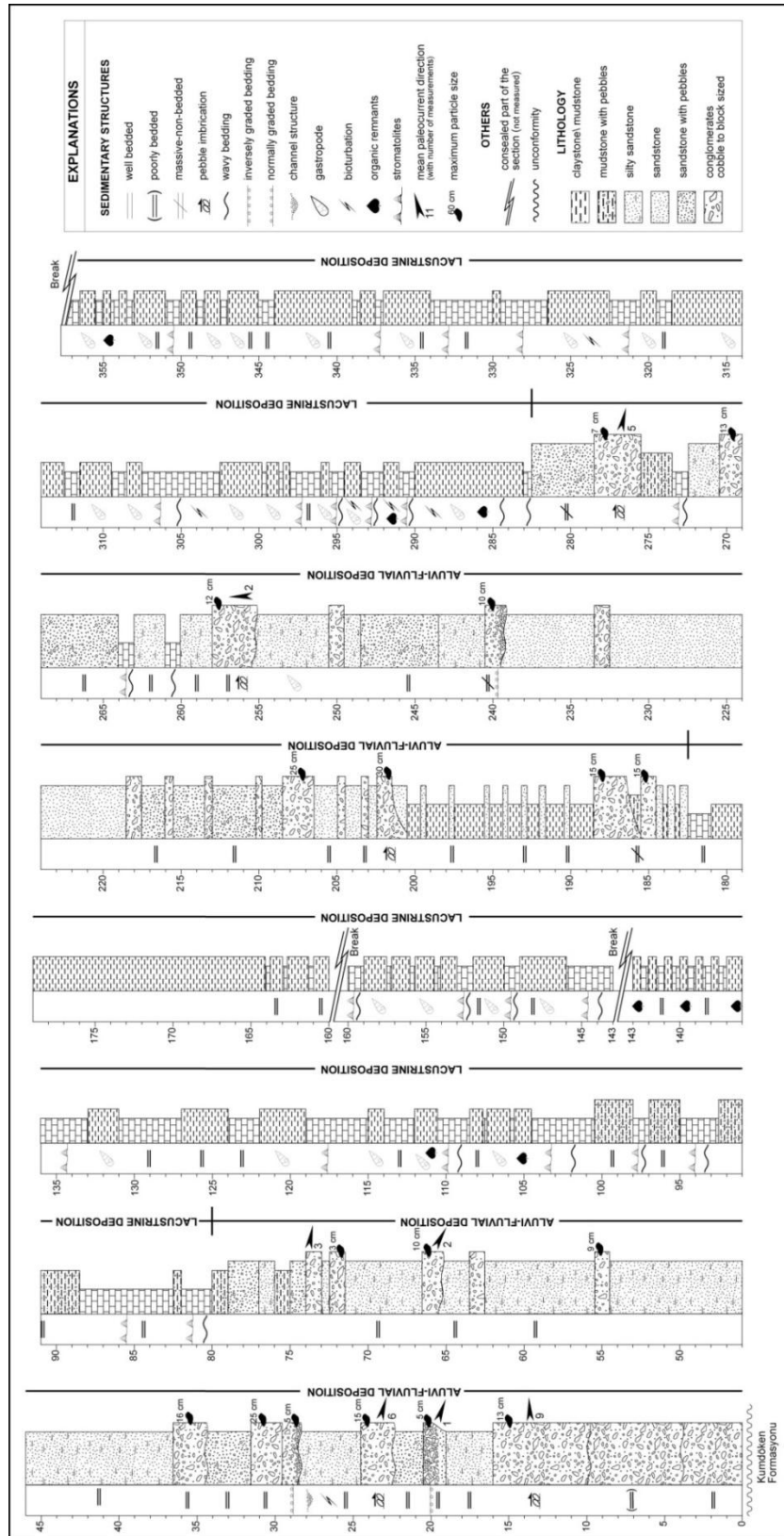


Figure 3.7. Measured section of the Aşağıçığil formation. The sequence basically consists alluvi-fluvial facies units interfingering with lacustrine facies units.



Figure 3.8. Field views of the typical facies changes of the ACFm. Basal conglomeratic unit shows matrix (a) and clast (b) supported characteristics. Close up view of the basal conglomerate with normal graded beds (c) and imbricated clasts (d). Conglomerates intercalated with intensely bioturbated coarse sandstone (e) which contains channel structures filled with medium to coarse pebbles (f). Fresh water gastropods (g) bearing siltstone/mudstone and fresh water stromatolitic limestone (h) alternation.

section represents a lateral equivalent of the (upper part of) SC1. In Figure 3.1d, another measured section (SC3) is showed as line C-C', which is the equivalent of the SC2 since the structure takes the broad anticlinal form in this part of the basin. It has more thicker than the SC2, approximately 130 m.

Koçyiğit et al. (2000) documented that the age of this formation based on vertebrate fossil assemblages including *Byzantinia bayraktepenis*, *Byzantinia cf. ozansoyi*, *Cricetulodon sp.*, *Pliospalax cf. canakkalesis*, *Spermophilinus cf. bredai*, *Schizogalerix sp.*, *Myocricetodon sp.*, *Myomimus sp.*, which characterizes MN7-8 zone (A2 horizon in Figure 3.2). Saraç (2001) also reported fossil vertebrates *Rodentia-Cricetinae* (MN6-8 zone, S1 in Figure 3.2) from lacustrine deposits corresponding to the upper part of the AÇFm. Based on these literature information and our $Ar^{40}-Ar^{39}$ age (11.61 ± 0.02 Ma) Middle to Late Miocene age is assigned for the Aşağıçiğil formation.

Boulder to block size, sub-angular to sub-rounded, matrix-supported conglomerates without any appreciable sedimentary structures (chaotic) and occasional reverse grading indicate alluvial fan or alluvial apron deposition (bajada) (Mial 1996). Angular/sub-rounded and clasts-supported conglomerates with sedimentary structures including pebble imbrication, channel lag deposits and normal graded bedding is best interpreted to reflect fluvial environment. Moreover, the presence of floating pebbles in the sandstone and an obviously water-laid conglomerate beneath may suggest, a stream-flow origin (Glennie, 1970). Alternation of these different type conglomeratic units suggests that the AÇFm was deposited in alluvial fan to braided to low sinuosity fluvial environment including slope and channel processes. Particle size gradually decreases from western margin towards the east, which indicates facies organizations from basin margin to basin center that changes from coarse grained to mud/clay, marl, and limestone facies towards the interior part of the basin. Organic rich levels may indicate marshy areas in the periphery of a lake (Walker and James, 1992; Talbot and Allen, 1996). These lithologic characteristics and fresh water fossil content suggest a shallow lacustrine environment. Intercalation of the fine grained units with conglomerates in the whole sequence indicates that the depositional environment of the Ilgın Basin laterally changes from alluvial-fluvial to a quiet lacustrine environment (Figure 3.7) in the depocenter during Middle Miocene.

3.1.3 Belekler Formation (BLFm)

The Belekler formation (BLFm) is characterized by reddish-brown poorly consolidated conglomerate, sandstone, and mudstone alternations. It is widespread in the basin, near Belekler. To the west of Ilgın Basin, near Ayaşlar and around Balkı, topography provides a well-exposed outcrop of the BLFm. The formation was first named by Umut et al., (1987) and its locality is near Belekler (Figure 3.1). The Belekler formation

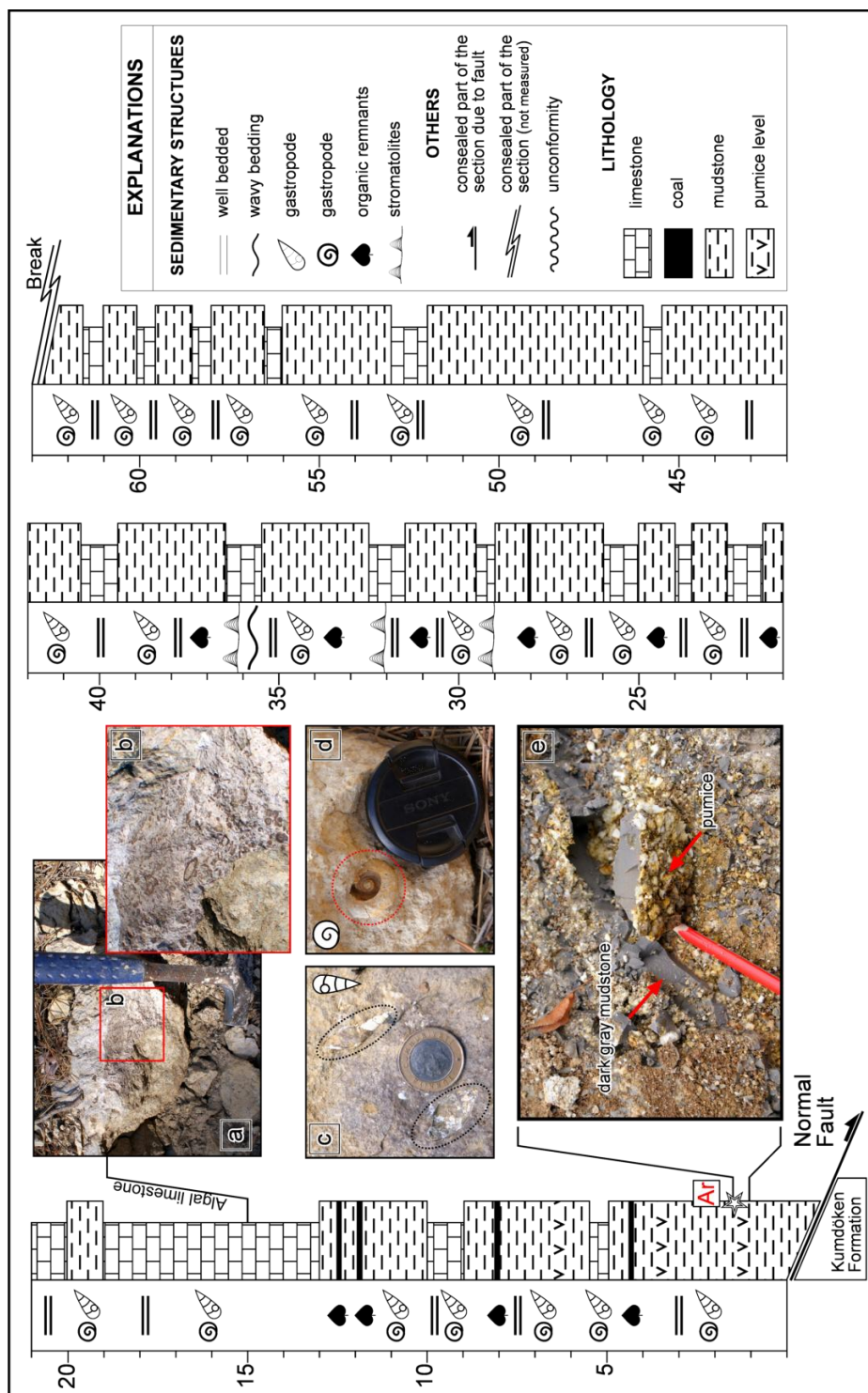


Figure 3.9. Measured section succeeded by fresh water gastropods bearing mudstone, marl alternations (c and d) and intercalations of well-cemented, thick-bedded algal limestone (a and b). Close-up view pumice level (e) from which sample was collected for Ar/Ar dating.

unconformably rests on the Aşağıcığıl formation (Figure 3.6) in the south of the basin. Similar relation was also observed in the northern part of the basin (Figure 3.10). To the SW of Ayaşlar, the formation is composed of loosely cemented, unsorted and polymict, angular, pebble- to block-size (occasionally up to 50 cm diameter), matrix-supported conglomerates (Figure 3.11a). Clasts generally consist of polymict limestones, quartzites and schists, i.e., lithologies that are abundant in the basement of Ilgın Basin. The clasts are floating in a reddish muddy/sandy matrix. Conglomerates are generally structureless/massive and they do not display any primary sedimentary structures. The arrangement of the clasts is chaotic, with neither any preferred orientation nor sorting. Towards the east, around Balkı, the facies changes laterally and the grain size gradually decreases into mudstone (Figure 3.11b). The sketch cross-section given in the Figure 3.11 illustrates the lateral facies changes of the Belekler formation from Ayaşlar to Balkı. From west to east, the distal part of the sequence is composed of alternation of red mudstones and white marls (Figure 3.12). The maximum thickness of the unit was reported by Koçyiğit et al. (2000) as 319 m for the alluvial fan deposits and 280 m for the flood plain deposits based on data from boreholes provided by Çuhadar (1977). In this study, the thickness of fine grained deposits representing relatively basinal facies is measured to be 200 m (Figure 3.12).

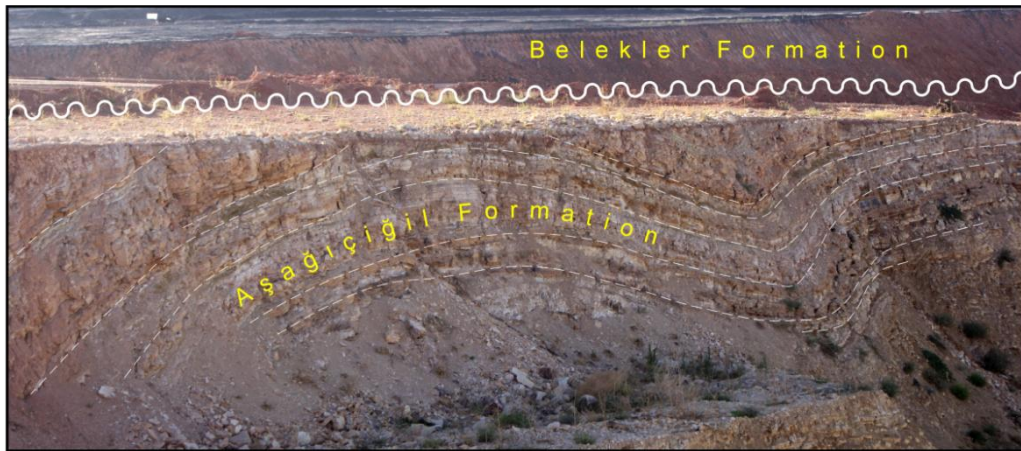


Figure 3.10. Field view of the contact relation between the BLFm and AÇFm in the north of the basin. The photo was taken from coal mine in the Çavuşçugöl area. View to West.

Saraç (2001) reported fossil vertebrates including *Hipparion* sp. from the fluvial deposits located around Belekler. This fossil fauna is characteristic for the MN9-12 zone (S4 horizon in Figure 3.2) and Saraç (2001) assigned a Late Miocene age for this unit. In the north of the basin, around Argıthanı, Koçyiğit (2000) and Saraç (2001) reported fossil vertebrates from the same locality, but at different levels of the Belekler



Figure 3.11. Belekler formation from west to center of the basin. Note that the formation characterizes loosely consolidated angular conglomerates (a) in the west of the basin and it consists of mudstone (b) in the central part of the basin. Cross-section interprets the grain size changes of the Belekler formation.

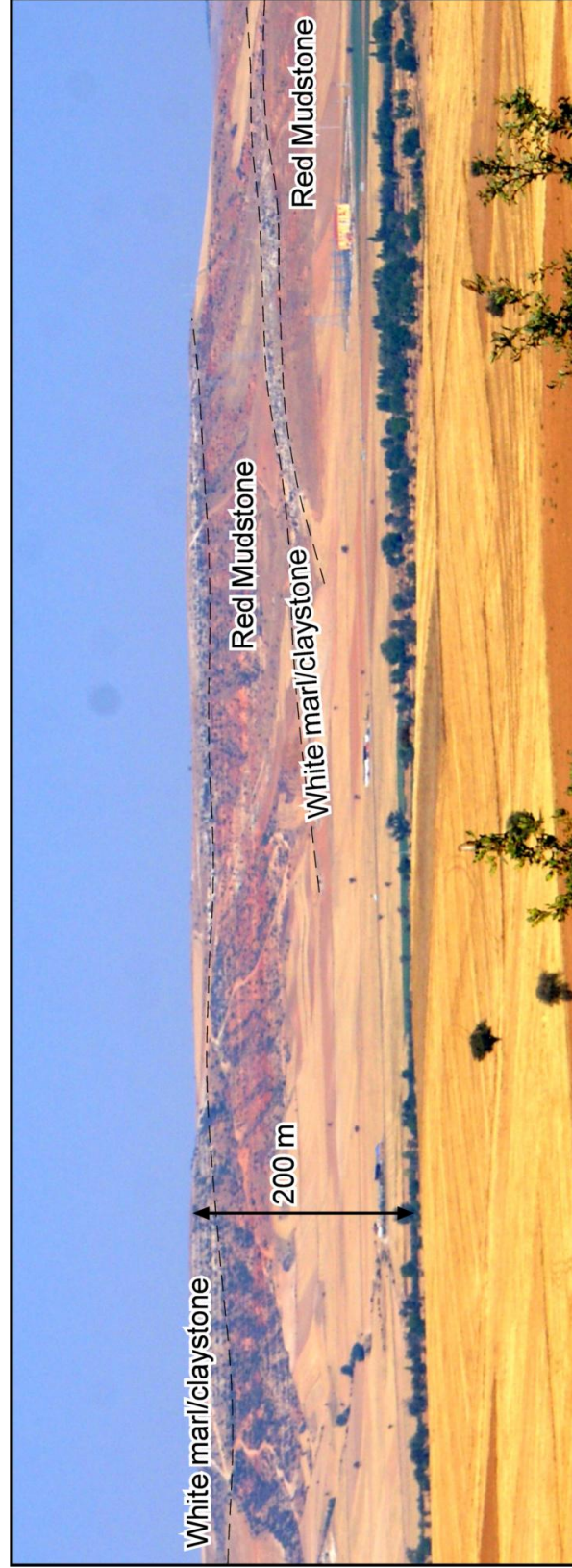


Figure 3.12. Field view of lateral facies changes of the Belekler formation. Alternation of red mudstone with white marl/claystone along the Ilgin-Beyşehir road. View to west.

formation. Saraç (2001) reported *Hipparion sp.* and *Gazella sp.* collected from the fluvial deposit and this assemblage is assigned to Late Miocene (S3 horizon in Figure 3.2). The samples (A3 horizon in Figure 3.2) collected from the lacustrine deposits by the Koçyiğit et al., (2000) indicate Early-Middle Pliocene age. Another fossil level of the BLFm was found around Gözpinarı by Saraç (2001) (S5 in Figure 3.2) and based on its mammal fossil content Early Middle Pliocene age (MN 15 Zone) was assigned. For this study, the Late Miocene-Middle Pliocene age is adopted based on given fossil assemblage in the previous studies.

Thick, structureless, matrix-supported conglomerates of Belekler formation, which mainly outcrops at the marginal parts of the basin, indicate the alluvial-fluvial origin for the facies. Fine grained mudstone units with fresh water gastropods represent transitions from the distal part of the alluvial-fluvial deposition to lacustrine environment. Alternation of these mudstone levels with the white claystone/marl unit towards the center of the basin indicates lacustrine origin. This information collectively indicates that the Ilgın Basin was characterized by facies associations, from the basin margin to the basin center, ranging from alluvial fan, low sinuosity fluvial to back swamps and lacustrine environment, which is in fact almost the same present day configuration of the basin.

3.1.4 Quaternary Units (Qua)

The Quaternary units in the basin are represented by presently active alluvial deposits along the permanent to temporary streams, presently active lacustrine Çavuşcugöl Lake and marshy environments around the streams.

Oldest Quaternary units are encountered Dursunlu village (A4 in Figure 3.2). From this locality Koçyiğit et al. (2000) provided a very wide list of various mammal fossils, *Lepus sp.*, *Ochotona sp.*, *Mimomys savini*, *Lagurus arankae*, *Microtus(Allophaiomys) nutiensis*, *Ellobius sp.*, *Apodemus sp.*, *Micromys sp.*, *Allactaga euphratica*, *Cricetulus migratorius*, *Mesocricetus auratus*, *Spalax leucodon*, *Spermophilus sp.*, *Trogontherium cuvieri*, *Carnivora sp.*, *Mammuthustrogenthherii*, *Equus sp.*, *Hippopotamus trogontherii sp.*, *Cricetulus sp.* and *Bos primigenius*, that indicate Early Pleistocene.

3.2 ⁴⁰Ar/³⁹Ar Geochronology

Age assignments for the Ilgın Basin so far rely on mammalian fossil fauna and spores/pollen assemblages (Koçyiğit et al., 2000; Saraç, 2001 and Karayiğit et al., 1999). To acquire quantitative age information, here it is provided an ⁴⁰Ar/³⁹Ar age from a pumice bearing horizons from Aşağıçiğil formation (Figure 3.2 and Figure 3.9).

Table 3.1. Summary of $^{40}\text{Ar}/^{39}\text{Ar}$ data. Full data tables are given in the appendix. Errors are reported with 2σ uncertainty and represent analytical error. Full external errors are reported between brackets. MSWD is Mean Square Weighted Deviate. N is the number of analysis included in the weighted mean age, between brackets the number of experiments excluded.

Irradiation ID	Location		Material	Weighted Mean Age	MSWD	N	Inverse Isochron	$^{40}\text{Ar}/^{36}\text{Ar}$ Intercept
	Long	Lat						
VU78B-S4	31,883544	38,080778	Sanidine	$11.61 \pm 0.02(0.24)$	1.59	9(1)	$11.62 \pm 0.02(0.24)$	286 ± 58

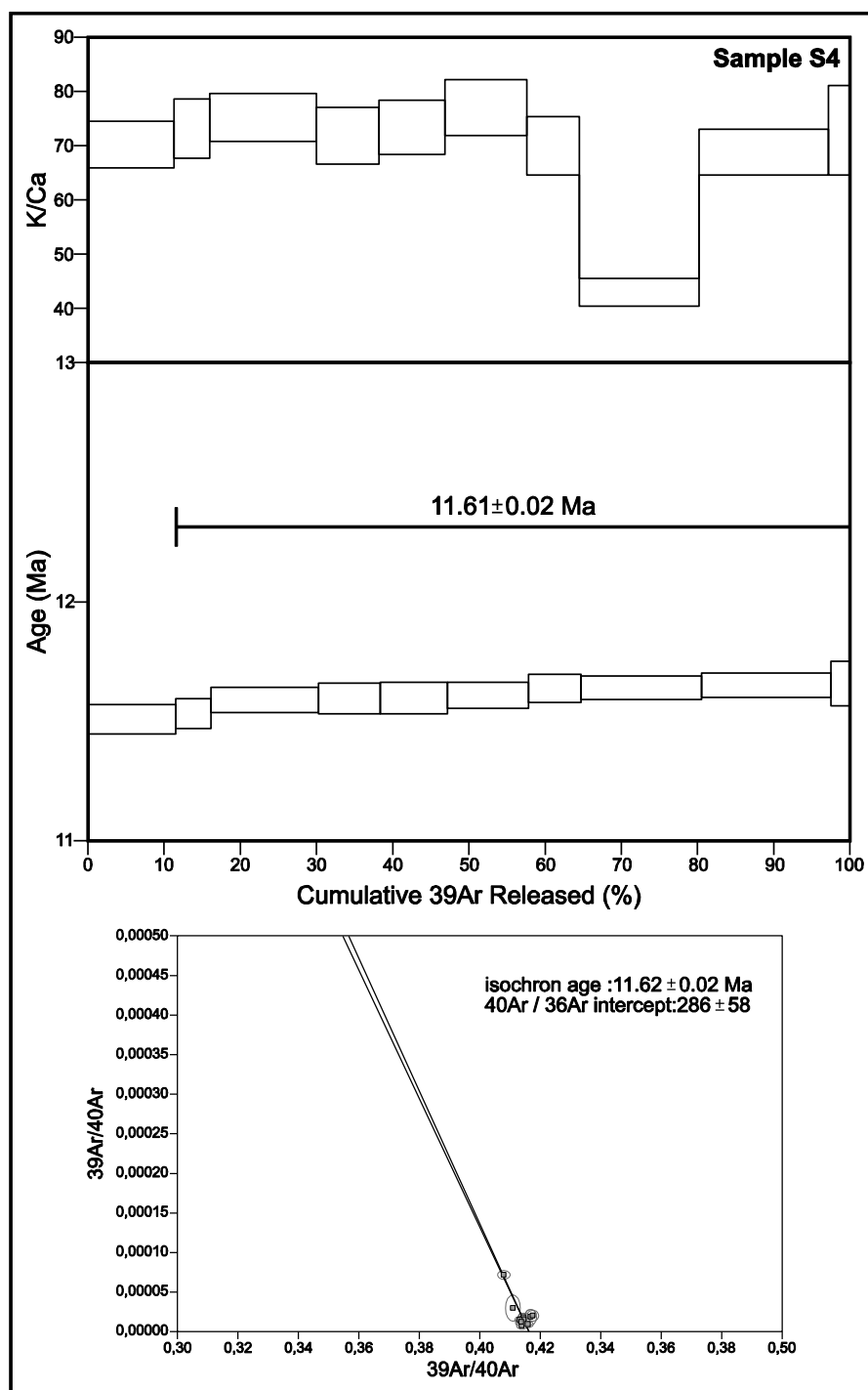


Figure 3.13. Replicate single crystal fusion $^{40}\text{Ar}/^{39}\text{Ar}$ ages are plotted versus the % of $^{39}\text{Ar}/\text{K}$ released in each fusion analysis for the three pumice samples from the Ilgin Basin. The width of the bars/steps represents the 2σ analytical error. On top the K/Ca ratio (grey area, width is 2σ error) is displayed. Weighted mean ages are given. The lowermost graph shows the inverse isochron diagram.

Sample preparation process is given in previous sections. And in order to avoid repetition, these processes will not be repeated here (for full account of the sample preparation is referred to Section 2.2 in Chapter 2 and Koç et al., 2012). Ages are calculated using the in-house (Free University of Amsterdam) developed ArArCalc software (Koppers, 2002) with Steiger and Jäger (1977) decay constants and they are calculated relative to the FCs of 28.198 ± 0.23 Ma (Kuiper et al. 2008, note that this study reports 28.201 Ma using decay constants of Min et al., 2001, which converts to 28.198 Ma using Steiger and Jäger, 1977). Correction factors for neutron interference reactions are $(2.64 \pm 0.04) \times 10^{-4}$ for $(^{36}\text{Ar}/^{37}\text{Ar})\text{Ca}$, $(6.73 \pm 0.08) \times 10^{-4}$ for $(^{39}\text{Ar}/^{37}\text{Ar})\text{Ca}$, $(1.211 \pm 0.006) \times 10^{-2}$ for $(^{38}\text{Ar}/^{39}\text{Ar})\kappa$ and $(8.6 \pm 1.4) \times 10^{-4}$ for $(^{40}\text{Ar}/^{39}\text{Ar})\kappa$. The $^{40}\text{Ar}/^{36}\text{Ar}$ ratio of 295.5 of Nier (1950) is used in the calculations. Errors are reported at 2 sigma level. Outliers are identified by comparing MSWD with the T-student distributions. The summary of the $^{40}\text{Ar}/^{39}\text{Ar}$ result is given Table 3.1 and plateau and isochron is given in Figure 3.13.

Sample S4 containing high sanidine yields a weighted mean age of 11.61 ± 0.02 Ma (analytical error); or ± 0.24 Ma (full external error including standard age and decay constant uncertainties). The sample has high radiogenic $^{40}\text{Ar}^*$ contents and therefore data points cluster together on the isochrones.

3.3 Structural Geology

This part of the thesis mainly focused on the detailed description and analysis of the major structures which shaped the Ilgın Basin. Analysis of lineaments, fault patterns, lithological discriminations and geomorphologic characteristics based on remote sensing data are given in this part of the chapter. These structures were mapped using satellite images and verified in the field. During the field studies, numerous mesoscopic faults with no more than a few meters offset as well as major faults were studied to collect kinematic data for construction of paleostress configurations. Hence, formation of the Ilgın Basin within the context of kinematics, geometry and characteristics of the structures was provided in this part of the thesis.

3.3.1 Lineament Analysis from Remotely Sensed Data

During the extraction of the lineaments, various enhancement techniques were used in order to improve the spectral and spatial resolution of the used images which includes Landsat ETM+ and Quickbird images obtained from Google Earth. Low resolution (30m) multispectral bands of the Landsat ETM+ were combined with a high resolution panchromatic image (15m) to generate a higher resolution fused color image (pansharpening). This process is used to improve spatial resolution of multispectral

channels of the satellite images. Additionally, various digital image processing techniques were used to enhance the spectral resolution of the images. Among these techniques contrast enhancement, color composite, principal component analysis (PCA) and decorrelation stretching (DS) techniques are used to improve the visual interpretability of an image. The processed images were draped on 25*25 resolution digital elevation models (DEM's) prepared from 1/25.000 scale topographic maps to improve 3D visualization in different directions (Figure 3.14).

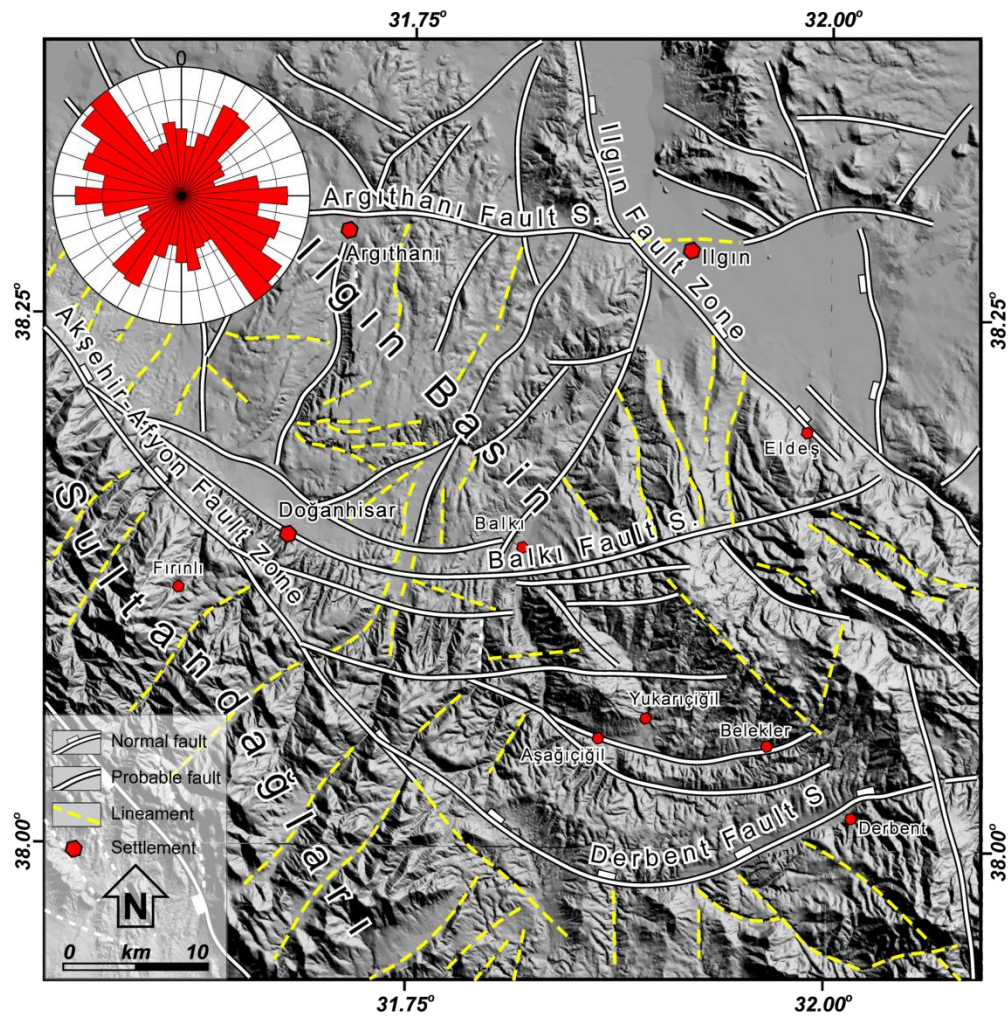


Figure 3.14. Lineament map of the Ilgin Basin. Rose diagram (length weighted) shows orientations of both faults and lineaments. Base image is Digital Elevation Model produced from the 1/25.000 scale topographic maps.

Similarly as mentioned in previous chapters, lineaments were extracted manually on the images since expert perception can easily interpret geomorphologic signatures and discriminate them into lineaments. Resultant lineament map is given in Figure 3.14 together with weighted segment rose diagram prepared from the trends of these structures. Rose diagrams (Figure 3.14) including orientations of both faults and lineaments shows three dominant directions; NE-SW, NW-SE and E-W. Lineaments with NE-SW orientation correspond to well-developed river networks of the study area which is approximately at 90° angles to NW-SE directed Akşehir-Afyon Fault Zone (AAFZ). E-W directed lineaments reflect the secondary faults bifurcated and curved away from the major faults displaying horse-tail pattern.

3.3.2 Field Observation

Ilgın Basin is approximately 27 km wide, 50 km long and NNW-SSE trending intra-montane basin (Figure 3.1 and Figure 3.15). The major active structure controlling the Ilgın Basin is the Akşehir-Afyon Fault Zone which delimits southwestern eastern margin of the basin and morphologically it is very well expressed by a sharp and linear boundary between the basement and basin infill. During the field studies, mesoscopic faults which developed during and after the sedimentation in the basin have also documented and noticed that two dominant fault trends, NE-SW and E-W, control the tectonic of the region.

3.3.2.1 Faults

Two major structural trends are identified in the study area during field studies in addition to information obtained from satellite images and directional analysis of the lineaments. These trends include NE-SW and E-W striking faults. All of these faults are characterized by normal faults with minor sinistral or dextral components. In addition to the normal faults, also the strike-slip faults are recorded and they occurred within the basin infill.

3.3.2.1.1 Akşehir-Afyon Fault Zone (AAFZ)

The Akşehir-Afyon Fault Zone (AAFZ) is the most prominent structure being more than 400 km long and associated with a vertical throw of up to 2000 m between the Ilgın Basin floor and the Sultandağları basement (Koçyiğit et al., 2002). It is morphologically easily recognized as a NW-SE oriented linear mountain front rising steeply in the western margin of the Ilgın Basin (Figure 3.16).

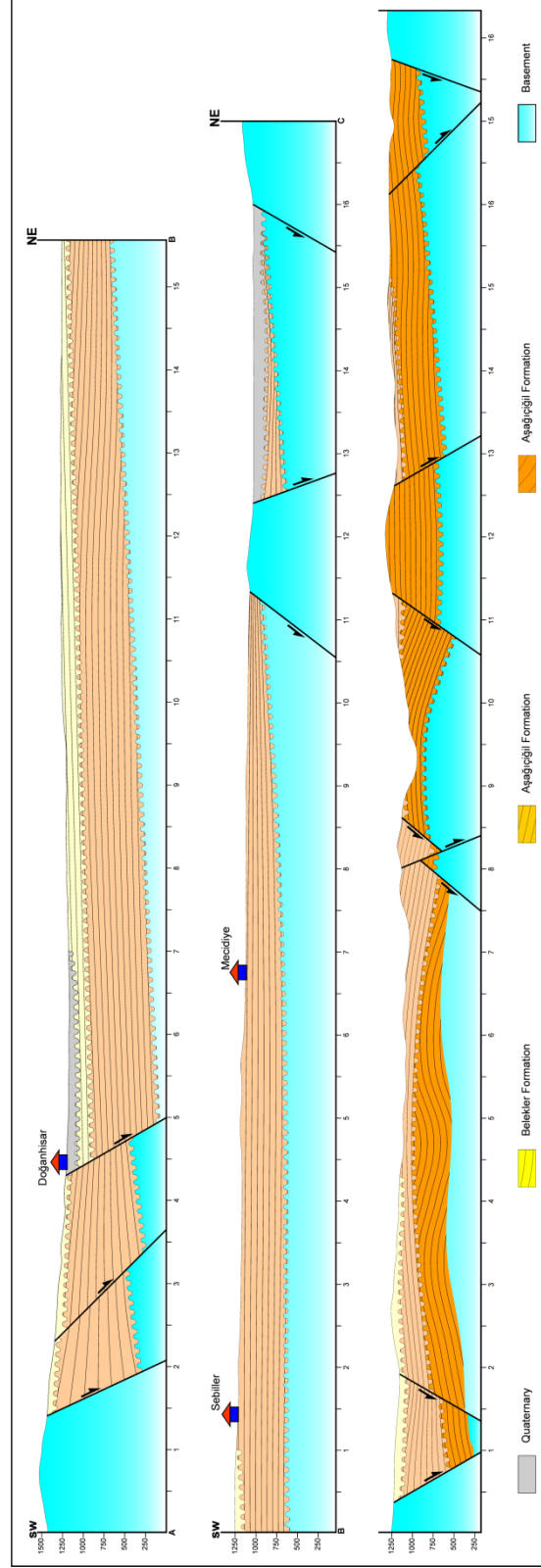


Figure 3.15. Structural cross-sections produced from the geological map given in Figure 3.1.

At the western margin of the Iğın Basin, along the southern part of the Sultandağları range, mass flow conglomeratic units are very well expressed and exposed along several outcrops at the Fırınlı and Tekkeköy (Figure 3.17). These mass flows, originated from the Sultandağları basement range and deposited on the hanging-wall of the Akşehir fault (i.e. basinward), are normal faulted and dragged along the fault planes (Koopman, 2011). The total throw on the western section of the AFZ was interpreted to be at least 870 m since the Late Pliocene (Koçyiğit and Özacar, 2003). This would suggest a maximum rate of motion along the western section of the AFZ of about 0.3 mm/yr.

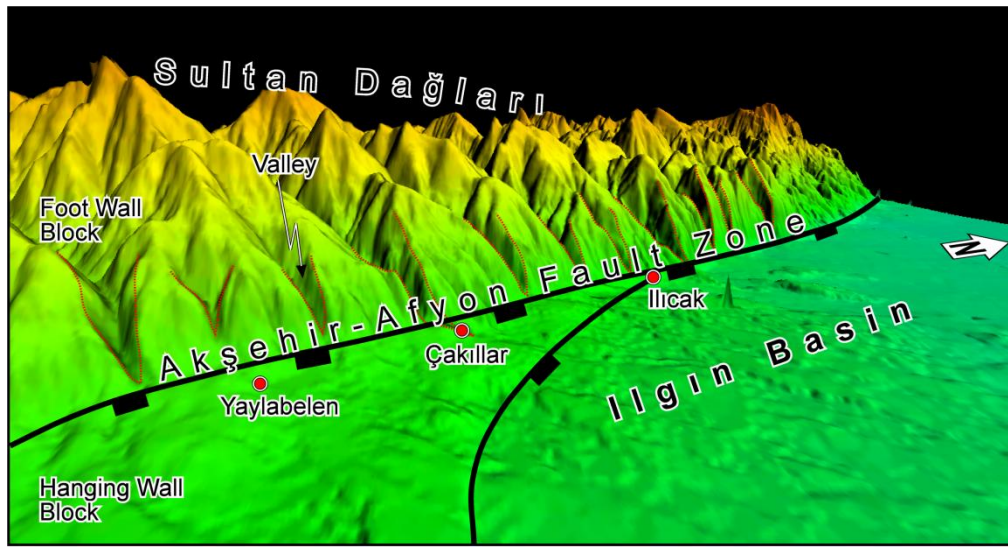


Figure 3.16. Digital Elevation Model (DEM) with 25*25 spatial resolution prepared from 1/25.000 scale topographic maps shows 3D view of the NE dipping Akşehir-Afyon Fault Zone (AAFZ) at the western margin of the Iğın Basin. Sultandağları contains several NE-SW trending valleys which are indicated by red dash lines. Flat-iron morphologic structure along the fault zone is characteristic for normal fault activity.

The main fault plane displays northeasterly dipping normal fault, and dip of the fault surface ranges between 29° and 85° (Koçyiğit et al., 2000). Morphologically, the northern continuation of the AAFZ is clearly traceable on aerial photographs and satellite images, and can easily be extracted from the DEM (Figure 3.16), however the southeastern continuation could not be followed easily since there is a more gradual change in elevation. Additionally, the AAFZ bifurcates into several segments and creates horsetail structure possibly due to space problem related to fault termination processes.

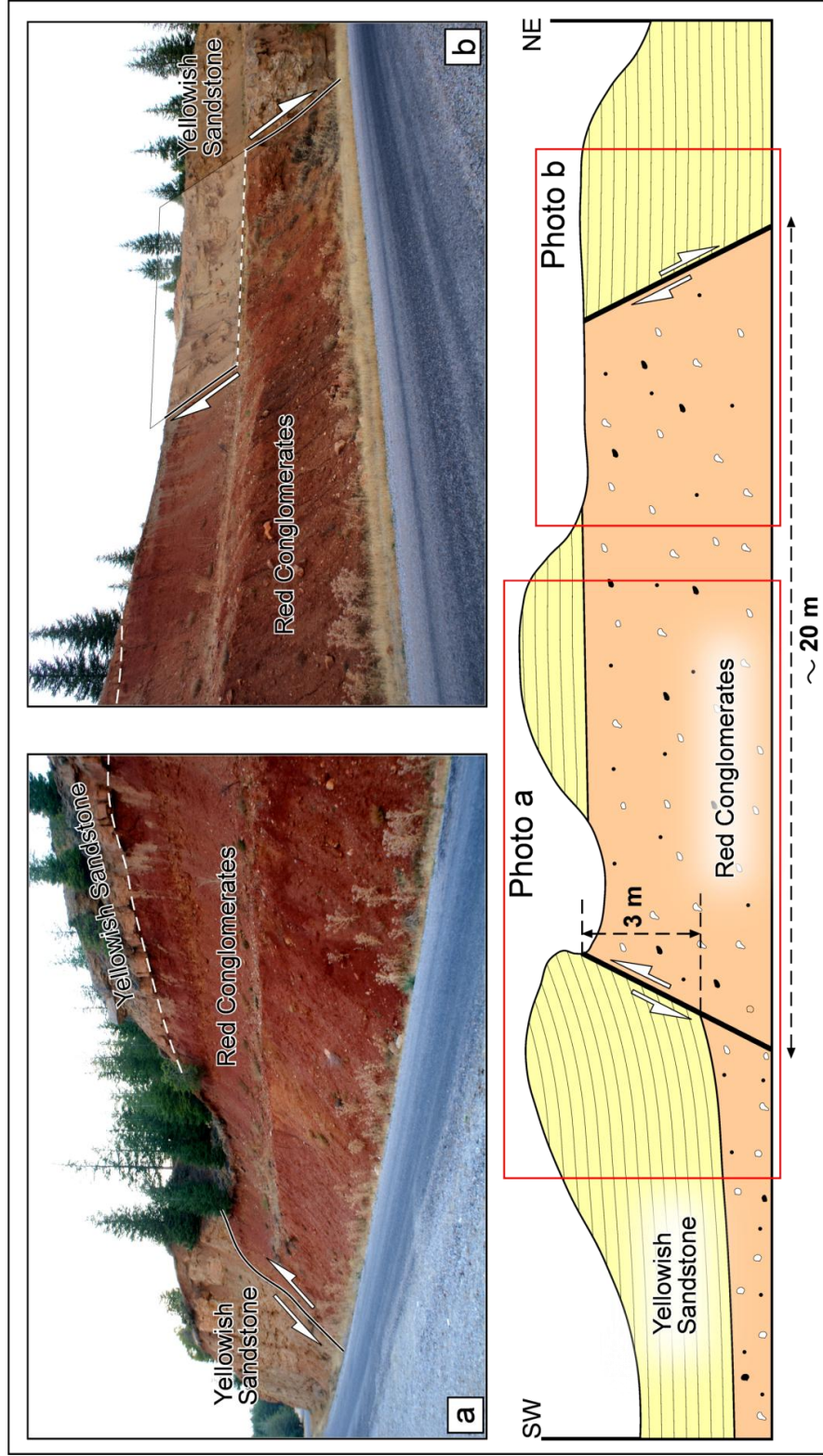


Figure 3.17. Cross-section along the Doğanhisar-Fırınlı road shows N20W striking faults of the Akşehir-Afyon Fault Zone. Faults are conjugate and dipping towards and away to basin center. The rectangle areas on the cross-section indicate the location of the photos a and b.

The AAFZ has previously been interpreted as a thrust fault (Boray et al., 1985; Şaroğlu et al., 1987, Barka et al., 1995). However, recent studies including focal mechanism solutions, GPS studies, and outcrop observations clearly demonstrate that the AAFZ is a normal fault with minor oblique-slip component that change depending on the location and fault orientation (Koçyiğit, 1984; Koçyiğit et al., 2000; 2003, Aktuğ et al., 2010; Ergin et al., 2009; Koopman, 2011).

The sudden break in slope, the well-developed fault scarp, including multiple triangular facets (Figure 3.16), formation of the hanging wall valley and juxtaposition of different lithologies are considered as primary geomorphologic criteria for the recognition of the

AAFZ. Additionally, Koçyiğit et al., (2003) reported outcrop observation of slickenside with striation and the stereographic plot of fault-slip data on the Schmidt's lower hemisphere net showing the characteristics of the Akşehir Master Fault as an oblique-slip normal fault dipping at average 60° NE with a minor amount of dextral and/or sinistral strike-slip component. The orientation of the principal paleostress was given by Koçyiğit et al., (2003) as follows: $\sigma_1 = 241^\circ\text{N}/76^\circ$, $\sigma_2 = 124^\circ\text{N}/06^\circ$ and $\sigma_3 = 032^\circ\text{N}/13^\circ$ and suggesting extensional deformation.

3.3.2.1.2 Ilgın Fault Zone (IFZ)

The Ilgın Fault Zone (IFZ) is a well-exposed structure comprising a 50 km long N-S trending normal fault, with a vertical displacement of at least 240 m between basin floor and Paleozoic and Mesozoic basement units. It controls the eastern margin of the Ilgın Basin and separates Miocene Ilgın Basin fill (footwall block) from the Pliocene-Holocene Çavuşçu graben (hanging wall block). An approximately N-S trending abrupt change in topography provides morphological evidence for presence of the faulting. The main fault plane due east and dip of the fault surface ranges between 45° and 88° depending on the curvature of the fault plane. The northern continuation of the IFZ is clearly traceable near the vicinity of the Gavurdağ, where it dies out within the high topography. The IFZ preserves its N-S orientation along the Çavuşçu Lake and changes its orientation near Ilgın town center by about 20 degrees towards an easterly direction and it disappears in the vicinity of Gökçeyurt.

Along the Ilgın-Çavuşçu Lake road, fault scarps are exposed (Figure 3.18). These fault scarps were developed within the basement metamorphic rock units and are coated by reddish/white fault clay. Adjacent to the fault surface, intensely fractured and brecciated materials with variable sized angular clasts clearly identify the shear zone (Figure 3.18). In the Ilgın town center, hot springs are common and some fault surfaces are altered by upwards percolations of the geothermal water. Therefore, most of the slickensided fault surfaces are most probably washed out during this process. However, the observed,

slickenlines on the fault surfaces show generally down-stepping characteristics, which indicate a normal sense of displacement (Figure 3.18). Rake of the slickenlines range from 35° to 87° . The shallower values of the rakes are coming from undulations of fault surfaces. Stereographic projection of the collected fault-slip data from the IFZ are given in Figure 3.18 indicates E-W directed extension.

Therefore, a sudden break in slope, juxtaposition of different lithologies, formation of fault breccia/clay, hydrothermal alteration, hot springs and well-developed slickensides are used as criteria for the recognition of the IFZ. The stereographic plot of fault-slip data shows that the IFZ is a normal fault. The orientation of the inferred principal stress and the stress ratio are as follows: $\sigma_1 = 281^{\circ}\text{N}/74^{\circ}$, $\sigma_2 = 184^{\circ}\text{N}/02^{\circ}$, $\sigma_3 = 093^{\circ}\text{N}/16^{\circ}$ and indicate extensional deformation. The stress ratio is $\Phi=0.506$, which represents a well-developed tri-axial stress conditions (Figure 3.18).

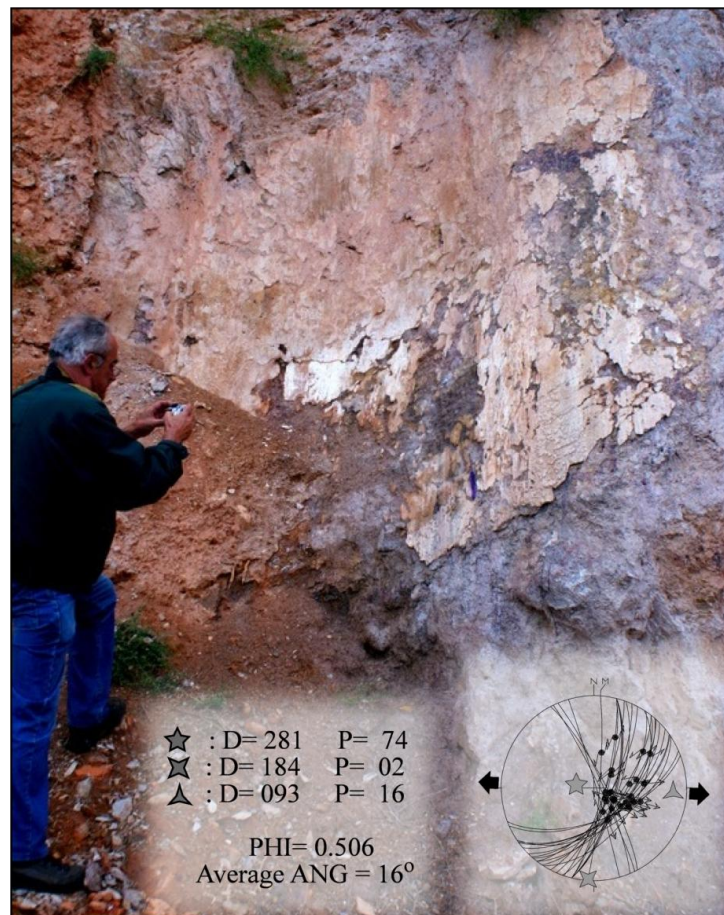


Figure 3.18. The fault scarp (a) and stereographic plot of fault-slip data (b) from Ilgın Fault Zone (IFZ).

3.3.2.1.3 Argıthanı-Balkı-Derbent Fault Zone (ABDFZ)

In the southern part of the Ilgın Basin, E-W trending splay faults bifurcate from the NW-SE oriented Akşehir-Afyon Fault Zone and form three major fault segments namely 1) Argıthanı Segment, 2) Balkı Segment and 3) Derbent Segment (Figure 3.14). These parallel segments are studied as elements of single fault zone which is named Argıthanı-Balkı-Derbent Fault Zone (ABDFZ). The attitudes of these segments are firstly interpreted in detail in this study.

The Argıthanı Segment (AS) is located in the north of the basin and is approximately 40 km long. It bifurcates from the AAFZ at the vicinity of the Akşehir in the west, continues towards Argıthanı and it is delimited by Ilgın Fault north of the Çavuşçu Lake in the east. The trace of the AS is difficult to observe in the field and in remotely sensed data due to the absence of prominent topographic changes. Koçyiğit and Özacar (2003) reported that AS shows north dipping normal fault characteristics. Although primary geomorphological indicators such as sudden topographic changes and direct shear zone indicators such as fault breccia/clays could not be observed along the fault zone. However, two destructive earthquakes namely the 1921, September 26 Argıthanı-Akşehir earthquake (Mw=5.4) and 1946, February 21 Ilgın-Argıthanı earthquake (Mw=5.5) were located very close to this fault segment (Taymaz and Tan, 2001).

Along the road between Argıthanı and Kabaklı, a small fault scarp is exposed. It is oriented approximately E-W, which is compatible with the inferred trend of the Argıthanı Segment (Figure 3.19). It shows very steep dip amount ranging between 75° and 90° due south. Drag folds on the hanging wall block is used to identify sense of movement of the fault.

The stereographic plot of fault-slip data indicates that the fault has a normal fault characteristic (Figure 3.19). The orientation of the principal stresses and the stress ratio are found as follows: $\sigma_1 = 320^\circ\text{N}/71^\circ$, $\sigma_2 = 058^\circ\text{N}/02^\circ$, $\sigma_3 = 149^\circ\text{N}/18^\circ$ and $\Phi=0.299$ (Figure 3.19). These results indicate extensional deformation.

The Balkı Segment (BS) is the central segment of this fault zone and is approximately 45 km long. It bifurcates from the AAFZ in the vicinity of İlyaslar in the west, passes through Karaağa, Çınaroba, and then bends to Doğanhisar and Balkı (Figure 3.14). It dies out at the vicinity of the Eldeş in the east. The trace of the BS is clearly extracted from the topographic break which shows an abrupt change in the elevation around Doğanhisar and Balkı.

The Balkı Segment (BS) is encountered at a small outcrop in a road cut 2 km south of the Eldeş during field studies. In this locality it juxtaposes limestone basement unit and Early-Late Miocene lacustrine sequence (Figure 3.20). The fault plane of the BS shows

well-developed slickensided surfaces with well-preserved slickenlines. Fault planes dip towards the north at angles of 46° to 89° and rakes of slickenlines range between 52° and 88° . The hanging wall block is located to the north of the fault zone. The stereographic plot of slip data collected from this fault illustrates normal character of the fault (Figure 3.20). The orientation of the principal stress and the stress ratio are $\sigma_1 = 320^{\circ}\text{N}/71^{\circ}$, $\sigma_2 = 058^{\circ}\text{N}/02^{\circ}$, $\sigma_3 = 149^{\circ}\text{N}/18^{\circ}$ and $\Phi = 0.299$ (Figure 3.20) again illustrating extensional deformation.

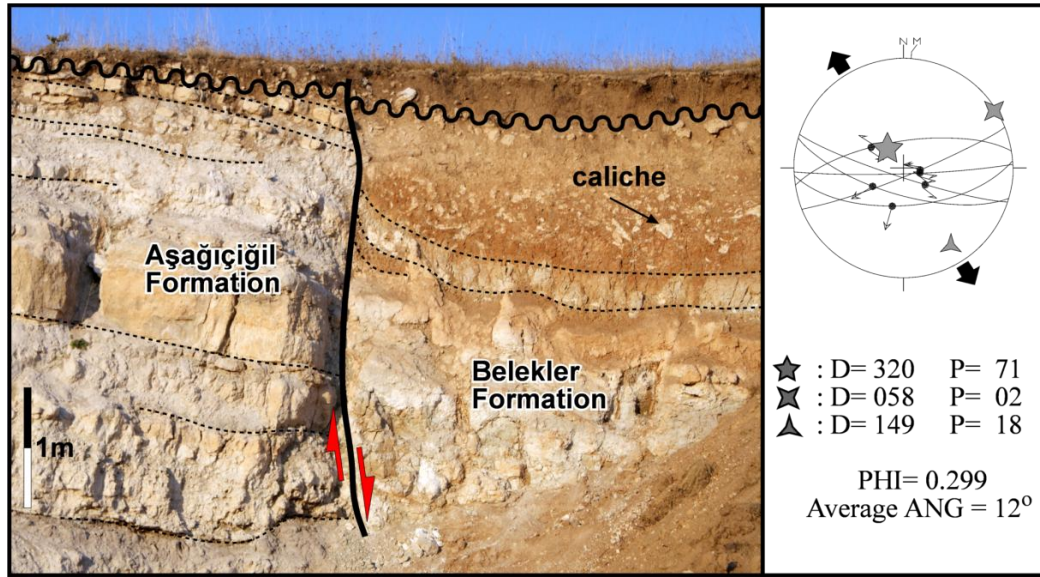


Figure 3.19. Field view of the Argithani Segment of ABDFZ along the Argithani-Kabaklı road. Note the folds on the hanging wall beds against the fault. View to east.

The Derbent Segment (DS) is the other splay fault bifurcating from the AAFZ and is located at the southern edge of the basin. It is approximately 40 km long and splays from the AAFZ to the north of Dıǵrak. From Dıǵrak to Yassıören, it has an approximately NW-SE trending trace, then it bends to east and gains E-W striking character from Yassıören to Derbent (Figure 3.21). Further to the east the Derbent segment traces E-W along a river channel in Ilgın Basin towards the Altınapa Basin. These two river channel are separated from each other by the Mülâyim Fault Zone (see Chapter 2).



Figure 3.20. Field view of the Balkı Segment (BS) at the 2 km south of the Eldeş. Note the juxtaposition of basement limestone and Aşağıcığıl formation. View to west. Lower-hemisphere Schmidt projection of fault-slip data and constructed paleostress configurations. Note that large arrows indicate approximately N-S extensional deformation. D and P indicate the dip direction and plunge, respectively.



Figure 3.21. Field view of E-W trending fault scarp of the Derbent Segment. Black line indicates the trace of the fault which juxtaposes Belekler formation and recent river deposits. View to south.

Morphologically, approximately E-W trending north dipping fault scarp is easily recognized in the field by the abrupt change in topography towards the northern downthrown block (Figure 3.21). The fault plane of the Derbent Segment is covered by an apron of alluvial fan deposits possibly due to high sedimentation rates with respect to the fault displacement rate. Therefore, fault-slip measurements could be obtained only from short fault segments that developed parallel to the Derbent Segment.

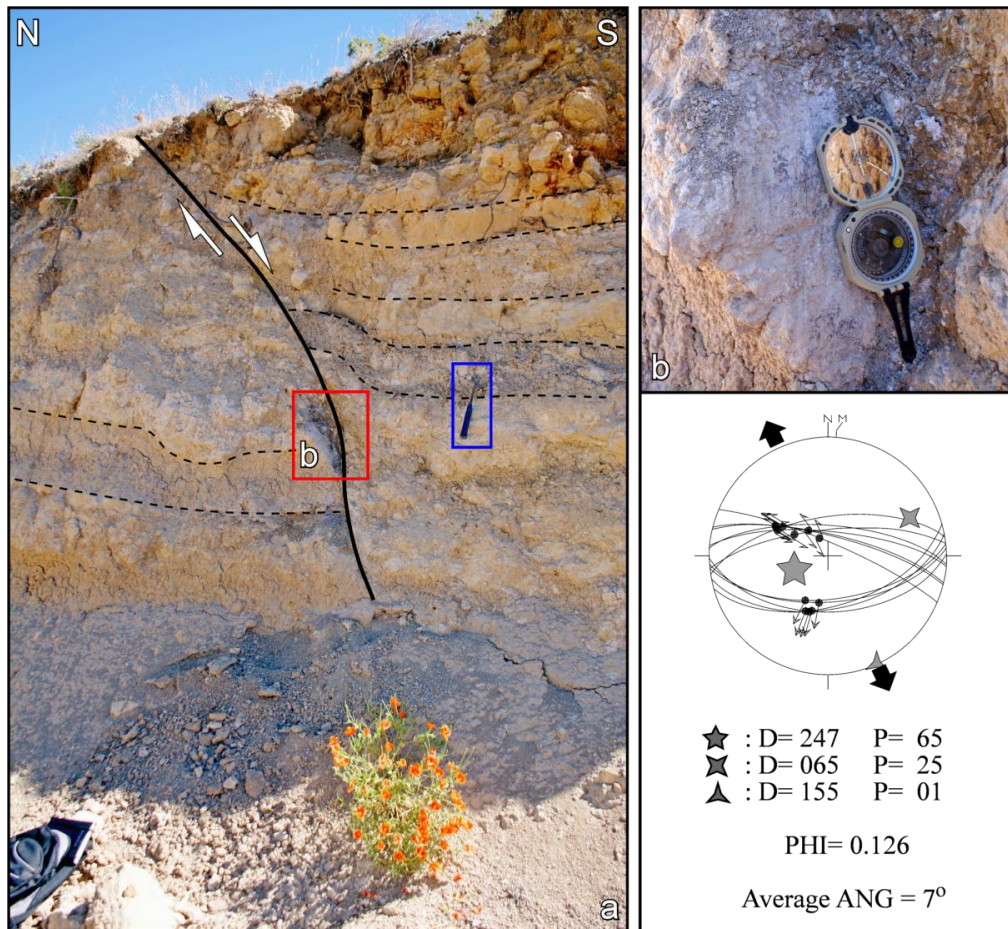


Figure 3.22. Field view of the normal fault within the Derbent segment along the Ilgin-Derbent road. Red rectangle indicates the close-up view of the (b). Lower-hemisphere Schmidt projection of fault-slip data and constructed paleostress configurations is also given. Blue rectangle is used to indicate the hammer as a scale. View to east.

In an outcrop along the Ilgın-Derbent road at 4 km north of the Yassıören, the cross-sectional view of a lacustrine limestone unit belonging to Aşağıcığıl formation is displaced by Derbent segment (Figure 3.22a). The fault plane shows well-developed slickenlines which indicate the normal sense of movement (Figure 3.22b). In this locality the fault zone also has conjugate sets. On these faults fault-slip data were collected and the measurements indicate fault planes dips towards both north and south with angles of 46° to 89° and rakes of slickenlines range between 50° and 82°. The constructed paleostress configurations indicate normal character of the fault. The orientation of the principal stresses and the stress ratio are $\sigma_1 = 320^\circ\text{N}/71^\circ$, $\sigma_2 = 058^\circ\text{N}/02^\circ$, $\sigma_3 = 149^\circ\text{N}/18^\circ$ and $\Phi = 0.299$ (Figure 3.22c) and vertical major principal stress indicate extensional deformation.

3.4 Paleostress Analysis

In this study two different data sets were used to construct and analyze paleostress configurations. The first data set includes vein orientation data. The vein data provides minor principal stress orientations which are perpendicular to the general trend of the vein. However, intermediate and major principal stress are approximately parallel to the vein orientation and therefore, veins data are insensitive to the orientation of these stress. On the other hand, the spatial organization of some special types of veins, such as en echelon gush veins can be used to deduce intermediate and major principal stress directions.

The second data set for construction of paleostress configurations comprise the fault slip data. The fault-slip data collected from mesoscopic faults in the field are very successful in construction of paleostress configurations and they help to understand the kinematic evolution of a region and are employed in this study for the Ilgın Basin for its spatio-temporal evolution. For the reconstruction of the paleostress configurations, Angelier's software is used. For the sake of simplicity and to avoid repetition no detail description of the inversion procedure is given in this chapter. The full account of the procedure is given in Chapter 2, section 2.4.1.

3.4.1 Veins

This section contains the documentation of open mode fractures and dominantly calcite-filled veins which can successfully be used to determine major extension directions. The vein fill and the host rock can be separated from each other by distinct color contrast and texture. In the study area the encountered veins are emplaced mainly within the basement rock and lacustrine limestone unit of the Aşağıcığıl formation. During field studies a total of 64 vein data from 3 different locations were collected and are used to deduce paleostress configurations during their formation.

3.4.1.1 Paleostress Inversion From Mode 1 Fractures

The shape, orientation and internal structures of veins reveal information about paleostress field, deformation kinematics and fluid pressure (Bons et al., 2012). Therefore, the collected vein data from Ilgin Basin, are used to reconstruct paleostress configurations. The assumption in the stress inversion procedure using open mode (Mode I) fractures is like following:

1. Pole to the vein is the direction of minor stresses which mostly tensile.
2. Intermediate and major stress are parallel to the fracture plane
3. In the case of population of veins, the intersection of mean great circle obtained from poles to fractures and mean great circle of the fracture is either intermediate or major stress.
4. In order to determine if the stress axis determined in step 3 belongs to intermediate or major stress, Andersonian (1951) principal can be applied. This necessitates the knowledge of tectonic regime during the vein formation. So, if the tectonic regime is;
 - a. Extensional, then major stress (σ_1) is (close to) vertical and intermediate stress (σ_2) is 90° apart from it along the vein plane.
 - b. Strike-slip, then intermediate stress (σ_2) is (close to) vertical and major stress (σ_1) is 90° apart from it along the vein plane.
 - c. Contractional (thrusting), it's difficult to determine the orientation of intermediate (σ_2) and major stress (σ_1). The only way is to determine the long axis of the veins, which corresponds to major stress (σ_1).

In addition, Dunne and Hancock (1995) argued that mineral growth direction are perpendicular to fracture walls and are parallel to the σ_3 , which confirms that the veins are formed perpendicular to the minimum effective principal stress (σ_3). Based on these assumptions, vein data collected during field studies is analyzed and used for paleostress inversion.

The first vein data sets obtained from the veins that have been emplaced within the basement limestone units (Figure 3.23a) located 6 km NW of Ilgin, along the Çavuşçugöl road. The data set contains 11 vein measurements and these exposed NE-SW striking veins (Figure 3.23a) are generally up to 3-4 cm thick (Figure 3.23b).

In most of the veins, vein bands are symmetrical on either side of the wall rock indicating symmetric growth. The innermost band is generally has larger crystals than the ones adjacent to the wall rock. The average width of the veins is approximately 1-2 cm (Figure 3.23b). The crystal faces of the vein fill is not well-developed, and also the comb structure is slightly observable (Figure 3.23b). Wherever, comb structure or calcite

fibers are observed they developed perpendicular to the vein wall indicating normal opening and no shearing was involved during their development. Therefore, they are pure open mode fractures and the minor principal stress σ_3 was perpendicular to the vein wall (Dunne and Hancock, 1995). In the light of this information, collected vein data were analyzed to deduce paleostress configurations of the region during the vein formation. In Figure 3.24 a stereographic plot of the veins and their pole is given. Using the contour diagram, the attitude of best fit great circle which supposed to contain σ_1 and σ_2 and perpendicular to σ_3 is found to be $328^\circ\text{N}/71^\circ$ (MGC). The dominant pole position corresponds to σ_3 and is $149^\circ\text{N}/02^\circ$ (MLV) (Figure 3.24b). The best plane (MGC) contains the σ_1 and σ_3 and is perpendicular to σ_2 . Therefore, the orientations of principal stress are as follows; σ_1 : $066^\circ\text{N}/71^\circ$, σ_2 : $238^\circ\text{N}/19^\circ$, σ_3 : $329^\circ\text{N}/02^\circ$.

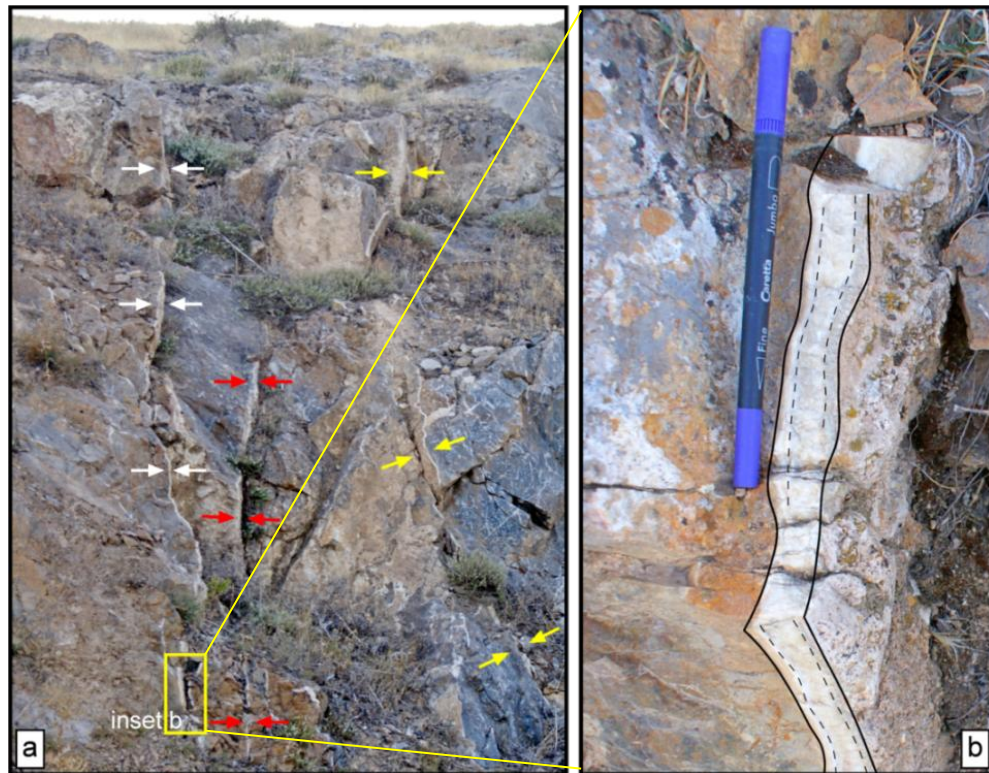


Figure 3.23. Field view of the veins emplaced within the basement limestone unit. Approximately NE-SW striking calcite veins (6 km north of Ilgin, view to SW). a) Different vein occurrences are indicated with color arrows. b) Close-up image of a vein.

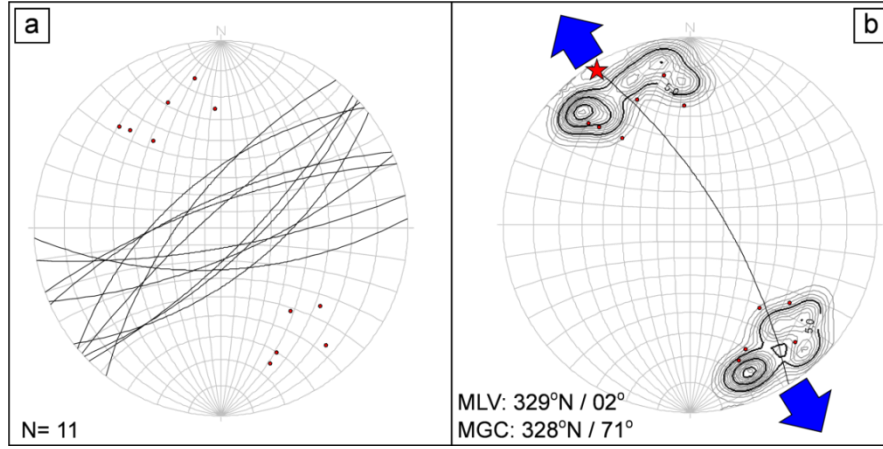


Figure 3.24. Stereographic plot of the vein measurements within the basement in the vicinity of Çavuşçugöl. a) Cyclographic traces of the veins on the lower hemisphere equal-angle net. Red dots represent the pole of the vein planes. b) Contour diagram of the veins based on their poles and orientation of the best fit plane, and direction of paleostress configurations. MLV: Mean Lineation Vector of the pole of the vein planes and identified by red star, MGC: Mean Great Circle passing through the pole of the vein planes.

On the other hand, rarely same vein surfaces contain slicken fibers (Figure 3.25) which contains movement is not perpendicular to the vein walls. Generally, it is thought that these veins are not related to pure dilation (Mode I fracture). However, Ramsey and Chester (2004) demonstrated a continuous transition in macroscopic fracture orientation across the transition from classic extension fractures to shear fractures (Figure 3.25c). Pre-existing fractures and pore fluids are important aspect relating to strength of the material and may result in stepped-crack hybrid fractures under the same stress conditions. Therefore, this movement creating oblique striations on the vein surfaces does not need to satisfy the shear stress conditions. These types of veins were not included in vein data analysis.

According to vein analysis, the extension direction is estimated as NW-SE direction, which is not compatible with reconstructed extension direction based on the paleostress data collected from the Ilgın Fault (Figure 3.18). Therefore, the extension direction should be older than the recent stress regime causing Ilgın Fault formation (N-S extension in Figure 3.18) or they operate at the same time. The last case means the multi-directional extension or stress perturbation between σ_2 and σ_3 .

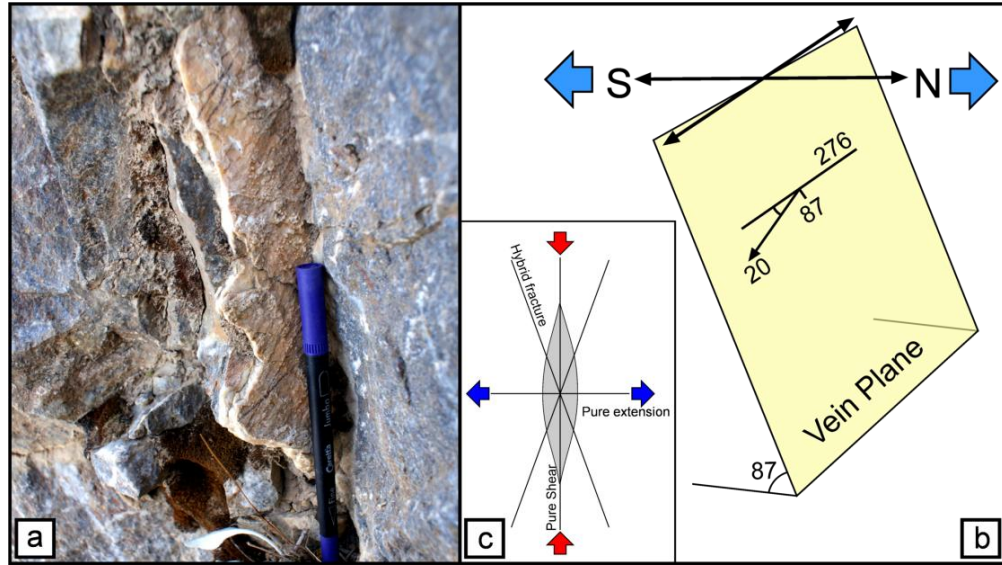


Figure 3.25. Vein formation with slicken-fiber (a). The orientation of the vein surface with slicken-fibers (b), and theoretical idea (Ramsey and Chester, 2004) behind the occurrence of the hybrid fractures (c). Blue and red arrows show extension and compression directions, respectively.

The second vein data set was also collected from basement limestones located at the western edge of Ilgin town center (Figure 3.26). This data set consists of 10 vein measurements. The average orientation of the veins is about 180° . Thickness of the veins (Figure 3.26) vary from 5 cm up to about 60-70 cm and veins show banded structures with different colors (ranging from red to dark gray) developed from both walls towards the vein center. This indicates syntaxial symmetric growth of the veins. Mineral growth directions are perpendicular to fracture walls, which confirm that direction of the dilatational stress did not change during the vein formation. The direction of extension can be estimated roughly on the basis of basic assumption that the opening is perpendicular to vein planes. The projection of the strike and dip of the veins were analyzed using stereographic projection (Figure 3.27a). Best fit great circle attitude is found to be $290^\circ\text{N}/39^\circ$. The best fit surface passing through the poles of vein surfaces indicates the average crystal growth direction and also contains σ_1 and σ_3 , while σ_2 corresponds to the pole position of the best fit surface. Based on this information the orientation of the principal stress directions are found to be; σ_1 : $334^\circ\text{N}/30^\circ$, σ_2 $199^\circ\text{N}/39^\circ$ σ_3 : $086^\circ\text{N}/18^\circ$. The horizontal component of σ_3 is approximately E-W (Figure 3.27b) indicating the extension direction was approximately E-W during the emplacement of these veins.

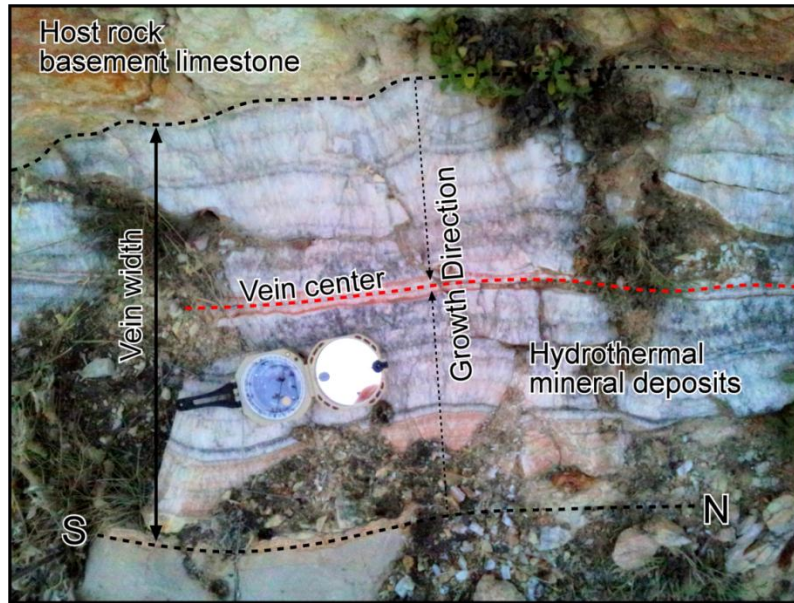


Figure 3.26. Vein formation in the basement limestone. Approximately N-S striking, syntaxial hydrothermal vein, where crystals grow from the wall rock into the vein (younger in the center, older close to the vein wall).

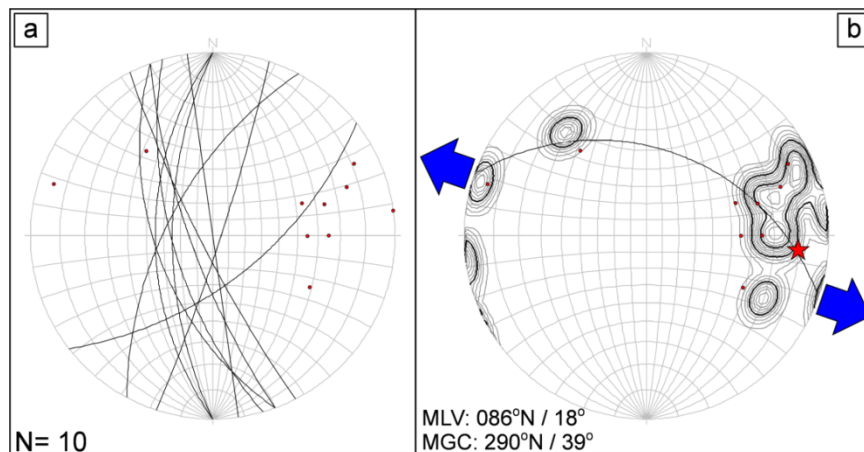


Figure 3.27. Stereographic plot of the vein measurements within the basement located at the vicinity of the Ilgın. a) Cyclographic traces of the veins on the lower hemisphere equal-angle net. Red dots represent the pole of the vein planes. b) Contour diagram of the veins based on their poles and orientation of the best fit plane, and direction of paleostress configurations. MLV: Mean Lineation Vector of the pole of the vein planes and identified by red star, MGC: Mean Great Circle passing through the pole of the vein planes.

The last location where vein data collected were located 2 km northwest of Göstere (Figure 3.1) and calcite veins have been emplaced within travertines of the Aşağıçiğil formation (Figure 3.28). This data set consists of 37 vein measurements (Figure 3.29a). Strikes of the veins range between 50° and 90° along sub-vertical veins (Figures 3.28 and 3.29). The veins range in length from cm scale to a few meters and in thickness from less than 2 mm up to 5 cm. Veins have one single growth band and the central part of the veins are generally still open, and blocky calcite crystals are perpendicular to the vein wall and are developed symmetrically from both walls towards the vein center (Figure 3.28).

The attitudes of the veins are plotted on the lower hemisphere equal-angle net (Figure 3.29a). Best fit great circle representing the average crystal growth direction is found to be $166^\circ\text{N}/49^\circ$ (MLV). The plane is also contains σ_1 and σ_3 , and the pole of the best fit surface corresponds to σ_2 . Therefore, the orientation of the principal stress directions are found to be; σ_1 : $254^\circ\text{N}/49^\circ$, σ_2 $076^\circ\text{N}/41^\circ$ σ_3 : $345^\circ\text{N}/01^\circ$. The horizontal component of σ_3 is approximately N-S (Figure 3.29b) indicating the extension direction was approximately N-S during the emplacement of these veins.

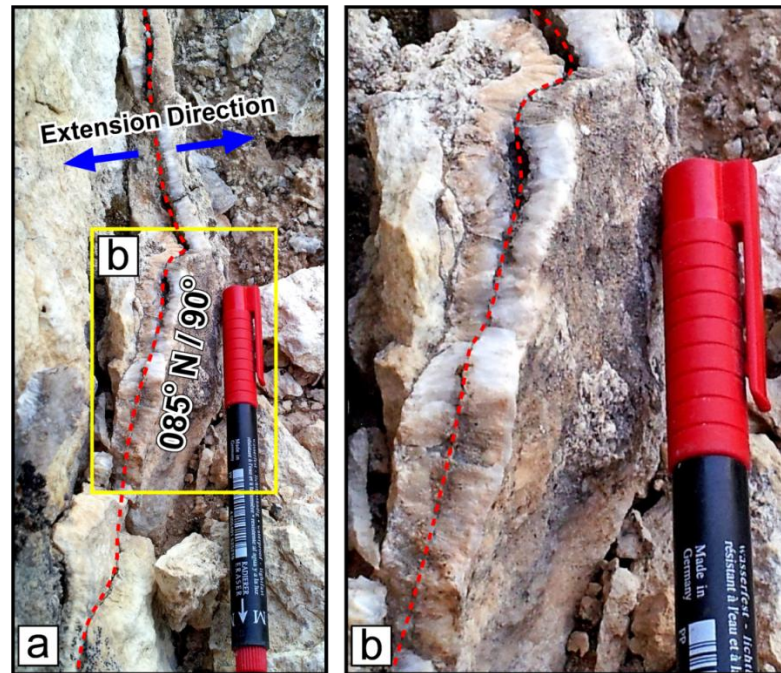


Figure 3.28. Vein formation in the limestone unit of the Aşağıçiğil formation. Approximately E-W striking calcite veins (a). Blue arrows indicate extension direction. Location of the photo b is showed by yellow rectangle on the photo a. Dash lines show the vein center.

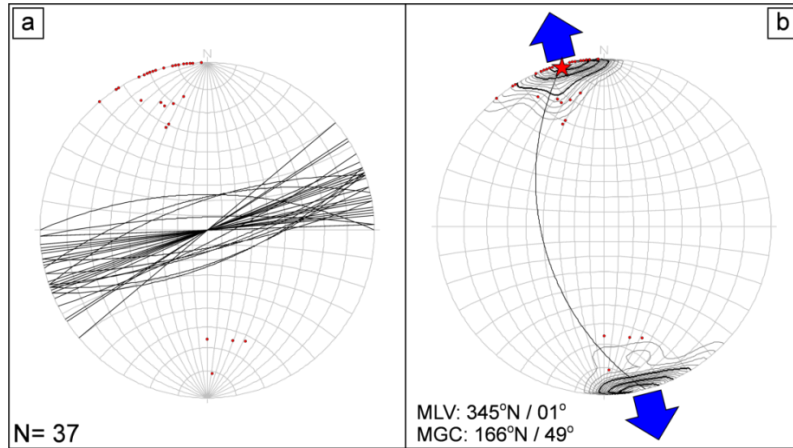


Figure 3.29. Stereographic plot of the vein measurements within the limestone at the vicinity of Ilgın. a) Cyclographic traces of the veins on the lower hemisphere equal-angle net. Red dots represent the pole of the vein planes. b) Contour diagram of the veins based on their poles and orientation of the best fit plane, and direction of paleostress configurations. MLV: Mean Lineation Vector of the pole of the vein planes and identified by red star, MGC: Mean Great Circle passing through the pole of the vein planes.

3.4.2 Fault Slip Data

A total of 561 fault-slip measurements including direction and sense of relative movements were collected from 47 locations during the field work in the Ilgın Basin. Fault slip data were recorded from mesoscopic faults within the Ilgın Basin fill as well as from major faults which control the basin boundaries. The data were thus collected from units ranging from pre-Neogene basement, to Miocene basin infill and recent deposits.

Most of the measured faults in the study area are striking E-W or NE-SW as shown on the rose diagram (Figure 3.30a). Histogram of the dip of the faults as indicated in Figure 3.30b ranges between 30° and 89°.

During the paleostress analysis, 561 fault-slip data were analyzed using direct inversion method (INVD) developed by Angelier (1994) and 51 stress configurations were constructed (Figure 3.31 and Table 3.2). Maximum angular deviation (ANG) and quality estimator (RUP) values were chosen as 22.5° and 45°, respectively. The smaller values are regarded as good match (Angelier, 1994). Faults with greater angular deviations were considered as spurious and they were not used in the construction of the stress tensor. In this data set, 32 fault slip measurements are regarded as spurious, which is approximately 5.7% of the whole data set.

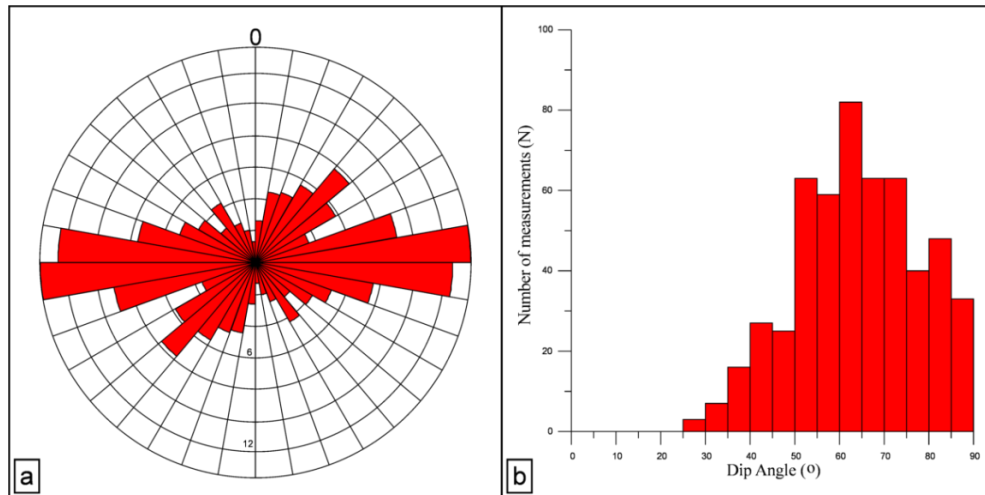


Figure 3.30. a) Bidirectional rose diagram shows the strike of the measured fault planes. Note bimodal distribution in N80°-90°E (dominant direction) and N40°-50°E. b) The histogram of the fault dip amounts.

Inverted stress configurations in site 17, 38 and 40 were divided into two different slip data sets and analyzed separately even though they were collected from same unit and the same locality. This situation refers to heterogeneity of the fault data (Angelier, 1979; Armijo et al., 1982; Huang, 1988; Yamaji, 2000) caused by polyphase deformation. For example, mesoscale conjugate normal faults having dihedral angle of approximately 60° (Anderson, 1951) and dextral strike-slip faults are recorded in Pre-Neogene basement limestone in Site 40, but strike-slip fault is cut by conjugate sets of normal faults, which indicates that normal faulting postdates strike slip faulting (Figure 3.32). Conjugate sets whose orientation and slip directions are related to the principle stress axes provide a convenient way to rapidly determine paleostress axes (Huang and Angelier, 1989).

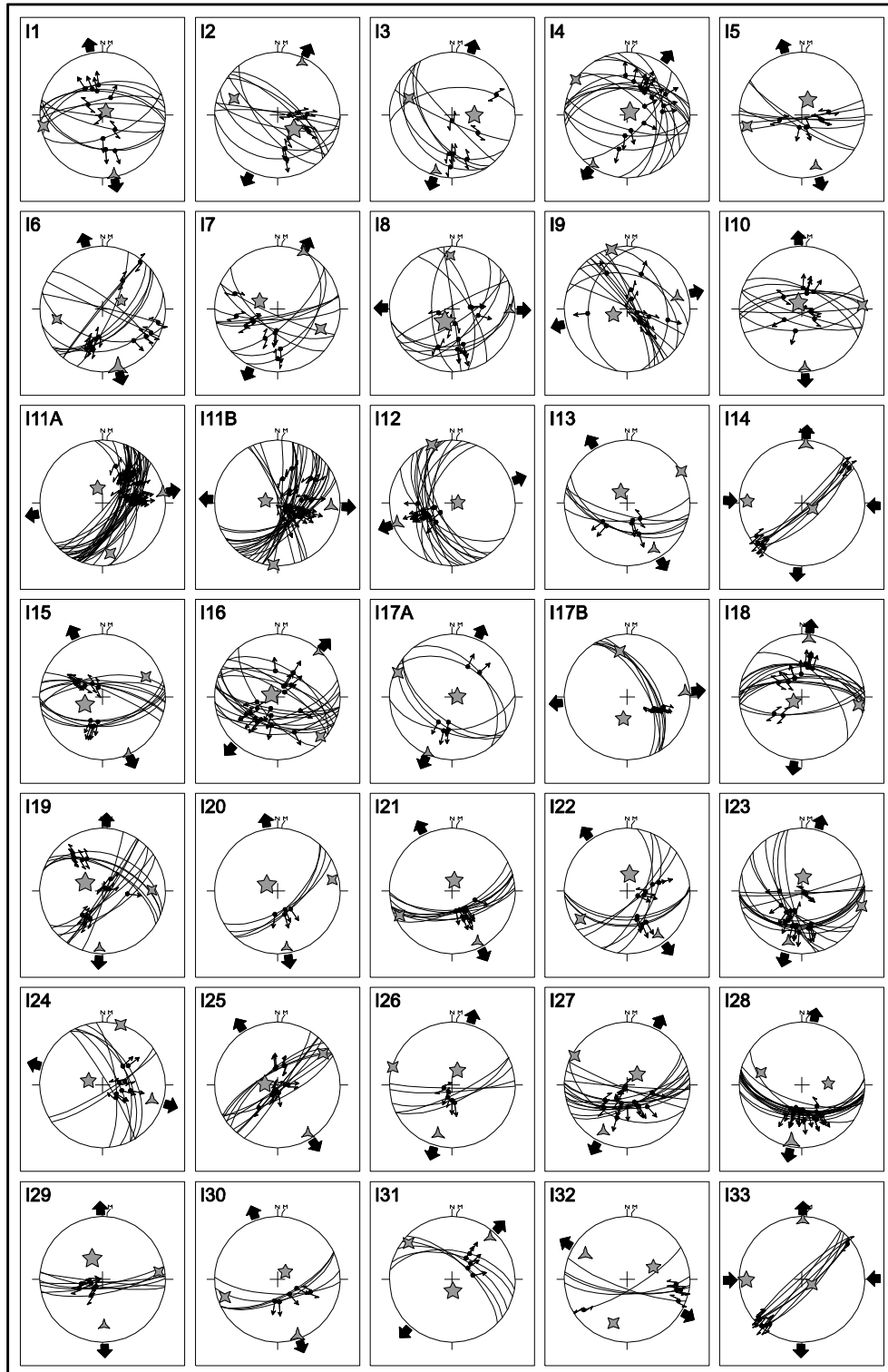


Figure 3.31. Stereoplots showing constructed paleostress orientations, fault planes and slip lineations (lower hemisphere equal area projection) for each location.

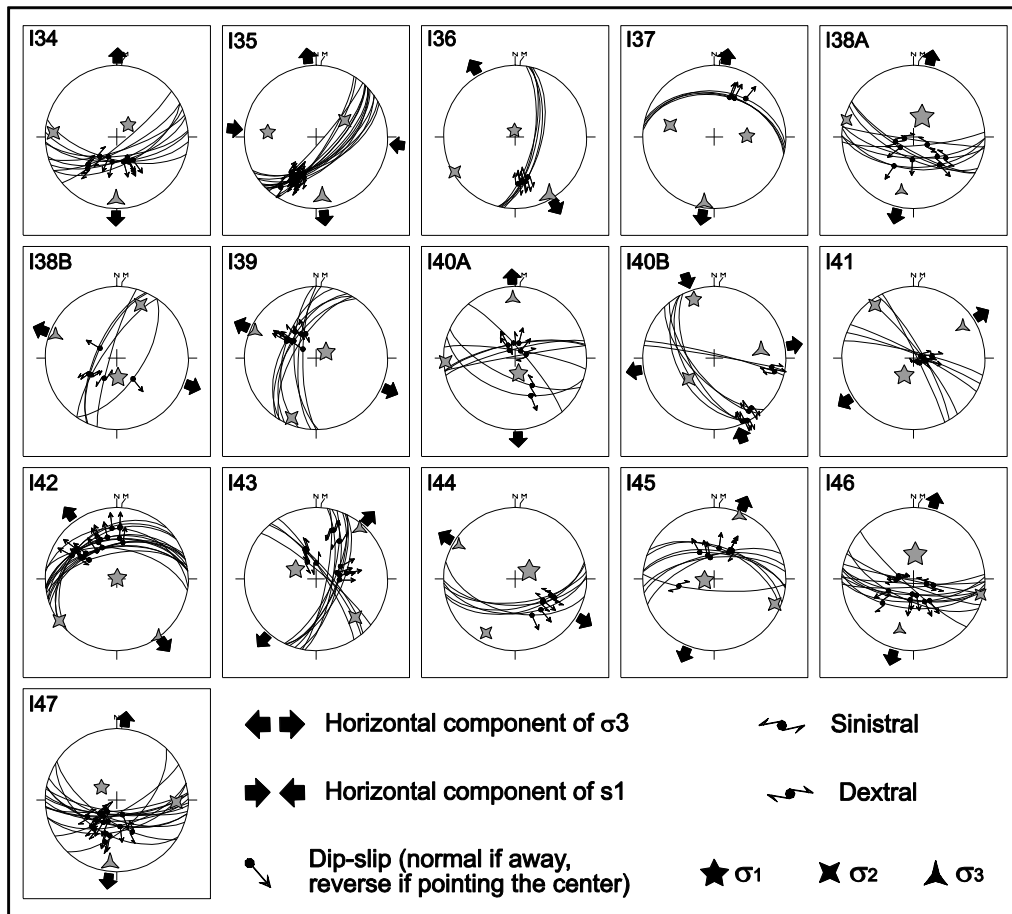


Figure 3.31. Continued

Table 3.2. Locations and paleostress orientations from Ilgın Basin.

Loc	Long	Lat	$\sigma_1(D^0/P^0)$	$\sigma_2(D^0/P^0)$	$\sigma_3(D^0/P^0)$	Φ	Mean ANG	Mean RUP	N
I1	31.85088	38.19095	040/83	260/05	169/04	0.445	9	29	11
I2	38.12399	31.66351	130/62	291/27	025/08	0.087	13	44	10
I3	38.11452	31.73580	090/61	291/27	197/09	0.114	14	34	7
I4	38.11331	31.73529	043/85	305/01	215/05	0.215	9	26	16
I5	38.12139	31.81230	021/69	258/12	165/17	0.232	14	34	7
I6	38.01675	31.89772	065/63	258/26	165/05	0.840	18	36	12
I7	38.02812	32.02481	294/65	115/25	025/00	0.383	17	39	10
I8	38.31920	31.85933	211/71	358/16	091/10	0.074	13	43	11
I9	38.29280	31.75265	248/71	345/03	076/19	0.392	12	37	12
I10	38.34614	31.85381	330/81	087/04	177/08	0.206	16	51	10
I11A	38.34614	31.85381	342/70	171/20	080/03	0.449	11	23	30
I11B	38.29517	31.75802	281/74	184/02	093/16	0.506	16	36	29
I12	38.08479	31.82328	086/83	340/02	250/07	0.514	6	14	14
I13	38.08488	31.82334	330/74	060/00	150/16	0.374	12	29	6
I14	38.01720	31.89772	272/14	120/74	004/07	0.661	7	13	7
I15	38.01865	31.89784	247/65	065/25	155/01	0.126	7	30	12
I16	38.08604	31.82481	290/82	133/08	042/03	0.182	10	35	18
I17A	38.08604	31.82481	085/83	294/06	204/03	0.324	4	9	6
I17B	38.11204	31.73563	190/61	351/27	085/08	0.739	2	5	6
I18	38.11204	31.73563	241/78	098/10	007/07	0.431	12	26	14
I19	38.18345	31.99435	295/65	089/23	183/10	0.166	20	38	13
I20	38.18974	31.99170	301/74	078/12	171/10	0.141	6	14	4
I21	38.11608	31.82401	011/76	245/08	153/11	0.153	5	11	9
I22	38.11741	31.82146	008/68	239/14	145/16	0.218	4	26	9
I23	38.10466	31.79358	005/72	104/03	195/18	0.380	14	36	17
I24	38.05904	31.81691	287/71	017/00	107/19	0.460	6	28	8
I25	38.17599	31.83689	275/74	056/13	148/10	0.418	19	57	11
I26	38.14568	31.75565	020/70	287/01	196/20	0.372	2	24	5
I27	38.07674	31.84462	043/71	299/05	207/18	0.376	13	34	15
I28	38.07667	31.84400	087/56	287/33	191/06	0.770	11	22	17
I29	38.07489	31.84275	333/60	178/28	082/11	0.218	6	18	7
I30	38.05650	31.81689	046/76	252/13	160/06	0.546	16	30	5
I31	38.07508	31.82947	176/75	310/10	042/11	0.167	4	11	5
I32*	38.19082	31.85090	065/52	197/28	301/24	0.543	8	38	5
I33	38.08567	31.82396	269/13	117/76	001/06	0.313	5	10	8
I34	38.08488	31.82348	043/71	274/12	181/14	0.647	10	23	10
I35	38.08466	31.82331	276/33	060/52	174/18	0.764	6	16	14
I36	38.08432	31.82447	353/83	240/03	150/07	0.747	3	25	5
I37	38.05122	31.83894	088/52	285/36	189/08	0.622	4	15	4
I38A	38.38145	31.84358	023/65	193/24	284/04	0.155	16	31	9
I38B	38.38240	31.84318	176/68	024/20	291/10	0.262	15	38	5
I39	38.38240	31.84318	059/77	202/11	294/08	0.331	7	15	8
I40A	38.38280	31.84502	167/72	267/03	358/18	0.350	10	33	8
I40B	38.32201	31.85929	341/15	231/52	081/34	0.720	11	43	7
I41	38.32201	31.85929	208/68	324/10	057/20	0.249	5	24	6
I42	38.13818	31.66580	021/89	234/01	144/01	0.363	13	26	15

Table 3.2. Continued

Loc	Long	Lat	$\sigma_1(D^\circ/P^\circ)$	$\sigma_2(D^\circ/P^\circ)$	$\sigma_3(D^\circ/P^\circ)$	Φ	Mean ANG	Mean RUP	N
I43	38.22934	31.54675	296/64	134/24	041/07	0.518	12	39	12
I44	38.38161	31.84562	060/72	209/16	301/09	0.184	4	18	6
I45	38.08150	31.84820	264/79	112/10	021/05	0.390	11	31	8
I46	38.28209	31.71155	004/62	195/28	103/05	0.174	12	26	12
I47	38.07689	31.83691	310/67	092/18	186/13	0.702	9	22	16

σ_1 , σ_2 , σ_3 magnitude ratios of principle stresses; D/P, direction/plunge; Φ stress ratio; ANG, maximum allowed angular divergence RUP, maximum allowed quality value N, number of measurement for each site.

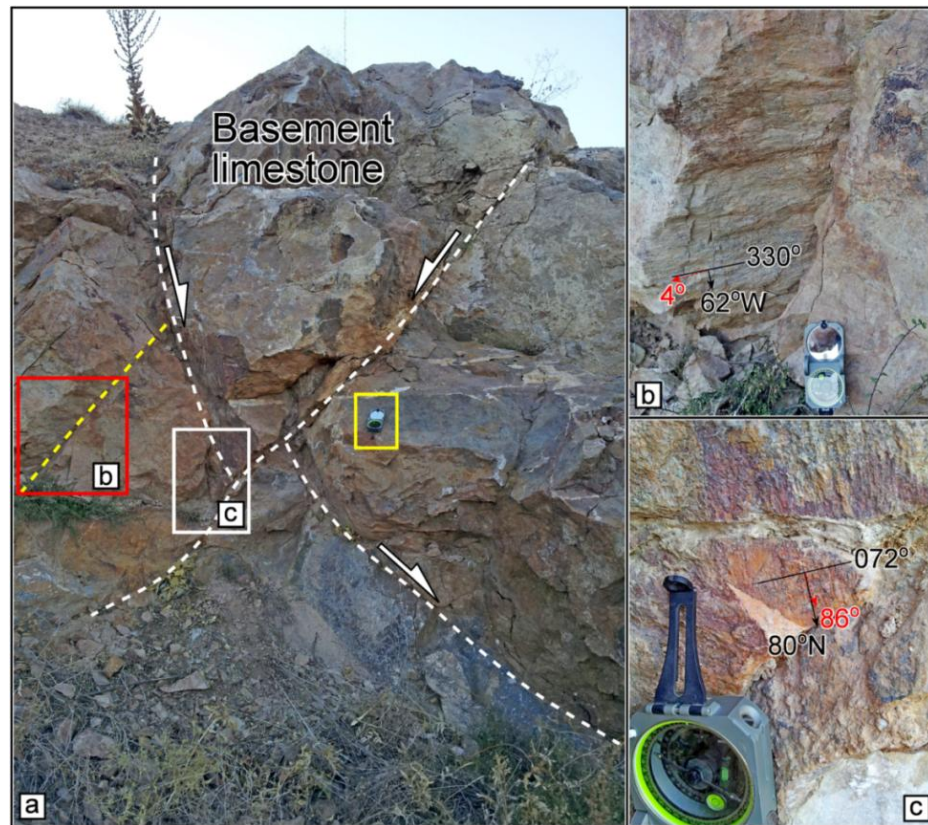


Figure 3.32. Mesoscale conjugate normal faults (white dash line) and strike-slip fault (yellow dash line) in Pre-Neogene basement limestone in site I40 (a). Note that dextral strike-slip is cut by normal faults. Red rectangle indicates the close-up view of the strike slip movement (b) and white rectangle shows the close-up view of slickenlines produced by dip-slip normal movement (c). Note compass (yellow rectangle) for scale.

Syn-sedimentary faults indicating sediment accumulation around active structure provide a powerful tool for relative chronology of fault slip sets since the age of the faults can be determined from the age of the sedimentation. Syn-sedimentary faults in the Ilgın Basin are recorded during the fieldwork to distinguish district tectonic regimes. For example the stress configurations from site 13 and 34 where step like syn-sedimentary normal faults developed within the Kumdöken formation indicate that the during the deposition of the Kumdöken formation (Figure 3.33) the tectonic regime was extensional and the orientation of the minimum principal stress was approximately E-W.

Similar relationships were also observations within the Aşağıcığil formation. The principal stress orientations reconstructed from the syn-sedimentary faults documented in sites 24, 29 and 36 indicates that the tectonic regime was extensional during the deposition of the Aşağıcığil formation. This is evidenced by vertical maximum principal stress. However two different dominant extension directions were prevailed during the deposition of Aşağıcığil formation.

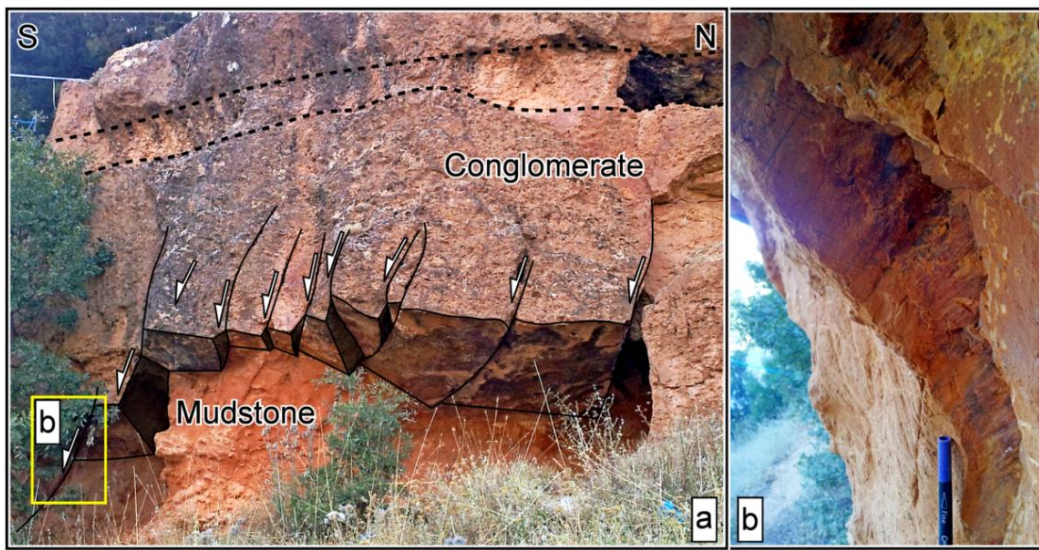


Figure 3.33. Mesoscale syn-sedimentary step like normal faults within the Early Miocene Kumdöken formation in Site 34 (a). Yellow rectangle indicates the close-up view of the slickenlines on the fault surfaces (b). Note that fault orientation is approximately E-W.

In addition to normal faults, a number of NE-SW striking strike-slip faults are also encountered in the study area (Figure 3.34), but they are not common. In such areas, the intermediate principal stress found to be vertical, which indicates transcurrent deformation. However, these data sets need not to be interpreted as separate tectonic

phases since their stress configurations (although magnitudes might be different) are consistent with the overall mechanism of N-S extension. Therefore, they can be considered as transfer faults that transfer deformation between two or more normal faults. Hence, they might be transfer faults developed between the E-W trending normal faults.

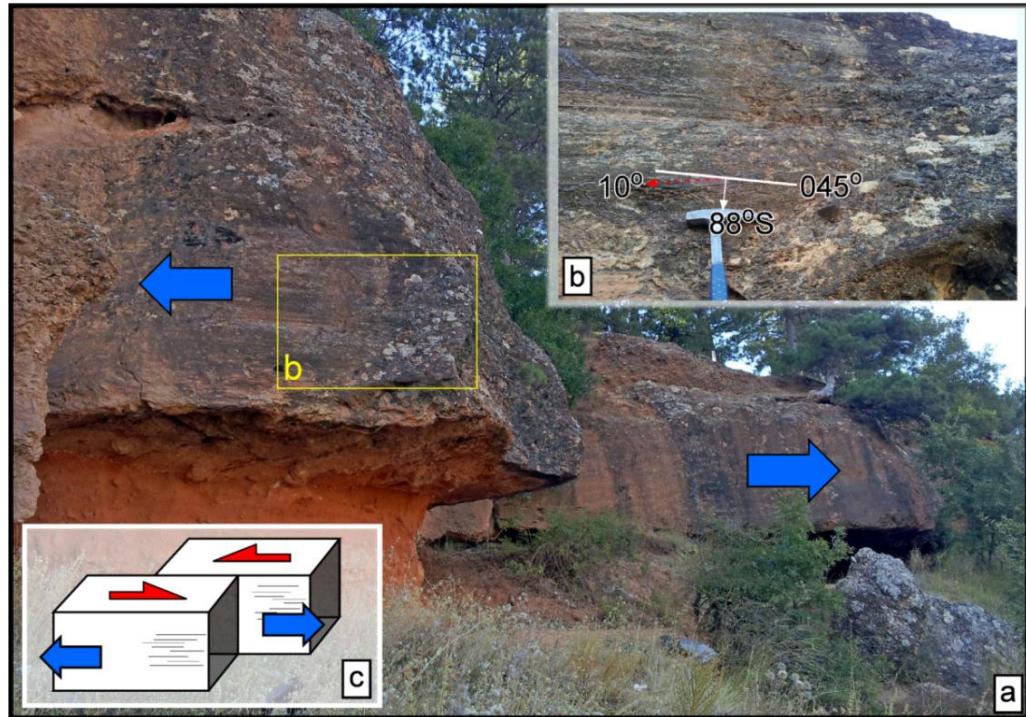


Figure 3.34. Field view and sketch of the pure strike-slip faults observed within the Early Miocene Kumdöken formation in Site 33. Yellow rectangle indicates the close-up view of the slickenlines on the fault surfaces which is given in inset b. Note that fault orientation is approximately NE-SW. Simplified sketch of the block movement is given in inset c. Blue arrows indicates the relative movement of fault blocks. Red arrows show movement on horizontal plane.

3.4.3 Spatial Characteristics

Identification of the stress field that controlled the deformation in the Ilgın Basin is performed by fault analyses. Detailed analyses of reconstructed deviatoric stresses may help to understand the type of stress regime and the resulting deformation. For these purposes, the density diagram of principal stress orientations (σ_1 , σ_2 and σ_3) and a histogram of ϕ values were prepared for the whole data set (Figure 3.35). Orientations

of σ_1 are generally (sub-) vertical and well concentrated in the center of the diagram except for a few sites which have strike-slip solutions (Figure 3.35a). The average σ_1 orientation as shown in Figure 3.35a is found to be $346^\circ\text{N}/84^\circ$ which is very close to vertical orientation. Two main clusters can be identified on the σ_2 and σ_3 distribution plots given in the Figure 3.35b and 3.35c, respectively, although, these stress orientations scattered largely in all directions. The scattering may be explained by the presence of two different fault sets (N-S and E-W) in the area which seems to perturb the regional stress which seems to be uniaxial and constrained some of the stress orientations inline with the orientation of these fault sets. This event is known as tendency of σ_2 and σ_3 permutation (Angelier, 1994; Homberg et al., 1997) that take place especially close to major faults and when the magnitude of intermediate and minor stress are equal or close to equal (Kaymakci 2006). The average σ_2 and σ_3 orientations are (sub-) horizontal and are found to be $270^\circ\text{N}/03^\circ$ and $180^\circ\text{N}/05^\circ$ respectively. Deformation of the Iğın Basin is obviously extensional, as shown by the vertical orientation of σ_1 , and is accommodated by the major normal faults in the basin.

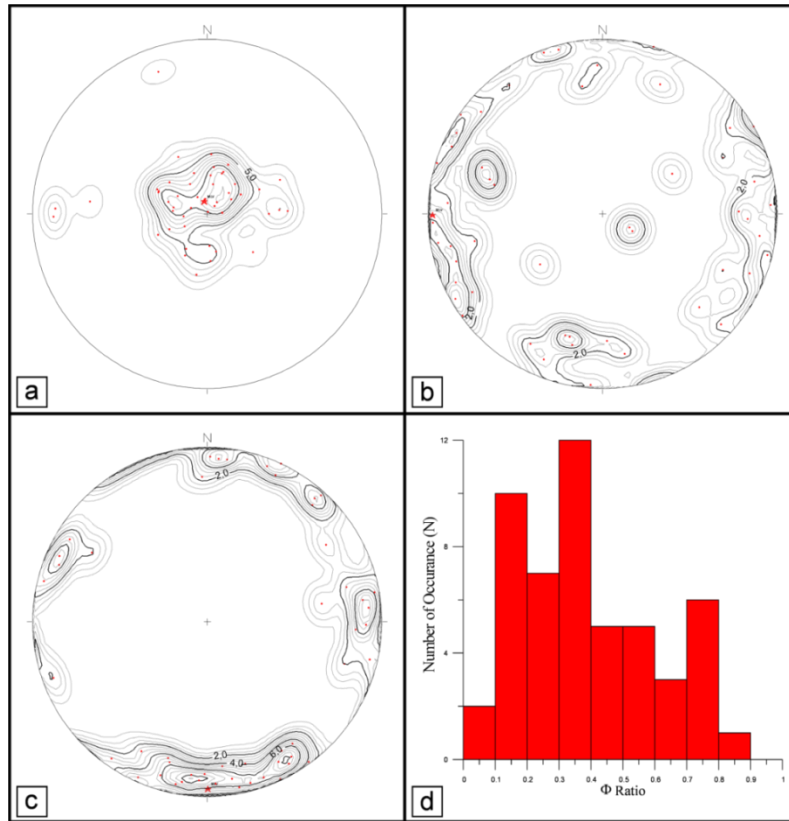


Figure 3.35. Density diagrams for principle stress orientations (σ_1 , σ_2 and σ_3 , in a, b and c respectively) and frequency distribution of Φ values for whole data (d). Notice that the σ_1 is significantly (sub-)vertical while σ_2 and σ_3 orientations are horizontal.

The shape ratio (Φ) of the stress ellipsoid provide information about the tectonic regime that may change from radial to axial based on the relative magnitudes of σ_2 , with respect to σ_1 and σ_3 . The Φ ratio varies from 0.074 to 0.840 for all the sites (Figure 3.35d) and has a peak value at 0.35. In more than 30 sites, Φ values are less than 0.4. This low value of Φ suggests that σ_2 is close to σ_3 in magnitude, therefore σ_2 and σ_3 permutations are likely.

The spatial distributions of the minimum principal stress (σ_3) directions are showed on the map (Figure 3.36) and it reveals whether the constructed paleostress configurations are compatible with regional structures. Structural studies indicated two major fault sets, which have mainly NW-SE and E-W orientations and they seems to control the evolution in the Ilgın Basin. Accordingly two σ_3 directions, N-S and E-W, are obtained in the area and they are (near-) orthogonal to the dominant trends of the nearby major faults. In addition, as seen in Figure 3.36a, σ_3 directions changes as the strike of the associated major fault changed from west to east in Sites 41, 3, 4 and 17. This pattern indicates that the constructed paleostress orientations are represent local stress and are not directly related to the regional stress orientations.

In Figure 3.36b, horizontal component of the minor principal stress (σ_3) directions including strike-slip solutions (sites 14, 33 and 35) show clearly N-S extension and they are highly correlated with the orientations of the nearby major structures. The strike-slip solutions are regarded as smaller scale transfer faults between two adjacent normal faults undergoing differential extension. Also Figure 3.36c indicates σ_3 directions which indicate N-S extension direction (sites, 37, 38* and 40*) in the Çavuşçugöl region whereas σ_3 directions collected from the tectonically active Ilgın Fault Zone (sites 9, 11*, 38*, 43 and 49) including strike-slip solutions (site 40*) represent that E-W extension controls the deformation of the Ilgın Fault Zone.

This stress pattern implies two different possibilities; 1) σ_1 directions are stationary and vertical, while σ_2 and σ_3 directions are horizontal, but unstable since their magnitudes are so close to each other that they are interchangeable ($\sigma_1 > \sigma_2 \cong \sigma_3$); 2) uniaxial stress condition ($\sigma_1 > \sigma_2 = \sigma_3 = 0$) implies unconstrained slip (somewhat similar to free fall of hanging-wall blocks along fault planes) along the major normal faults. Therefore, each paleostress configuration represents specific characteristics of a particular faulted zone from which they are constructed.

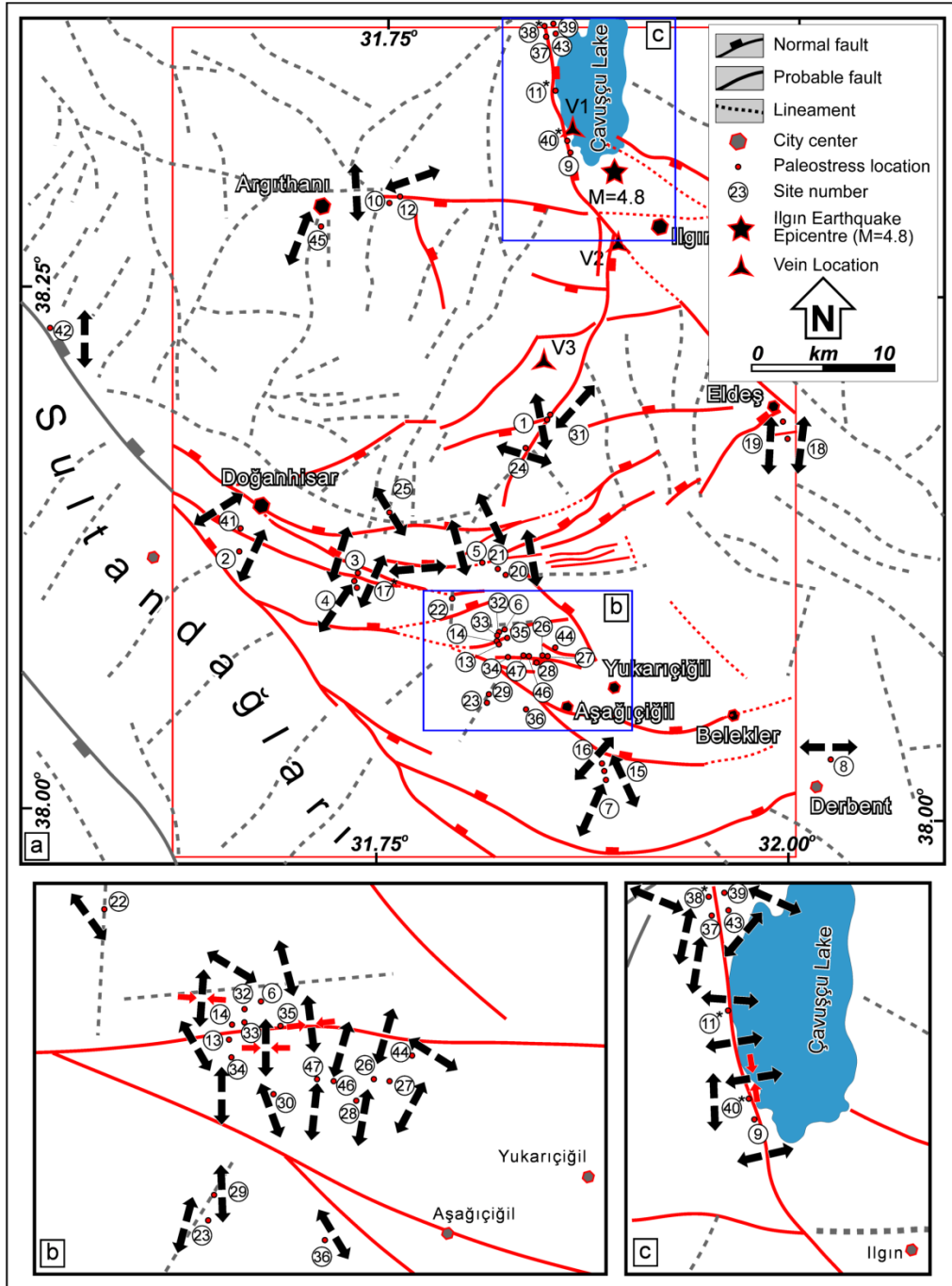


Figure 3.36. Spatial distribution of the paleostress measurements on the major faults and lineament map of the Ilgın Basin. Arrows indicate horizontal component of the minor principle stress (σ_3). Numbers indicate locations of paleostress measurement which correspond the site numbers in Figure 3.31 and Table 3.2. Blue rectangle areas in the base map show the location of the close-up view of the inset maps which are labeled as b and c. Red rectangle area represents mapped area given in Figure 3.1

3.4.4 Temporal Relationships

Taking stratigraphic information into account is very important to unravel temporal changes of the paleostress configurations throughout the stratigraphy, enabling us to reconstruct the tectonic evolution of the basin (Kleinspehn et al., 1989; Hippolyte et al., 1993). In paleostress stratigraphy, it is expected that the entire paleostress history during the basin formation should be recorded potentially in basement rock units whereas the youngest tectonism is only recorded in the upper most part of the basin infill as a single phase (Kleinspehn et al., 1989). Theoretically the younger events need to be extracted from the older ones, successively from younger to older. Based on this idea, the constructed extension directions for each formation were plotted separately. Ordered paleostress data in Figure 3.37 is produced based on the age of the rocks from which slip data were collected and the age of the youngest unit which is cut by faulting. The resultant configuration suggests that younger deposits contain N-S and E-W extension directions. Moreover, paleostress tensors that were coeval with sedimentation in the Aşağıçiğil formation confirm N-S (Site 29 and 36) and E-W extension directions (Site 24). In addition, E-W oriented growth faults observed in the coal mine (Figure 3.38) at the western edge of the Çavuşçugöl graben whose western boundary is controlled by seismically active N-S trending Ilgın Fault Zone provide evidence for two coeval extension directions in the Ilgın Basin. Apart from the distinct E-W and N-S extension, there are some hybrid solutions (sites 43, 16, 31, 44 and 32).

Presently active extension direction in the Ilgın Basin is dominated by the Akşehir-Afyon, Ilgın and Argıthanı fault zones. AAFZ is represented by sites 2, 4 and 41 and the extension direction trends approximately NE-SW. The IFZ is represented by sites 11, 9, 38 and 39 and E-W extension dominated along this fault zone. The AFZ is represented by sites 10 and 45 and N-S directed extension characterizes AFZ. All of these paleostress orientations and the tectonic regime prevailed in the region since the Middle Miocene (possibly since the Early Miocene) is conformable with the focal mechanism solutions of the recent earthquakes in the region that include 3 February 2002 Sultandağ Earthquake ($M=6.4$, Taymaz et al., 2004), the Ilgın Earthquake (27 July 2011, $M_w=4.7$ ERD, $M_w=4.6$ GFZ) and Argıthanı Earthquakes (26 September 1921, $M=5.9$ and 21 February 1946, $M=5.9$)

Therefore, extension directions range from E-W to N-S (Figure 3.37), attesting to the fact that the region has strongly varying σ_3 directions while σ_1 is (sub-) vertical.

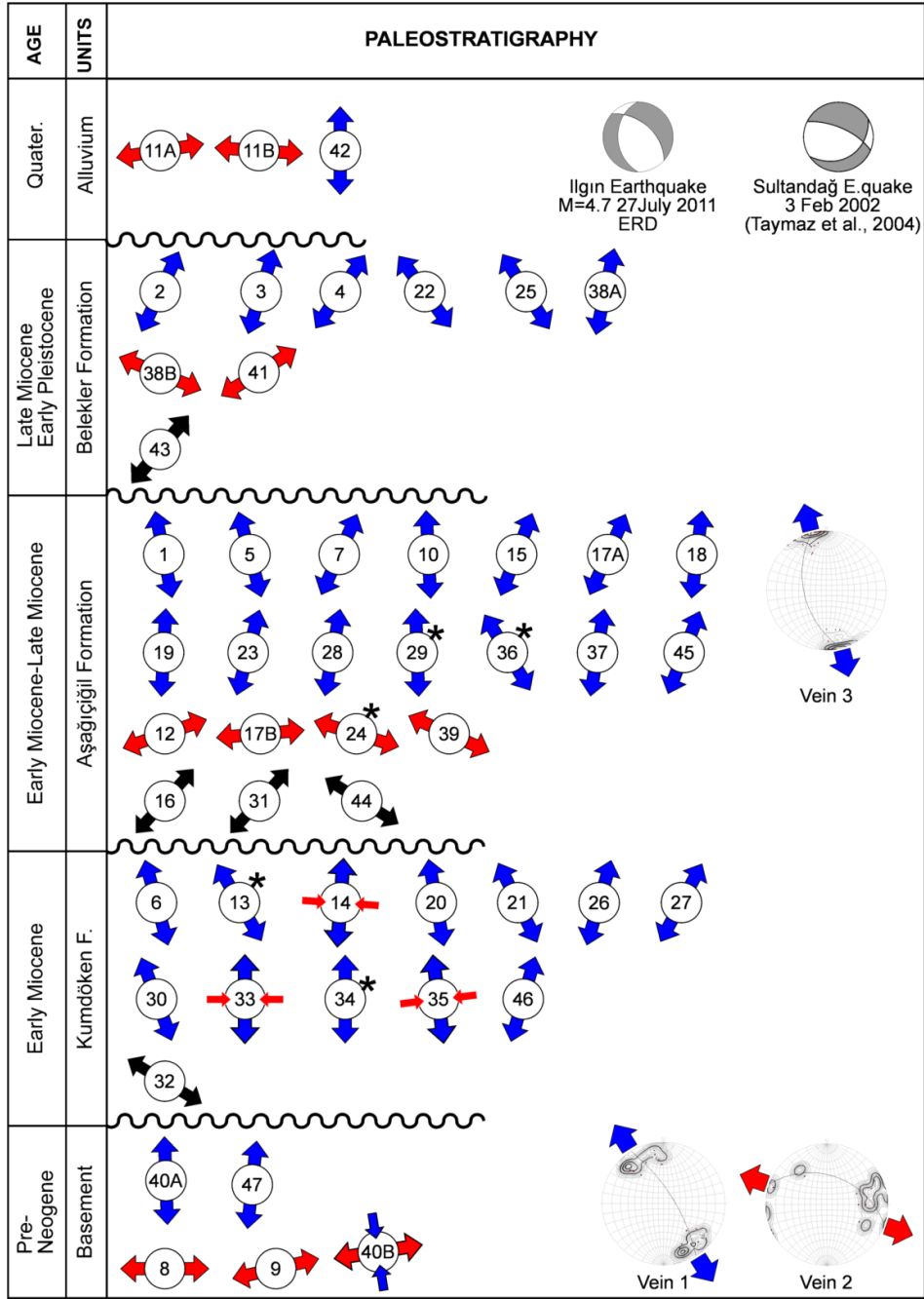


Figure 3.37. Paleostress stratigraphy of the Ilgın Basin from the Early Miocene to Recent. Arrows represent σ_3 directions. Red, blue and black arrows indicate E-W extension, N-S extension and hybrid paleostress solution, respectively. Black star are used to represent syn-sedimentary fault-slip solution. Focal solutions are belong to 27 July 2011 Ilgın Earthquake (M=4.7 ERD and M=4.6 GFZ) and 3 February 2002 Sultandağ Earthquake (M=6.4 Taymaz et al., 2004). Stratigraphic location of the vein data is also given. Note that nature of σ_3 directions and extension directions of the earthquakes and the vein data in the region.

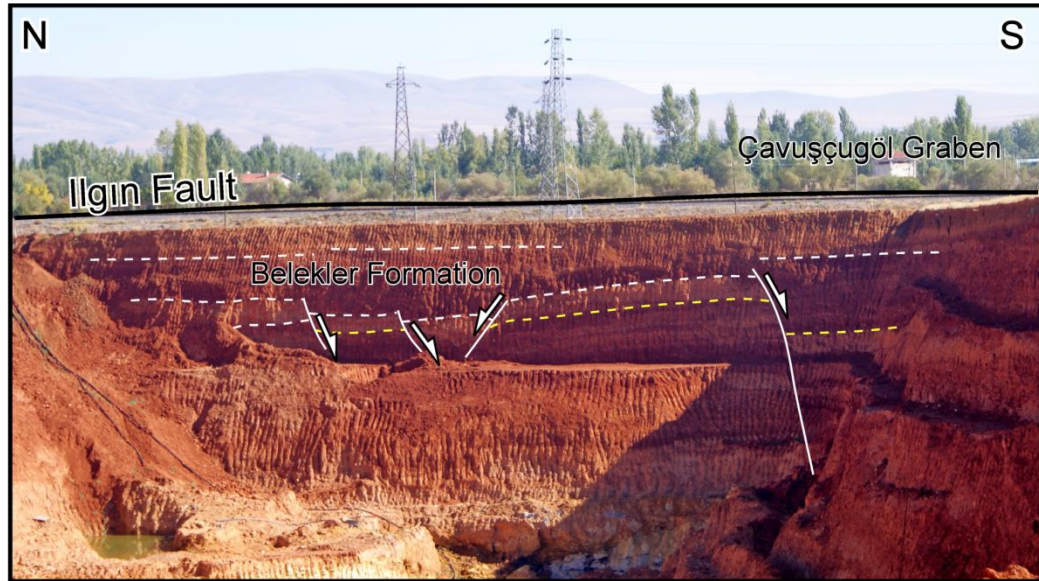


Figure 3.38. Normal faults which indicates coeval N-S and E-W extension direction. White solid lines represents the E-W trending growth fault displacement and solid black line states the trace of the Ilgın Fault which delimits western boundary of the Çavuşçugöl graben.

CHAPTER 4

TECTONO-SEDIMENTARY EVOLUTION AND GEOCHRONOLOGY OF THE MIOCENE YALVAÇ BASIN (ISPARTA)

In this chapter, the general stratigraphic framework and the geological structures of the Yalvaç Basin are documented and described in detail. Collected fault-slip data are also analyzed and interpreted in spatial and temporal context.

The continental Yalvaç-Yarıkkaya sedimentary basin started to form during an ill-defined time interval in the Neogene. It is one of the well exposed internal basins within the Tauride mountain range (Figure 4.1) and contains a continental clastic infill of more than 800m thick (Yağmurlu, 1991) resting on pre-Neogene meta-sediments and non-metamorphic carbonates ranging in age from Ordovician to Cretaceous as well as Cretaceous ophiolite complexes (Yağmurlu, 1991a).

4.1 Lithostratigraphy

The infill of the Yalvaç Basin comprises continental clastic sediments. The first studies that concentrated mainly on lignite-bearing Neogene units were performed by several researchers (Lahn, 1940; Wedding, 1954; Füst, 1955; Göktunalı, 1957; Pekmezçiler, 1958) on behalf of the Mineral Research and Exploration Institute (MTA) of Turkey in order to reveal the lignite potential of the basin. After these pioneering studies, a more detailed Neogene stratigraphy of the basin has been established by Yağmurlu (1991a) which provided additional stratigraphic data. The formation nomenclature of Yağmurlu (1991a) is adopted for this study, dividing the lithostratigraphy of the Neogene deposits in the Yalvaç Basin into four main stratigraphic units, from older to younger including, (1) the Bağkonak formation, (2) the Yarıkkaya formation, (3) the Göksöğüt formation and (4) the Kırkbaş formation (Figure 4.2). Below, we describe their lithology, age and contact relationships, and provide an interpretation of their depositional environments (Figure 4.1 and Figure 4.2).

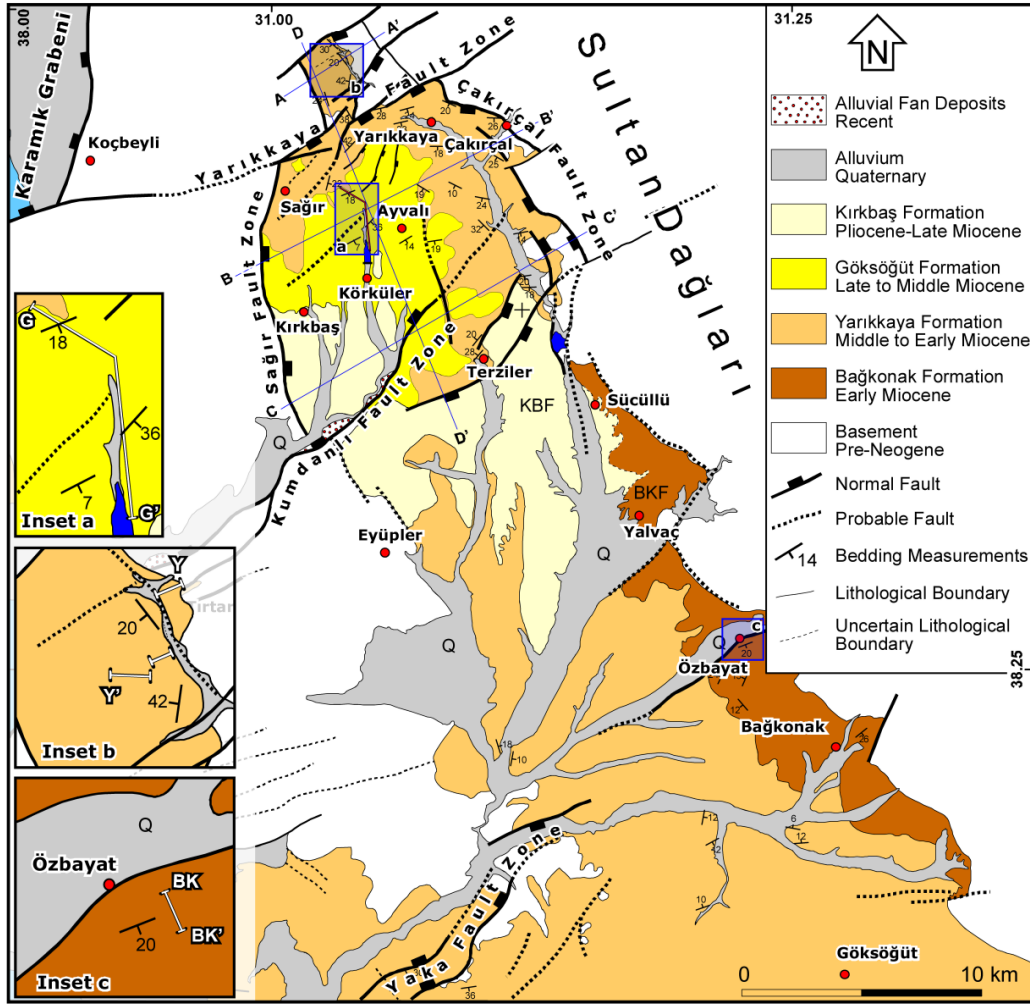


Figure 4.1. Revised geological map of the study area based on the field studies and remotely sensed data. Blue rectangle areas are used to indicate the location of the measured sections of the lithological units. Inset map a for Göksöğüt formation (GSFm), inset map b for Yarıkkaya formation (YKFm) and inset map c for Bağkonak formation (BKFm). Routes of the measured sections are indicated by white solid lines (G-G' for GSFm, (Y-Y') for YKFm and (BK-BK') for BKFm (see Appendix for larger scale of this map).

AGE	UNITS	LITHOLOGY	DESCRIPTION	FOSSILS/ SPORE AND POLLEN
Quater.	Alluvium		alluvial plain and alluvial fan sediments (gravel, sand, silt, and mud)	
Pliocene	Kırkbaş Fm.		partly consolidated, unsorted, matrix supported polygenetic red conglomerate, sandstone and mudstone	Mammals -Mastodon Sp. -Hipparion Sp.
Late Miocene	Göksöğüt Formation		poorly sorted, clast-supported polygenetic conglomerates. Clasts of which derived from limestone. The clasts are pebble to boulder sized and maximum clast size is less than 70 cm.	
			dark color, poorly sorted, rounded coarse sandstone and granule to pebble sized conglomerates alternation.	
			light-brown/white-creamy thick-bedded with irregular bed surfaces, well cemented, algal limestone.	
Middle Miocene	Yarıkkaya Formation		light-brown thick-bedded, well cemented algal limestone.	Pollen/Spores -Laevigatosporites heardti -Leiotriletes microadriensis -Baculatisporites primarius -Gleicheniidites -Monocolpopollenites -Monopropollenites gramineoides -Inaperturopollenites hiatus -Inaperturopollenites dubius -Inaperturopollenites polyformosus -Pityosporites microalatus -Pityosporites labdacus -Triatriopollenites rurensis -Triatriopollenites bituitus -Triatriopollenites myricoides -Triatriopollenites coryphaeus -Triporopollenites simpliformis -Subtriporopollenites simplex -Intratriporopollenites instructus -Polyvestibulopollenites venus -Polyporopollenites undulosus -Tricolpopollenites densus -Tricolpopollenites librarensis -Tricolpopollenites villersis -Tricolpopollenites pseudocingulum -Tricolpopollenites cingulum -Tricolpopollenites helmsi ted tensis -Tricolpopollenites microreticulatus -Tetracolpopollenites microellipsus -Teiracolpopollenites microrhombus -Periporopollenites stigmatus -Periporopollenites muhiporatus
			creamy-white siltstone, shale and marl alternation, intercalated with thinly bedded limestone, and organic rich horizons.	
			greenish mudstone intercalated with organic rich horizons (coal horizons).	
Pre-Neogene	Bağkonak Fm.		1 poorly sorted, clast-supported, fining upwards, polygenic conglomerates intercalated with mudstone and organic rich horizons. Clasts of which derived from limestone (90%) and metamorphic rocks (%10). The maximum clast size is less than 15 cm. It belongs to Yarıkkaya Formation.	Mammals -Rodentia Cricetinae
			2 unsorted, angular, matrix-supported red conglomerates which derived from nearby metamorphic rocks. The clasts are pebble to cobble sized and maximum clast size is less than 30 cm. This unit belongs to Bağkonak Formation.	
Pre-Neogene	Basement		NONCONFORMITY Ordovician-Permian meta-carbonates and meta-clastics consisting of slate, phyllite and quartzite. Jurassic platform type thick carbonates, and Ophiolitic melange composed of serpentinite, radiolarite, serpentinized peridotite and pyroxinite were emplaced during Lutetian.	

Figure 4.2. Generalized stratigraphic column for the Yalvaç Basin.

4.1.1 Baękonak Formation (BKFm)

The Baękonak formation (BKFm) is characterized by continental red clastics including conglomerates at the bottom and intercalating sandstone and sandy-mudstone at the upper levels of the formation. This unit was first defined by Demirkol (1982) and was later modified by Yaęmurlu (1991a), who determined the maximum observable thickness of these red, coarse-grained deposits as approximately 250 m. The unit is well-exposed around Özbayat and Baękonak located at the south of Yalvaę, which was selected as the type locality for the BKFm. The formation unconformably overlies the pre-Neogene units (Figure 4.3 and Figure 4.4) that include low-grade metamorphic rocks and carbonates, and it grades vertically and laterally into the Yarıkaya formation.



Figure 4.3. Field view of the angular unconformity between Baękonak formation and basement limestone. View towards the north.

In the measured section which is located south of Özbayat, the sequence starts at the bottom with angular, unsorted, well-cemented, and thinly to thick bedded reddish conglomerates (10 cm to 2 m) (Figure 4.5). Pebbles of the conglomerates ranging from gravel to boulder-size (occasionally up to 50 cm diameter) and are derived from the slightly-foliated greenish metamorphic rocks (90%) and light to dark grey carbonates (10%) from the nearby exposed Sultandaęları Mountain (Figure 4.6a). The arrangement of the pebbles is generally chaotic, and fining-upwards sequences within layers was clearly observed. They are typically clast-supported conglomerates suggesting rapid, chaotic sedimentation at lower part. Towards the upper parts the conglomerates become gradually matrix supported. Sedimentary structures such as pebble imbrications, cut-and-fill structures (channel deposits) are occasionally observed. However, erosional base and shale clasts (%50) consisting of approximately 3-4 cm diameters at the bottom of the conglomerate beds are very remarkable and they signifies erosional and depositional processes took place at the same time next to each other. These levels are

followed upwards by thinly to medium bedded (10-50 cm), brick red to purple sandstone and sandy-mudstone alternating with conglomerates. Further in the upper parts, the unit is characterized by more than 67 m of monotonously matrix-supported polygenic conglomerates. The pebble sized (less than 5 cm) clasts are dispersed in a poorly sorted, finer matrix which consists of sand and sandy-mud. The overall sequence shows decrease in the grain size from boulder to block sized reddish conglomerates to fine grained, matrix-supported reddish/yellowish conglomerates. The BKFm has a minimum thickness of 131 m.

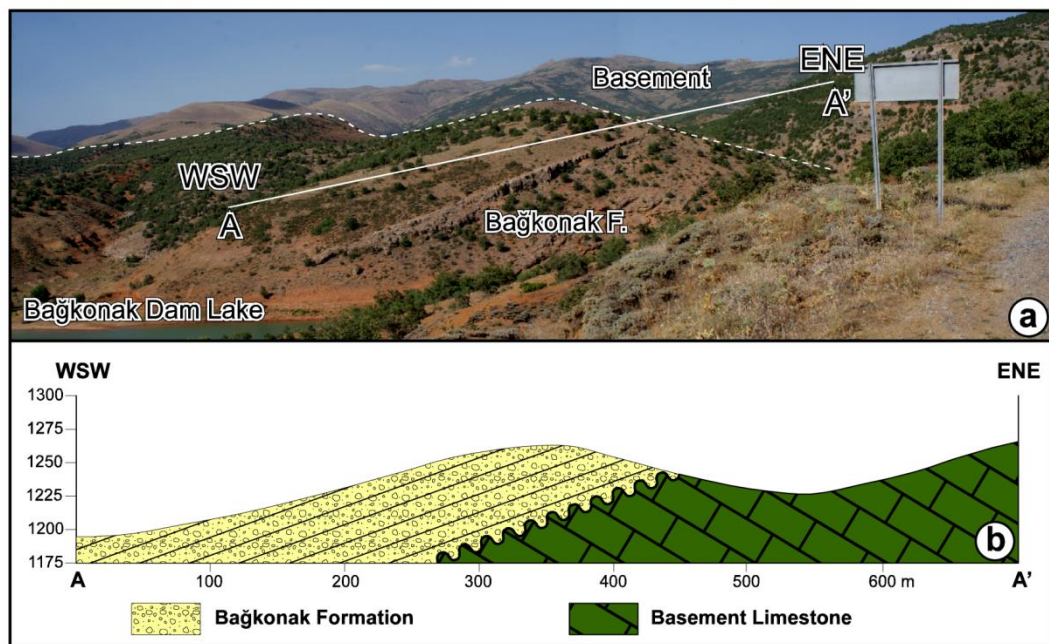


Figure 4.4. General view of the angular unconformity between the Bağkonak formation (BKFm) above and the Pre-Neogene basement limestone units below. Un-interpreted figure is given in (a) and interpreted figure is showed in (b). North east of the Bağkonak and view to north.

To the south of the Yalvaç-Yarıkkaya Basin near Bağkonak, an erosional window provides exposure of the nonconformity between the BKFm and the underlying basement (Figure 4.3 and Figure 4.4). From the Sultandağları Mountain in the east towards the central parts of the basin, there is a gradual decrease in the grain size from reddish conglomerates to fine grained yellowish/white marly deposits of the Yarıkkaya formation (Figure 4.7). In the north, the BKFm is conformably overlaid by Yarıkkaya formation.

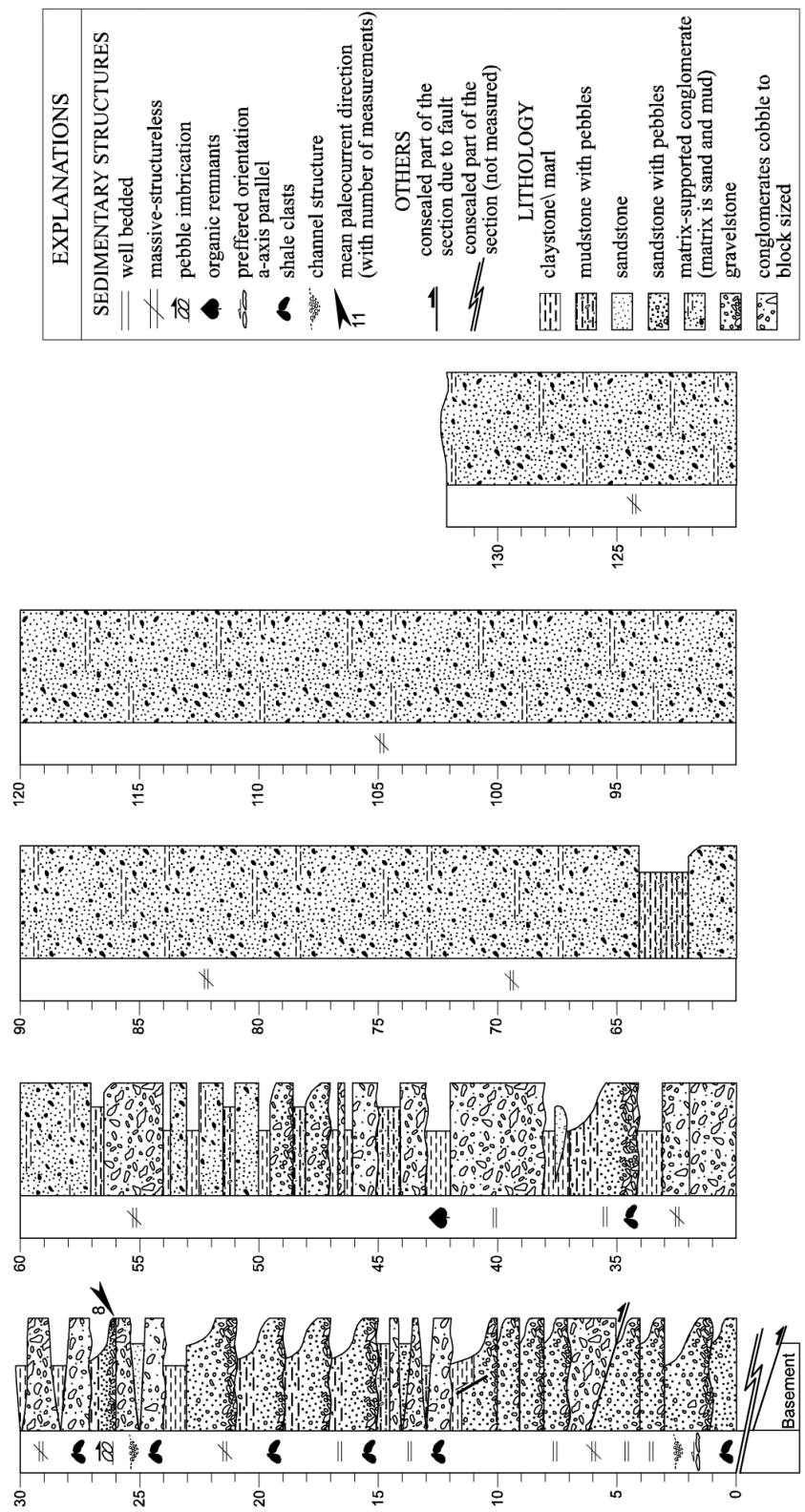


Figure 4.5. Measured section of the Bağkonak formation.

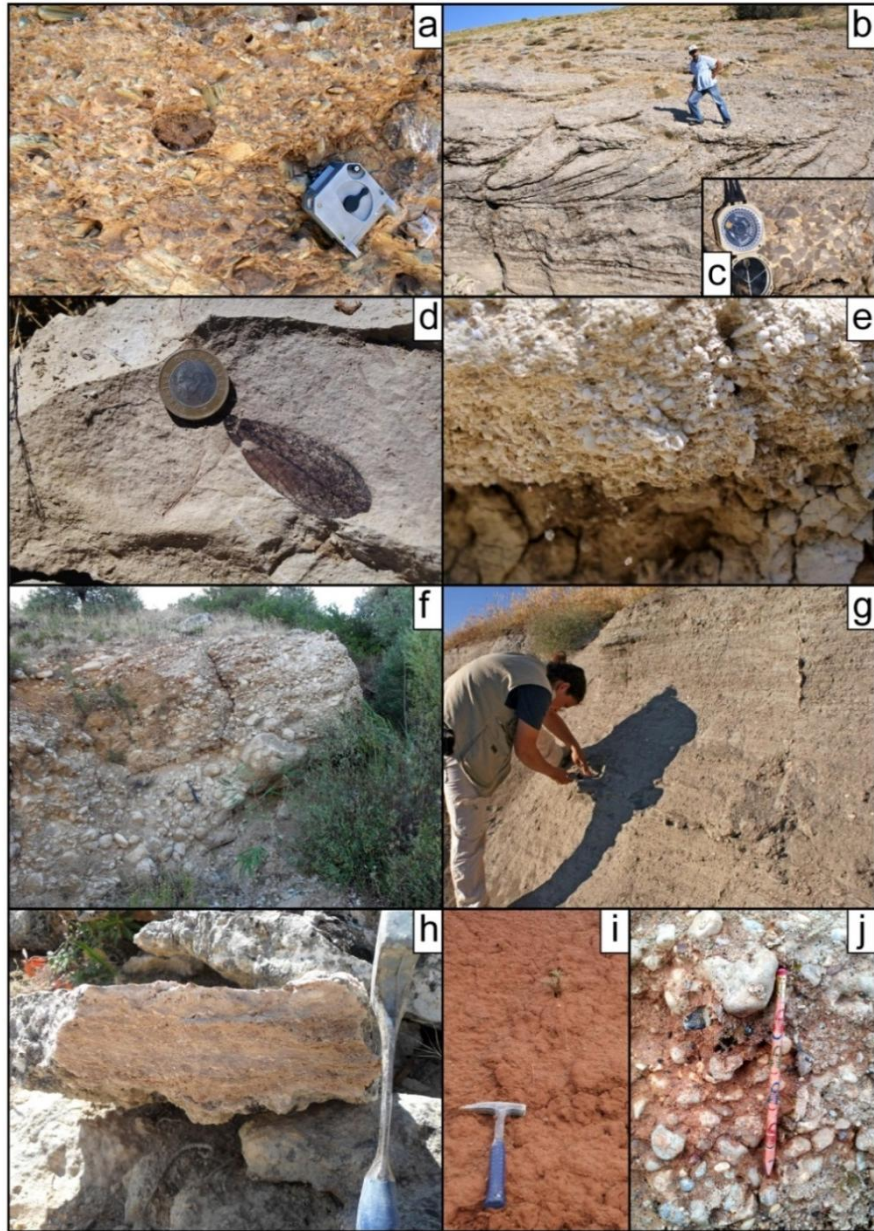


Figure 4.6. Basal conglomerate of the BKFm around the Özgüney (a), cross-bedding in the conglomerates is observed in the lower part of the YKFm around north of the Yarikkaya (b), close up view of the conglomerates with pressure solutions at the edge of the conglomerates (c), mudstone from the YKFm containing trace fossils (d), close up view of the gastropod rich level in the YKFm (e), block-sized, poorly sorted, sub-angular to sub-rounded conglomerates belonging to GSFm (f), black sandstone level in the GSFm (g), buff to brown, banded and porous possibly lacustrine algal limestone in the GSFm (h), red mudstone and conglomerate unit of the KBFm (i, j respectively).



Figure 4.7. General view of the Bağkonak formation. The white dashed-line represents the boundary between formations. Note that coarse, poorly sorted, sub-angular coarse clastics dominate along the NE margin while the unit gradually become finer-grained to marl-dominated towards SW (view to NE).

No fossil assemblage was encountered in the samples collected from BKFm. Similarly, previous studies (Demirkol, 1982; Yağmurlu, 1991a) did not report any fossil assemblage from the unit. However, Yağmurlu (1991a) suggested that Yarikkaya formation is laterally interfingering with BKFm and proposed Middle Miocene age based on the fossil and pollen assemblages of the Yarikkaya formation. In this study, the rodent data reported by Saraç (2001) near Yarikkaya and lateral gradation to the BKFm are taken into account and the Middle Miocene age is adopted for the BKFm.

Unsorted, angular, and boulder- to pebble-sized reddish/brownish conglomerates in the lower part of the unit indicate a very close proximity to the source. In addition, grading and erosional base of the bedding signify an energetic environment and usually explained as a result of a large amount of mixed sediments being discharged into quiet water. The largely structureless nature and overall fining upward character of upper part of the unit suggest an origin as gravity flows with sediment transported in turbulent suspension. Hence, the BKFm was probably deposited in alluvial fans and terrestrial debris flows along the basin margin.

4.1.2 Yarikkaya Formation (YKFm)

The YKFm is composed of coarse, sub-rounded, poorly sorted, grain-supported conglomerates at the bottom and grades upwards into sandstone and mudstone. The sequence continues upward with boulder to block-sized, sub-angular, matrix and grain supported conglomerates. Demirkol (1982) was the first to name this unit and suggested that the YKFm is younger than Göksöğüt formation (GSFm). This was later modified by Yağmurlu (1991a) who proposed an alternative stratigraphic order for YKFm and GSFm. The maximum observable thickness of the YKFm was given by Yağmurlu (1991a) as approximately 200 m. The YKFm is well-exposed around Yarikkaya located to the north of Yalvaç, which is the type locality of the YKFm. The formation unconformably overlies pre-Neogene units including low-grade metamorphic rocks and carbonates in the north, and conformably overlies the BKFm in the south (Figure 4.7). The GSFm delimits the upper boundary of the formation. The stratigraphic relation between these two formations is unconformable in the north, but conformable in the south.

The measured section for the YKFm is a composite section based on two different locations, separated by the Yarikkaya Normal Fault. Based on the geometry of the structure, the first measured section of the unit is located in the footwall block of the Yarikkaya Fault and comprises the lower part of the YKFm (Figure 4.8). It is located approximately 4 km north of Yarikkaya where, a basal conglomeratic unit and pre-Neogene basement are exposed (Figure 4.9). The sequence starts with sub-rounded, unsorted, well-cemented, and medium to thick-bedded (30-40 cm) polygenic conglomerates (Figures 4.6b and 4.6c), overlying carbonates and low-grade

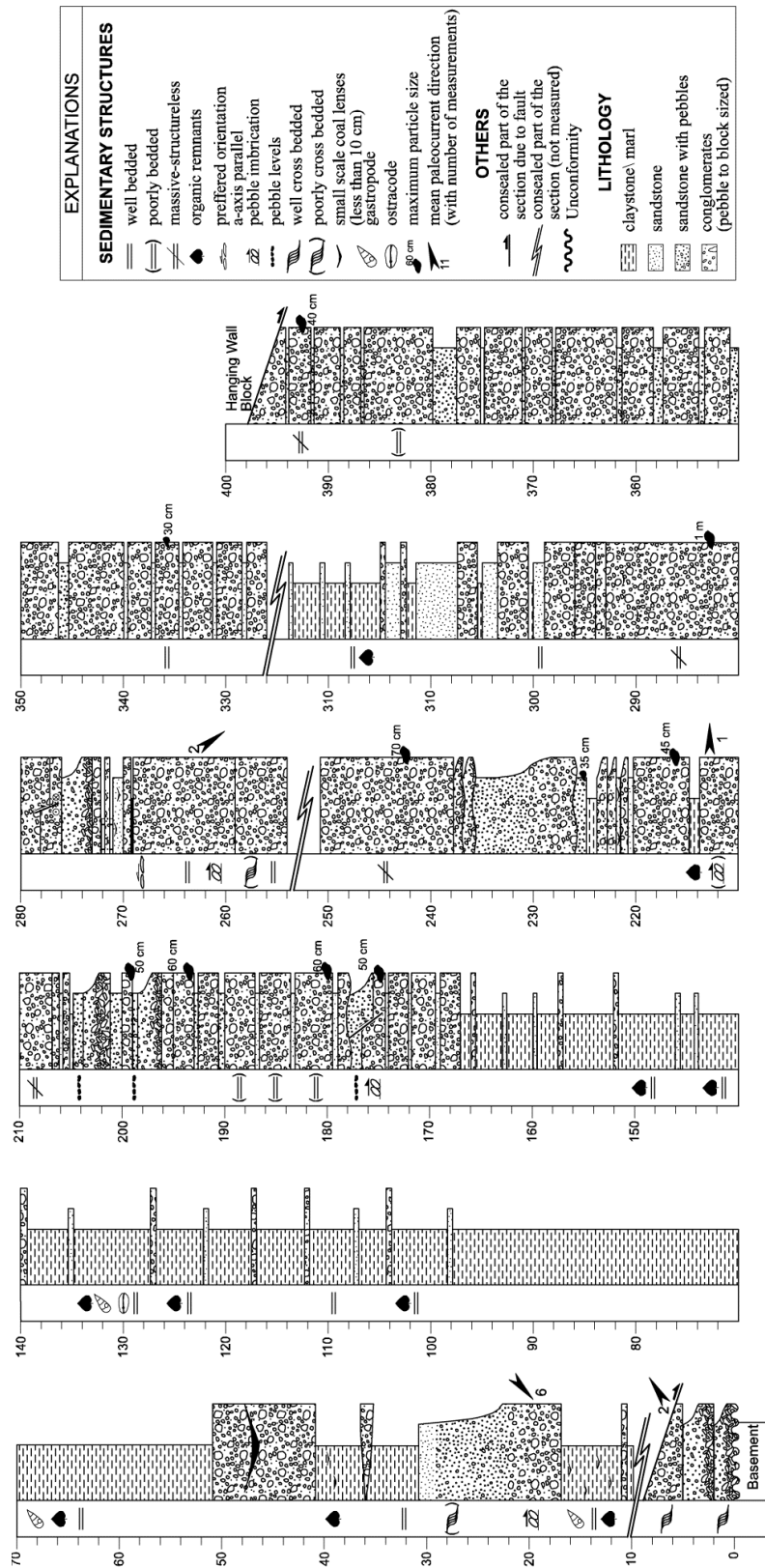


Figure 4.8. Measured section of the lower part of the Yarıkkaya formation (in the footwall block).

metamorphic rocks of Sultandağları Mountain (Figure 4.9). Clasts of the conglomerates ranging from pebble to cobble-size (occasionally up to 20 cm diameter) derived from light to dark gray limestone (95%) and green metamorphic rocks (5%). The pebbles are randomly arranged and pressure solution pits are occasionally observable at pebble contacts, suggesting significant compaction. Locally graded bedding is very common to most of the conglomerates. They also display imbrication and cross bedding which provides hints for the flow conditions of the transporting medium (Figure 4.6b). In the middle parts, the section comprises thin to medium bedded (less than 30 cm), green/blue organic-rich mudstone (Figure 4.6d) and white marls alternating with conglomerates and sandstones. The sequence continues upward with coarse, sub-angular to sub-rounded, unsorted, occasionally grain or matrix supported, polygenic conglomerates alternating with sandstone. Clasts of the conglomerates range from pebbles to block-size (15 cm to 1m) comprising light to dark limestone and green, slightly foliated metamorphic rocks. Although, the limestones versus metamorphic rock content in the conglomerates vary in each level, however, the mean ratio is generally and is around 1/4 respectively. At these levels, sedimentary structures such as cross-bedding and pebble imbrication are occasionally observed. The measured thickness of YKFm is ~400 m in the footwall block of the Yarikkaya Fault.

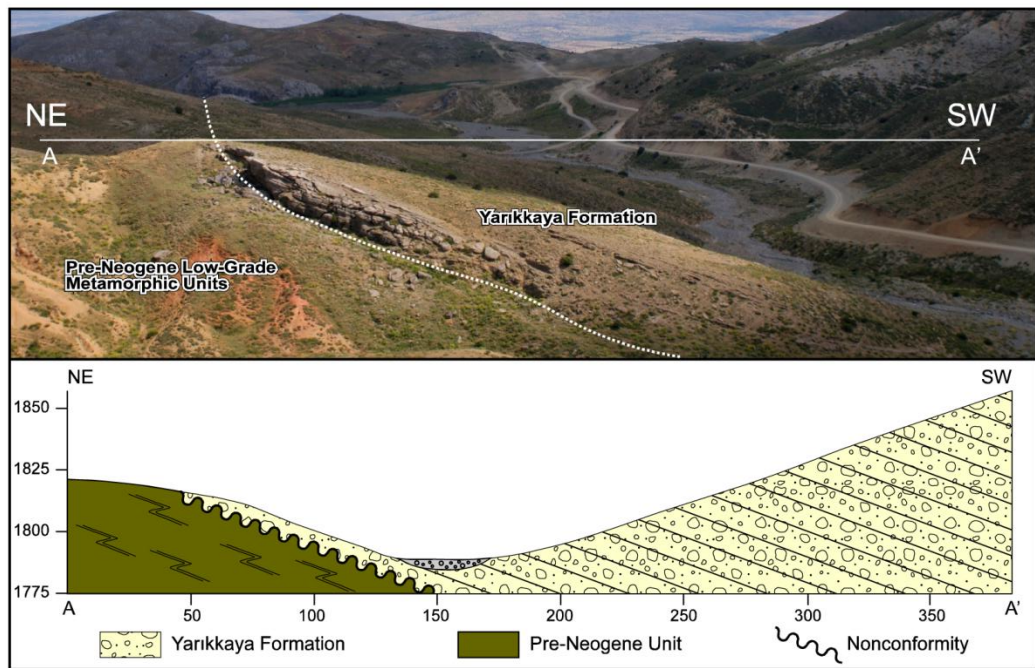
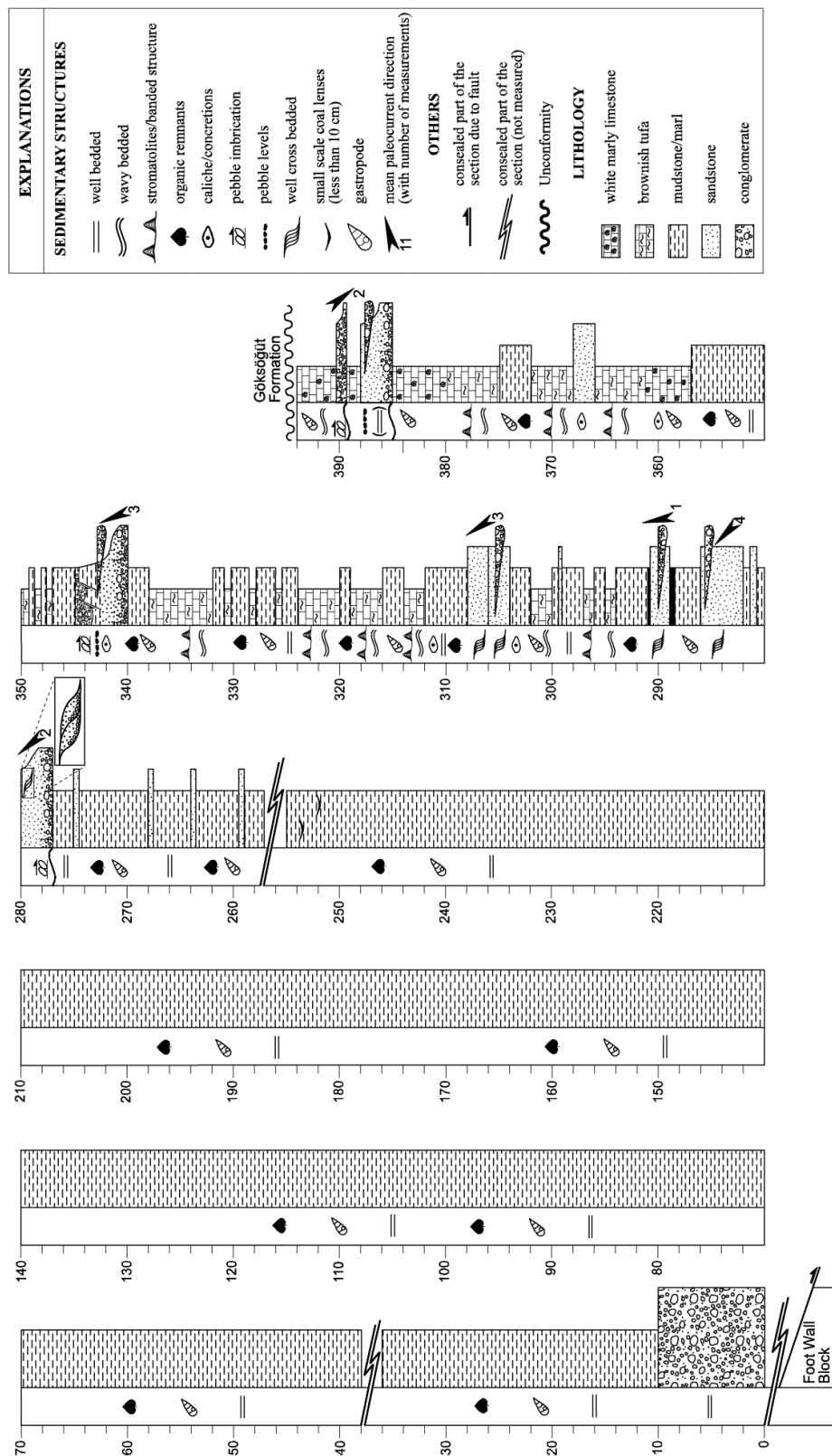


Figure 4.9. General view of the nonconformity between Pre-Neogene low metamorphic basement unit and Yarikkaya formation (dashed line) and cross-section along the line AB (solid white line).

The second measured section is located in the hanging wall of the Yarikkaya Normal Fault and corresponds to a lateral stratigraphic continuation of the measured section in the footwall block representing the upper part of the YKFm (Figure 4.10). This section is approximately 3 km northwest of Yarikkaya where tufa, lacustrine marly limestone and conglomerate units of the YKFm are exposed. The sequence starts at the bottom with coarse, (sub)-angular, well-cemented and clast-supported conglomerates overlying carbonate basement. Size of the conglomerate clasts ranges from pebble to boulder (up to 30 cm) and are consisted mostly of limestone (>95%) comparable to the underlying carbonate basement lithology. The sequence continues upwards with creamy white marl/claystone containing fresh water gastropods (Figure 4.6e) and fossil leaves. This is followed by a green mudstone and coal seams. In this locality, the outcrops are disrupted and obscured by coal mining activities. The measured section continues upwards with white, fossiliferous marly-limestone and banded, undulated, highly porous tufa alternation which is intercalated with medium to thick bedded, clast supported, poorly sorted conglomerates and cross-bedded, yellowish sandstone. Clasts of the conglomerates are well rounded, clean and dominantly they are derived from >95% light to dark limestone. The thickness of the YKFm was approximated by different methods including direct measurements in the field and indirect measurements using trigonometric principals (dip of the bedding and distance between the locations were taken as approximately 15° and 600 m along the dip direction, respectively). According to these calculation and measurements, the YKFm has a minimum thickness of 394 m in the hanging wall of the Yarikkaya Normal Fault. From the northern tip of the Sultandağları Mountain to the south, toward the center of the basin, the YKFm displays a gradual decrease in the grain size from conglomerate to marly-limestone and tufa deposits. To the north of the Yalvaç-Yarikkaya basin, an uplifted footwall block of the Yarikkaya Normal Fault provides an exposure of the nonconformity between the YKFm and the underlying basement. To the north of the Körküler, the Göksöğüt formation unconformably overlies the Yarikkaya formation (Figure 4.11).

As mentioned in previous section, Yağmurlu (1991a) reported fresh-water fossils in the mudstone and claystone levels of the YKFm, including *Planorbis* sp. and *Limnea* sp. In addition, Yağmurlu (1991a) reported some pollen and spore assemblages collected by Dr. E. Akyol and Dr. F. Akgün (Dokuz Eylül University, İzmir) and assigned a Middle Miocene age to the YKFm. On the other hand, Saraç (2001) reported fossil vertebrates *Rodentia-Cricetinae* from lacustrine deposits corresponding to the upper part of the Yarikkaya formation, and ascribed Early-Middle Miocene for the age of the formation. Therefore, based on these information, Middle Miocene age is adopted for the Yarikkaya formation.



In the lower part of the sequence, boulder to block-sized, sub-angular to sub-rounded, matrix and grain supported conglomerates with sedimentary structures including cross-bedding and pebble imbrications indicate that the lower part of YKFm was probably deposited in fluvial environment including slope and channel processes. Particle size gradually decreases from the northern part of the basin towards the south, with lithologies changing from coarse grained conglomerates to mud/clay, marly limestone and tufa towards the basin center. These lithologic characteristics and fossil content suggest a shallow lacustrine environment. Intercalation of the fine grained units with conglomerates along the whole sequence indicates lateral transition from fluvial to lacustrine deposition. Therefore, the YKFm comprises facies associations extending from alluvial apron to low sinuosity stream along the basin margin towards the north to lacustrine facies in the central parts of the basin.

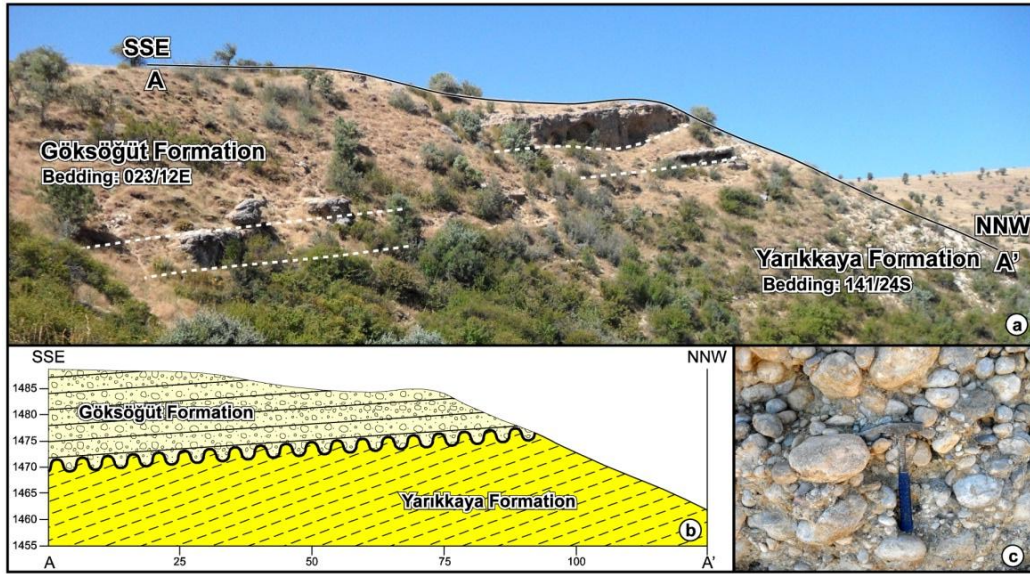


Figure 4.11. General view of the unconformity between Yarıkkaya formation and Göksöğüt formation (a). White dashed line represents the bed surfaces. Black solid line indicates line of the cross-section which is given in (b). Close-up view of the Göksöğüt formation is given in (c).

4.1.3 Göksöğüt Formation (GSFm)

The Göksöğüt formation (GSFm) is generally composed of banded, highly porous brownish limestone at the bottom, it become coarser upwards and grades into rounded, poorly sorted, grain-supported conglomerate. The formation grades laterally, from north to south, into black sandstone and algal limestone. This unit was named first by Demirkol (1982) who suggested that GSFm is conformably overlain by the YKFm. Later, updated stratigraphic order of the basin fill was constructed by Yağmurlu (1991a). The formation is well-exposed north of Körküler and around Ayvalı where the type locality of for the GSFm (Figure 4.12) is located. It progressively overlies the YKFm, and it is unconformably overlain by the Kırkbaş formation.

Based on the geometry of the bedding, the section measuring was performed in three locations north of the Körküler in order to include maximum possible extend of the sequence (Figure 4.12). The oldest observable unit of the sequence starts with banded, highly porous, buff to brownish limestone (Figure 4.6f) (Section 2 in Figure 4.12), intercalated with rounded, unsorted, pebble to cobble-sized (up to 7 cm diameter), matrix-supported conglomerates and coarse sandstones with floating pebbles. Clasts of the conglomerates consist mostly of limestones (>95%) and are set in a carbonate matrix such that differentiation of the clasts from the matrix is almost impossible at first glance; they appear like massive limestone in the outcrop. This oldest part of the unit is approximately 45 m thick. The sequence continues upwards with angular to rounded, unsorted, thick bedded, grain-supported conglomerates (Figure 4.6g and Figure 4.10c) (Section 1 in Figure 4.12). Clasts of the conglomerates at this level range from pebble to block sized (occasionally up to 1 m of the long block axis) and consist of light to dark grey limestone (>95%) and occasionally green metamorphic rocks. The arrangement of the clasts is generally chaotic, but at some levels grain size gradually decreases from bottom to top suggestive of gradual decrease in transport energy. Sedimentary structures such as pebble imbrications, cross-bedding, channels and erosion surfaces at the base of the bedforms (scour-and-fill structures) are commonly observed at some levels of the sequence. Around Ayvalı, these conglomeratic units laterally become finer grained and grades into sandstone and limestone alternations (Section 3 in Figure 4.12). The sandstones at this level are dark colored to black (Figure 4.6h) and consist of lithic fragments including carbonates and greenish/reddish metamorphic rocks and pebble-sized (less than 4 cm) clasts are dispersed in a poorly sorted sandstone indicating that they are litharenites. Primary sedimentary structures like cross-bedding and grading within beds occasionally observed in this part of the section. Limestones alternating with sandstone are light brownish, usually porous and banded, but at some levels they are buff, massive and well-cemented. The limestones are medium to thick (up to 60 cm) bedded. The minimum thickness of the GSFm measured to be 155 m (Figure 4.12).

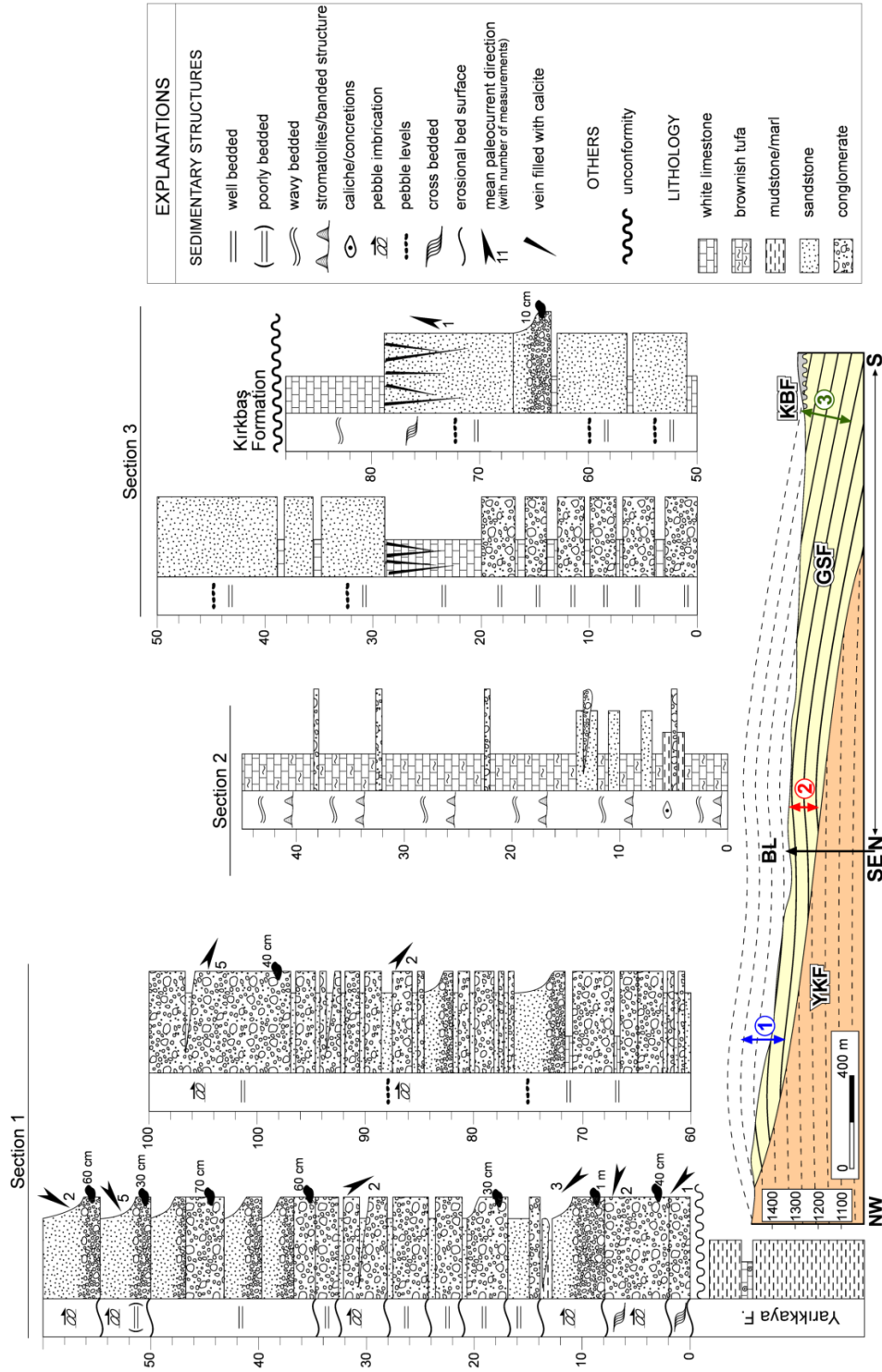


Figure 4.12. The measured section of the Gökösögüt formation and the location of the sections over the cross-section.

From north to south, there is a gradual decrease in grain size and facies from conglomerate to creamy white marly limestone with organic rich levels. The thickness of this marly limestone unit is about 45 m in the north, whilst it reaches 200 m in the south.

It is not observed any fossils in the conglomeratic unit of the GSFm. However, fresh water gastropods in the marl and claystone levels of the GSFm, including *Planorbis sp.* and *Limnea sp.* are encountered. In addition Yağmurlu (1991a) also reported such fossil assemblages in this part of the GSFm, but argued that these fossils are endemic and are not suitable for dating and are subject to large uncertainties. Late Miocene age is assigned for GSFm in this study, based on its stratigraphic relationships with other units. This time interval also encompasses the uncertainties related to the encountered endemic fauna.

Rounded, unsorted and grain supported conglomerates indicate that the GSFm was deposited in alluvial fan to low sinuosity fluvial environment. When the block size (approximately 1 m) is taken into account, they are formed in alluvial fans and debris flow environments. Alternation of these conglomerates with laminated, highly porous, buff to brownish algal limestone in the northern part of the basin indicates a shallow water environment in a lacustrine part of the basin. From the northern margin towards the south through the basin center, decrease in particle size and change in the facies into white, marly limestone with fresh water gastropods indicates a facies belt ranging from alluvial fan to lacustrine environment.

4.1.4 Kırkbaşı Formation (KBFm)

The KBFm consists of reddish poorly consolidated conglomerate, sandstone and mudstone alternation. The formation has a widespread distribution in the basin. It is included in Alluvium unit by Demirkol (1982), and Yağmurlu (1991a) who named this unit as Kırkbaşı formation. The KBFm unconformably overlies the Göksöğüt formation and older units and overlain by Quaternary alluvium. It is well exposed east of Terziler and around Kırkbaşı in the western part of the basin.

The formation is dominated by partly consolidated, poorly-sorted and polymict, angular to sub-rounded, pebble to boulder size clasts (< 30 cm), matrix supported reddish conglomerates (Figure 4.6j). Clasts are composed of mostly milky-white and grey limestones from the basement, but which also include creamy-white to gray lacustrine limestones originated from Neogene units of the basin. Another common facies within this unit comprise alternations of sandstone, siltstone and mudstone with floating pebbles (Figure 4.6i). Stratification is not well developed within the unit. However, well-developed carbonate concretions in the red mudstones at some levels indicate

development of thick soil profile which is probably the main reason for the obliteration of bedding.

From the KBFm around Tokmacık, Yağmurlu (1991a) reported fossil vertebrates including *Hipparion sp.* and *Mastodon sp.* collected from a red conglomeratic horizon. This assemblage indicates Pliocene age for the formation.

Matrix supported, unsorted and pebble to boulder-sized reddish conglomerates with angular clasts indicates that the Kırkbaş formation was deposited in a fluvial environment including alluvial fans and debris flows.

4.2 Structural Geology

This section focuses on the detailed description and analysis of the geological structures that developed and deformed the Yalvaç Basin. The section also comprises analysis of remotely sensed data that include lineaments, means of lithological discrimination, and geomorphologic characteristics, as well as analysis of fault geometries and patterns in their spatio-temporal context based on remote sensing data are given in this part of the chapter. In this regard analysis of field observations and results of kinematic data collected from both macroscopic and mesoscopic structures are also provided.

4.2.1 Lineament Analysis from Remotely Sensed Data

Lineaments originate from two types of sources. Firstly, lineaments may form due to tectonic activity and this type of lineaments generally corresponds to faults, joints and/or lithological boundaries. The other type of lineaments is due to man-made features including roads, railroads, crop field boundaries or any kind of variations in land use patterns. First type of lineaments, occurred by the tectonic activity, is the main concern of geologic studies.

Delineation of the lineaments from remotely sensed data is a complex process and includes some uncertainties related to spatial resolution and spectral characteristics of the used images. Various enhancement techniques may help to reduce some uncertainties by improving the visual interpretability of an image (Lillesand and Keifer, 1999). In this study, some enhancement techniques including contrast enhancement, color composite, principal component analysis (PCA) and decorrelation stretching (DS) are used. For this purpose, Landsat ETM⁺, Advanced Spaceborne Thermal Emission and Reflection Radiometer (ASTER), aerial photographs and Quickbird images obtained from the Google Earth were used to improve delineation and characterizing the lineaments in the study area. All these data have different spatial and spectral resolution,

which might be effective for determination of structures in various scales. In order to aid lineament extraction studies additionally 25*25 resolution digital elevation models (DEM's) prepared from 1/25.000 scale topographic maps were also used to improve 3D visualization in different directions.

Lineament extraction process was performed manually on the images since expert perception can easily interpret geospatial signatures and discriminate them. Resultant lineament maps of Yalvaç region is given in Figure 4.13 together with length weighted rose diagram of the extracted lineaments. The map includes both discriminated faults, based on field observations and literature data and also lineaments extracted during this study. The rose diagram (Figure 4.13) including both faults and lineaments shows two dominant directions in NE-SW (N45°-55°E) and NW-SE (N35°-45°W). These two directions are approximately perpendicular to each other. This implies that the tectonics of the area has been controlled by two major orthogonal zones of weakness.

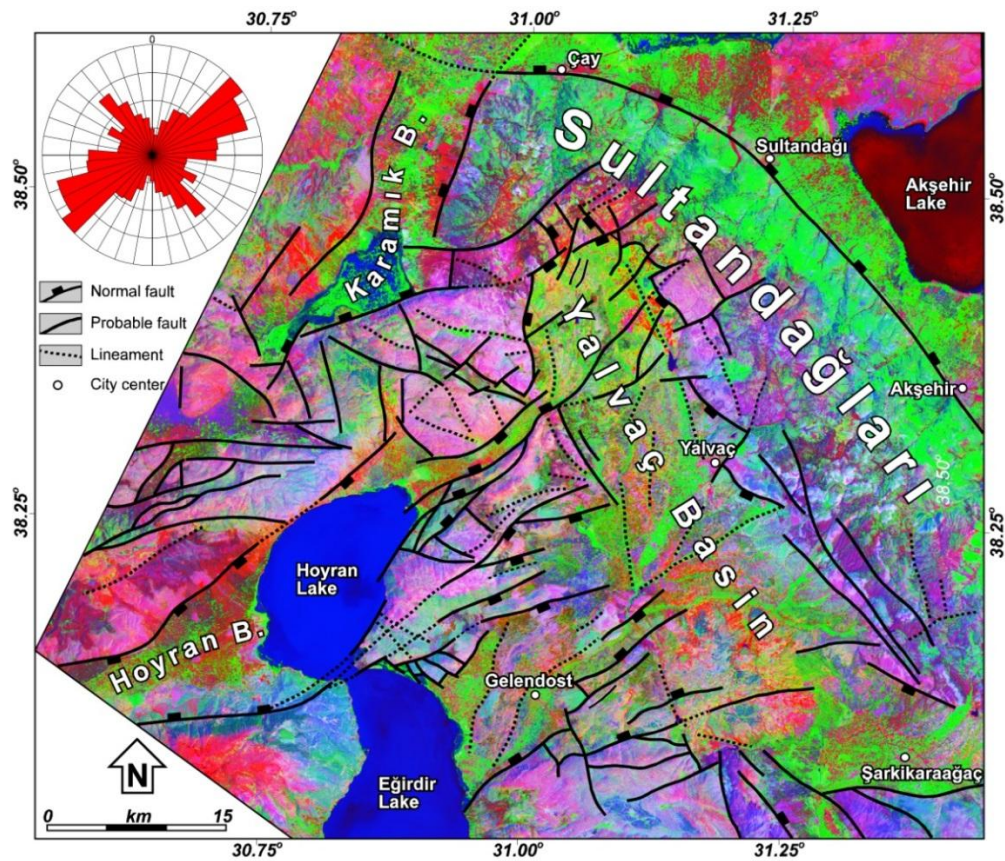


Figure 4.13. Structural map of the Yalvaç Basin, indicating faults and lineaments. Rose diagram (length weighted) is prepared from both discriminated faults and lineaments. Background image is shaded relief of DEM with 25*25 grid spacing.

4.2.2 Field Observation

The Yalvaç Basin is a 15 km wide, 55km long, NNW-SSE trending intra-montane basin (Figures 4.2 and 4.13). The major structures that shaped the Yalvaç Basin are normal faults (Figure 4.14). Morphologically, they are generally recognized at the boundary of the basin infill and basement rock as linear to curvilinear sharp contacts and juxtaposition. In addition, numerous mesoscopic faults which developed during and after sedimentation were also encountered and data about them are recognized and measured during the field studies.

4.2.2.1 Faults

Based on the field studies, morphological evidence obtained from the remotely sensed data and statistical analysis of the lineaments, two major trends are identified: 1) ENE-WSW striking faults and 2) NNW-SSE striking faults. All of these faults are normal faults with minor sinistral and dextral strike-slip components.

4.2.2.1.1 Yarikkaya Fault Zone (YFZ)

Yarikkaya Fault Zone (YKFZ) is oriented ENE-WSW and approximately 7-8 km long. Morphologically, it is the most prominent fault zone in the study area. and it consists of three segments. It is recognized as a linear mountain front rising steeply in the north of the Yarikkaya (Figure 4.15). The main fault plane dips south and ranges between 60° and 90° depending on the curvature of the fault plane. It controls the northern margin of the basin and it juxtaposes the Miocene Yarikkaya formation and basement units (Figure 4.15). Within 5-6 km from the Yarikkaya to the north, a south facing step-like morphology is very prominent. These steps are parallel to the YKFZ and are developed within the basement rocks, implying that these steps are resulted from the secondary faults of the YKFZ. Morphologically, the western continuation of the YKFZ is traceable on aerial photographs and satellite images, which was named as Karacaören Fault by Çiçek and Koçyiğit (2009) and it controls the south-eastern margin of the Quaternary Karamık graben, however, the dip direction of this segment is opposite direction (northwards) indicating that it cannot be the western continuation of YKFZ. In the east the fault dies out within the Sultandağları.

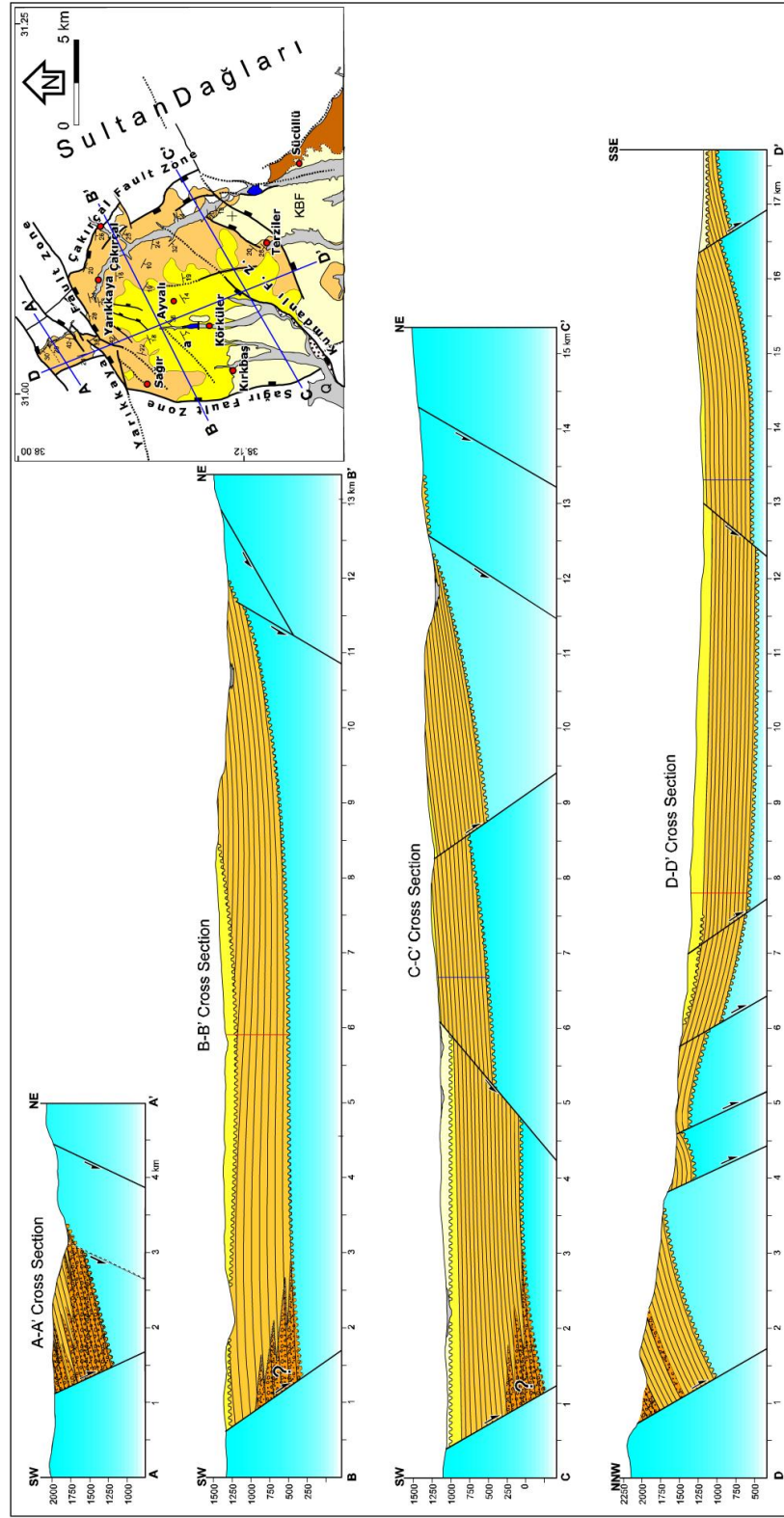


Figure 4.14. Structural cross-sections produced from the geological map. Inset map shows the locations of the sections.

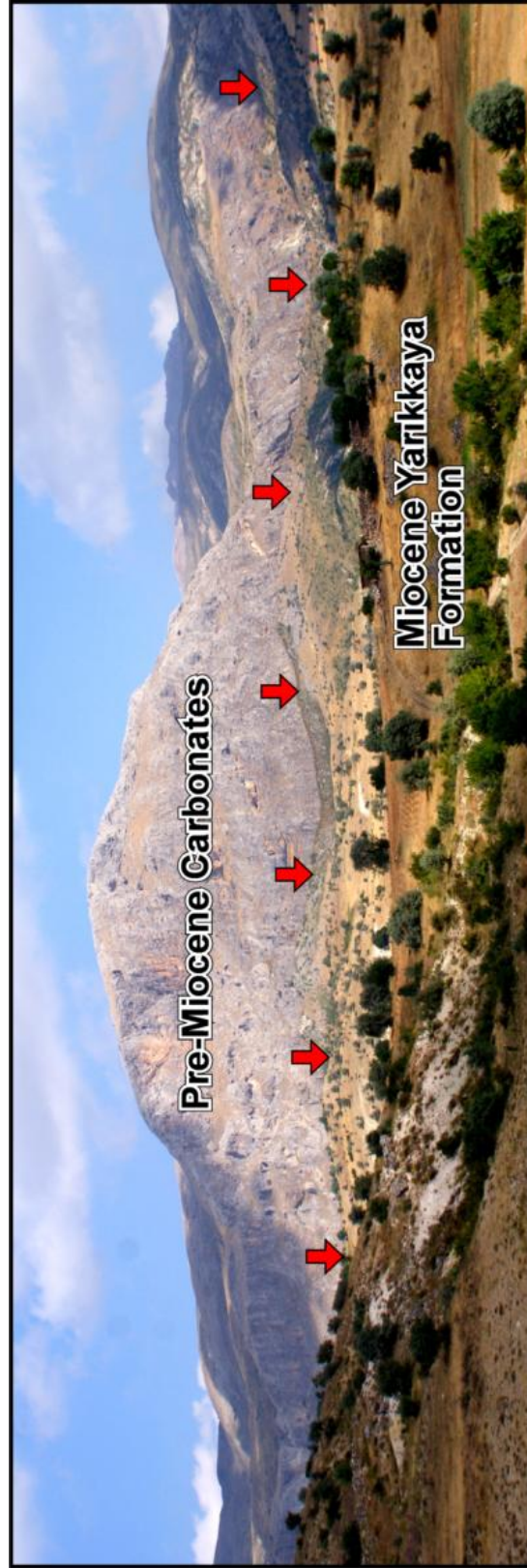


Figure 4.15. General view of the western segment of the Yarikkaya Fault Zone (view to NE). Vertical red arrows indicate the trace of the fault.

It is observed that recent activity of the Yanikkaya Fault Zone produced a hanging valley on the footwall side of Yanikkaya Fault (Figure 4.16). Hanging valleys along the YKFZ were determined from stream profiles which were extracted from the Digital Elevation Model (DEM) which are produced from the 1/25000 scale topographic map by applying watershed algorithm. Produced stream profiles are identified in Figure 4.16 and they are highlighted by red color solid lines on the DEM image. Among them, the stream profile 3 shows the high elevation difference along the waterway.

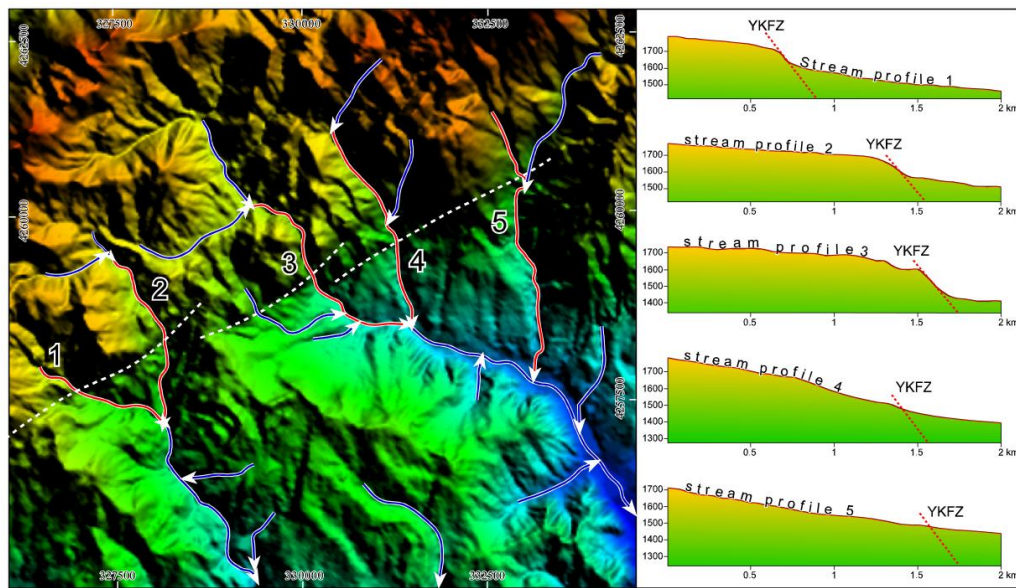


Figure 4.16. Hanging valleys along the YKFZ (dashed lines) overlaid on DEM (25*25 grid spacing). Red and blue lines with arrows indicate streams and their flow directions. Red lines refer to analyzed profiles. Note sharp change in topography (knick points) on the profiles along the YFZ.

The sudden break in slope, the steeply sloping fault scarp, hanging valleys, juxtaposed different lithologies and well-developed slickensides are used as criteria for the definition of the YKFZ. Based on fault slip data collected from the YKFZ the orientation of the principal paleo-stress and the stress ratio are as follows: $\sigma_1 = 350^\circ\text{N}/79^\circ$, $\sigma_2 = 216^\circ\text{N}/08^\circ$, $\sigma_3 = 125^\circ\text{N}/08^\circ$ and $\Phi = 0.177$ (Figure 4.17), consistent with extensional deformation.

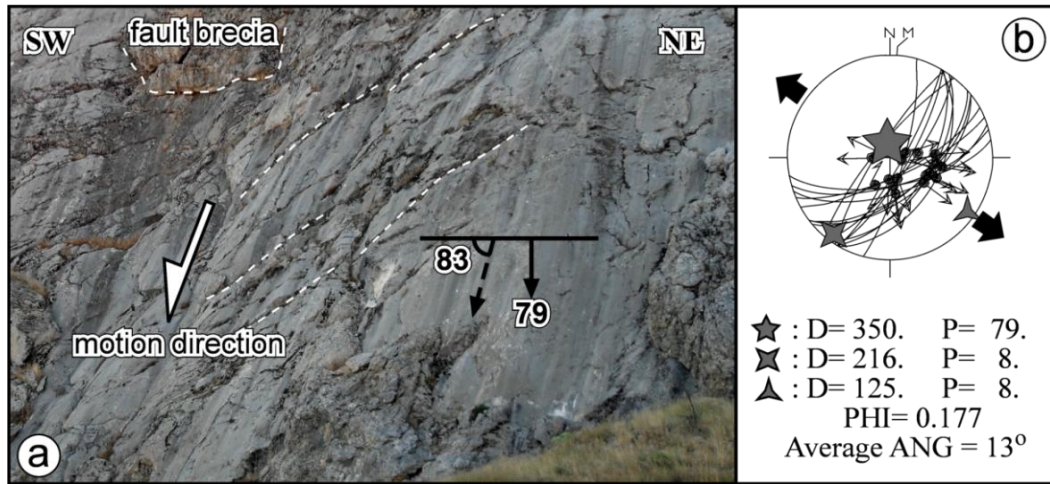


Figure 4.17. a) Fault plane of YKFZ and b) constructed paleostress configuration based on the collected slickensides from the YKFZ (equal area, lower hemisphere projection). White dash lines show the Reidel faults on the fault surface and indicate the movement direction of the hanging-wall block.

4.2.2.1.1.1 Yarikkaya Relay Ramp (YRR)

A relay ramp is defined as a transfer zone located between two overstepping segments of a normal fault zone (Larsen, 1988; Peacock and Sanderson, 1991 and 1994). One of the ways of linkage of different segments of YKFZ takes place as relay ramps which are fully developed between the western and the central segments of the YKFZ (Figure 4.18). These segments dip in the same direction and the displacement along the faults is transferred from one segment to another through a relay ramp. The overlap zone between the bounding segments ranges approximately 1 km in length (overlapping) and 600 m in width (separation) (Figure 4.18b). For full account of relay ramps we refer to Gibbs (1984), Peacock and Sanderson (1994), Trudgill and Cartwright (1994), Çiftçi and Bozkurt (2007).

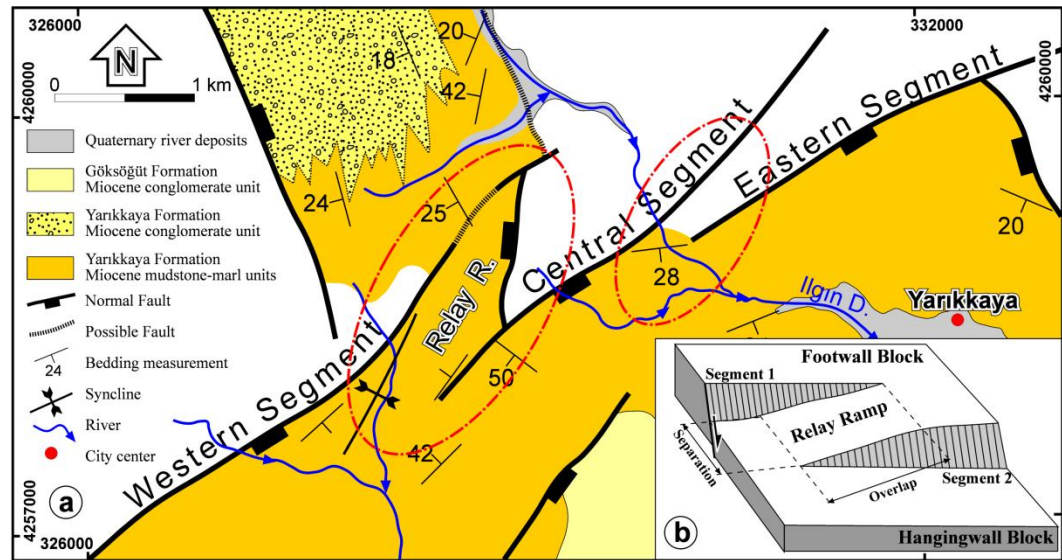


Figure 4.18. a) Map view of the Yarikkaya fault segments and relay ramps between them. b) Schematic block diagram of a typical relay ramp between two overstepping segments of a normal fault zone (adopted from the Çiftçi and Bozkurt (2007)).

4.2.2.1.2 Çakırçal Fault Zone (ÇFZ)

Çakırçal Fault Zone (ÇFZ) is more than 15 km long. It consists of three different segments, recognized from juxtaposition of the basin infill and the basement rock in the north of Çakırçal to Sücüllü along N-S zone. The main fault surfaces are observed to the north of Çakırçal and display a westerly dipping normal fault (Figure 4.19). The dip of the fault surface ranges from 20° to 60° in the northern segment of the fault; however in the southern segment it ranges between 60° and 85°. It controls the eastern boundary of the basin and separates Miocene basin infill from the pre-Neogene carbonates and low-grade metamorphic unit of the Sultandağları Mountains (Figures 4.19 and 4.20). It shows a westerly facing step-like geometry, which is obvious in the vicinity of Çamharman. Fault segments are linked by E-W trending transverse faults (Figure 4.21). The northern continuation of the ÇFZ is cut and displaced by the eastern segment of the YKFZ indicating that it is older than YKFZ. The southern continuation of the fault is difficult to follow on the topography.

The ÇFZ is recognized in the field by sudden changes in vegetation (Figure 4.19) along the fault trace and juxtaposition of different lithologies. Slickensided surfaces were observed within the fault zone and fault-slip data were collected from the several locations (see section 3.3). The kinematic indicators in the fault zone indicate that the ÇFZ is a normal fault.



Figure 4.19. Çakırçal Fault Zone between Yarikkaya formation and Pre-Neogene basement. Note the change in the thickness of the Yarikkaya formation.



Figure 4.20. General view of the central segment of the Çakırçal Fault Zone (view to NE). Vertical red arrows indicate the trace of the fault.

The reconstructed orientation of the principal paleo-stress and the stress ratio based on fault slip data are as follows: $\sigma_1=214^\circ\text{N}/75^\circ$, $\sigma_2=012^\circ\text{N}/14^\circ$, $\sigma_3=103^\circ\text{N}/06^\circ$ and $\Phi=0.219$ (Figure 4.21b). This stress configuration indicates E-W extensional deformation. However, an approximately E-W striking fault segment within the ÇFZ is also observed. The pitch of slickensides on this fault plane indicates that it is dominantly strike-slip in character (Figure 4.21a). The constructed stress configuration is in agreement with this fault. Therefore, it is deduced that this segment is one of the transfer faults of the ÇFZ.

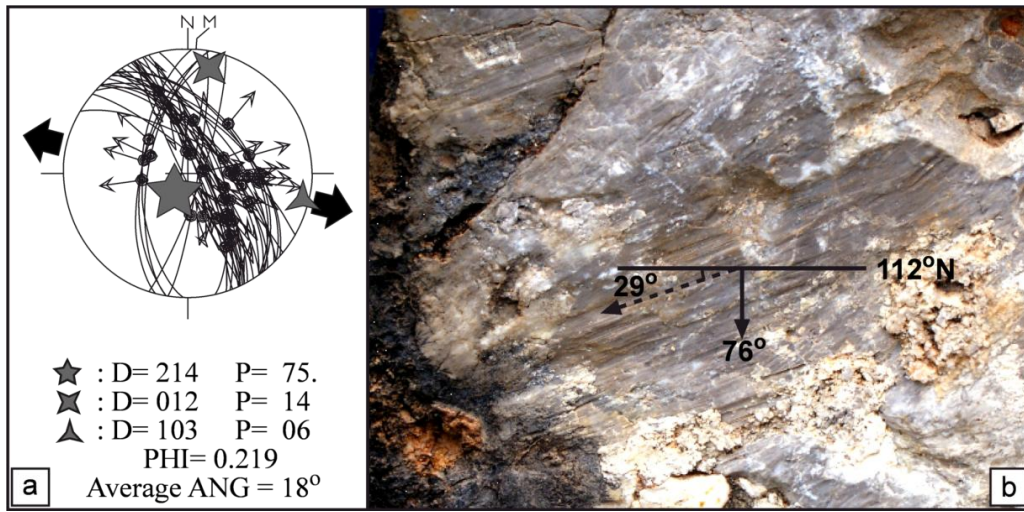


Figure 4.21. a) Configuration of reconstructed paleostress orientations (equal area, lower hemisphere projection) b) close-up view of slickensides one of the E-W striking segments of ÇFZ around Sücüllü (view to north). Note low pitch of the slickensides (29°W).

4.2.2.1.3 Sağır Fault Zone (SFZ)

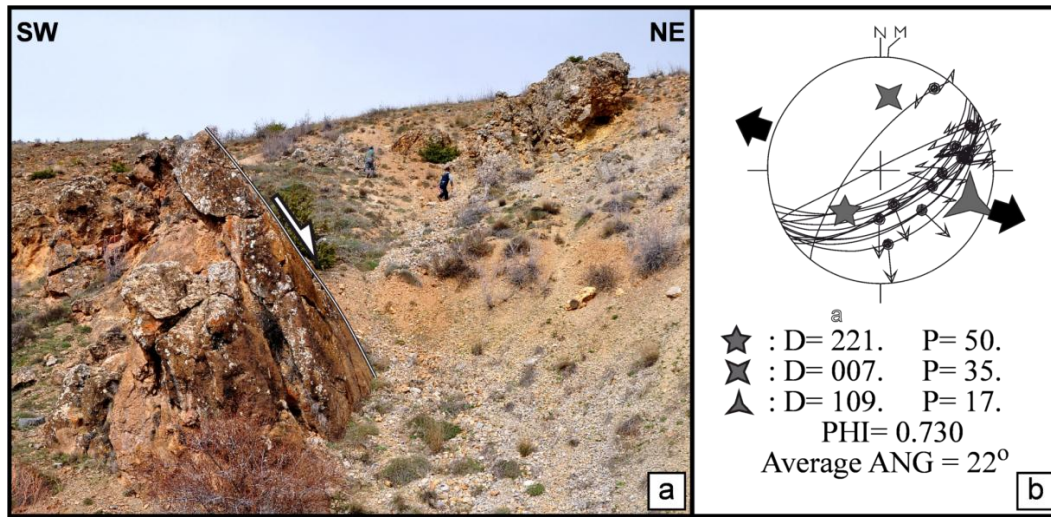
The Sağır Fault Zone (SFZ) is more than 18 km long and is recognized as a NNE-SSW oriented, linear valley to the west of Sağır. It continues to the north along a NNE-SSW oriented linear mountain front rising gently to the west of Kırkbaş. The main fault is an easterly dipping normal fault plane and the dip of the fault surface ranges between 50° and 75° depending on the along strike curvature of the fault plane (Figure 4.22). It delimits the western margin of the basin and separates basin infill from basement carbonate units. Morphologically, the southern continuation of the SFZ can be traced on aerial photographs and satellite images up to the vicinity of Eyüpler. It is cut by Yarıkkaya Fault Zone (YKFZ) in the north and is also cut by NE-SW striking



Figure 4.22. General view of Sağır Fault Zone (view to west). White dash line indicates the trace of the fault.

Kumdanlı Fault Zone (KFZ) in the south. According to these cross-cutting relationships, the SFZ must be older than both YKFZ and KFZ.

The sudden break in slope and the juxtaposition of different lithologies are used as criteria for the recognition of the SFZ. At some localities along the SFZ, slickensided surfaces were occasionally observed and from these localities fault slip data were collected. The collected fault-slip data were analyzed using direct inversion routine (INVD) of Angelier's stress tensor (TECTOR) program. The obtained paleostress configurations indicate that SFZ is dominated by normal faulting and developed under approximately E-W extensional strain (Figures 4.23a and 4.23b).



4.2.2.1.4 Kumdanlı Fault Zone (KFZ)

The Kumdanlı Fault Zone (KFZ) is 20 km long, includes a NE-SW trending normal fault which is defined as an active fault according to MTA (General Directorate of Mineral Research and Exploration of Turkey) geologists. It extends from about 2 km south of Mısırlı to the south of Aşağıtirtar and then enters into the Hoyran Lake. It shows a northwesterly facing step-like morphology and the dip of the fault plane ranges between 70° and 88° depending on the along strike curvature of the fault trace. It separates Plio-Quaternary infill of the Hoyran basin from pre-Neogene basement units

in the west. In addition, it also cuts and displaces the infill of the Yalvaç Basin. Morphologically, the north-eastern continuation of the KFZ dies out within the infill of the Yalvaç Basin (Figure 4.24a), whereas the south-western continuation of the fault can be followed on the aerial photographs and satellite images. The direction of the KFZ is compatible with the Fethiye-Burdur Fault Zone (FBFZ) (Dumont et al. 1979). According to this relationship, Karaman (1989) and Yağmurlu (1991) suggested that the KFZ is the northeastern continuation of the FBFZ. The fault zone shows evidence for left-lateral slip between the Çeleptaş and Kumdanlı near the NE Hoyran basin since the Pliocene.

The KFZ is recognized as a NE-SW oriented linear mountain front rising steeply in the north of Aşağıtirtar, as a well-developed fault scarp, is associated with the development of active colluvial wedge, and tectonically juxtaposes older units with younger ones and well-preserved slickensides. The analysis of fault-slip data shows that the KFZ is a normal fault and the orientation of the principal paleo-stress and the stress ratio are as follows: $\sigma_1=093^\circ\text{N}/74^\circ$, $\sigma_2=095^\circ\text{N}/03^\circ$, $\sigma_3=186^\circ\text{N}/16^\circ$ and $\Phi=0.201$ (Figure 4.24b) and indicate approximately E-W extensional strain.



Figure 4.24. a) Field view of the northeastern tip of the Kumdanlı Fault Zone (white dashed line). Note colluvial wedge, unconsolidated sediment accumulated at the break of the steep slope. b) KFZ delimits the southeastern boundary of the Plio-Quaternary Hoyran basin. c) Configuration of paleostress orientations based on fault slip data collected from KFZ around Aşağıtirtar (equal area, lower hemisphere projection).

4.2.2.1.5 Yaka Fault Zone (YAFZ)

The Yaka Fault Zone (YAFZ) (Figure 4.25a) is an about 6 km wide and more than 20 km long, nearly NE-SW trending normal fault zones (Figure 4.25c). The southwestern tip of the fault is located to the north of Hacilar and it extends to the southeastern part of Madenli. The dip of the fault surface ranges between 45° and 70°. It controls the southern margin of the basin and it separates the Miocene Yarikkaya formation from carbonate basement units. Within 5-6 km from Bağlılı to the southeast of Balçı, the YAFZ shows a step-like morphology facing the basin. Following a southeastern step, the YAFZ was named as the Balkı Fault by Yağmurlu (1991a, 1991b), whereas, it was evaluated as a part of the YAFZ. At some places, the YAFZ is cut by NW-SE trending faults.

A sudden break in topography, well-preserved fault scarps (Figure 4.25a and Figure 4.25b) and juxtaposition of basement rock and basin fill is common morpho-tectonic features that are used for the recognition of the YAFZ. Additionally, well-preserved slickensides are also present along the fault zone. Their kinematic analysis was performed and a stereographic plot displays fault-slip data consistent with normal motion. The orientation of the principal stress and the stress ratio are as follows: $\sigma_1=183^\circ\text{N}/83^\circ$, $\sigma_2=043^\circ\text{N}/05^\circ$, $\sigma_3=312^\circ\text{N}/04^\circ$ and $\Phi=0.346$ (Figure 4.25c), indicating the presence of approximately NE-SW extensional deformation.



Figure 4.25. Field view of the eastern tip of the Yaka Fault Zone (YAFZ) (a). Well-developed slickenline on the fault surface (b) and stereographic plot of these slip data on the Schmidt's lower hemisphere net (c).

4.3 Paleostress Analysis

Apart from analysis of major faults, a detailed kinematic analysis from mesoscopic structures is also carried out to unravel paleostress configurations during the development of the Yalvaç Basin. For reconstruction of the paleostress configurations Angelier's direct inversion routine (INVD) is used (Angelier 1994). Detailed description of the stress inversion procedure and methods is discussed previously (see section 2.4.1).

4.3.1 Veins

A number of gash veins (Mode I = Opening Mode fractures) are encountered within the Göksöğüt formation (Figure 4.26a). They are easily recognized by distinct color contrast between the vein-fill and their host rock. The orientation data of these veins indicated that two veins sets exist: 1) a dominant E-W striking set and 2) a subordinate N-S striking set. Most of the E-W striking veins are up to 25 cm thick (Figure 4.26a) but are generally trend of the vein thickness is around 10 cm. N-S striking veins are very thinly developed and maximum vein thickness is around 1-2 cm (Figure 4.26b). Crosscutting relationship between these vein sets suggest that N-S striking veins generally post-date the E-W striking vein set (Figure 4.26b).

The growth pattern of these veins is variable, some veins were developed symmetrically, where the vein growth took place from both walls towards the center and have almost equal thickness. However, most veins show asymmetric growth, such that the thickness of the veins on either side of the vein wall is not equal. Nevertheless, in most of the veins calcite overgrowth pattern and banded structure of the infill calcite are well developed (Figure 4.26a). Where ever observed, the vein filling calcites are roughly equant, and show crystal faces. Occasionally, veins may contain fragments of the host rock (breccia zones) coated with a calcite layer (Figure 4.26b).

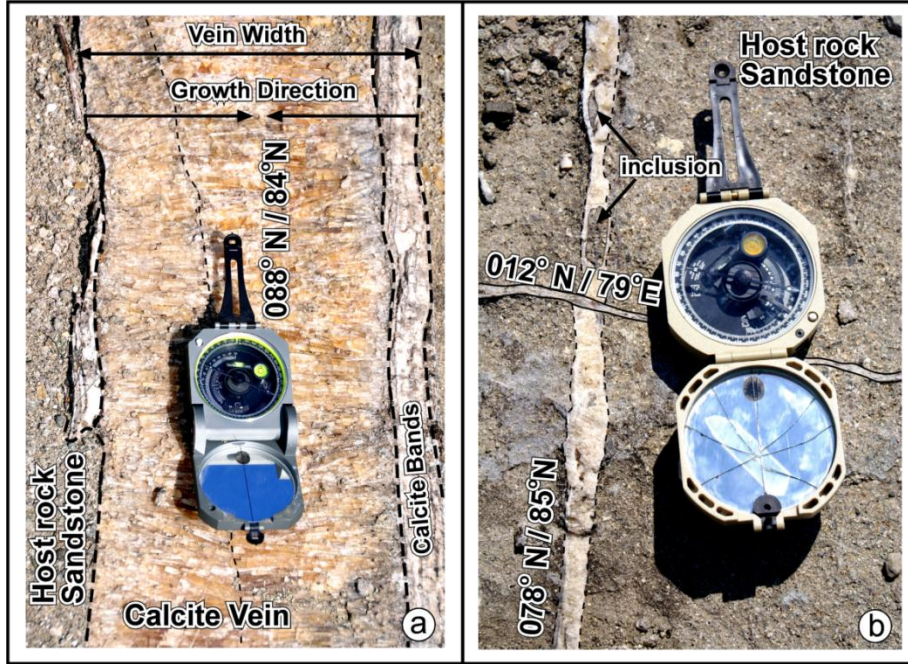


Figure 4.26. Vein formation in the Göksöğüt formation. (a) Approximately E-W striking, syntaxial calcite vein, where crystals grow from the wall rock into the vein. (b) Crosscutting relationship between vein sets. Young vein (approximately N-S striking) cuts through and offsets the older vein (approximately E-W striking).

Based on the assumptions which are explained in previous chapter, 40 vein data collected during field studies is analyzed and used for paleostress inversion. The strikes of the collected veins range between 057°N and 107°N (Figure 4.27a). Best fit great circle (MGC) passing through the poles of the vein planes is found to be $347^{\circ}\text{N}/81^{\circ}\text{E}$. The plane contains σ_1 and σ_3 and is perpendicular to σ_2 . The pole of the plane corresponds to the intermediate principle stress (σ_2). Mean lineation vector (MLV) represents mean vector of the vein poles and corresponds to the minimum effective principal stress (σ_3) (Figure 4.27b). It is found $167^{\circ}\text{N}/04^{\circ}$. Intersection of the mean great circles for the veins and the great circle containing the poles (auxiliary plane) is close to vertical. Knowing that the tectonic regime during the emplacement of these veins was extensional, therefore, this intersection must correspond to the major principal stress (σ_1) which is $045^{\circ}\text{N}/80^{\circ}$. Therefore, the orientation of intermediate stress is 90° apart from (σ_1) along the mean great circle of vein planes and it is $256^{\circ}\text{N}/09^{\circ}$ (σ_2). The horizontal component of σ_3 is approximately N-S (Figure 4.27b) indicating the extension direction was approximately E-W during the emplacement of these veins. The extension direction is compatible with the extension direction inferred from the vein data collected from the Aşağıçiğil formation in the Ilgın Basin (see section 3.4.1 in Chapter 3).

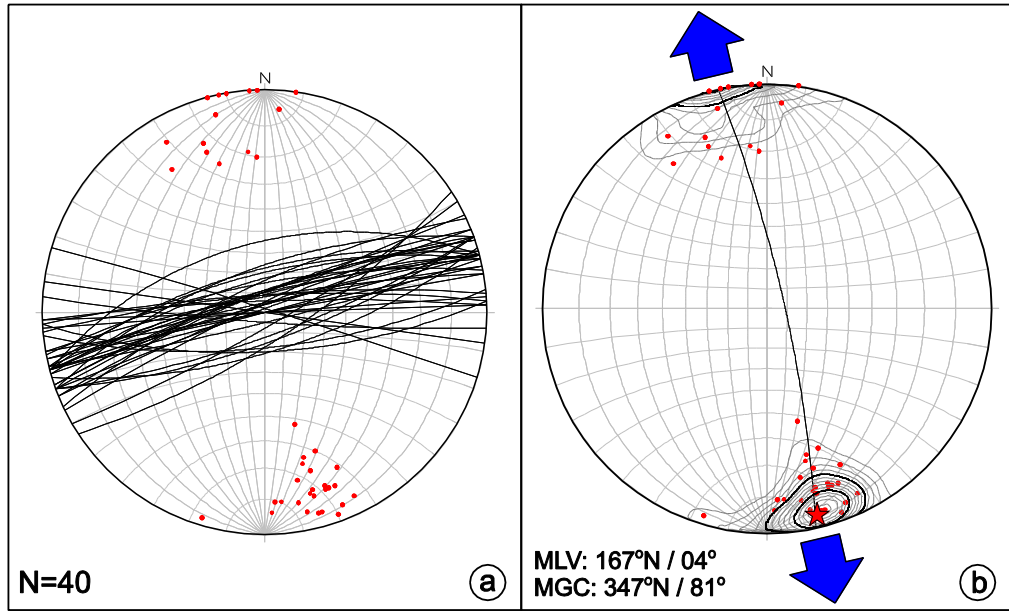


Figure 4.27. a) Stereographic projections of veins and b) contour diagrams of poles to the veins (red dots) and orientation of constructed principal stress directions (equal angle, lower hemisphere projection).

4.3.2 Fault Slip Analysis

From 78 sites, 1304 fault-slip measurements (Figure 4.28 and Table 4.1), including orientation of the containing planes, slip directions and senses of relative movements were collected from mesoscopic faults within the Yalvaç Basin fill and the major faults juxtaposing basement and basin-fill units. The rose diagram prepared from the strikes of the fault planes indicates that they are oriented mainly in NE-SW directions (Figure 4.28a). Dip amounts of the faults are shown in Figure 4.28b range from 15 to 90 degrees. However, the highest dip amount frequency is between 50° and 75°.

Stress inversion was carried out for each site separately and for this purpose 1181 fault slip data have been analyzed using the direct inversion method (INVD) (Angelier, 1994). From 78 sites, 92 stress configurations were constructed (Figure 4.28c and Table 4.2). According to Angelier (1994) a maximum angular deviation (ANG) value smaller than 22.5° is regarded as a good match whereas those between 22.5° – 45° characterize poor match. A value larger than 45° refers to very poor consistency between the measured slip data and the computed stress tensor. In this study, the maximum ANG value was chosen 25° for computation of stress tensors. Faults with greater angular deviations (>45°) were considered as spurious and were not used in the construction of stress tensors. As a result, 122 fault slip measurements were regarded as spurious, corresponding to 9.3% of the data.

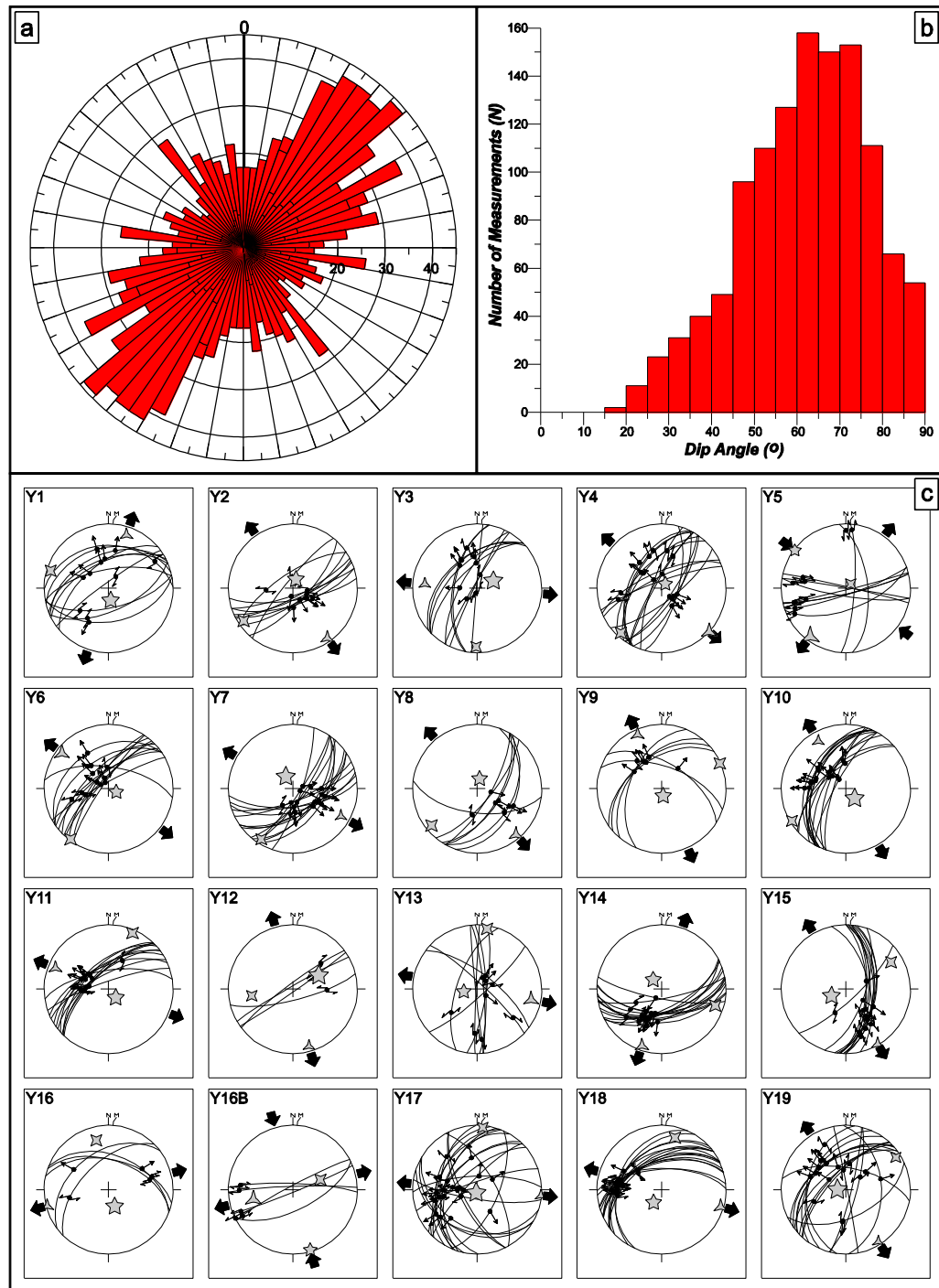


Figure 4.28. (a) Bidirectional rose diagram of all fault strikes. Note that dominant direction is NE-SW. (b) Graph shows the histogram of the fault dip amounts. (c) Stereographic plots of fault planes, slip-lines and constructed paleostress orientations (equal area lower hemisphere projection).

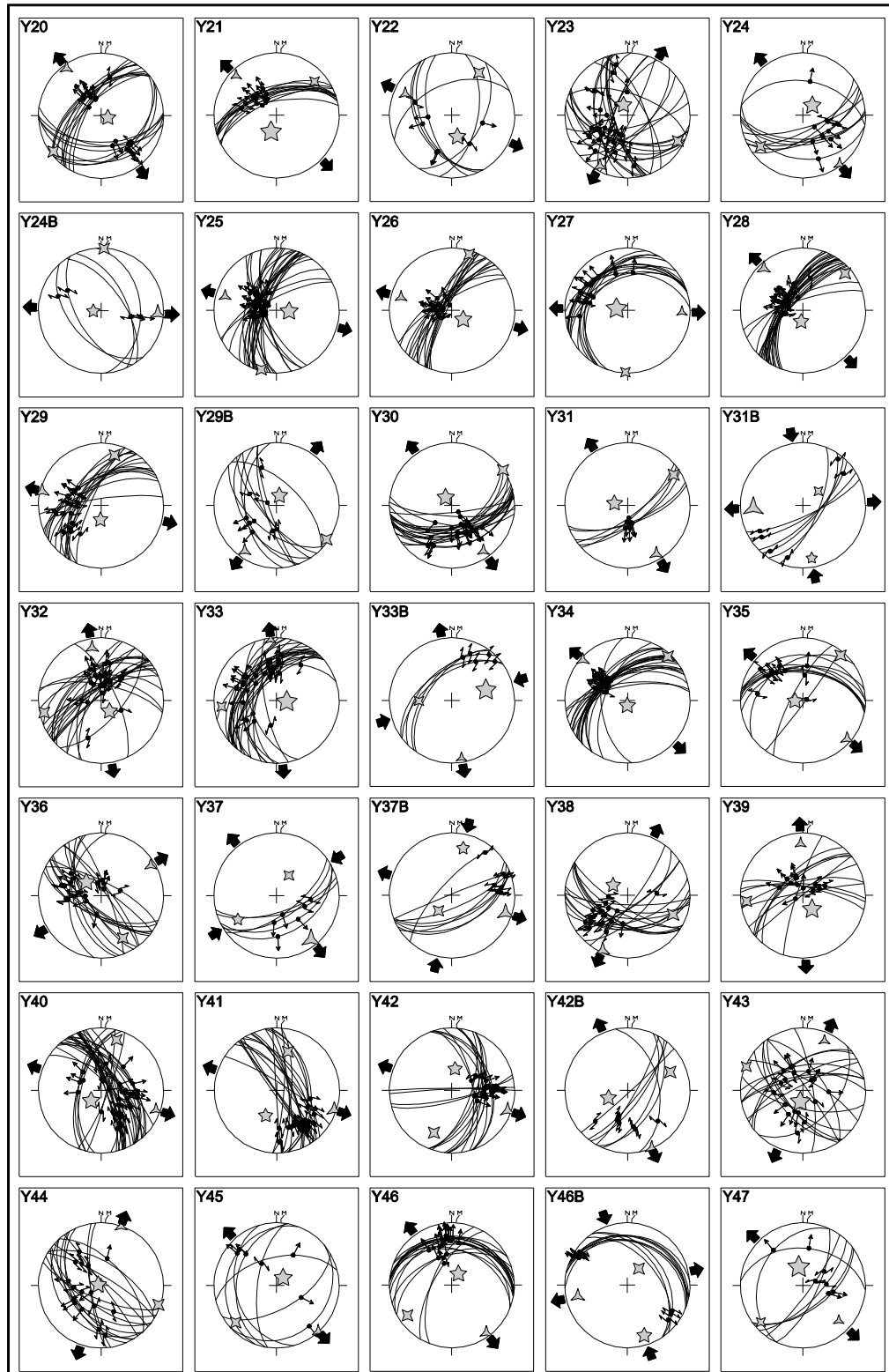


Figure 4.28. Continued

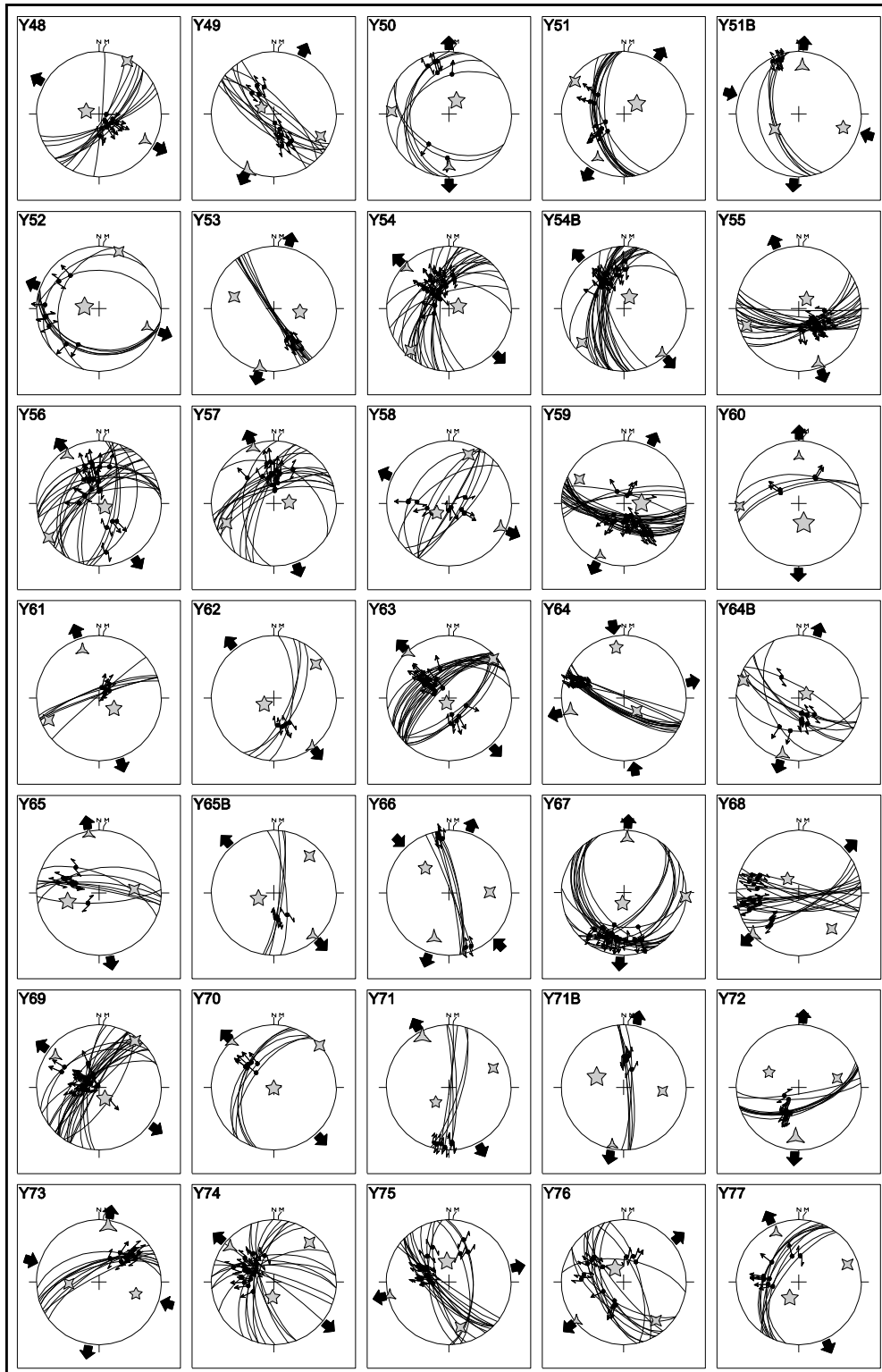


Figure 4.28. Continued

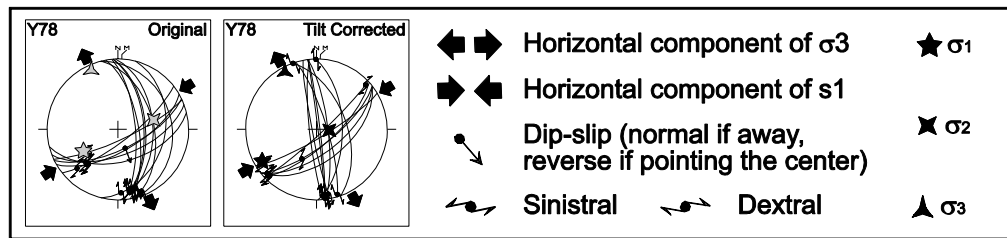


Figure 4.28. Continued

Using the misfit criteria and separation procedure, the sites 16, 31, 33, 42, 46, 51, 64 and 65 produced two different paleostress configurations. The separated configurations are labeled as “B” and resultant stress configurations are depicted in Figure 3.28 and Table 4.1.

In some of the sites overprinting slickensides (Figure 4.29) were encountered. In such sites, each slip direction is analyzed separately and is used for supporting evidence for presence of at least two different deformation phases and reactivation. However, overprinting slickensides are encountered only in (sites 31 and 46) basement rocks. Therefore, it is very difficult to determine the timing of these slickensides and which deformation phase they belong to. Nevertheless, they are used together with other results.

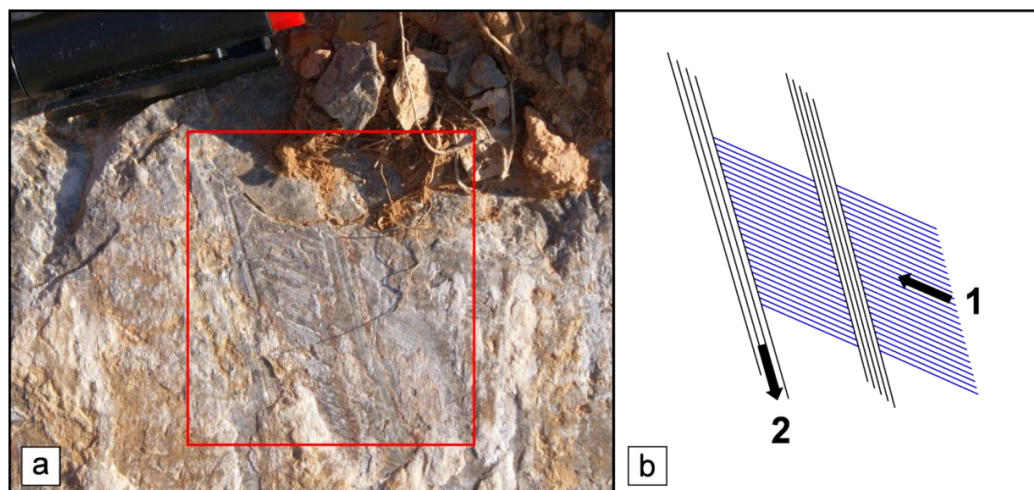


Figure 4.29. a) Close-up view of overprinting slickensides and b) schematic illustration of their order. Numbers indicate the sense of movement (1: dip-slip normal sense, 2: Strike-slip sense)

Table 4.1. Locations and paleostress orientations from Yalvaç Basin.

Loc	Long	Lat	$\sigma_1(P^0/D^0)$	$\sigma_2(P^0/D^0)$	$\sigma_3(P^0/D^0)$	Φ	Mean ANG	Mean RUP	N
Y1	31.13771	38.38782	170/75	287/07	019/14	0.362	14	42	11
Y2	31.05173	38.46330	018/78	236/09	145/07	0.477	11	38	10
Y3	31.03761	38.45680	065/68	181/10	275/20	0.234	15	37	10
Y4	31.03901	38.47502	041/83	222/07	132/00	0.602	14	40	16
Y5	31.03195	38.48403	050/82	307/02	216/08	0.771	11	27	10
Y6	31.03806	38.47789	113/80	217/03	307/10	0.554	10	31	12
Y7	31.03245	38.45948	330/72	212/08	120/15	0.162	12	27	15
Y8	31.10152	38.36944	014/77	231/10	140/08	0.464	10	25	7
Y9	31.10028	38.15304	167/81	067/02	336/09	0.432	9	21	6
Y10	31.09762	38.14761	137/74	239/03	330/16	0.230	8	25	14
Y11	31.04696	38.11092	139/76	023/06	292/12	0.354	9	22	12
Y12	30.98069	38.44016	062/53	261/36	164/09	0.025	29	64	4
Y13	30.99456	38.43732	260/73	009/06	101/16	0.540	23	50	9
Y14	31.04422	38.42888	319/74	107/14	199/08	0.424	6	16	14
Y15	30.98357	38.58922	246/70	059/20	150/02	0.346	17	35	12
Y16	30.95261	38.57671	160/68	346/22	255/02	0.329	11	32	6
Y16B	30.95261	38.57671	070/53	164/03	256/37	0.766	18	63	4
Y17	30.91048	38.44091	198/86	005/04	095/01	0.185	15	39	20
Y18	30.88609	38.42271	212/71	014/18	106/05	0.470	7	17	16
Y19	30.87961	38.42013	271/80	057/09	148/06	0.166	21	43	17
Y20	30.87036	38.41647	105/81	233/06	324/07	0.345	8	17	19
Y21	30.79975	38.38981	199/68	315/10	048/20	0.202	9	20	12
Y22	30.80767	38.39748	166/62	032/20	295/19	0.428	12	44	7
Y23	30.81740	38.39989	339/76	117/11	209/09	0.406	20	46	26
Y24	30.58279	38.14960	043/72	234/17	143/03	0.184	8	23	10
Y24B	30.58279	38.14960	267/80	003/01	093/10	0.660	3	17	5
Y25	30.91619	38.26183	093/74	195/03	286/16	0.201	5	16	27
Y26	30.91792	38.26483	129/71	017/07	285/17	0.206	5	17	17
Y27	30.98231	38.303755	280/76	182/02	092/14	0.103	17	32	14
Y28	30.95462	38.29039	189/75	049/11	317/09	0.407	9	24	23
Y29	30.94765	38.26587	183/72	015/18	284/04	0.540	16	32	17
Y29B	30.94765	38.26587	017/77	124/04	215/13	0.388	18	38	9
Y30	30.93503	38.13651	321/77	055/01	145/13	0.264	13	27	20
Y31	30.86395	38.14495	279/73	057/13	149/11	0.327	3	15	6
Y31B	30.86395	38.14495	047/63	171/16	267/22	0.895	9	31	6
Y32	31.11251	38.11220	142/73	258/08	350/15	0.395	10	27	23
Y33	30.96482	38.05288	096/77	264/13	355/03	0.097	21	39	24
Y33B	30.96482	38.05288	073/43	171/08	269/46	0.456	9	20	5
Y34	30.96522	38.05007	183/83	043/05	312/04	0.346	4	10	22
Y35	30.98866	38.02596	267/80	040/07	131/08	0.433	13	37	11
Y36	31.09925	38.15094	312/64	153/25	059/08	0.231	16	50	17
Y37	31.00132	38.43218	238/28	031/59	142/12	0.597	12	31	6
Y37B	31.00132	38.43218	013/24	221/64	108/11	0.816	9	27	8

Table 4.1. Continued

Loc	Long	Lat	$\sigma_1(P^0/D^0)$	$\sigma_2(P^0/D^0)$	$\sigma_3(P^0/D^0)$	Φ	Mean ANG	Mean RUP	N
Y38	31.03165	38.48628	306/67	112/22	204/05	0.563	15	31	17
Y39	31.05372	38.46439	146/69	264/10	358/18	0.159	10	30	12
Y40	31.16047	38.35874	224/71	017/17	109/08	0.308	15	38	31
Y41	31.16080	38.36128	204/54	016/36	109/04	0.640	8	24	21
Y42	31.14420	38.38292	008/62	203/28	110/06	0.570	11	31	17
Y42B	31.14420	38.38292	249/63	067/27	157/01	0.373	7	28	7
Y43	31.22980	38.25979	194/75	293/02	023/15	0.168	15	43	18
Y44	31.29319	38.22349	282/86	109/04	019/00	0.370	25	51	16
Y45	31.28874	38.22342	041/77	228/13	138/02	0.311	17	37	7
Y46	31.32863	38.15713	030/73	236/15	144/07	0.393	7	23	17
Y46B	31.32863	38.15713	161/17	035/63	258/20	0.503	3	24	10
Y47	31.12237	38.39617	347/65	134/21	229/12	0.136	7	22	7
Y48	31.05158	38.45823	284/73	028/04	119/16	0.339	6	22	11
Y49	31.14262	38.36721	298/72	115/18	205/01	0.786	17	51	11
Y50	31.11767	38.45198	029/70	273/09	180/18	0.361	11	33	7
Y51	31.08758	38.46440	051/69	304/07	211/20	0.435	16	37	11
Y51B	31.08758	38.46440	107/26	238/53	004/24	0.815	3	19	5
Y52	31.08700	38.46478	278/71	019/04	111/19	0.308	20	39	8
Y53	31.08590	38.46465	097/55	287/34	194/05	0.465	5	21	8
Y54	31.04024	38.46373	075/78	223/11	314/07	0.338	13	28	21
Y54B	31.04024	38.46373	026/73	231/15	139/07	0.342	8	23	21
Y55	31.04049	38.46835	038/74	252/13	160/09	0.470	7	18	22
Y56	31.04261	38.46814	122/81	236/04	327/08	0.429	13	32	22
Y57	31.04261	38.46814	085/70	248/19	340/06	0.480	8	23	16
Y58	31.04259	38.46911	233/70	022/17	115/10	0.532	9	39	9
Y59	31.24080	38.27233	090/67	299/20	205/10	0.132	16	43	26
Y60	31.21275	38.16514	166/64	000/26	267/06	0.178	14	32	4
Y61	31.03743	38.48212	125/66	246/13	341/20	0.174	5	22	6
Y62	31.03293	38.48301	237/75	051/15	142/02	0.358	1	13	4
Y63	31.22607	38.25913	206/83	048/07	318/03	0.466	6	21	23
Y64	31.14301	38.36819	351/19	135/66	257/13	0.776	6	15	15
Y64B	31.14301	38.36819	061/79	287/08	196/08	0.592	8	28	8
Y65	31.11001	38.45832	255/47	350/05	085/43	0.306	15	35	8
Y65B	31.11001	38.45832	250/69	044/19	137/09	0.367	3	22	4
Y66	31.11613	38.45385	316/44	089/35	198/25	0.551	6	31	6
Y67	31.11763	38.45219	187/76	094/01	003/14	0.466	11	25	20
Y68	31.03185	38.48398	048/02	138/24	314/66	0.386	12	38	17
Y69	31.03806	38.47789	152/74	038/07	306/15	0.330	9	28	24
Y70	31.04023	38.46365	184/89	048/01	318/01	0.393	4	11	6
Y71	31.08752	38.46455	222/64	067/24	332/10	0.711	7	28	11
Y71B	31.08752	38.46455	291/52	096/37	191/08	0.353	9	25	
Y72	31.04509	38.43022	077/37	297/45	184/21	0.977	5	16	9
Y73	31.09907	38.15264	107/38	267/50	009/10	0.896	6	14	10
Y74	31.09888	38.15169	185/70	042/16	309/11	0.479	14	39	17

Table 4.1. Continued

Loc	Long	Lat	$\sigma_1(P^0/D^0)$	$\sigma_2(P^0/D^0)$	$\sigma_3(P^0/D^0)$	Φ	Mean ANG	Mean RUP	N
Y75	31.09896	38.15155	355/63	165/27	257/04	0.152	11	29	17
Y76	31.09926	38.15096	328/69	140/21	231/03	0.199	20	47	13
Y77	31.09750	38.14603	209/66	070/18	335/14	0.397	13	37	9
Y78O	31.03101	38.48634	238/42	075/47	336/09	0.337	17	49	13
Y78TC	31.03101	38.48634	234/17	104/65	330/18	0.570	17	46	13

σ_1 , σ_2 , σ_3 major, intermediate, and minor principle stresses, D/P: direction/plunge, Φ : stress ratio, ANG: maximum allowed angular divergence, RUP: maximum allowed quality estimator, N: number of measurement for each site.

During the field studies, syn-sedimentary structures were also encountered (Figure 4.30). These structures are very crucial for paleostress stratigraphy. Because the age of the host units in such sites directly corresponds to the maximum age of the constructed paleostress configurations for that particular site. In site 78 (Figure 4.30), which is located at the base of the Middle Miocene Yarikkaya formation, syn-sedimentary faults with dextral strike-slip movement (Figure 4.30b) is also encountered. This is the only site with syn-sedimentary faults with strike-slip slickensides; therefore, it is proposed that these faults belong to a transfer zone within the Yarikkaya Fault Zone. Additionally, in site 69, which is located at the base of the Yarikkaya formation, syn-sedimentary normal faults are also recorded (Figure 4.31a and Figure 3.31c). The fault slip data is well-preserved (Figure 4.31b) and the strikes of the fault planes is changing from N-S to NE-SW. The inferred extension direction from the fault slip data collected from the location is NW-SE. The sites 5, 60, 65, 68, 69 and 78 contain such information. In all of these sites major stress is vertical and the orientation of minor stress is variable, almost radial except for N80-90E orientation (Figure 4.31d). This implies that the horizontal components of intermediate and minor stress were not constrained in any direction while major stress was vertical. This indicates stress permutation (Homberg et al. 1997) that is common in uniaxial stress conditions where magnitudes of two principal stresses are equal or close to equal (Kaymakci 2006).

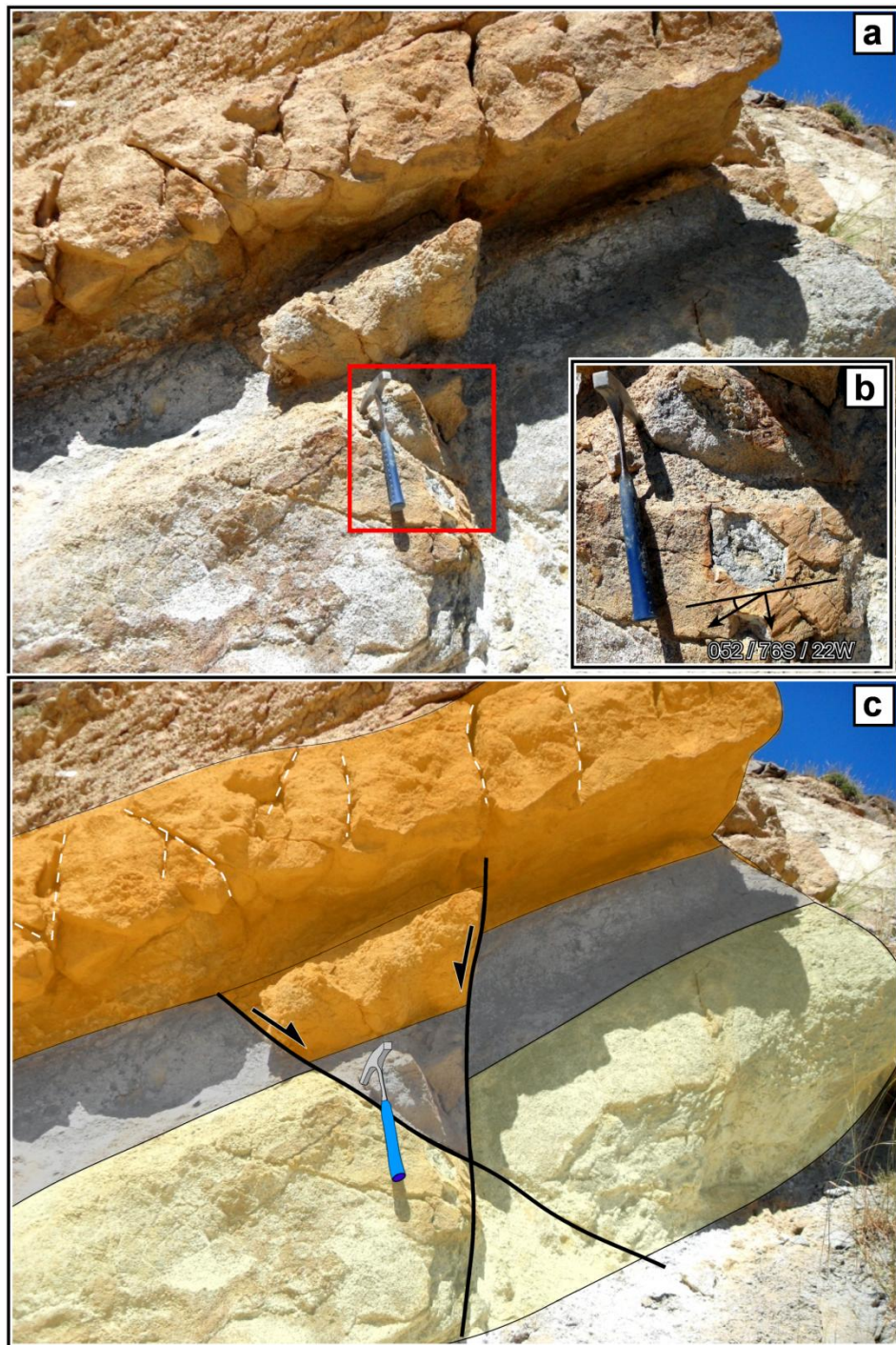


Figure 4.30. a) Syn-sedimentary faults with at the base of the Yarikkaya formation. b) Close up view showing dextral strike-slip slickensides. c) Interpreted image.

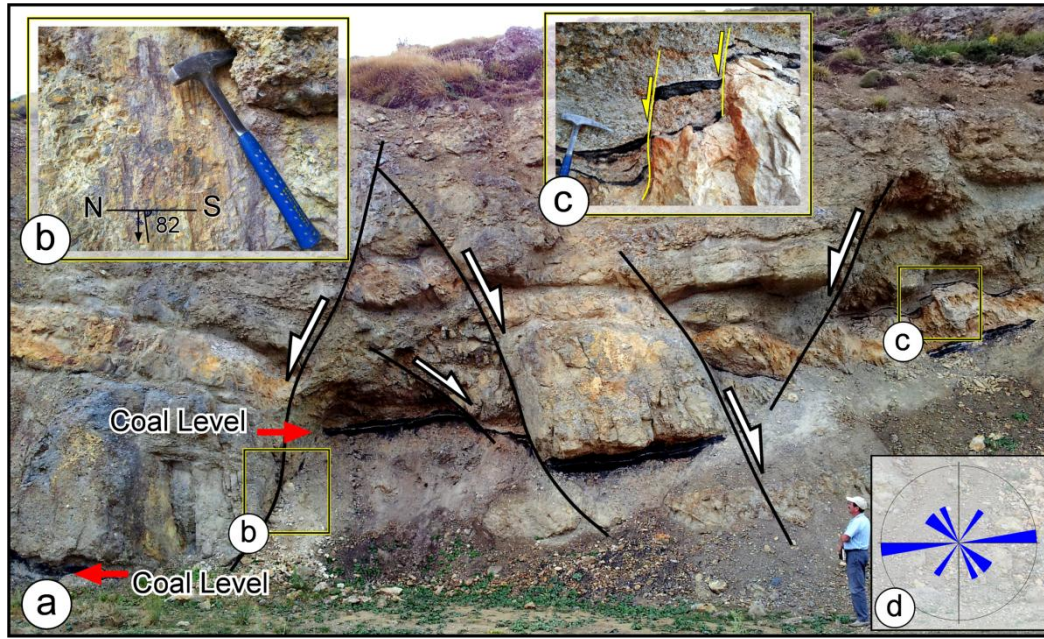


Figure 4.31. a) Syn-sedimentary normal faults with at the base of the Yarikkaya formation, b) close up figure showing slickensides indicate normal sense of movement, c) close-up view of the mesoscopic scale syn-sedimentary normal fault which causes vertical displacement of the coal levels, d) rose diagram shows the direction of the all syn-sedimentary faults, notice that orientation of minor stress is variable.

4.3.3 Spatial Characteristics

Paleostress measurements in the Yalvaç Basin help us to construct which stress regimes prevailed in the region. To this end, detailed analyses of the constructed paleostress orientations were performed and their compatibility with regional structural elements is checked. Figure 4.32 shows the density diagram of principal stress orientations (σ_1 , σ_2 , and σ_3 , respectively) as well as histograms of the ϕ values for the whole data set. Orientations of σ_1 are generally (sub-)vertical in all sites (Figure 4.32a) and are concentrated in the center of the diagram. Stereographic projections of σ_2 and σ_3 orientations show very wide scatter although they are consistently sub-horizontal (Figure 4.32b and c). This scattering may be due to stress permutations or equal or near equal explained by local stress magnitude changes due to complex fault geometry or may be related to a tendency of σ_2 and σ_3 permutation discussed in previous section. Anyways, the tectonic regime controlled the evolution of the Yalvaç Basin was clearly extensional, as evidenced by the vertical orientation of σ_1 , and normal nature of basin bounding faults.

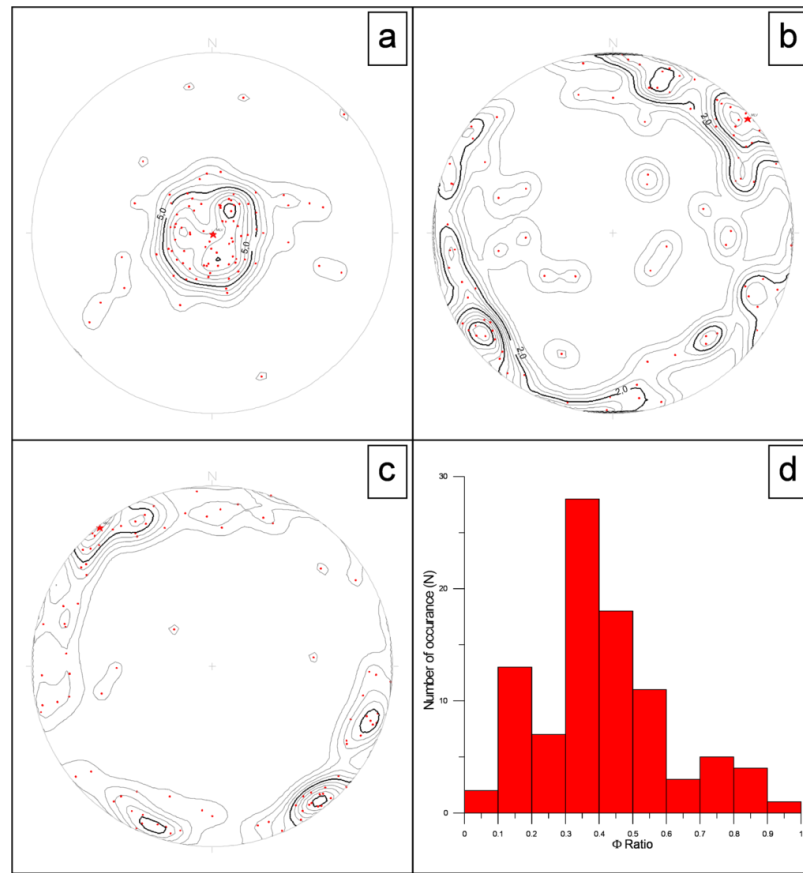


Figure 4.32. Density diagrams (a, b and c) for principle stress orientations (σ_1 , σ_2 and σ_3 , respectively) and frequency distribution of Φ values for whole data (d). Notice that the σ_1 is significantly (sub-)vertical while σ_2 and σ_3 orientations are horizontal.

Horizontal component of the minimum principal stress (σ_3) directions are plotted on the map (Figure 4.33). According to structural studies given in section 3.2, two approximately NE-SW and NW-SE trending major fault sets control the structural framework of the area. Most of the σ_3 directions, including strike-slip solutions (sites 5, 16B, 31B, 33B, 37B, 46B, 51B, 64, 66, 73 and 78), indicate two dominant extension directions (Figure 4.33c). It seems that these directions are controlled mainly by the geometry of associated major faults, rather than regional stress pattern. As seen in Figure 4.33, the orientation of minor stress (σ_3) is almost always perpendicular to the adjacent major fault which is constrained mainly into two directions. Field studies and observed geomorphic features indicate that almost all of these faults are of normal in nature and they have been operated at the same time. This is evidenced by development of normal faults in all directions which implies that major stress was vertical (gravity) and the magnitude of minor and intermediate stresses were almost equal. Therefore, the faults are not constrained in to any direction and the fault blocks moved freely under vertical major stress.

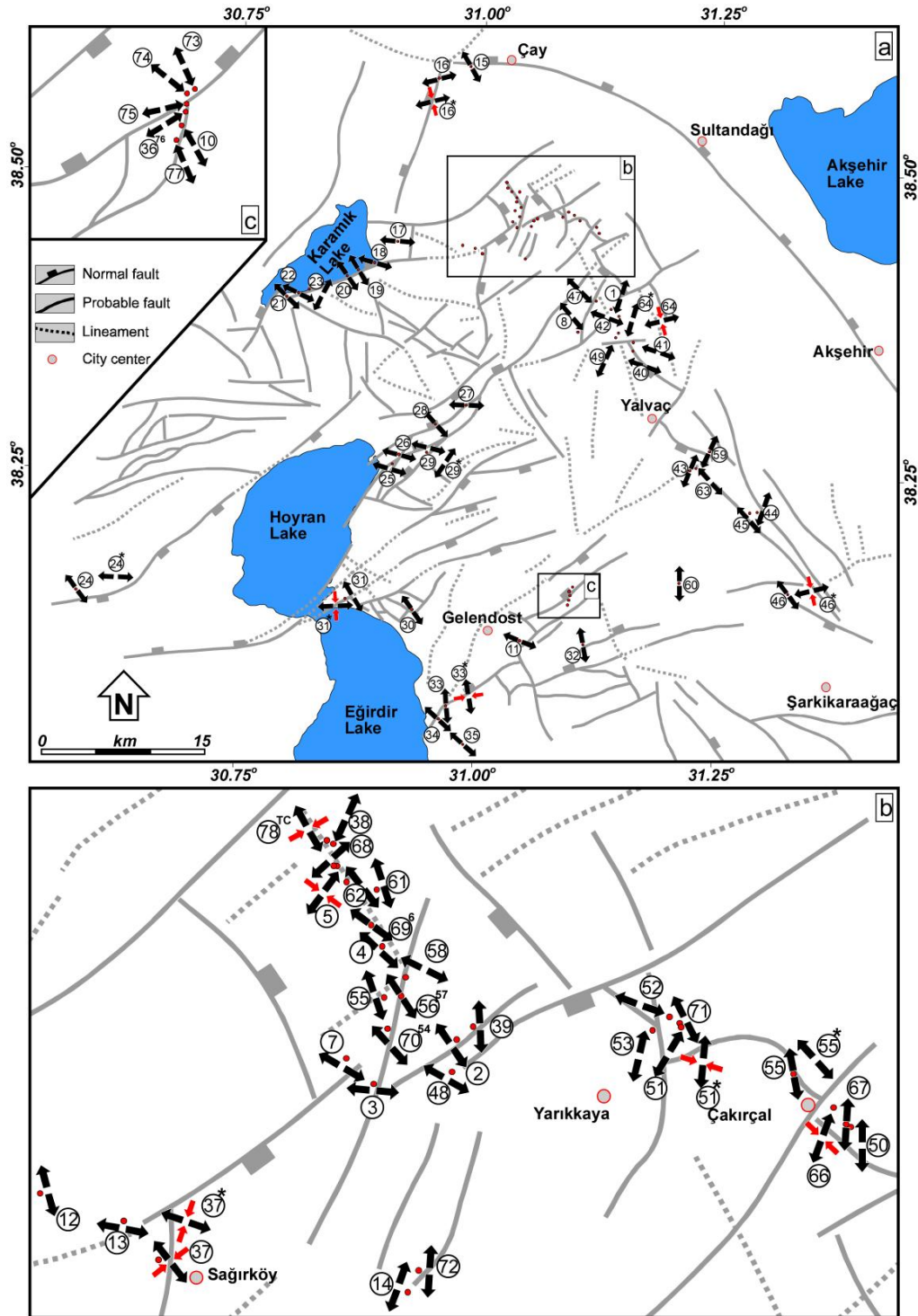


Figure 4.33. Spatial distribution and minor stress (σ_3) orientations (black arrows). Numbers refer to sampling sites. Red arrows indicate strike-slip solutions. Note that minor stresses tend to be orthogonal to nearby major faults.

4.3.4 Temporal Characteristics

Temporal changes of the paleostress configurations throughout the stratigraphy are very important to reveal paleostress changes starting from the time of basin formation to recent. Basin strata records paleostress tensors that were coeval with sedimentation (Figure 4.30 and 4.31), while the basement potentially record the entire stress history during the formation of the basin (Kleinspehn et al., 1989). Temporal characteristics of the basin are given in Figure 4.34. Relative age of the paleostress data are ordered based on 1) the age of the rocks which the fault-slip data were collected from and 2) cross-cutting relationships between the faults and the units. There is no any time order between the paleostress configurations within the same stratigraphic unit.

In Figure 3.34, the basement shows extension directions changing from E-W to N-S. Similarly, the youngest, still active extension direction in the Yalvaç Basin is reflected by the Kumdanlı Fault, Yaka Fault and Karamık Fault and extension directions trend approximately E-W to NW-SE (Figure 4.34), which consistent with current tectonic regime in the central Turkey, strongly varying σ_3 directions while σ_1 is (sub-) vertical. This is consistent with the paleostress patterns obtained throughout the stratigraphical successions of the Yalvaç Basin.

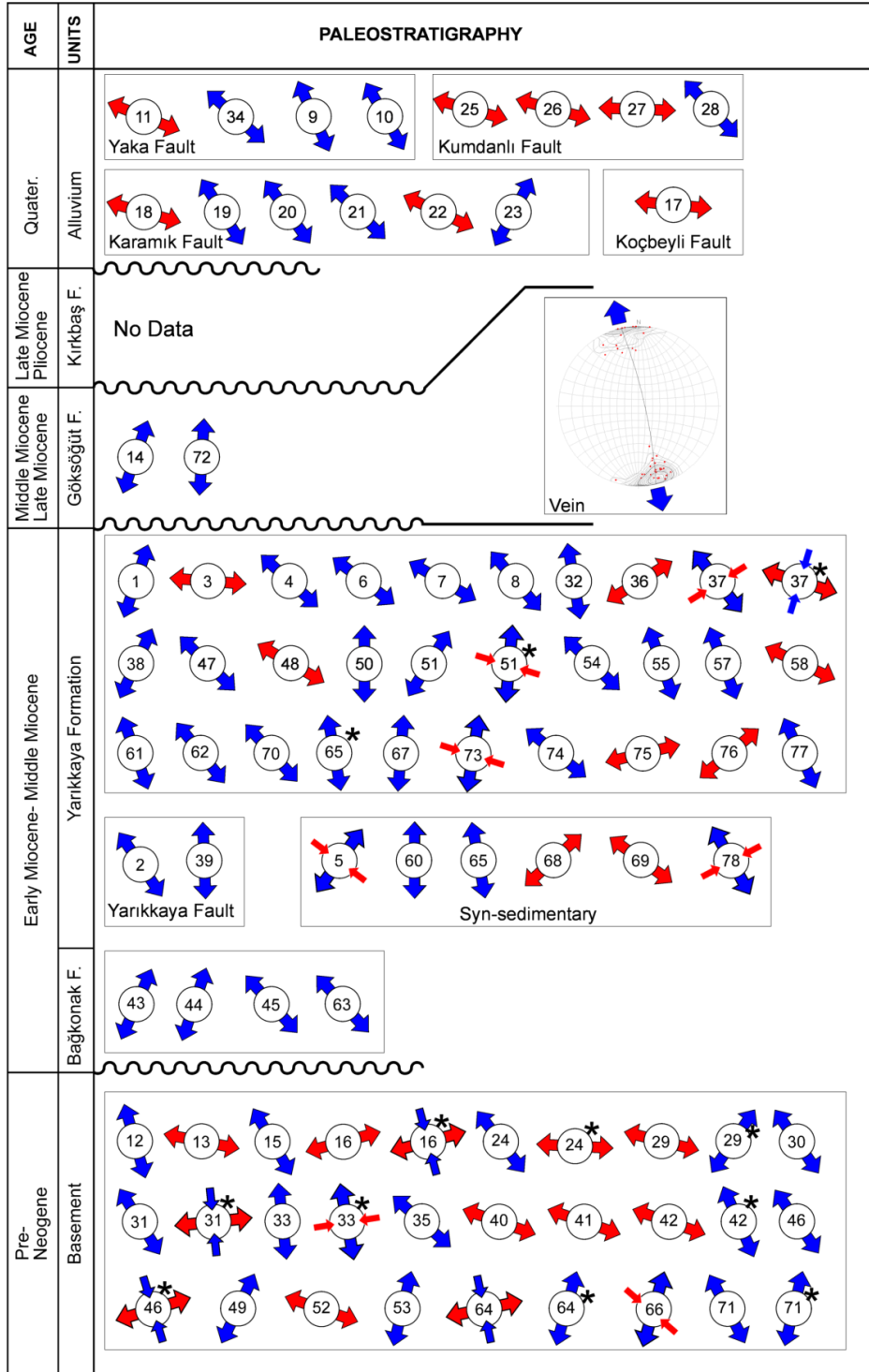


Figure 4.34. Temporal distribution and minor stress (σ_3) orientations (red and black arrows). Numbers refer to sampling sites. Red and blue arrows are used to indicate roughly E-W and N-S extension direction. Note that extension directions changing from E-W to N-S.

CHAPTER 5

SYNTHESIS

This chapter integrates and synthesizes the information presented in previous chapters. In this regard, stratigraphic and structural relationships within and between the Altınapa, Ilgın and Yalvaç basins are discussed in local and regional context. In doing so, in addition to newly provided information previous studies are used extensively. Finally, the tectonic and paleogeographic settings of these basins are also discussed within the geodynamics of Eastern Mediterranean region.

5.1 Temporal Relationships

In this part, first the temporal relationships within each basin is discussed independently, then the obtained results are used for developing larger scale geodynamic scenarios for the evolution of the region and their bearing on the uplift history of the Central Taurides.

5.1.1 Altınapa Basin

The Altınapa Basin developed unconformably on top of the Taurides fold-thrust belt which itself formed during subduction and collision from late Cretaceous to perhaps Oligocene times. The onset of sedimentation in the basin predates 11.8 Ma, which is the oldest age we obtained from the upper Altınapa group (UAG). The age of the onset of sedimentation remains unknown, but if sedimentation rates in the lower Altınapa group (LAG) were comparable to those in the UAG, the onset of sedimentation may also be of Middle Miocene age. However, UAG and LAG are separated by angular unconformity with an unknown stratigraphic hiatus, which means that LAG may also be older.

The fining upwards sequence in the LAG, together with the unconformable contact with the overlying lacustrine UAG suggests that most of the accommodation space was formed during deposition of UAG. The dominance of wedge-like coarse clastic sedimentation along the southwestern fault-controlled margin together with the onlap of the UAG over the northeastern basin margin suggests that initial subsidence was fault (NW-SE) controlled which resulted in the development of a half-graben geometry to the basin.

The angular unconformity observed between the LAG and UAG indicates that some erosion occurred prior to UAG deposition. This angular unconformity may mark lake level fall or complete drought possibly due to climatic changes. Alternatively, emplacement of magmatic centers at the eastern margin of the Altınapa Basin might have led to local uplift and tilting of the LAG units. It seems unlikely that uplift was related to a local enhancement of relief, as the UAG is characterized by lacustrine deposition, and is fine-grained in nature. Rather, it is most probably related to regional geodynamics.

5.1.2 Ilgın Basin

Compared to Yalvaç or Altınapa basins, the Ilgın Basin is relatively poorly exposed basin. The sedimentation in the basin starts before Middle Miocene (Serrevallian). It is the oldest radiometric age that we obtained from the Aşağıçiğil formation, which is underlain by Kumdöken formation and it is stratigraphically the oldest unit in the basin. Within the studied portion of Ilgın Basin no relative or absolute age data could be obtained. However, its age is based on rodent fauna obtained from north of Ilgın Basin at a stratigraphical horizon laterally corresponding to the same position with the Kumdöken formation. The thickness of the Kumdöken formation in the measured section is around 375 m assuming that its sedimentation rate is similar to those in the Aşağıçiğil formation (which is dominated by finer grained clastics and marls) total span of deposition of Kumdöken formation must be less than 1 My. This implies that the inception age and hence onset of sedimentation in the basin must also be Early Miocene (MN 2 Zone). Kumdöken formation is distinctly identified by its red color in the field, which reflects relatively arid climate conditions during Early Miocene. Additionally, the Kumdöken formation is separated from the lacustrine Aşağıçiğil formation by angular unconformity. This may be resulted from break in sedimentation possibly due to climatic conditions during ongoing tectonic activity, or two different tectonic phases operated in the region. First one was during the Early and the second one was Middle Miocene onwards. However, our paleostress inversion studies indicated that the stress tensor did not changed much since the inception of the basin. The other possibility is that the observed unconformities are related to block rotations that gave way to a series of north facing half grabens. It seems that this is most likely scenario and climatic changes enhanced the periods of non-deposition and rapid deposition.

The stratigraphic and sedimentological relationship within these two successions suggest that the most of the accommodation space was produced during deposition of the Middle Miocene Aşağıçiğil formation. The dominance of coarse clastic sedimentation along the western fault-controlled margin, together with the onlap of the Aşağıçiğil formation over the basement in the eastern basin margin suggests that subsidence was fault (striking NW-SE) controlled and eastern margin was passively subsided giving rise to an asymmetric NE facing graben.

In the Iğın Basin, the sedimentation started especially under arid climatic conditions during the Early Miocene (Kumdöken formation), which later replaced by relatively humid climate during the deposition of Aşağıçiğil formation. In the Middle Miocene, the lacustrine conditions were dominating. The basin was hydrologically open and was connected to the Altınapa Basin. This is evidenced by presence of pumice thinly bedded layers which produced same radiometric ages with the pumices collected from Altınapa Basin. This indicates that both basins received volcanic material from the same sources.

5.1.3 Yalvaç Basin

Yalvaç Basin formed unconformably on top of the allochthonous Hoyran-Beyşehir-Hadım nappes which experienced the effect of southward directed nappe emplacement and crustal loading related to the convergence of Africa and Eurasia (Robertson, 2000). The onset of sedimentation in the basin is not known precisely. The oldest age data from the basin is obtained from the upper levels of the Yarikkaya formation which is the oldest unit in the basin. The total thickness of the Yarikkaya formation is around 700 m. If we considering that the sedimentation rate of Yarikkaya formation is similar to the sedimentation rate of upper Altınapa group which is around 1.4 mm/y, the total duration of Yarikkaya formation is around 1 My. This implies that the Yalvaç Basin is opened during the Middle Miocene.

The fining upwards sequence in the Yarikkaya formation, together with the unconformable contact with the overlying conglomeratic Göksöğüt formation suggests that type of sedimentation, depositional base level, and sediment supply/source area changed. Most of the accommodation space was formed during deposition of Yarikkaya formation. This is evidenced by the presence of thick coarse clastic deposits along the northwestern fault controlled margin together with the onlap geometry of the Yarikkaya formation onto the basement. In addition, presence of approximately NW-SE striking syn-sedimentary mesoscopic faults along the eastern basin margin indicate that initial subsidence was controlled by approximately NW-SE trending faults which produced half-graben geometry for the Yalvaç Basin.

The unconformity between the Yarikkaya formation and the Göksöğüt formation must be related to tectonic movements there is angular relationship between these units. However, there is also possibility that the break in sedimentation could also be due to climatic changes. In that case, sediment supply was cut off temporarily or it was not sufficient enough to keep up with ongoing tectonic deformation or tilting during the duration of unconformity period. The climate seems to not be arid during the evolution of Yalvaç Basin as evidenced by lack of evaporitic rocks and red beds; most probably it was dominated most of the time with fluvio-lacustrine environments. In fact, it must be somewhat similar to present-day conditions like adjacent Beyşehir or Eğirdir Lake depositional systems.

5.1.4 Regional Implications

The stratigraphic and sedimentologic records from the Altınapa, Ilgın and Yalvaç basins are correlated in order to unravel paleo-geographic characteristics of the region. In this regard similarities and differences of these basins are compared and are listed in Table 5.1.

As seen in Table 5.1, Yalvaç Basin seems to be developed during the Middle Miocene although all other basins started to develop during the Early Miocene. They contain mainly lacustrine deposits at the central and eastern margins while coarse clastics dominate the western margins. Altınapa Basin contains volcanogenic deposits intercalated with basin infill and volcanic material dominates in its eastern margin and Ilgın Basin comprises pumice floats while Yalvaç Basin does not contain any volcanic material. Therefore, volcanism was not widespread in the region during the Middle Miocene except for Altınapa Basin. Pumice fragments are very fragile and they cannot be transported long distances provided that they are transported by waves as floating material. On the other hand, inexistence of volcanic material, although there were widespread Middle Miocene volcanism in the region, indicates that sedimentation in Yalvaç Basin took place after the Middle Miocene volcanism ceased and it was not hydrologically connected to the Altınapa or Ilgın basins. Other possible reason would be due to higher altitude of Yalvaç Basin. If the first option is correct, then the inception age of Yalvaç Basin is postdates the youngest volcanic activity in the region which is 11.54 Ma and prior to Late Miocene which is 11.2 Ma. This implies that the oldest deposits in Yalvaç Basin (Bağkonak and Yarikkaya formations) were deposited within approximately 300 Ky. This implies more than 3mm/y rate of deposition which is a reasonable rate for a continental basin.

Total sediment thickness in each basin is around 900 m for Altınapa, 700 m for Yalvaç, and 935m for Ilgın basins based on the measured and reference sections. The sediment thickness does not correspond to total basin subsidence and hence accommodation space since these are continental basins and there were periods of erosion during which some of the deposited material is removed most probably due to basins become hydrologically open, temporarily most probably due to tectonic activities or climatic changes.

Contrary to Altınapa Basin, Ilgın and Yalvaç basins contain lignite-bearing deposits of Middle Miocene age. Lignite deposits in Ilgın basin are associated with carbonate-dominated successions. This implies that they are formed most probably marshy mud-plain environment adjacent to a lacustrine system. On the other hand Yalvaç Basin contains mainly lignite of fluvial origin, which developed by levee or flood-plain or

oxbow lakes within a fluvial setting. This is evidenced by rapid lateral variation in thickness and organic matter content. In addition, the suitable conditions required for coal/lignite formation including heat and pressure was not generated in the Altınapa Basin.

In order to understand the relationships between basins, unconformity bounded lithologic units (cycles) are taken into account and correlation is performed based on these units (Figure 5.1). Three common unconformity surfaces are present in these basins. This means that erosion or interruption of sedimentation in each of the three basins took place approximately at the same time interval, except for the Yalvaç Basin where there is progradation into Late Miocene, whereas “*near top*” Middle Miocene unconformity is very well developed in Altınapa and Ilgın basins.

First erosional surface (Figure 5.1) occurred during the Middle Miocene which corresponds to time interval just prior to volcanic activity in the Altınapa Basin. Corresponding surface in the Ilgın Basin is identified by angular relationship between red clastics and fine grained lacustrine environment deposits, while this erosional surface in the Yalvaç Basin is characterized by onlapping of coarse clastics of fluvial origin on fine grained lacustrine deposits.

Second erosional period took place during the Late Miocene (Figure 5.1) which refers to the erosion of the lacustrine sediments in all basins which is followed by deposition of red coarse clastics of alluvi-fluvial environment. This erosional surface represents the terminal phase of the basins.

Final erosional surface (Figure 5.1) was developed at the base of alluvium during the Quaternary. It corresponds to the active alluvial deposition along stream courses.

Table 5.1. Tabulated information introduces the basic features for the each basin (Altınapa, Ilgın and Yalvaç basins).

Properties/Basin	Altınapa Basin	Ilgın Basin	Yalvaç Basin
Type	Continental	Continental	Continental
Environment	Lacustrine (inner part) Aluvi-Fluvial (margin)	Lacustrine (inner part) Aluvi-Fluvial (margin)	Lacustrine (inner part) Aluvi-Fluvial (margin)
Min. Thickness	~900 m (preserved)	~935 m	~700 m (preserved)
Max. Elevation	~1500 m (preserved)	~1500 m (preserved)	~2000 m (preserved)
Min. Elevation	~1200 m (preserved)	~1000 m (preserved)	~1000 m (preserved)
Oldest Age	Early/Middle Miocene	Early Miocene	Early/Middle Miocene
Youngest Age	Quaternary	Quaternary	Quaternary
Volcanism	Yes (lava, tuff, lahar)	Yes (tuff)	No
Age of volcanism	11,88 Ma (Oldest) 11,54 Ma (Youngest)	11,61 Ma	No
Biogenic sediment	Dark color mudstone	Coal	Coal
Chemical sediment	Limestone Carbonate Mud	Limestone Carbonate Mud	Limestone Carbonate Mud
Clastic sediment	Conglomerate Sand Silt and Clay	Conglomerate Sand Silt and Clay	Conglomerate Sand Silt and Clay
Transport direction of sediments	West to east	West to east	West to east
Age of coal	Early/Middle Miocene	Middle Miocene	Middle Miocene
Unconformity	Middle Miocene (1) Late Miocene (2) Pliocene (3)	Middle Miocene (1) Late Miocene (2) Pliocene (3)	Middle Miocene (1) Late Miocene (2) Pliocene (3)
Fault controlled margin	West	West	West
Onlap margin	East	East	East
Graben Geometry	Half Graben	Half graben	Half graben
Faults	Normal (Major) Strike-Slip (Minor)	Normal (Major) Strike-Slip (Minor)	Normal (Major) Strike-Slip (Minor)
Folds	Open	Undulation	Undulation
Stress regime	Extensional	Extensional	Extensional

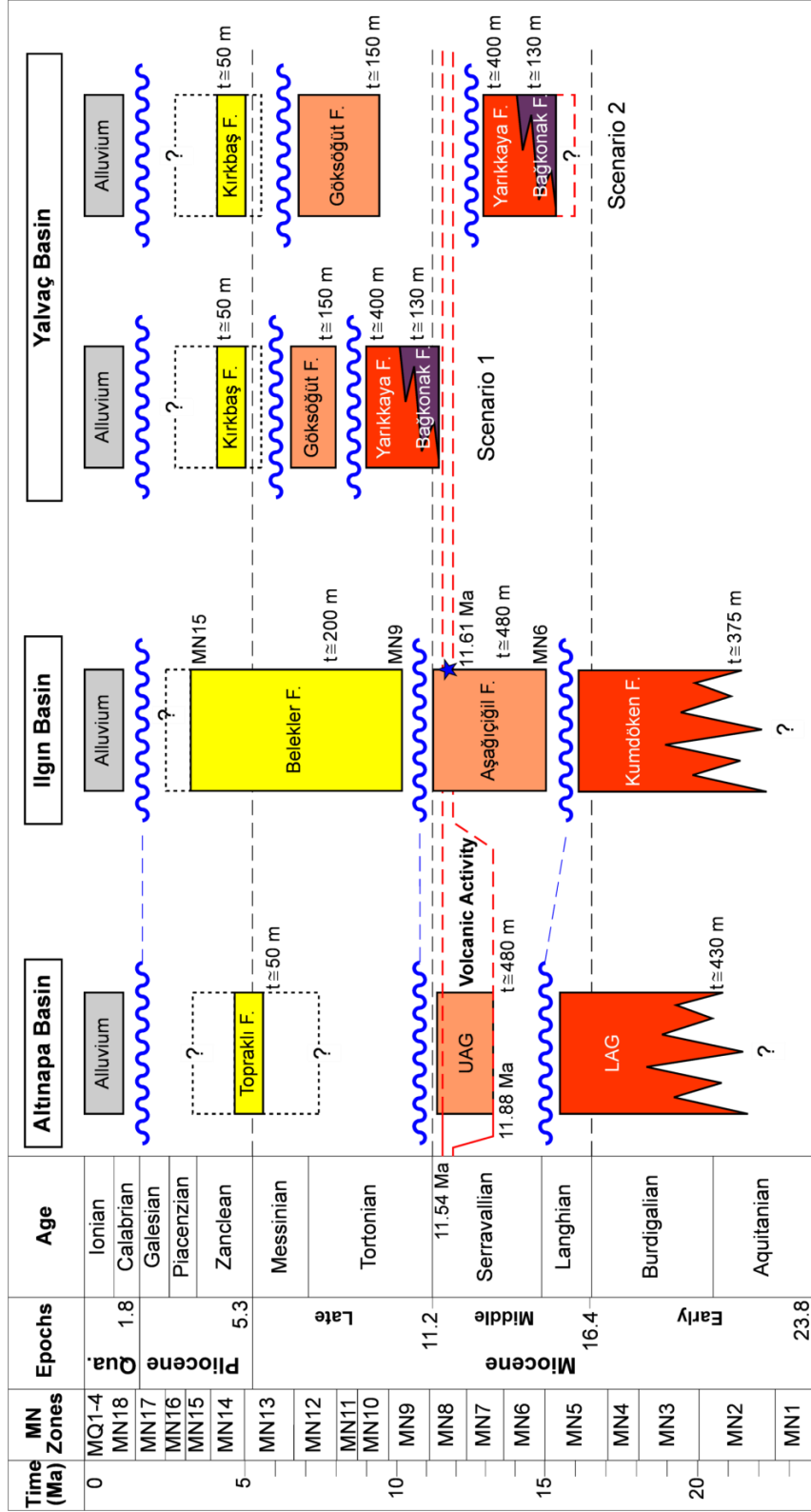


Figure 5.1. Correlation of the unconformity bounded lithologic units of each basin. Note that three basic angular unconformity surfaces in each basin are correlated with each other.

5.1.5 Regional Relationships: Extend of Continental-Marine Transition

Our stratigraphic and sedimentological studies on Miocene Altınapa, Ilgın and Yalvaç basins provide evidence that these basins formed within continental extensional setting, on top of a basement constituted by late Cretaceous to Oligocene fold-thrust belt, the Taurides. Basin development and deposition began in the Early Miocene in Ilgın Basin while its less well constrained from Altınapa and Yalvaç basins. However, both basins have well developed relatively thick Middle Miocene continental (fluvio-lacustrine) strata marked at the top with a regional unconformity. The youngest age obtained just below this unconformity is 11.54 Ma. The oldest age on top this unconformity is obtained from micro-mammal (rodents) fauna belonging to MN 9-12 Zone. This indicates that the overlying unit is of Late Miocene (Tortonian) in age.

Manavgat, Köprüçay and Aksu basins lie to the south of the study area, on the southern flank of Taurides (Figure 1.1). In these basins sedimentation appears to have also been started in the Early Miocene (Aquitainian) within marine conditions (Burton-Ferguson et al., 2005; Çiner et al., 2008; Şafak et al., 2005; Flecker et al., 2005; and Deynoux et al., 2003, Schildgen et al., 2012). This implies that the northernmost limits of paleo-shorelines of Mediterranean Sea during the Miocene time (Figure 5.2) was reaching to the northern margins of these basins. Contemporaneously, the basins, which lie at the northern flank (Altınapa and Ilgın basins) and within the inner apex of the Taurides (Yalvaç Basin) was dominated by continental (fluvio-lacustrine) conditions. In addition to these, Ilgar and Nemec (2005) reported that during the Early Miocene (Aquitainian) Ermenek Basin which is located in the southeastern continuation of the study area is dominated by continental settings. This record is important to estimate the eastern and northern limits of the shorelines during the Early Miocene (Figure 5.2a). However, during the Middle Miocene marine inundation occurred in Ermenek Basin while shorelines moved southeastwards as the Lycian Nappes advanced in the western flank of the Isparta Angle and no major change occurred in the position of paleoshorelines in the central part of the Isparta Angle close to the study area, during the Middle Miocene (Figure 5.2b). During this time interval, the Yalvaç Basin started to develop while Altınapa and Ilgın basins reached their maximum extend after a major intra-Mid Miocene unconformity and are accompanied with volcanism towards the end of Serravallian. Recent studies (Çiner et al. 2008, Cosentino et al. 2012, Schildgen et al 2012) indicated that the marine deposits that overlay Taurides are as young as Tortonian are encountered less than 30 km south of the study area, and now they are standing more than 2 km above mean sea level. This implies that marine continental transition was close to the study area during the Late Miocene.

Combinations of all these information obtained both from literature and acquired in this study have very important implications for the geological evolution of southern Anatolia as well as its topography. The Ermenek-Mut Basin was above sea level during the Early

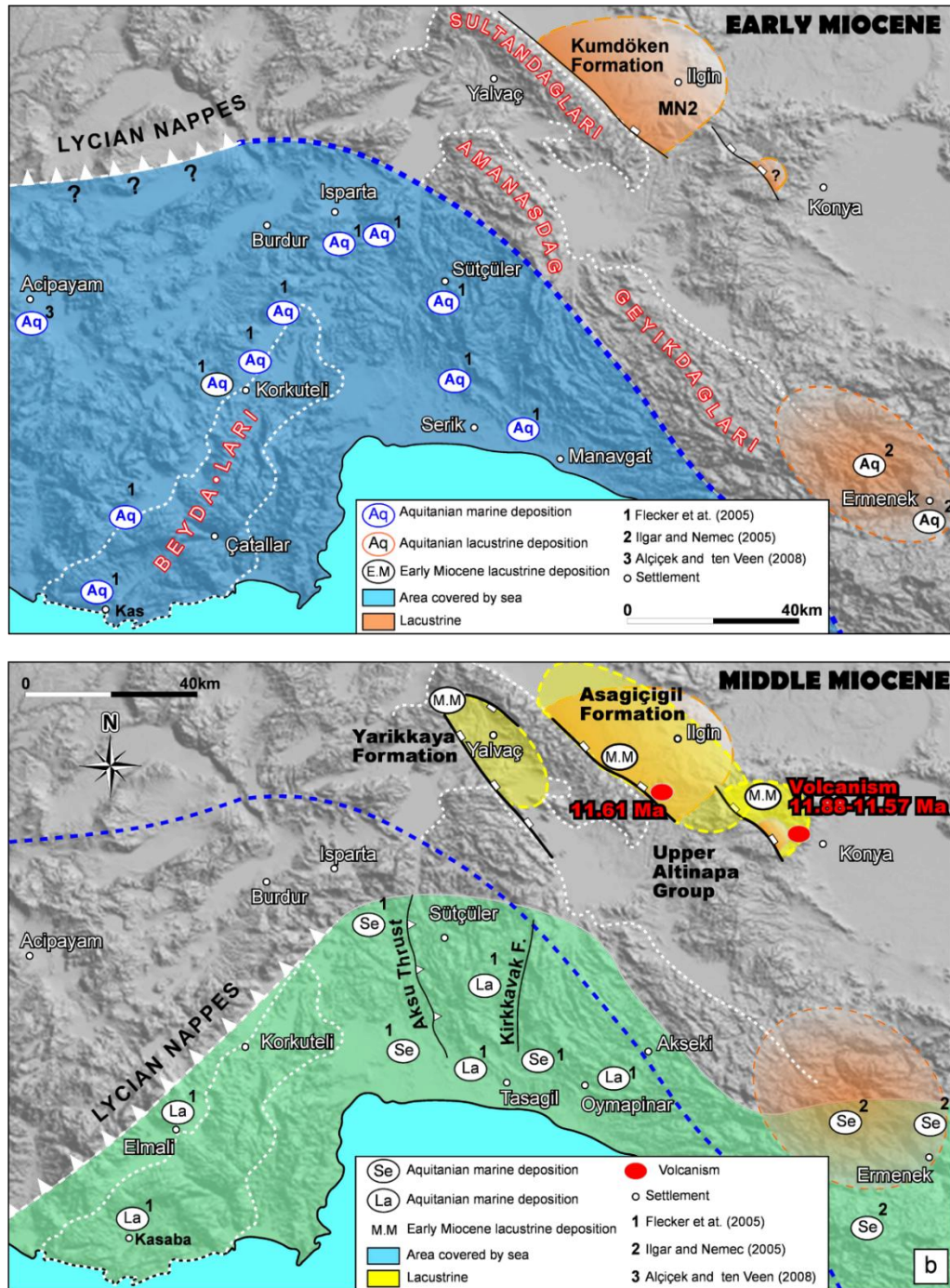


Figure 5.2. Paleogeographic maps showing the Early and Middle Miocene shorelines and the continental basins in the Isparta Angle (position of the Lycian Nappes adopted from Hayward 1984).

Miocene as did the basins in the study area, Ermenek Basin was inundated during the Middle Miocene and shorelines approached to the study area as close to as 30 km both from west and east. There is no major fault that could delimit the Ermenek basin and study area. This implies that the elevation of the basins in the study area was close to sea level and at most it was possibly rising northwards gradually. As seen in Figure 1.2. Ermenek-Mut basin and marine deposits distributed all over Taurides are now laying more than 2 km altitude. This means that more than 2 km uplift occurred in southern Anatolia since the Late Miocene (Cosentino et al., 2012). On the other hand the studied basins which were continental in character during the Early to Late Miocene lie currently at elevations around 1 km. No data are available to constrain the paleo-elevation of the Altınapa, Yalvaç and Ilgın basins during Middle Miocene sedimentation, but the fact that the Ermenek-Mut Basin lies presently at an about 1 km higher elevation than the lacustrine basins (Study Area) demonstrates that the late Neogene history of the southern Turkey was characterized by strong differential uplift, with the southern Tauride mountain range uplifting at least 1 km more than the intra-montane basins to their north. Cosentino et al. (2012) interpreted the uplift of the Taurides since the Late Miocene as a dynamic topographic effect, uplifting the entire Central Anatolian plateau. Although such dynamic topographic effects might have well played an important role, the major uplift difference between the continental basins and Ermenek-Mut basins illustrates that at least half of the uplift of the southern Taurides resulted from regional tectonics rather than Anatolia-wide dynamic topography. The Tauride range as exposed today therefore likely represents a horst system, with regions to the north and south showing smaller magnitudes of uplift than the range itself. We finally note that the modern topography of the Tauride range is thus a late post-Late Miocene (post-Tortonian) phenomenon that is unrelated to the late Cretaceous Oligocene folding and thrusting responsible for the dominant deformation within the range.

5.2 Structural Implications

The tectono-stratigraphic implications of the structures developed in the region are dealt first with basin scale then their regional implications are discussed in this section.

5.2.1 Altınapa Basin

Structural information obtained from the Altınapa Basin indicates that the basin bounded major faults and mesoscopic faults within the basin infill show normal fault character. Generally, multiple fault sets, dominantly E-W, NE-SW and NW-SE trend (Figure 5.3a), accommodated mainly N-S (II), NW-SE (III) and NE-SW (I) directed extension (Figure 5.3b) accordingly. The NW-SE direction is obviously related to the

Konya Fault Zone which is seismically active, however the N-S extension is the most prominent extension direction since the E-W striking faults controlled the deformation and also intensely deformed the basin. The second dominant extension direction oriented is related to the NE-SW basin bounding faults that are the result of NE-SW directed extension. Cross-cutting relationships between the faults (Figure 5.3) inferred from the remotely sensed data and the observations during the field studies indicate that development of fault sets of various strikes was coeval and therefore these faults were development simultaneously during the evolution of the basin. As seen in Figure 5.3b the horizontal component of the minor principal stress directions are not constrained to any direction (multidirectional extension), though some directions dominate. This is the typical characteristics of a uniaxial stress regime in which vertical stress, gravity, is the major principal stress. Therefore, subsidence during the basin formation was most likely related to multi-directional extension in which N-S to NE-SW directions seems to dominate (Figure 5.3a).

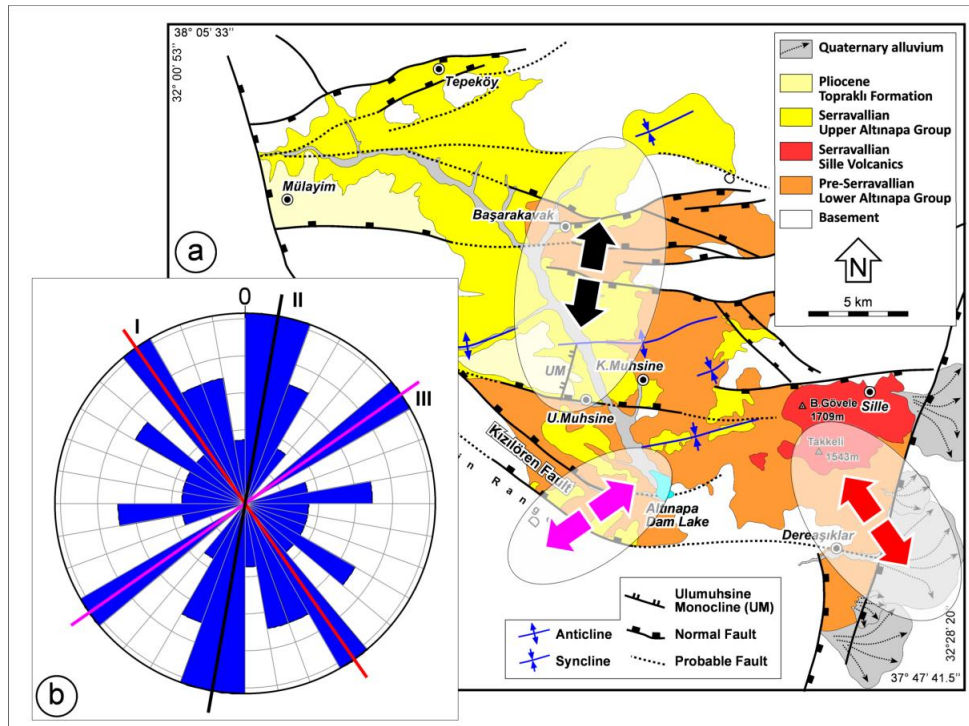


Figure 5.3. a) Geological map of the Altnapa Basin with major structures and dominant paleostress orientations (arrows) in its different parts. b) Rose diagram of horizontal component of minor principal stress directions prepared from whole data (σ_3). Note radial geometry of the extension directions where three sets dominate over other orientations.

The fault network (Figure 5.3a) shows several segments with approximately E-W orientation. This geometry may be explained as horsetail splay geometry. Such an interpretation requires a normal fault activity with left lateral slip along the boundary fault. Such geometry is similar to Ilgın Basin will be described further in the next section.

The E-W trending folds in the study area are probably related to normal faults that extended E-W direction. The major fold which is located at the north of the Küçük Muhsine is approximately parallels and lies between two hanging wall. Schlische (1995) used the term longitudinal to describe folds that lie parallel to the associated normal faults. Folds in the Altınapa Basin appear to fall into this category. The folding results from the space problem between the two hanging wall, therefore the lower Altınapa group was affected more than the upper Altınapa group. Another striking structure in the Altınapa Basin is the Ulumuhsine monocline which has been developed above a blind normal fault. The geometry and the deformation observed in the Ulumuhsine monocline is consistent with the Konya Fault Zone and it also affected the upper Altınapa group. This information together with the paleostress configurations obtained from both lower and upper Altınapa groups indicate that extensional regime started in the basin in the Middle Miocene and still prevails.

In conclusion, the Altınapa Basin has been dominated by a uniaxial extensional regime since the Middle Miocene.

5.2.2 Ilgın Basin

The structural studies on the Ilgın Basin show that NE-SW trending Akşehir-Afyon Fault Zone (AAFZ) is the major faults controlling the basin formation since the Middle Miocene. It delimits the basin in the west and the Ilgın Basin is located at the hanging wall block of the fault. Ilgın Fault Zone (IFZ) has approximately same trend with AAFZ and delimits the basin in the east. The basin is located footwall side of the IFZ. In the south, several E-W trending normal faults bifurcating from the AAFZ disrupt the basin sediments and produce step like geometry. In the Ilgın Basin, the basin bounded major faults and mesoscopic faults within the basin infill show obviously normal fault character. Generally, multiple fault sets, basically NW-SE, E-W and N-S trend (Figure 5.4a), accommodated dominantly NE-SW(II), N-S(I) and E-W(III) extension (Figure 5.4b). The NE-SW extension (II) which is poorly identified in the rose diagram is compatible with seismically active Akşehir-Afyon Fault Zone. Effects of the mesoscopic faults with respect to the major faults are more dominant in the rose diagram due to their higher abundance. N-S extension (I) directions represent E-W trending faults. The other extension direction highlighted in the rose diagram is E-W extension (III) which corresponds to N-S trending Ilgın Fault which is seismically active.

Basic structures in the Ilgın Basin are the Akşehir-Afyon Fault Zone and its E-W trending splay faults (Figure 5.4a), which means they were coeval. The rose diagram of the minimum horizontal stress directions given in Figure 5.4b states the strongly varying extension direction; however the determined extension directions are perpendicular to the strike of the major faults, which means that these directions are controlled mainly by the geometry of associated faults. This is the typical characteristic of the uniaxial stress regimes, which causes free fall of hanging wall.

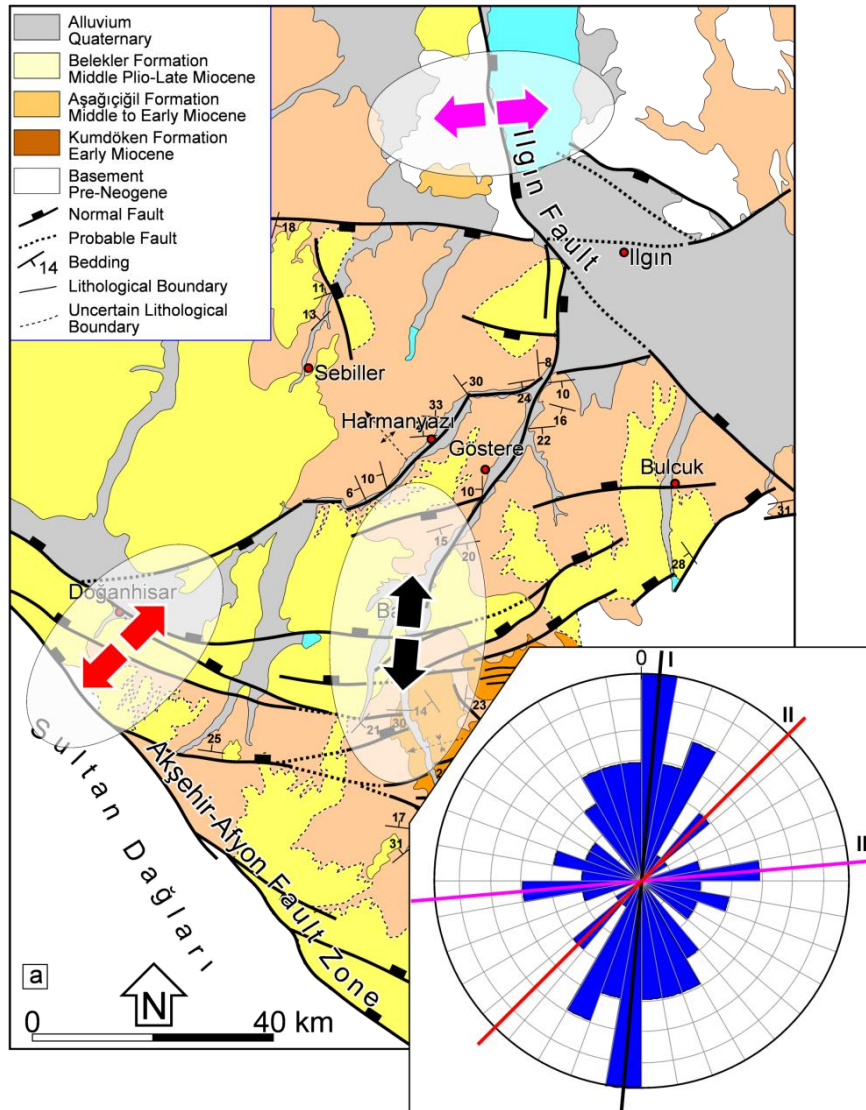


Figure 5.4. a) Geological map of the Ilgın Basin with major structures and dominant extension directions (arrows) b) Rose diagram prepared from horizontal component of minor principal stress orientations. Note radial geometry of the extension directions where three sets dominate over other orientations.

The fault pattern in the Ilgın Basin seems like horse-tail splay; however the horse-tail configuration needs to left-lateral movement along Akşehir-Afyon Fault Zone. Alternatively, the formation of the E-W trending faults may be driven by the subsidence in the north of the basin, seismically active part of the Akşehir-Afyon Fault Zone. It causes bending, uplifting and stress accumulation in the south, along the E-W trending splays. 26th September 1921 Argıthanı and the 21st February 1946 Ilgın-Argıthanı Earthquakes were reported by Eyidoğan et al., (1991), which testify to the stress accumulation in these segments.

5.2.3 Yalvaç Basin

Structural studies on the Yalvaç Basin show that the basin bounded major faults and mesoscopic faults observed within the basin infill states the deformation of the basin controlled by normal faults. Two basic fault sets, mainly N-S and NE-SW trend (Figure 5.5a), control the structural grain in the basin. As shown in Figure 5.5b, three different extension directions, mainly N-S (III), NW-SE (II) and ENW-WSW (I), dominated the basin. Roughly N-S directed faults are the main basin bounding faults and as expected the extension direction for this fault sets is approximately E-W.

This configuration implies that the extension direction during Middle Miocene and in recent show the same direction. In addition to Karamık Graben, there are some other active faults, namely Kumdanlı Fault Zone and Yaka Fault Zone, have NE-SW strike and the corresponding extension direction for these faults is NW-SE which is clearly seen in the rose diagram (direction II in Figure 5.5b). The Yarıkaya Fault Zone also have same trend, but there is no any evidence for the recent activity. We know from the field study that Yarıkaya Fault zone is younger from the Çakırçal and Sağır Fault Zone, whereas should be older than the other faults. In this circumstance, the recent stress regime faults are clearly extensional and two dominant extension directions are determined, which are WNW-ESE and NW-SE (I and II, respectively in Figure 5.5b). The determined extension directions are perpendicular to the strike of the major faults, which means that these directions are controlled mainly by the geometry of associated major faults, rather than regional stress pattern.

The fault pattern in the basin (Figure 5.5a) consists of two orthogonal sets, NE-SW and NW-SE. The development of the these faults implies the locally orthogonal extension in NW-SE and NE-SW directions, that results from local stress field changes associated with growth of the faults. On the other hand, this type of arrangement may indicate the permutations between σ_2 and σ_3 since their values are close in magnitudes (Angelier, 1994) and they are interchangeable depend on the local stress relaxation.

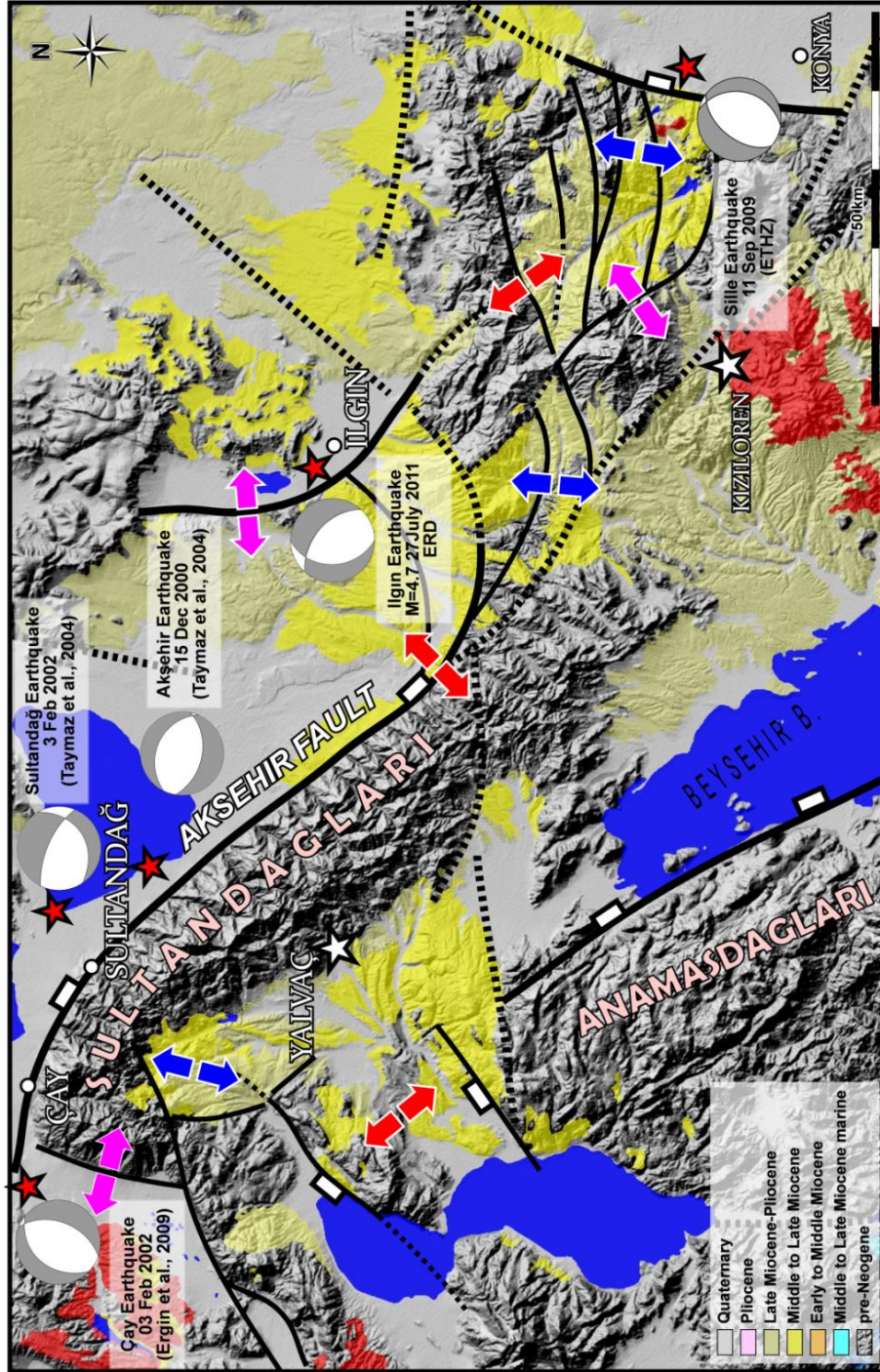


Figure 5.6. The major structures and dominant stress orientation directions and moment tensor solutions of major earthquakes overlaid on shaded relief image and Neogene units of the study area.

the Yalvaç Basin is also variable, showing almost radial characteristic (Figure 5.7). This implies that intermediate and minor stress were not constrained in any single direction while major stress was vertical during the evolution of the basins in the Middle Miocene and onwards. In this regard, the most likely explanation for the domination of some extension directions within uniaxial stress conditions is most probably due to the expression of local stress states that are controlled by the structural grain of the basement. Under uniaxial stress conditions all of the pre-existing structures with favorable orientations reactivate (Sibson 1990). Therefore, large faults in turn perturb the regional stress orientations and gave way local stress orientations deviating from it as high 90° (Bai and Pollard 2000). We propose that the similar types of relationships are also valid for the study area, in which, uniaxial stress pattern is perturbed by large scale structures. This relationship is perfectly expressed by near perpendicular orientation of horizontal component of minor stress to the nearby major fault (Figure 5.6).

During the field studies, possible active faults such as Konya Fault (Altınapa Basin); Akşehir-Afyon Fault Zone and Ilgın Fault Zone (Ilgın Basin); Karamık, Kumdanlı and Yaka faults (Yalvaç Basin) were studied in detail and fault slip data were collected from these faults in order to determine the characteristics of the recent tectonic regime in the region. Extension directions from these faults are given in Figure 5.7, which vary from E-W to NW-SE in Altınapa and Yalvaç basins; meanwhile in Yalvaç Basin it shows multiple directions. In addition, the focal mechanism solutions of the major earthquakes (Figure 5.6) also states that the major stress (σ_1) is vertical and other principal stresses (σ_2 and σ_3) are not constrained in any particular directions and they vary in all over directions in the region (Ergin et al., 2009 and Aktuğ et al., 2010).

During the field studies, possible active faults such as Konya Fault (Altınapa Basin); Akşehir-Afyon Fault Zone and Ilgın Fault Zone (Ilgın Basin); Karamık, Kumdanlı and Yaka faults (Yalvaç Basin) were studied in detail and fault slip data were collected from these faults in order to determine the characteristics of the recent tectonic regime in the region. Extension directions from these faults are given in Figure 5.7, which vary from E-W to NW-SE in Altınapa and Yalvaç basins, meanwhile in Yalvaç Basin it shows multiple directions. In addition, the focal mechanism solutions of the major earthquakes (Figure 5.6) also states that the major stress (σ_1) is vertical and other principal stresses (σ_2 and σ_3) are not constrained in any particular directions and they vary in all over directions in the region (Ergin et al., 2009 and Aktuğ et al., 2010).

In conclusion, the paleostress orientations since the Early Miocene (Ilgın and Altınapa basins) are more or less same with the Recent stress field obtained from earthquake moment tensor solutions. This implies that a similar tectonic condition has been prevailed in the region at least since the Middle Miocene. Otherwise, the region experienced co-axial deformation that is similar with the Recent tectonic regime.

However, the paleostress data has been obtained from the basin fills that are almost continuous (except some short duration unconformities) since the Middle Miocene and they did not provide any incompatible stress configurations. This implies that stress regime was also uninterrupted and co-axial deformation is unlikely. This further implies that the region has been experiencing the same tectonic regime since the Middle Miocene, which, in fact, might be started during the Early Miocene.

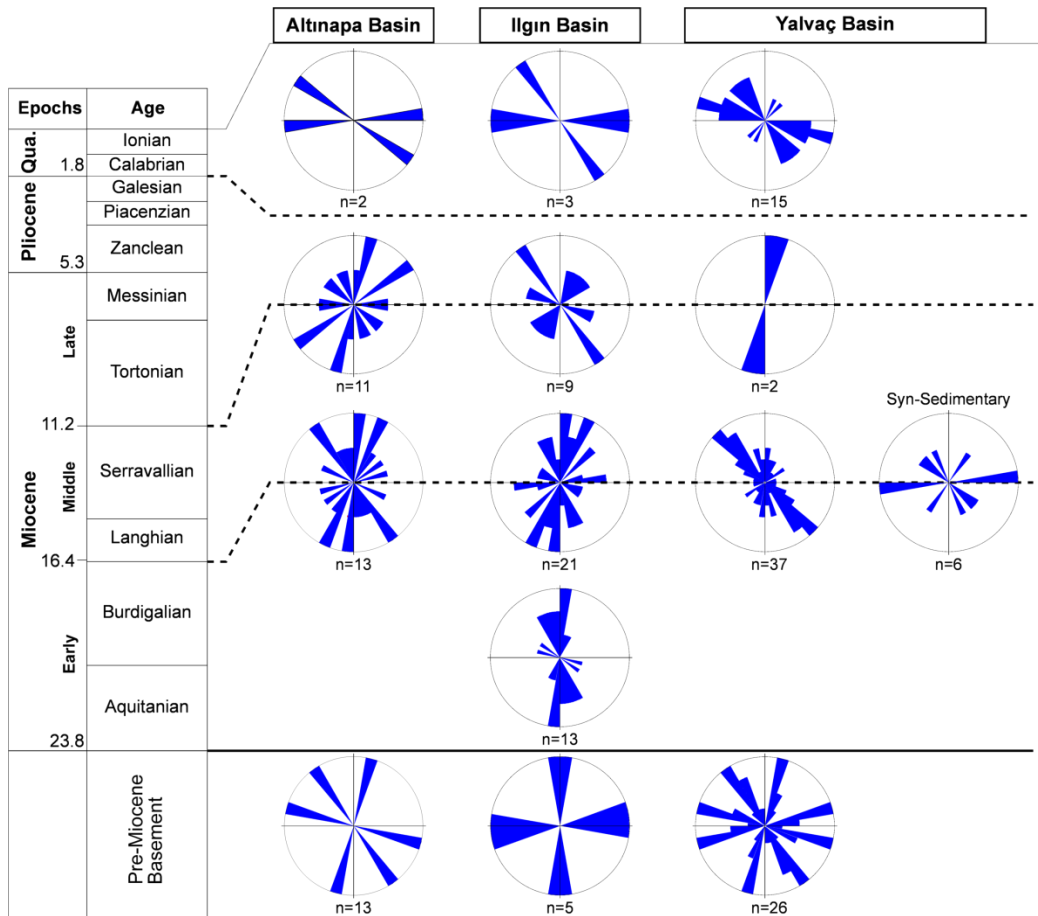


Figure 5.7. Paleostress stratigraphy of study area. Rose diagrams show horizontal component of the minimum stress (σ_3) for each basins since Early Miocene. Note that although, there is roughly domination of NW-SE and NNE-SSW directed extension, in reality, the horizontal component of the minor stress is not constrained in any particular direction and it is multidirectional over time. This implies uniaxial vertical stress conditions.

5.2.5 Regional Implications

Our structural and geochronological analysis of the Altınapa, Ilgın and Yalvaç basins provide evidence that extension to the north of the Tauride mountain range was already active since Middle Miocene time, and formed intra-montane, continental basins on top of the late Cretaceous to Oligocene Taurides fold-thrust belt (Figure 5.6). At a larger scale, Miocene extension appears to be spatially restricted to the region north of the Cyprus subduction zone. To the east of the Adana Basin (Figure 1.1), Middle Miocene and younger deformation has been dominated by N-S compression and strike-slip faulting related to westward Anatolian escape as a result of the Arabia-Europe collision (e.g., Şengör et al., 2003; Faccenna et al., 2006; Hüsing et al., 2009; Kaymakci et al., 2010), and to the west of the central Taurides, Middle-Late Miocene deformation was transpressional, related to vertical axis rotations of the Bey Dağları platform and Lycian Nappes at the eastern limit of the Aegean-west Anatolian orocline (Kissel and Poisson, 1987; Morris and Robertson, 1993; Poisson et al., 2003; van Hinsbergen, 2010; van Hinsbergen et al., 2010a; b). The spatial restriction of NE-SW to NW-SE extension to the region north of the Cyprus subduction zone suggests a direct relationship to the dynamics of the eastern Mediterranean subduction system, which has likely been in a state of relative southward trench retreat since at least Middle Miocene time (see also Over et al., 2004). The analysis shows that not only the forearc, but also the volcanic arc region of the Cyprus subduction zone, to which the Altınapa Basin belongs, has been affected by this extension for at least during the last ~12 Ma. On the other hand, the basin margin faults are generally N-S and NW-SE striking normal faults and propose E-W to NE-SW extension, which seems to be questionable in a regime of N-S Africa-Europe convergence. However, one of the main implications of obtained paleostress orientations is that the region was subjected to uniaxial stress conditions with vertical major stress, and horizontal intermediate and minor stresses, since the Middle Miocene. This is reflected as multi-directional extension directions (Figure 5.7). Such stress conditions are very common in regions of vertical uplift that are driven by bouncy (dome like or plateau uplift) rather than the stress driven by plate margin processes. Most likely mechanism therefore is mantle driven uplift due to asthenospheric flow below the Isparta Angle (Gans et al. 2009, Biryol et al. 2011). Therefore, extension in the region is most probably the result combination of mantle driven vertical uplift and backarc type extension due to roll-back of Cyprian Slab below the Taurides in Isparta Angle.

CHAPTER 6

CONCLUSIONS

This study represents the following conclusions:

- I. Stratigraphical studies demonstrate that
 - a. The Altınapa Basin is an extensional basin, with a fluvio-lacustrine basin infill that is subdivided as lower and upper Altınapa groups. Volcanic deposits in the upper Altınapa group have been dated with $^{40}\text{Ar}/^{39}\text{Ar}$ geochronology, and demonstrate an age range of ~11.88–11.57 Ma. Extension-related subsidence was controlled along large basin-bounding faults and produced half-graben geometry. Open folds affect the lower Altınapa group more than the upper Altınapa group, between which an angular unconformity exists. This, together with the fact that the lower Altınapa group has a well-defined fining upward sequence, suggests that the main basin forming phase predates 11.88 Ma.
 - b. The Ilgın Basin is an extensional Basin, with a stratigraphy that is divided into as Kumdöken, Aşağıçığıl and Belekler formations. Volcanic deposits in the Aşağıçığıl formation have been dated with $^{40}\text{Ar}/^{39}\text{Ar}$ geochronology, and demonstrate an age of 11.61 Ma which gives the oldest age obtained from the basin Aşağıçığıl formation. Extension-related subsidence controlled along large basin-bounding faults especially the NW margin of the basin. Kumdöken formation is stratigraphically the oldest unit in the basin and it is clearly separated from the lacustrine Aşağıçığıl formation by an angular unconformity. This indicates that the main basin forming phase predates 11.61Ma. Sediment thickness indicates that most of the accommodation space was formed during deposition of Aşağıçığıl formation and initial subsidence was controlled by approximately NW-SE trending faults which produced a series of half-graben geometry of the Ilgın Basin.
 - c. The Yalvaç Basin is an extensional Basin, with a stratigraphy that is subdivided as Bağkonak, Yarikkaya, Göksöğüt and Kırbaş formations. The onset of sedimentation in the basin is Middle Miocene or shortly predates it. The fining upwards sequence in the Middle Miocene Yarikkaya formation, together with the unconformity with the overlying Late Miocene Göksöğüt formation indicates that most of the accommodation space was formed during deposition of Yarikkaya formation and initial subsidence was controlled by approximately N-S trending faults which produces a half-graben

geometry of the Yalvaç Basin. Inception age of the Yalvaç Basin seems to be relatively younger than the Altınapa and Iğın basins.

- d. Three common regional unconformity surfaces that include intra-Middle Miocene, base Late Miocene, and top Pliocene are present in all of these basins. The most prominent unconformity was occurred during the Middle Miocene which is marked by a volcanic activity.
- e. Sedimentation began prior to Middle Miocene in all of these three basins, and they are deposited mainly lacustrine environment together with marginal clastic component. In all of the basins, the lowermost sequence and to some extend the younger sequences have wedge-like geometry with the thickest and the most proximal side is located next to a major basin bounding fault. This indicates that all of these basins have their own local depocenters, which means that these basins were small local self-standing basins, and they are not a part of later dissected parts of a single large basin.
- f. During the Early Miocene, the paleo-shoreline was located further north of Acıpayam in the west, however lacustrine Ermenek Basin produces the eastern limit of the paleo-shoreline. Marine continental transition was very close to the study area, especially during the Late Miocene, in which continental settings prevailed and their southern limits defined the northern edge of the marine environments.
- g. The continental Middle Miocene deposits of the Altınapa Basin lie, at present, at an elevation of ~1 km, whereas partly contemporaneous marine deposits in the Mut Basin and near Beyşehir, to the south, on top of the Tauride range, are elevated up to 2 km. This demonstrates that the southern Tauride range uplifted at least 1 km more than the flanking intra-montane basins to the north, attesting to strong differential uplift in the late Neogene of southern Turkey.

II. Structural studies demonstrate that

- a. In the Altınapa Basin, the basin deformation is controlled by NW-SE trending boundary fault in the west which bifurcates into several E-W branches resembling to horse-tail splay pattern. The dominant extension direction responsible for formation of the basin is oriented approximately E-W to NE–SW although multi-directional extension prevailed in the basin and extension commenced prior to 11.8 Ma. The recent seismic activity in the region indicates that extensional regime still prevails in the region.
- b. In Iğın Basin, the basin formation is controlled by NW-SE oriented Akşehir-Afyon Fault Zone (AAFZ) in the west and it bifurcates several E-W branches similar to Altınapa Basin. The formation of the basin is controlled by ~E-W to NE-SW extension although basin experienced multi-directional extension prevailed in the region. The extension started prior to Middle Miocene and the

recent seismicity in the Iğın Basin indicates that extensional deformation and AAFZ is still active. This implies that the inception age of the Akşehir-Afyon Fault Zone is at least Middle Miocene.

- c. In the Yalvaç Basin, the general trends of the basin bounding faults are N-S to NW-SE and started at least by the Middle Miocene. The dominant extension directions are ~E-W to NE-SW likewise the basin experienced multi-directional extension.
- d. Determined extension directions in this study are consistent with recent regional pattern of NE–SW to NW–SE extension along the southern Taurides, which seems to be controlled by the Cyprus Subduction Zone (CSZ). This implies that CSZ is most likely been in a state of relative southward trench retreat since at least Middle Miocene time.

REFERENCES

- Aktuğ, B., Kaypak, B., Çelik, R. N., 2010. Source parameters for the Mw=6.6, 03 February 2002, Çay earthquake (Turkey) and aftershocks from GPS, Southeastern Turkey. *J. Seismol*, v. 14, pp. 445-456. DOI 10.1007/s10950-009-9174-y.
- Alçiçek, H., 2010. Stratigraphic correlation of the Neogene basins in southwestern Anatolia: Regional palaeogeographical, palaeoclimatic and tectonic implications. *Palaeogeography, Palaeoclimatology, Palaeoecology*, v. 291, pp. 297-318.
- Alçiçek, M. C. and ten Veen, J. H., 2008. The late Early Miocene Acipayam piggy-back basin: refining the last stages of Lycian nappe emplacement in SW Turkey. *Sedimentary Geology*, v: 208, pp. 101-113.
- Altınır, D., Yılmaz, I.O., Özgül, N., Akcar, N., Bayazitoglu, M. and Gaziulusoy, Z.E., 1999. High-resolution sequence stratigraphic correlation in the Upper Jurassic (Kimmeridgian)-Upper Cretaceous (Cenomanian) peritidal carbonate deposits (Western Taurides, Turkey). *Geological Journal*, v. 34, pp. 139-158.
- Andrew, T. and Robertson, A.H.F., 2002. The Beyşehir-Hoyran-Hadım nappes: genesis and emplacement of Mesozoic marginal and oceanic units of the northern Neotethys in southern Turkey. *Journal of the Geological Society of London*, v. 159, pp.529-543.
- Angelier, J., 1979. Determination of mean principal direction of stress for a given fault population. *Tectonophysics*, v. 56, pp. T17-T26.
- Angelier, J., 1990. Inversion of field data in fault tectonics to obtain the regional stress—III. A new rapid direct inversion method by analytical means. *Geophysical Journal International*, v. 103, pp. 363-376.
- Angelier, J., 1994. Fault slip analysis and paleostress reconstruction. In: P.L. Hancock (Editor), *Continental deformation*. Pergamon Press, Oxford, p. 53-101.
- Armijo, R., Carey, E. and Cristernas, A., 1982. The inverse problem in microtectonics and the separation of tectonic phases. *Tectonophysics*, v. 82, pp.145-160.

- Bai, T. and Pollard, D.D., (2000). Fracture spacing in layered rocks: a new explanation based on the stress transition. *J Struct Geol* v: 22, p: 43–57.
- Barka, A. Reilinger, R., Şaroğlu, F. and Şengör, A.M.C. 1995. The Isparta Angle: its importance in the neotectonics of the Eastern Mediterranean Region. *Proceedings of the International Earth Sciences Colloquium on the Aegean Region*, v. 1, pp.3-18.
- Barrier, E. and Vrielynck, B., 2008. MEBE Atlas of Paleotectonic maps of the Middle East. Commission for the Geological Map of the World.
- Bassant, P., van Buchem, F.S.P., Strasser, A. and Görür, N., 2005. The stratigraphic architecture and evolution of the Burdigalian carbonate-siliciclastic sedimentary systems of the Mut Basin, Turkey. *Sedimentary Geology*, v. 173, pp. 187-232.
- Bektimuroğlu, O., 1978. Konya ili Ilgın ilçesivarındaki kil yatakları hakkında ön rapor. M.T.A Rapor No:6238.
- Besang, C., Eckhart, F.J., Harre, W., Kreuzer, G. and Muller, P., 1977. Radiometrische Alterbestimmung am neogenen Eruptivgesteinen der Türkei. *Geol. Jb.*, v. 25, pp. 3-36.
- Biryol, C.B., Beck, S.L., Zandt, G. and Ozacar, A.A., 2011. Segmented African lithosphere beneath the Anatolian region inferred from teleseismic P-wave tomography. *Geophysical Journal International*, v. 184, pp. 1037-1057.
- Blumenthal, M.M., 1963. Le système structural du Taurus sud Anatolies. *Bull. Soc. Géol. Fr. Livre à Mémoire de Professor P. Fallot, Mémoir hors-série*, v. 1, pp. 611-662.
- Bons, P.D., Elburg, M.A., Gomez-Rivas, E., 2012. A review of the formation of tectonic veins and their microstructures. *Journal of Structural Geology*, v. 43, pp. 33-62
- Boray, A., Şaroğlu, F. and Emre, Ö., 1985. Isparta büklümünün kuzey kesiminde D-B daralma için bazı veriler. *Jeoloji Mühendisliği*, v. 23, pp. 9-20.
- Burton-Ferguson, R., Aksu, A.E., Calon, T.J. and Hall, J., 2005. Seismic stratigraphy and structural evolution of the Adana Basin, eastern Mediterranean. *Marine Geology*, v. 221, pp. 189-222.

- Carey, E. and Burinier, B., 1974. Analyse théorique et numérique d'un modèle mécanique élémentaire appliqué à l'étude d'une population de failles. Comptes Rendus Academie Science Paris, D279, pp. 891-894.
- Colby, B.R. 1963: Fluvial sediments – a summary of source, transportation, deposition, and measurement of sediment discharge. United States Geological Survey Bulletin 1181A.
- Cosentino D., Schildgen T. F., Cipollari, P., Faranda, C., Gliozzi, E., Hudácková, N., Lucifora, S. and Strecker, M.R., 2011. Late Miocene surface uplift of the southern margin of the Central Anatolian Plateau, Central Taurides, Turkey. Geological Society of America Bulletin, published online 21 October 2011, doi: 10.1130/B30466.1
- Çağlar, A.T. and Ayhan, A., 1991. Haremköy – Ilgın (Konya) çevresinin jeolojik özellikleri ve linyit yatakları. Selçuk Üniversitesi Mühendislik Mimarlık Fakültesi Dergisi, v. 2, pp. 20-31.
- Çiçek, A., 2009. Neotectonics of the Karamık Graben-Afyon, Isparta Angle, SW Turkey. Master Thesis, Middle East Technical University, Natural and Applied Sciences, Ankara, Turkey.
- Çiçek, A. and Koçyiğit, A., 2009. A NNE-trending active graben in the Isparta Angle, SW Turkey: Karamık Graben, its geometry, age and earthquake potential, Trabajos de Geología, Universidad de Oviedo, v.29, pp. 168-174.
- Çiftçi, B. and Bozkurt, E., 2007. Anomalous stress field and active breaching at relay ramps: a field example from Gediz Graben, SW Turkey. Geological Magazine, v. 144, pp. 687-699.
- Çiner, A., Karabiyikoglu, M., Monod, O., Deynoux, M. and Tuzcu, S., 2008. Late Cenozoic sedimentary evolution of the Antalya Basin, Southern Turkey. Turkish Journal of Earth Sciences, v. 17, pp. 1-41.
- Çuhadır, G., 1977. Akarçay havzası hidrojeolojik etüd raporu, General Directorate of State Hydraulic Works (DSİ) Reports (unpublished, in Turkish).
- Darbaş, G. and Nazik, A., 2010. Micropaleontology and paleoecology of the Neogene sediments in the Adana Basin (South of Turkey). Journal of Asian Earth Sciences, v. 39, pp. 136-147.

- Demirkol, C., 1982. Yalvaç-Akşehir dolayının stratigrafisi ve Batı Toroslarla denetrimi. TMMOB Jeoloji Mühendisliği Dergisi, v. 14, pp. 3-14.
- Demirkol, C. 1984. Sultandağ kuzeybatısının jeolojisi ve Beys,ehir-Hoyran Napları ile ilişkileri. Maden Tektik ve Arama Report, Project TBAG-382.
- Demirkol, C., Sipahi, H., Çiçek, S., Barka A. and Sönmez Ş. 1977. Sultandağının stratigrafisi ve jeoloji evrimi. MTA, Rapor No: 6305.
- Demirkol, C. and Sipahi, H., 1979. Bağkonak – Çimendere - Muratbağı (Isparta) yöresinin jeolojisi. Jeoloji Mühendisliği Dergisi, v.7, pp. 29-38.
- Demirkol, C. and Yetiş, C., 1985. Sultandağ kuzeybatısındaki allokton birimler ve jeolojisi. Jeoloji Mühendisliği Dergisi, v. 22, pp. 3-11.
- Derman, A.S. and Gürbüz, K., 2007. Nature, provenance and relationships of Early Miocene palaeovalley fills, northern Adana Basin, Turkey: their significance for sediment-bypassing on a carbonate shelf. Turkish Journal of Earth Sciences, v. 16, pp.181-209.
- Doğan, A., 1975. Sizma - Ladik (Konya) Civa Sahasının Jeolojisi ve Maden Yatakları Sorunlarının İncelenmesi. I.Ü. Fen Fakültesi Min. Pet. Kürsüsü, Yük. Müh. Diploma Çalışması, İstanbul. 40.
- Dumont, J.F., Poisson, A. and Sahinci, A., 1979. Sur l'existence de coulissements sinistres recentes a l'extémité orientale de l'arc ageen (sud-ouest de la Turquie). Comptes Rendus Acadademie Science Paris, 289: 261-264.
- Dunne, W.M., and Hancock, P.L., 1994. Paleostress analysis of small-scale brittle structures. P.L. Hancock (Editor), Continental deformation. Pergamon Press, Oxford, pp. 101-120.
- Eren Y., 1990. Engilli (Akşehir) ve Bağkonak (Yalvaç) Köyleri Arasında Sultan Dağları Masifinin Tektonik Özellikleri. Türkiye Jeol. Bült. 33/1, 39-50.
- Eren, Y., 1992. Eldes- Gökçeyurt- Derbent (Konya kuzeybatısı) Dolaylarında Kocaçaldağ Yükseltisinin Jeolojisi. S.Ü. Arastırma Fonu, Proje No: 88-026.

- Eren, Y., 1993. Eldes-Derbent-Tepek y-S g t z  Arasinin Jeolojisi, PhD Thesis, S. . Fen Bil. Enst. Konya, Turkey. 224.
- Eren, Y., 1996. Ilgin-Saray n  (Konya) g neyinde Bozda lar Masifinin Yapısal  zellikleri. Geological Bulletin of Turkey, 39: 49-64.
- Ergin, M., Aktar, M.,  zalaybey, S., Tapırdamaz, M.C., Selvi, O. and Tarancıo lu, A., 2009. A high-resolution aftershock seismicity image of the 2002 Sultandagi- ay earthquake (Mw = 6.2), Turkey. Journal of Seismology, 13: 633-646.
- Eri , K.K., Bassant, P. and  lgen, U.B., 2005. Tectono-stratigraphic evolution of an Early Miocene incised valley-fill (Derin ay Formation) in the Mut Basin, Southern Turkey. Sedimentary Geology, 173: 151-185.
- Eyido an, H., G  l , U., Utku, Z., De irmenci 1991. T rkiye B y k Depremleri Makro Sismik Rehberi (1900-1988). Istanbul Technical University, Faculty of Mining, Department of Geophysical Engineering Publications [in Turkish with English abstract]
- Etchecopar, A., Vasseur, D. and Daigni res, M., 1981. An inverse problem in microtectonics for determination of stress tensors from faults striation analysis. Journal of Structural Geology, 3: 51-65.
- Faccenna, C., Bellier, O., Martinod, J., Piromallo, C. and Regard, V., 2006. Slab detachment beneath eastern Anatolia: A possible cause for the formation of the North Anatolian Fault. Earth and Planetary Science Letters, 242: 85-97.
- Flecker, R. Poisson, A. & Robertson, A.H.F., 2005. Facies and palaeogeographic evidence for the Miocene evolution of the Isparta Angle in its regional eastern Mediterranean context. In: Kelling, G., Robertson, A.H.F. & Vanbuchen, F. (eds), Cenozoic Sedimentary Basins of South Central Turkey. Sedimentary Geology 173, 277-314.
- F rst, M., 1955. Yarıkkaya (Yalva ) linyit zuhurları hakkında rapor. MTA Rapor No: 2430 (unpublished).
- Gans, C.R., Beck, S.L., Zandt, G., Biryol, C.B. and Ozacar, A.A., 2009. Detecting the limit of slab break-off in central Turkey: new high-resolution Pn tomography results. Geophysical Journal International, 179: 1566-1572.

- Gibbs, A. D., 1984. Structural evolution of extensional basin margin, Geological Society of London Journal, v: 141, p. 609-620.
- Glennie K. W., 1970. Desert sedimentary environments, Elsevier, Amsterdam, p. 148.
- Glover C, Robertson A.H.F. 1998. Neogene intersection of the Aegean and Cyprus arcs: extensional and strike-slip faulting in the Isparta Angle, SW Turkey. Tectonophysics, 298: 103–132.
- Göğ r, E. and K ral, K., 1969. Kizil ren Dolayinin Jeolojisi. M.T.A. Rapor, 5204.
- G ktunal , K., 1957. Yarıkkaya b lgesi linyitli Neojen'in jeolojik et d . MTA Rap. 2976 (yayımlanmamı .), Ankara.
- G rm  , M., 1984. Kizil ren (Konya), Dolayinin Jeoloji İncelemesi. S.  . Fen Bil. Enst. M. Sc, Konya, Turkey. 67.
- G l, M., 2007. Effects of antecedent topography on reefal carbonate deposition: Early-Middle Miocene of the Adana Basin, S Turkey. Journal of Asian Earth Sciences, 31: 18-34.
- G ly z, E., Kaymakc , N., Meijers, M.J.M., van Hinsbergen, D.J.J., Lefebvre, C.J.C., Vissers, R.L.M., Hendriks, B.W.H., and Peynircio lu, A.A. submitted, Late Eocene synsedimentary folding of the   ekda ı basin, Central Turkey, during the final stages of the K r ehir block-Pontide collision, Tectonophysics 602, 286-299.
- Hippolyte, J. C., Angelier, J., Bergerat, F., Nury, D., Guieu, G., 1993. Tectonic-stratigraphic record of paleostress time changes in the Oligocene basins of the Provence, southern France. Tectonophysics, V. 226(1–4), pp. 15–35.
- Homberg, C., Hu, J.C., Angelier, J., Bergerat, F. and Lacombe, O., 1997. Characterization of stress perturbations near major fault zones: insights from field studies (Jura Mountains) and numerical modelling. Journal of Structural Geology, 19: 703-718.
- Huang, Q., 1988. Computer based method to separate heterogeneous sets of fault slip data into subsets. Journal of structural geology, v. 10, pp. 297-299.

- Huang, Q. and Angelier, J., 1989. Inversion of field data in fault tectonics to obtain the regional stress-II. Using conjugate fault sets within heterogeneous families for computing palaeostress axes. *Geophysical Journal*, v.96, pp. 139-149.
- Hüseyinca, M.Y. and Eren, Y. 2007. Iğın (Konya) kuzeyinin stratigrafisi ve tektonik evrimi. *Selçuk Üniversitesi Mühendislik Mimarlık Fakültesi Dergisi*, v.22, 1-2.
- Hüsing, S.K., Zachariasse, W.J., van Hinsbergen, D.J.J., Krijgsman, W., Inceöz, M., Harzhauser, M., Mandic, O. and Kroh, A., 2009. Oligo-Miocene foreland basin evolution in SE Anatolia: constraints on the closure of the eastern Tethys gateway. In: D.J.J. van Hinsbergen, M.A. Edwards and R. Govers (Editors), *Collision and Collapse at the Africa-Arabia-Eurasia subduction zone: Geological Society, London, Special Publication*, pp. 107-132.
- Ilgar, A., and Nemec, W., 2005. Early Miocene lacustrine deposits and sequence stratigraphy of the Ermenek Basin, Central Taurides, Turkey. *Sedimentary Geology*, v: 173(1); pp. 233-275.
- Janson, X., van Buchem, F.S.P., Dromart, G., Eichenseer, H.T., Dellamonic, X., Boichard, R., Bonnaffe, F. and Eberli, G.P., 2010. Architecture and facies differentiation within a Middle Miocene carbonate platform, Ermenek, Mut Basin, southern Turkey. In: F.S.P. van Buchem, K.D. Gerdes and M. Esteban (Editors), *Mesozoic and Cenozoic Carbonate Systems of the Mediterranean and the Middle East: Stratigraphic and Diagenetic Reference Models. Geological Society, London, Special Publications*, pp. 265-290.
- Kaaden, W.der G., 1966. The significance and distribution of glaucophane rocks in Turkey. *M.T.A Bull.*, 67: 36-67.
- Karabıyıkoglu, M., Tuzcu, S., Çiner, A., Deynoux, M., Örcen, S. and Hakyemez, A., 2005. Facies and environmental setting of the Miocene coral reefs in the late-orogenic fill of the Antalya Basin, western Taurides, Turkey: implications for tectonic control and sea-level changes. *Sedimentary Geology*, 173: 345-371.
- Karakaya, N., 1991. Altiekin (Konya) civarının jeolojisi ve mineralojik-petrografik incelenmesi. MSc thesis, Selçuk University, Konya.
- Karayığit , A.I., Akgün, F., Gayer, R.A., Temel, A., 1999. Quality, palynology, and paleoenvironmental interpretation of the Iğın lignite, Turkey. *International Journal of Coal Geology*, v. 38: 219-236.

- Kaymakci, N., Inceöz, M., Ertepinar, P. and Koç, A., 2010. Late Cretaceous to Recent kinematics of SE Anatolia (Turkey). In: M. Sosson, N. Kaymakci, R.A. Stephenson, F. Bergerat and V. Starostenko (Editors), *Sedimentary basin tectonics from the Black Sea and Caucasus to the Arabian Platform*. Geological Society, London, Special Publications, pp. 409-435.
- Kaymakci, N., Özçelik, Y., White, S.H. and van Dijk, P.M., 2009. Tectono-stratigraphy of the Çankiri Basin: late Cretaceous to early Miocene evolution of the Neotethyan suture zone in Turkey. In: D.J.J. van Hinsbergen, M.A. Edwards and R. Govers (Editors), *Collision and Collapse at the Africa-Arabia-Eurasia subduction zone*, Geological Society of London Special Publication, pp. 67-106.
- Keller, J., Jung, D., Burgath, K. and Wolff, F., 1977. Geologie und Petrologie des Neogenen Kalkalivulkanismus von Konya (Erenler Dagi, Alacadag Massiv, Zentral Anatolian). *Geologisches Jahrbuch*, B. 25: 37-117.
- Keskin, M., 2003. Magma generation by slab steepening and breakoff beneath a subduction-accretion complex: An alternative model for collision-related volcanism in Eastern Anatolia, Turkey. *Geophysical Research Letters*, 30(24): 8046, doi: 10.1029/2003GL018019.
- Khair, K. and Tsokas, G.N., 1999. Nature of the Levantine (eastern Mediterranean) crust from multiple-source Werner deconvolution of Bouguer gravity anomalies. *Journal of Geophysical Research*, 104: 25469-25478.
- Kissel, C. and Poisson, A., 1987. Étude paléomagnétique préliminaire des formations cénozoïques des Bey Dagları (Taurides occidentales, Turquie). *Comptes Rendus Academie Science Paris*, 304, Série II(8): 343-348.
- Kleinspehn, K. L., Pershing, J.C., and Teyssier, C., 1989, Paleostress stratigraphy: A new technique for analyzing tectonic control on sedimentary-basin subsidence: *Geology*, v. 17, p. 253–256. Koppers, A.A.P., 2002. ArArCALC-software for ⁴⁰Ar/³⁹Ar age calculations. *Computers & Geosciences*, 28: 605-619.
- Koç, A., Kaymakci, N., van Hinsbergen, D. J.J., Kuiper, K. F., Vissers, R. L.M., 2012. Tectono-Sedimentary evolution and geochronology of the Middle Miocene Altnapa Basin, and implications for the Late Cenozoic uplift history of the Taurides, southern Turkey. *Tectonophysics*, v. 532-535, pp.134-155.
- Koçyiğit, A., Ünay, E., and Saraç, G. 2000. Episodic graben formation and extensional neotectonic regime in west central Anatolia and the Isparta Angle: a case study

in the Akşehir-Afyon Graben, Turkey. Geological Society, London, Special Publications, 173, 405-421.

Koçyiğit, A., Bozkurt, E., Kaymakci, N., Şaroğlu, F., 2002. 3 Şubat 2002 Çay (Afyon) depreminin kaynağı ve ağır hasarın nedenleri: Akşehir Fay Zonu, Jeolojik ön rapor. Orta Doğu Teknik Üniversitesi, Jeoloji Mühendisliği Bölümü, Tektonik Araştırma Birimi, ANKARA.

Koçyiğit, A. and Özacar, A. A., 2003. Extensional Neotectonic Regime through the NE edge of the outer Isparta Angle, SW Turkey: New field and seismic data. Turkish Journal of Earth Sciences, v. 12, pp. 67-90.

Koçyiğit, A. and Deveci, Ş., 2007. A N–S-trending active extensional structure, the Şuhut (Afyon) Graben: Commencement Age of the extensional neotectonic period in the Isparta Angle, SW Turkey. Turkish J. Earth Sci., 16 (2007), pp. 391–416.

Koopman, M., 2011. A fault kinematic and geomorphological study of the Late Cenozoic Iğın Basin, Central Anatolia, Turkey. MSc Thesis, Utrecht University, The Netherlands.

Kuiper, K.F., Deino, A.L., Hilgen, F.J., Krijgsman, W., Renne, P.R. and Wijbrans, J.R., 2008. Synchronizing rock clocks of Earth history. Science, 320: 500-504.

Lahn, E., 1940. Aksaray – Konya – Isparta Mıntıkasının Jeolojik Hılasası. M.T.A. Deleme Raporu. No: 1240 (Unpublished).

Lahn, E., 1945. Batı Toros göllerinin jeomorfolojisi. M.T.A Dergisi, No: 2 (34): 387-400.

Larsen, P.H., 1988. Relay structures in a Lower Permian basementinvolved extension system, East Greenland. Journal of Structural Geology 10, 3–8.

Lillesand, M. and Keifer, R.W., 1999. Remote sensing and image interpretation, 4th edition, John Wiley and Sons, Inc, U.S.A.

Mackintosh, P. and Robertson, A.H.F., 2009. Structural and sedimentary evidence from the northern margin of the Tauride platform in south central Turkey used to test alternative models of Tethys during Early Mesozoic time. Tectonophysics, 473: 149-172.

- Meijers, M.J.M., Kaymakci, N., van Hinsbergen, D.J.J., Langereis, C.G., Stephenson, R.A. and Hippolyte, J.-C., 2010. Late Cretaceous to Paleocene oroclinal bending in the Central Pontides (Turkey). *Tectonics*, 29: TC4016, doi:10.1029/2009TC002620.
- Meijers, M. J. M., van Hinsbergen, D.J.J., Dekkers, M.J., Altiner, D., Kaymakci, N., Langereis, C.G. and Stephenson, R.A., 2011. Pervasive Paleogene remagnetization of the central Taurides fold-and-thrust belt (southern Turkey) and implications for rotations in the Isparta Angle. *Geophysical Journal International*, 184: 1090-1112.
- Mein, P. 1999. European Miocene mammal biochronology. Pp. 25–38 in Rössner, G.E. and Heissig, K. (eds.). *The Miocene Land Mammals of Europe*. Munich: Verlag Dr. Friedrich Pfeil, 515 pp.
- Miall, A.D., 1996. *The Geology of fluvial deposits, Sedimentary Facies. Basin Analysis and Petroleum Geology*. Springer, Berlin, pp. 582.
- Miall, A.D. and Smith, N. D., 1989. *Rivers and their deposits*. Soc. Econ, Paleont And Mineral. Tulsa, Oklahoma.
- Min, K., Mundil, R., Renne, P. R. and Ludwig, K.R., 2000. A test for systematic errors in $^{40}\text{Ar}/^{39}\text{Ar}$ geochronology through comparison with U/Pb analysis of a 1.1-Ga rhyolite. *Geochimica et Cosmochimica Acta*, 64: 73-98.
- Walker, T. R., 1967. Formation of red beds in modern and ancient deserts. *Bulletin of the Geological Society of America*, v. 78, pp. 353-368.
- Morgan, L. E., Renne, P.R., Taylor, R.E. and Wolde, G., 2009. Archaeological age constraints from extrusion ages of obsidian: Examples from the Middle Awash, Ethiopia. *Quaternary Geochronology*, 4: 193-203.
- Morris, A. and Robertson, A. H. F., 1993. Miocene remagnetisation of carbonate platform and Antalya Complex units within the Isparta Angle, SW Turkey. *Tectonophysics*, 220: 243-266.
- Niehoff, W., 1961. 1/100.000 ölçekli Akşehir 90/2 paftası, Ilgin 91/1, 91/3 ve 91/4 paftaları üzerinde 1961 yaz mevsiminde yapılmış revizyon çalışmaları hakkında rapor. . M.T.A. Rapor, 3387.

- Nier, A.O., 1950. A Redetermination of the Relative Abundances of the Isotopes of Carbon, Nitrogen, Oxygen, Argon, and Potassium. *Physical Review*, 77: 789.
- Öğütçü, Z., Horason, G. and Kalafat, D., 2011. Investigation of microseismic activity sources in Konya and its vicinity, central Turkey. *Natural Hazards*.
- Okay, A.I. and Özgül, N., 1984. HP/LT metamorphism and the structure of the Alanya Massif, Southern Turkey: an allochthonous composite tectonic sheet. In: J.E. Dixon and A.H.F. Robertson (Editors), *The Geological Evolution of the Eastern Mediterranean*, Geological Society Special Publication, pp. 429-439.
- Okay, A.I., Satir, M., Maluski, H., Siyako, M., Monié, P., Metzger, R. and Akyüz, S., 1996. Paleo- and Neo-Tethyan events in northwestern Turkey: geologic and geochronologic constraints. In: A. Yin and T.M. Harrison (Editors), *The tectonic evolution of Asia*. Cambridge University Press, Cambridge, pp. 420-441.
- Okay, A. I., and O. Tüysüz (1999), Tethyan sutures of northern Turkey, in *Mediterranean Basins: Tertiary Extension Within the Alpine Orogen*, edited by B. Durand et al., *Geol. Soc. Spec. Publ.*, 156, 475.
- Okay, A.I., Zattin, M. and Cavazza, W., 2010. Apatite fission-track data for the Miocene Arabia-Eurasia collision. *Geology*, 38: 35-38.
- Över, S., Ozden, S. and Ulugenc, U.C., 2004. Late Cenozoic stress distribution along the Misis Range in the Anatolian, Arabian, and African plate intersection region, SE Turkey. *Tectonics*, 23: TC3008, doi:10.1029/2002TC001455.
- Özcan, A., Göncüoğlu, M.C., Turhan, N., Uysal, Ş., Şentürk, K. ve Işık, A. 1988. Late Paleozoic evolution of the Kütahya-Bolkardağ Belt. *METU Journal of Pure and Appl. Sci.* 21, 1/3, 211-220.
- Özcan, A., Göncüoğlu, M.C., Turhan, N., Şentürk, K., Uysal, S. and Isik, A., 1990. Konya-Kadinhani- Ilgin Dolayinin Temel Jeolojisi. *M.T.A. Rapor*, 9535.
- Özkan, A.M., 1998. Konya Batısındaki Neojen Çökellerinin Stratigrafisi ve Sedimentolojisi, PhD Thesis, S.Ü. Fen Bil. Enst., Konya, Turkey, 208 pp.
- Özkan, A.M. and Sögüt, A.R., 1999. Dilekçi (Konya batısı) çevresindeki Neojen çökellerinin stratigrafisi. *Journal of Engineering Science*, 5: 1131-1138.

- Özer, E., Koç, H. and Ozsayar, T.Y., 2004. Stratigraphical evidence for the depression of the northern margin of the Menderes–Tauride Block (Turkey) during the Late Cretaceous. *Journal of Asian Earth Sciences*, 22: 401-412.
- Peacock, D.C.P., Sanderson, D.J., 1991. Displacements, segment linkage and relay ramps in normal fault zones. *Journal of Structural Geology* 13, 721–733.
- Peacock, D.C.P., Sanderson, D.J., 1994. Geometry and development of relay ramps in normal fault systems. *Bulletin of the American Association of Petroleum Geologists* 78, 147–165.
- Pekmezciler, S., 1958. Yarikkaya (Isparta vilayeti) linyit aramaları hakkında rapor. MTA Rapor No: 2640 (Unpublished).
- Poisson, A., Wernli, R., Sagular, E.K. and Temiz, H., 2003. New data concerning the age of the Aksu Thrust in the south of the Aksu valley, Isparta Angle (SW Turkey): consequences for the Antalya Basin and the Eastern Mediterranean. *Geological Journal*, 38: 311-327.
- Pourteau, A., Candan, O. and Oberhänsli, R., 2010. High-Pressure metasediments in central Turkey: constraints on the Neotethyan closure history. *Tectonics*, 29: TC5004, doi:10.1029/2009TC002650.
- Ramsey, J.M. and F.M. Chester, 2004. Hybrid fracture and the transition from extension fracture to shear fracture. *Nature*, v: 428(6978), pp. 63-66.
- Ricou, L.E., Argyriadis, I. and Marcoux, J., 1975. L'axe calcaire du Taurus, un alignement de fenêtres arabo-africaines sous des nappes radiolaritiques, ophiolitiques et métamorphiques. *Bulletin de la Société Géologique de France*, 17: 1024-1043.
- Robertson, A., 2000. Mesozoic-Tertiary tectonic –sedimentary evolution of a south Tethyan oceanic basin and its margins in southern Turkey. In: Bozkurt, E., Winchester, J.A. & Piper, J.D.A. (eds) *Tectonics and Magmatism in Turkey and the Surrounding Area*. Geological Society, London, Special Publications, v. 173, pp. 43–82.
- Şafak, Ü., Kelling, G., Gökçen, N.S. and Gürbüz, K., 2005. The mid-Cenozoic succession and evolution of the Mut basin, southern Turkey, and its regional significance. *Sedimentary Geology*, 173: 121-150.

- Saraç, G., 2001. Türkiye omurgalı fosil yatakları, Maden Tetkik ve Arama Genel Müdürlüğü Raporu (unpublished), Ankara.
- Schildgen, T.F., Cosentino, D., Caruso, A., Buchwaldt, R., Yıldırım, C., Bowring, S.A., Rojay, B., Echtler, H., Strecker, M.R., 2012. Surface expression of Eastern Mediterranean slab dynamics: Neogene topographic and structural evolution of the SW margin of the Central Anatolian Plateau, Turkey. *Tectonics*, 31(2). DOI: 10.1029/2011TC003021
- Schlische, R.W., 1995, Geometry and origin of fault-related folds in extensional settings: *American Association of Petroleum Geologists Bulletin*, v. 79, p. 1661-1678.
- Scholz, H. C. and Contreras, J. C., 1998. Mechanics of continental rift architecture. *Geology*, v. 26(11), pp. 967-970.
- Şengör, A.M.C., Özeren, S., Genç, T. and Zor, E., 2003. East Anatolian high plateau as a mantle-supported, north-south shortened domal structure. *Geophysical Research Letters*, 30(24): 8045, doi: 10.1029/2003GL017858.
- Şengör, A.M.C. and Yilmaz, Y., 1981. Tethyan evolution of Turkey: A plate tectonic approach. *Tectonophysics*, 75: 181-241.
- Soliva, R. and Benedicto, A., 2004. A linkage criterion for segmented normal faults. *Journal of Structural Geology*, 26: 2251-2267.
- Steiger, R.H. and Jäger, E., 1977. Subcommittee on geochemistry: convention on the use of decay constants in geo- and cosmochemistry. *Earth and Planetary Science Letters*, 36: 359-362.
- Steininger, F. 1999. Chronostratigraphy, geochronology and biochronology of the Miocene "European Land Mammal Mega-Zones (ELMMZ)" and the Miocene "Mammal Zones (MN-Zones)". Pp. 9–24 in Rössner, G.E. and Heissig, K. (eds.). *The Miocene Land Mammals of Europe*. Munich: Verlag Dr. Friedrich Pfeil, 515 pp.
- Şaroğlu, F., Emre, Ö., and Boray, A. 1987. Türkiye'nin Diri Fayları ve Depremselliği [Seismicity and Active Faults of Turkey]. General Directorate of Mineral Research and Exploration (MTA) Report No. 8174.

- Talbot, M.R. and Allen, P.A., 1996. Lakes. In reading, H.G. (ed.) Sedimentary environments: Process, Facies, Stratigraphy. Blackwell Science Ltd. Oxford.83-124.
- Taymaz, T. and Tan, O., 2001. Source parameters of June 6, 2000 Orta-Çankırı (Mw=6.0) and December 15, 2000 Sultandağ-Akşehir (Mw=6.0) earthquakes obtained from inversion of teleseismic P and SH body-waveforms. Scientific Activities 2001 Symposia Book, İstanbul Technical University, Faculty of Mines, May 8, 2001, İstanbul, Turkey, 96–107.
- Taymaz, T., Tan, O. and Yolsal, S., 2004. Seismotectonics of western Turkey: a synthesis of source parameters and rupture histories of Recent earthquakes. Eos Transactions AGU, 85: 47.
- Temel, A., Gündoğdu, M.N. and Gourgaud, A., 1998. Petrological and geochemical characteristic of Cenozoic high-K calcalkaline volcanism in Konya, Central Anatolia, Turkey. Journal of Volcanology and Geothermal Research, 85: 327-354.
- Torsvik, T.H. and Cocks, L.R.M., 2009. The Lower Palaeozoic palaeogeographical evolution of the northeastern and eastern peri-Gondwanan margin from Turkey to New Zealand. In: M.G. Bassett (Editor), Early Palaeozoic Peri-Gondwana terranes: New insights from tectonics and biogeography. Geological Society, London, Special Publications, pp. 3-21.
- Tunoğlu, C. and Çelik, M., 1995. The Ostracoda association and environmental characteristics of Lower Miocene squence of Ilgın (Konya) District, Central Anatolia, Turkey, Ostracoda and Biostratigraphy, Riha (ed.), 229-235 Balkema, Rotterdam.
- Trudgill, B. and Cartwright, J., 1994. Relay-ramp forms and normal-fault linkages, Canyonlands National Park, Utah. Geological Society of America Bulletin, 106 (9): 1143-1157.
- Umut, M., Karabıyıkoglu, M., Saraç, G., Bulut, V., Demirci, A. R., Erkan, M., Kurt, Z., Metin, S., and Özgönül, E., 1987. Tuzlukçu-Ilgın-Doğanbey (Konya ili) ve dolayının jeolojisi. M.T.A. Rapor No: 8246 (Unpublished).
- Umut, M., Bilgin, A., Z., and Güner, E., 1990. Kadınhanı – Sarayönü – Sülüklü (Konya) dolayının jeolojisi. M.T.A. Rapor No: 9030 (Unpublished).


- Van Hinsbergen, D.J.J., 2010. A key extensional metamorphic complex reviewed and restored: the Menderes Massif of western Turkey. *Earth-Science Reviews*, 102: 60-76.
- Van Hinsbergen, D.J.J., Dekkers, M.J., Bozkurt, E. and Koopman, M., 2010a. Exhumation with a twist: paleomagnetic constraints on the evolution of the Menderes metamorphic core complex (western Turkey). *Tectonics*, 29: TC3009, doi:10.1029/2009TC002596.
- Van Hinsbergen, D.J.J., Dekkers, M.J. and Koç, A., 2010b. Testing Miocene remagnetization of Bey Dagları: Timing and amount of Neogene rotations in SW Turkey. *Turkish Journal of Earth Sciences*, 19: 123-156.
- Van Hinsbergen, D.J.J., Kaymakci, N., Spakman, W. and Torsvik, T.H., 2010c. Reconciling the geological history of western Turkey with plate circuits and mantle tomography. *Earth and Planetary Science Letters*, 297: 674-686.
- Vissers, R.L.M, Koopman, M., Koç, A. and Kaymakci, N., 2012. Structure and tectonics of the Neogene Iğın Basins. 65th Geological Congress of Turkey, Ankara.
- Walker, R.E. and James, N.P., 1992. Facies Models: Response to Sea-level Change. *Geol. Ass. Can. Waterloo, Ontario*, p: 238.
- Wedding, H., 1954. Yalvaç'ın şimalinde Yarıkkaya linyit zuhuru hakkında rapor: MTA Rapor No: 2200 (Unpublished)
- Wiesner, K., 1968. Konya civa yatakları ve bunlar üzerindeki etütler. *M.T.A. Dergisi*, Sayı, 70: 178-213.
- Yağmurlu, F., 1991a. Stratigraphy and depositional environments of Yalvaç-Yarıkkaya Neogene basin, SW-Anatolia. *Geological Bulletin of Turkey*, 34: 9-19.
- Yağmurlu, F., 1991b. Yalvaç-Yarıkkaya Neojen havzasının tektono-sedimanter özellikleri ve yapısal evrimi. *M.T.A. Dergisi*, Sayı, 112: 1-13.
- Yağmurlu, F., Savaşçın, Y, Ergün, M. 1997. Relation of alkaline volcanism and active tectonism within the evolution of the Isparta Angle, SW Turkey. *Journal of Geology* 105: 717-728.

- Yamaji, A., 2000. Multiple inverse method: a new technique to separate stresses from heterogeneous fault-slip data. *Journal of Structural Geology*, v. 22, pp. 441-452.
- Yetiş, C., 1988. Reorganization of the Tertiary stratigraphy in the Adana basin, southern Turkey. *Newsletters in Stratigraphy*, 20: 43-58.

APPENDIX A

PUBLISHED RESEARCH PAPER

Published research paper from the thesis is given in the next pages.




ELSEVIER

Tectonophysics 532–535 (2012) 134–155

Contents lists available at SciVerse ScienceDirect

Tectonophysics

journal homepage: www.elsevier.com/locate/tecto



Tectono-Sedimentary evolution and geochronology of the Middle Miocene Altınapa Basin, and implications for the Late Cenozoic uplift history of the Taurides, southern Turkey

Ayten Koç^{a,*}, Nuretdin Kaymakci^a, Douwe J.J. van Hinsbergen^{b,c}, Klaudia F. Kuiper^d, Reinoud L.M. Vissers^e

^a Department of Geological Engineering, Middle East Technical University, Ankara, 06531, Turkey
^b Physics of Geological Processes, University of Oslo, Sem Sælands vei 24, NO-0316 Oslo, Norway
^c Center for Advanced Study, Norwegian Academy of Science and Letters, Drammensveien 78, 0271 Oslo, Norway
^d Department of Petrology, Free University of Amsterdam, De Boelelaan 1085, 1081 HV Amsterdam, The Netherlands
^e Department of Earth Sciences, Utrecht University, 3508 TA Utrecht, The Netherlands

ARTICLE INFO

Article history:
Received 22 July 2011
Received in revised form 23 December 2011
Accepted 18 January 2012
Available online 1 February 2012

Keywords:
Miocene basins in Turkey
⁴⁰Ar/³⁹Ar geochronology
Paleostress inversion
Eastern Mediterranean

ABSTRACT

The Tauride range in southern Turkey is flanked and overlain by Neogene sedimentary basins. To the south and on top of the high range, these basins are mainly marine, whereas poorly studied intramontane basins dominated by continental deposits are exposed to the north. In this paper, we study the stratigraphy and structure of the continental Altınapa Basin, and provide ⁴⁰Ar/³⁹Ar geochronology for volcanic deposits in the stratigraphy. The stratigraphy can be subdivided into a Lower Group, displaying ~400 m of fining upward fluvio-lacustrine sediments, unconformably overlain by an Upper Group with ~500 m of lacustrine deposits, andesitic lavas and volcanoclastic sediments. ⁴⁰Ar/³⁹Ar dating of three volcanoclastic samples across the Upper Group provide 11.8–11.6 Ma ages. The Altınapa Basin is an extensional basin, which formed predominantly due to N–S to NE–SW directed stretching. The main basin forming phase occurred during deposition of the Lower Group, prior to 11.8 Ma. Paleostress inversion analyses demonstrate uniaxial stress, with highly variable extension directions that are consistent with currently observed seismicity patterns. The Middle Miocene extension history of the Altınapa Basin is consistent with a regional pattern of Middle Miocene NE–SW to NW–SE extension north of the Cyprus subduction zone. This suggests that the Cyprus subduction zone has been in retreat relative to central Anatolia since at least Middle Miocene time. The continental Altınapa Basin is currently at an elevation of ~1 km, whereas partly contemporaneous marine sediments in the Mut Basin that lies on top of the Tauride range are elevated to 2 km. This shows strong late Cenozoic differential uplift in southern Turkey, with at least 1 km more uplift of the Tauride range than of the intramontane basins to the north. We conclude that the current high elevation of the Taurides is related to late Neogene extension and does not result from the late Cretaceous to perhaps Oligocene folding and thrusting that deformed the rocks in the range.

© 2012 Elsevier B.V. All rights reserved.

1. Introduction

In the eastern Mediterranean region (Fig. 1), convergence between Africa and Europe since the Cretaceous was accommodated by northward subduction of various branches of the Neotethys Ocean (Barrier and Vrielynck, 2008; Şengör and Yılmaz, 1981). As a result, the geology of Turkey includes a number of suture zones that demarcate the former positions of now subducted oceans. The most important of these is the İzmir–Ankara–Erzincan suture zone, where the Pontides to the north, belonging to Eurasia since the early Mesozoic (Torsvik and Cocks, 2009), and the Tauride–Anatolide Platform to the south, rifted away from Gondwana in the Triassic, collided after the complete subduction of the Northern Branch of the Neotethys. The collision of the Tauride–Anatolide Platform with the Pontides started at the end of Cretaceous and may have lasted until the end of the Eocene (Kaymakci et al., 2009; Meijers et al., 2010; Okay and Özgül, 1984; van Hinsbergen et al., 2010c). A second Cretaceous to Paleocene subduction zone existed to the south of the İzmir–Ankara suture zone, between the Kırşehir Block and the Taurides in central Turkey (the Inner Tauride Suture; e.g. Okay et al., 1996; Pourteau et al., 2010) and led to the formation of the Tauride fold-thrust belt in southern Turkey.

South of the Taurides, oceanic crust of the Southern Branch of the Neotethys still subducts today in the Cyprus subduction zone (Khair and Tsokas, 1999) (Fig. 1). In Eastern Turkey, this Southern Branch

* Corresponding author. Tel.: +90 3122105743.
E-mail address: kayten@metu.edu.tr (A. Koç).

0040-1951/\$ – see front matter © 2012 Elsevier B.V. All rights reserved.
doi:10.1016/j.tecto.2012.01.028

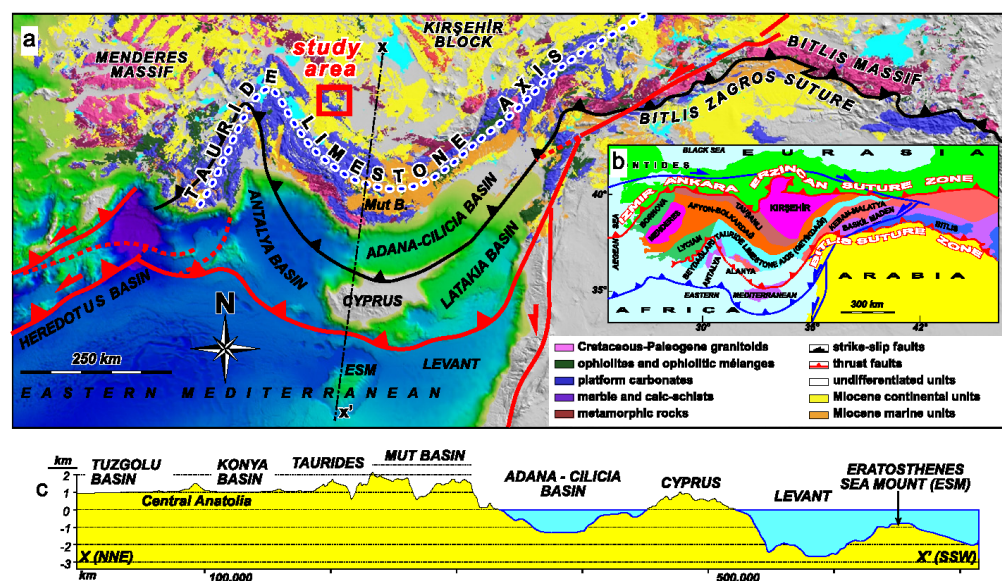


Fig. 1. a) Major tectonic zones of Turkey (modified from Okay et al. (1996) and Kaymakci et al. (2010)). b) simplified geological map of southern Turkey overlaid on an SRTM topographic and bathymetric image (geological map is simplified from MTA 1/500,000 map series). c) Profile along the line XX'. Note that altitude of the Tauride range is ~1 km higher than the elevation of central Anatolia.

has been entirely subducted and is demarcated by the Bitlis suture zone, with the arrest of subduction at the end of the Middle Miocene (Faccenna et al., 2006; Hüsing et al., 2009; Keskin, 2003; Okay et al., 2010; Şengör and Yılmaz, 1981; Şengör et al., 2003). Subduction below the Taurides is in its latest stages, and was probably associated with slab break-off and slab roll-back processes since the Middle Miocene (Biriyol et al., 2011; Faccenna et al., 2006; Gans et al., 2009; van Hinsbergen et al., 2010c).

The Tauride fold-thrust belt forms a carbonate-dominated mountain range in southern Turkey, with dominantly southward thrusting until Late Eocene time (Altınır et al., 1999; Andrew and Robertson, 2002; Mackintosh and Robertson, 2009; Meijers et al., 2011; Özer et al., 2004; Ricou et al., 1975). Although the belt shows large wavelength folds and thrusts, its high topography today is bounded by normal faults associated with Neogene sedimentary basins. These basins filled by marine to continental sediments and volcanics, formed in the overriding plate of the present-day Cyprus subduction zone and their development may shed light on the geodynamic evolution of the eastern Mediterranean subduction zone since the Miocene. The dominantly marine basins are located mainly in the southern limb of the belt and include the well-described Adana, Mut and Antalya (including the Manavgat, Köprüçay and Aksu) basins (e.g. Bassant et al., 2005; Çiner et al., 2008; Darbas and Nazik, 2010; Derman and Gürbüz, 2007; Eriş et al., 2005; Gül, 2007; Janson et al., 2010; Karabiyiköğlu et al., 2005; Poisson et al., 2003; Yetiş, 1988). A diachronous marine transgression flooded the southern part of the belt in Cyprus from the late Oligocene onward, and reached the Antalya, Mut and Adana regions in the north during the Early Miocene (Bassant et al., 2005).

To the north of the present-day Taurides, intramontane basins started to form during an ill-defined time interval in the Neogene. These include the Alınapa, Yalvaç and Iğın basins (Fig. 2), descriptions of which are limited to Turkish language literature (Eren,

1993, 1996; Göğer and Kural, 1969; Özcan et al., 1990; Özkan, 1998; Özkan and Söğüt, 1999; Yağmurlu, 1991a,b). The Alınapa Basin, located in the eastern limb of the Isparta Angle (Blumenthal, 1963) (Fig. 2), is one of the best exposed of these intramontane basins. It has a clastic and volcano-sedimentary infill of more than 850 m thick and rests on metamorphosed Mesozoic carbonates of the Tauride Belt, as well as on late high-pressure rocks of the inner-Tauride suture zone (Pourteau et al., 2010). These high-pressure rocks, with Cretaceous to Paleocene metamorphic ages, include Silurian–Permian meta-carbonates, flysch-type metaclastics and meta-magmatic rocks (Karakaya, 1991), and massive Triassic–Cretaceous platform-type meta-carbonates, meta-dolerites and continental meta-clastics (Eren, 1996).

In this paper, the stratigraphic succession of the Alınapa Basin is described and $^{40}\text{Ar}/^{39}\text{Ar}$ geochronology from volcanics is provided. In addition, we show results from kinematic studies aided by remote-sensing and field mapping techniques, and discuss the evolution of the basin in the context of the regional geodynamics and uplift of the Anatolian Plateau during the late Neogene.

2. Lithostratigraphy

The infill of the Alınapa Basin is dominated by continental clastic sediments, lava flows and volcanoclastic deposits. It was first mapped by Göğer and Kural (1969), who included the entire Neogene stratigraphy in the Dilekçi Formation. After this pioneering study, various studies including Eren (1992, 1993, 1996), Özkan (1998), Özkan and Söğüt (1999), concentrated mainly on the Neogene stratigraphy. Eren (1993) made a detailed subdivision of the Neogene Dilekçi Formation into six lithostratigraphic units (Fig. 3). Özkan (1998) and Özkan and Söğüt (1999) provided additional stratigraphic data and introduced a revised stratigraphy and proposed five formations (Fig. 3). For the sake of convenience, we revise the lithostratigraphy

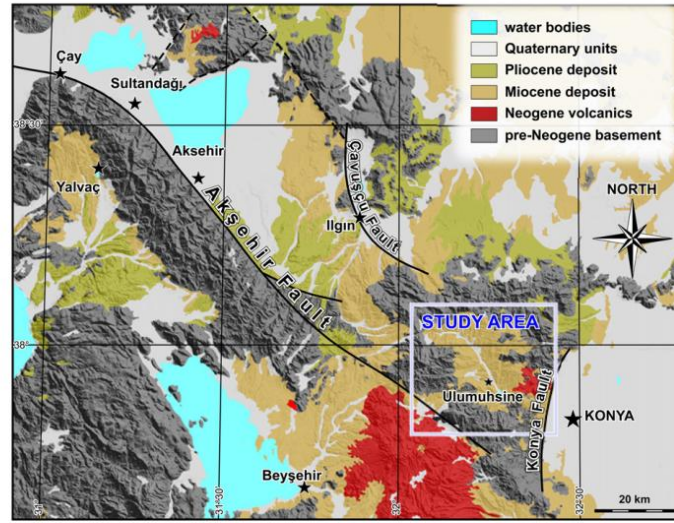


Fig. 2. Generalized geological map of the study area and its surrounding.

of the Neogene deposits in the Altınapa Basin and define three main stratigraphic units, namely the Lower and Upper Altınapa groups, and the Topraklı Formation, separated by regional unconformities. Below, we describe their lithology, age and contact relationships, and provide a first-order interpretation of their depositional environments (Fig. 4).

2.1. Lower Altınapa Group (LAG)

The LAG is characterized by conglomerate, sandstone and siltstone at the bottom, grading upwards and basinwards into claystone, marl, sandstone and medium to thick-bedded massive lacustrine limestones. These lithologies were included in the Dilekçi Formation by Göger and Kırıl (1969). Özkan and Söğüt (1999) divided this sequence into three separate formations, in which a lower conglomeratic unit is

named “Sille Formation”, an intermediate stromatolitic limestone unit “Yalıtepe Formation” and an upper limestone/marl unit “Ulumuhsine Formation” (4). These units are well-exposed along the Kızılören Fault (Figs. 5 and 6a), near Dereşıklar (Fig. 7) and north of Küçük Muhsine (Fig. 8) which was selected as the type locality for the LAG. It unconformably overlies Mesozoic basement, and is unconformably overlain by the Upper Altınapa Group.

The sequence starts at the bottom with coarse, angular, well-cemented, limestone-dominated breccias that grade upwards into reddish/purple, unsorted and polymict, subangular to subrounded pebble to boulder-size (occasionally up to 1 m diameter) conglomerates (Fig. 6b), overlying the high-relief carbonate basement of the Loras Mountain. At stratigraphically higher levels, sedimentary structures such as pebble imbrications and channel deposits are occasionally observed. The large clasts are dispersed in a poorly sorted, finer

Age	Niehoff, 1961 Konya, Iğın	Wiesner, 1968 Sızma, Ladik	Göger & Kırıl, 1969 Kızılören	Görmüş, 1984 Kızılören	Özcan et al., 1988 Kulaşya, Konya	Eren, 1993 Erdag, Topraklı	Özkan & Söğüt, 1999 Dilekçi, Konya	Revised Division	
QUATERNARY	Alluvium	Alluvium	Alluvium	Alluvium		Alluvium	Alluvium	Alluvium	Alluv.
CENOZOIC	Tertiary	Neogene Cover	Dilekçi Formation	Erenlerdağ Volcanics	Dilekçi Formation	Topraklı Formation	Topraklı Formation	Topraklı Formation	Topraklı Formation
							Yürükler Formation	Yürükler Formation	
						Dilekçi Formation	K. Muhsine Formation	K. Muhsine Formation	
							Ulumuhsine Formation	Ulumuhsine Formation	
CENOZOIC	Tertiary	Neogene Cover	Dilekçi Formation	Erenlerdağ Volcanics	Dilekçi Formation		Yalıtepe Formation	Yalıtepe Formation	U. Altınapa Group
							Sille Formation	Sille Formation	
								K. Muhsine Formation	
								Ulumuhsine Formation	
CENOZOIC	Tertiary	Neogene Cover	Dilekçi Formation	Erenlerdağ Volcanics	Dilekçi Formation			Ulumuhsine Formation	L. Altınapa Group
								Yalıtepe Formation	
								Sille Formation	

Fig. 3. Stratigraphic classification of the study area and its surroundings in previous studies, modified from Özkan (1998).

AGE	UNITS	LITHOLOGY	DESCRIPTION
Quat.	Alluvium		alluvial plain and alluvial fan sediments (gravel, sand, silt, and mud)
Plio-Late Miocene	Topraklı Fm.		partly consolidated, unsorted, matrix supported polygenic red conglomerate, sandstone and mudstone
			partly consolidated, unsorted, matrix supported polygenic red conglomerate, sandstone and mudstone
Middle Miocene	Upper Altınapa Group (UAG)		Ar/Ar age: 11.61 ± 0.24 Ma. pinkish block-and-ash deposits (clasts are derived from ~90% volcanics, and ~10% limestone) white tuff/tuffite
			creamy-white, thick-bedded, well cemented algal limestone.
			intercalations of marl and tuffites. Usually maximum bed thickness is 20–30 cm.
			pyroclastic material, volcanic blocks (60–70 cm) and lava flows with andesitic composition Ar/Ar age: 11.67 ± 0.24 Ma unwelded ignimbrite with floating pumice fragments (3–4 cm) Ar/Ar age is 11.88 ± 0.26 Ma
Early-Middle Miocene	Lower Altınapa Group (LAG)		white-creamy thick-bedded, well cemented algal limestone.
			variegated siltstone, shale and marl alternation, intercalated with thinly bedded limestone, and organic rich horizons.
			yellowish sandstone-bluish shale marl alternation sandstones are bioturbated, occasionally cross-bedded, fossil (fresh water gastropods) rich horizons. polygenic conglomerates clasts of which derived from limestones (80%) and nearby ophiolitic rocks (20%). Pebbles are unsorted, angular to subangular, grain-supported. The clasts are pebble sized and generally smaller than 10cm diameter. poorly sorted, matrix supported, upwards fining, polygenic conglomerates clasts of which derived from limestones (60%) and nearby ophiolitic rocks (40%).
Pre-Miocene	Basement		NONCONFORMITY Silurian-Permian meta-carbonates, turbiditic meta-clastics and meta-igneous rocks, Triassic-Cretaceous continental meta-clastics, platform type thick meta-carbonates and meta-dibasic dykes.

Fig. 4. Generalized stratigraphic column for the Altınapa Basin.

matrix and are typically matrix supported. These clasts consist mostly of sub-rounded limestones (60%) which have been deformed and contain calcite veins; subangular radiolarites, various radiolarian cherts and subrounded but ellipsoidal ultramafic rocks (~30%) dominated by serpentinites set in a silty-sandy matrix with ironoxide cement (Fig. 6c). The clast composition compares well with the regional basement lithology. The maximum observable thickness of this succession is approximately 200 m along the SW margin of the basin.

Around Dereşıkılar, the LAG turns to red, thick-bedded (Fig. 7), matrix supported (Fig. 6d) conglomerates, interfingering with dark gray to white, clast-supported, polymict conglomerates consisting of dominantly subangular to subrounded pebbles up to 10 cm diameter,

with chert (20%) and limestone (80%) derived directly from the nearby basement (Fig. 6e). It unconformably overlies the basement, which consists of ophiolitic mélangé (Fig. 7).

The location of the type section (Fig. 9) is chosen north of Küçük Muhsine village where, apart from the red basal conglomeratic unit, the complete sequence is exposed. In the type section, the sequence begins with conglomerates (Fig. 10a), which correspond to the dark gray to white, clast-supported, polymict conglomeratic unit in Dereşıkılar. The sequence continues upward with yellowish, occasionally cross-bedded and bioturbated, fresh-water gastropod bearing sandstones (Fig. 10b). It is succeeded towards the central and NE parts of the basin by rhythmic alternations of siltstone, green-blue coal bearing claystone, marls (Fig. 10d), and medium to thick (15 cm

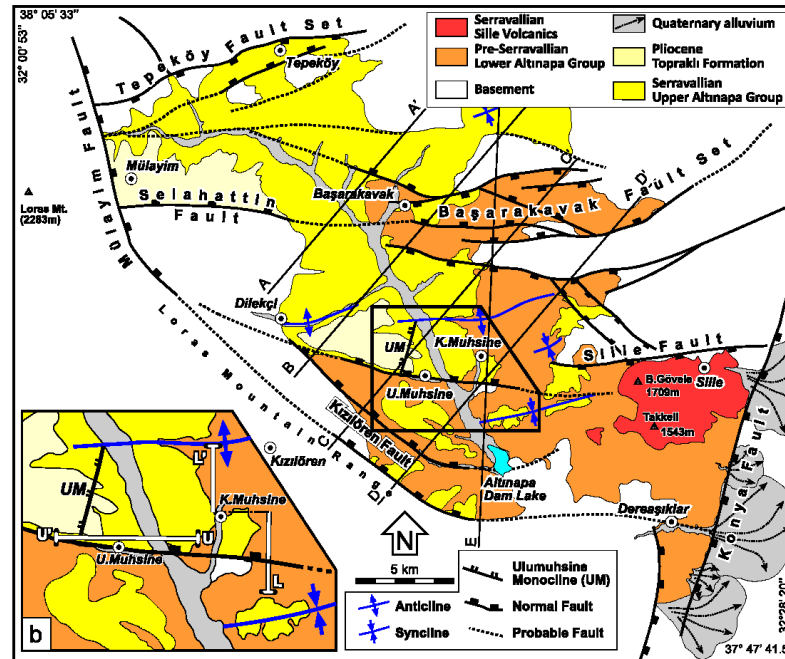


Fig. 5. (a) Revised geological map of the study area according to our mapping. (b) Inset map showing the location of the measured type sections for the Lower (L-L') and Upper (U-U') Altınapa groups. UM: Ulumuhsine Monocline. Dashed lines named as A, B, C, D and E indicate the trace of the cross-sections given in Fig. 20.

to 5 m) well bedded fresh water stromatolitic limestone (Fig. 10c). The LAG has a minimum thickness of 430 m.

From the Loras Mountain in the west to Küçük Muhsine village in the east, there is a gradual decrease in grain size from reddish conglomerates to fine grained yellowish/white marly deposits (Figs. 11 and 12). To the east of the Altınapa Lake near Küçük Muhsine Village, an erosional window provides exposure of the unconformity between the LAG and the underlying basement. The LAG in this area consists of much finer clastics than those adjacent to Loras Mountain. Similar grain size distributions are also observed elsewhere in the basin, and suggest that the basin detritus was dominantly shed from the SW margin. Note that the spatial distribution of the various lithologies as shown in Fig. 12 is consistent with that inference.

We did not observe fossils in the lower conglomeratic unit of the LAG, and previous studies (Eren, 1993; Özkan, 1998; Özkan and Söğüt, 1999) also did not report any fossil assemblages in this part of the LAG. To the west, however, around Kızılören, well outside of the Altınapa Basin, Görmüş (1984) reported fossil vertebrates including *Protoryx carolinae* Major, *Gazella deperdita* Gaudry, *Sus erymanthus* Roth and Wagner, *Prostreptocerus rothundicordis* Weithofes, *Ovis* sp., *Hiparion* sp., and *Ichtherium* sp. were collected from a red conglomeratic horizon pointing to Late Miocene–Pliocene age. Given the similar lithology, Özkan and Söğüt (1999) suggested a similar age for the LAG. We note, however, that the LAG underlies volcanics of the UAG, whereas the Kızılören overlies these. The age of the Kızılören unit therefore merely provides a minimum age for the LAG and UAG. On the other hand, Göger and Kural (1969) found fresh water fossils including *Unio* sp., *Radix* sp., ostracodes, bivalves and *Chara* sp. in limestones which have a lateral transition with these

reddish conglomerates, and they suggested a Pliocene age. Eren (1993) assigned a Late Miocene–Early Pliocene age based on stratigraphic orders together with K/Ar radiometric ages obtained from the Konya volcanics to the east (Keller et al., 1977). Furthermore, Özkan (1998) described *Schizotrix* sp., *Chara* sp., and *Scytonema* sp. from their Yalıtepe Formation, which corresponds to the central part of the LAG, and ascribed the formation to the Upper Miocene–Lower Pliocene. We note, however, that dating of endemic lacustrine fauna is subject to large uncertainties, and we will show that the age of the overlying Upper Altınapa Group is Middle Miocene based on our new $^{40}\text{Ar}/^{39}\text{Ar}$ data.

Unsorted, angular, occasionally reversely graded, matrix supported and boulder- to pebble-sized conglomerates indicate that the LAG was probably deposited in colluvial wedges, alluvial fans and terrestrial debris flows. From the SW margin towards the basin center, a gradual decrease occurs in the particles' size (Figs. 11 and 12), indicating a lateral transition from alluvial fans to lacustrine deposition. For the upper part of the LAG, lithologic characteristics (clay/siltstone and stromatolite limestone) and fossil content suggest a shallow lacustrine environment. Hence, the Lower Altınapa Group comprises facies associations extending from proximal alluvial fans along the basin margin to lacustrine facies in the central parts of the basin.

2.2. Upper Altınapa Group (UAG)

The UAG is characterized by limestones and marls interbedded with volcanic and volcanoclastic rocks. The limestone/marl and the volcano-sedimentary parts of the sequence have previously been subdivided into separate formations (Niehoff, 1961; Wiesner, 1968).

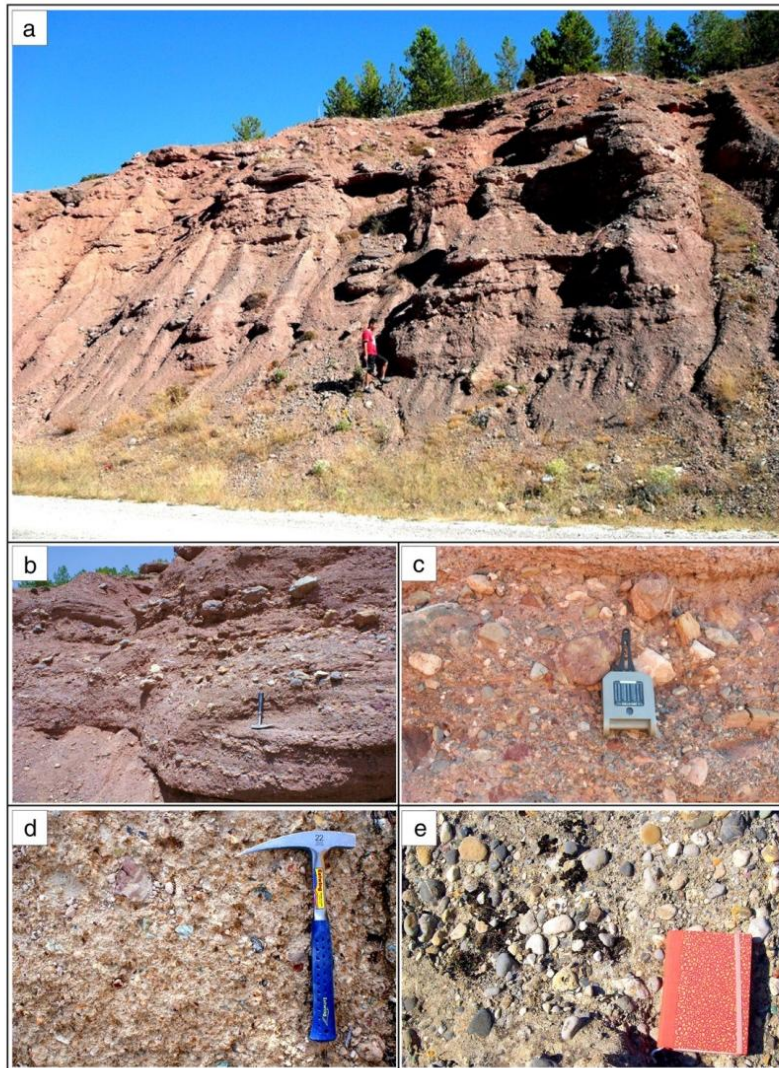


Fig. 6. Picture depicting basal conglomerates of the Lower Altınapa Group along the Kızılören Fault (a). Poorly bedded basal conglomerate observed along the Konya-Beyşehir Road (b). Close up view of the basal conglomerate with reverse graded beds (c). Note coarse, poorly sorted, subangular breccio-conglomerates. Matrix supported basal conglomerate, located close to Dereaşıklar (d). The conglomerate interfingers with clast-supported, polymict conglomerates (e).

Göğer and Kırıl (1969) included these rocks in the Dilekçi formation, in which the upper part of the sequence was named the Ulumuhsine limestone member, while the volcano-sedimentary parts were named the Küçük Muhsine Agglomerate Member and Erenkaya Tuff Member. On the other hand, Eren (1993) named the whole sequence, including limestone and volcanic rocks, Küçük Muhsine Formation (Fig. 3).

Around Küçük Muhsine (Figs. 8 and 12), the base of the UAG is defined by a well-exposed angular unconformity with the underlying

LAG. To the north of Başarakavak, it onlaps onto basement rocks (Figs. 12 and 13). The UAG is unconformably covered by conglomerates of the Topraklı Formation (Fig. 14).

Unlike the LAG, the UAG contains intervals of volcanogenic material composed of intercalations of ignimbrites, dark gray to buff tuffs and tuffites, andesitic lava, lapilli/tuff and volcanic breccias (ash and block), intercalated with white to buff lacustrine limestones and creamy-white to greenish marls. These volcanic rocks are calc-alkaline in character and interpreted as belonging to the Miocene

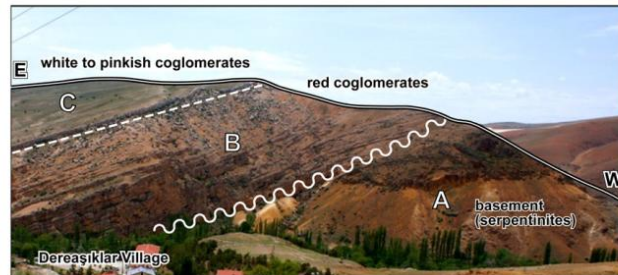


Fig. 7. Picture showing the basal conglomeratic unit of the Lower Altınapa Group near Dereaşıklar. Note the Neogene conglomeratic unit unconformably overlies Mesozoic ophiolitic mélangé. The white line is the Konya (normal) fault. View towards the East.

volcanic arc associated with the Cyprus subduction zone (Keller et al., 1977; Temel et al., 1998).

The type locality of the UAG starts from Küçükmühürsine Village where the sequence starts with partly consolidated tuffs at the bottom (Fig. 15) and comprising floats of pumice fragments having diameters as large as 3–4 cm (Fig. 16a, b). The size and concentration of the pumice fragments increase upwards in each tuff horizon. The sequence continues upwards with a thick layer of volcanic breccia with andesite and dacite blocks with maximum block sizes up to 70 cm diameter. This level is succeeded by well-consolidated, well-bedded tuffite sequences with bed thicknesses up to 1 m and a total thickness of approximately 300 m. Tuffaceous layers generally contain crystals of plagioclase, quartz, biotite, amphibole, and volcanic glass (Eren, 1992). These sequences are succeeded by clay-marl alternations and intercalations of thick-bedded, well-cemented algal limestones. The thickness of the limestones around Ulumuhsine Village, where they are best exposed, is approximately 65 m (Figs. 14 and 15), while they are approximately 90 m around NE of Başaraka-vak Village located at north-eastern part of the study area. The top of the sequence consists of white tuff and tuffites and pinkish block-and-ash deposits (Figs. 14 and 16c, d). These deposits contain angular, poorly sorted clasts comprising 90% of volcanogenic and 10% of limestone origin. The sizes of the contained clasts are less than 30 and 10 cm, respectively. The measured stratigraphic thickness of the UAG is 480 m.

As mentioned above, Göğür and Kırıl (1969) reported fresh water fossils in some limestone units, including *Unio* sp., *Radix* sp., *Planorbis*

sp., ostracodes, and *Chara* sp. and suggested a Pliocene age for this formation. Özkan and Söğüt (1999) also proposed Late Miocene–early Pliocene age for the unit based on gastropoda fossils such as *Radix* sp., *Planorbis* sp., bivalves such as *Unio* sp., and algae such as *Chara* sp. These ages do not fit in our stratigraphy and radiometric ages. However, Alçiçek (2010) observed similar fossil assemblages together with some mammal fossils in SW Turkey which are indicating MN 3–4 Zone, an age range starting in the Burdigalian. Additionally, K–Ar ages of volcanic units in the east of the Altınapa Basin start as old as 11.95 Ma (Besang et al., 1977; Keller et al., 1977), which indicates the age of the volcanic activity in the Altınapa Basin and fits with our observations and age range. Therefore, the ages proposed by Göğür and Kırıl (1969) and Özkan and Söğüt (1999) need to be revised.

The absence of conglomerates and channeled sandstones, as well as the dominance of clay/siltstone and limestone of the Upper Altınapa Group, and its fossil content indicate a quiet lacustrine environment, adjacent to volcanic centers.

2.3. Topraklı Formation

The Topraklı Formation unconformably covers the UAG (Fig. 14) and is characterized by reddish-brownish conglomerate, sandstone and occasional mudstone. It has a limited distribution close to the western boundaries of the basin (Fig. 12). The rocks were mapped as Topraklı conglomerates and Alluvium by Doğan (1975), and Eren (1993) and Özkan (1998) named the sequence “Topraklı Formation”.

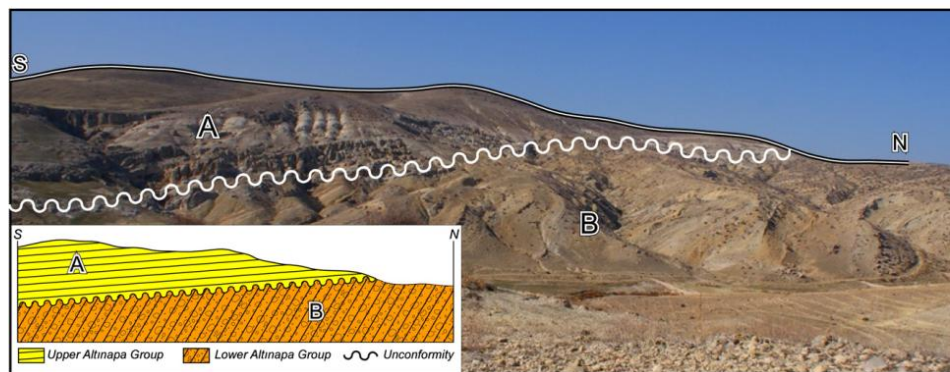


Fig. 8. Picture showing the angular unconformity between the Lower and Upper Altınapa groups.

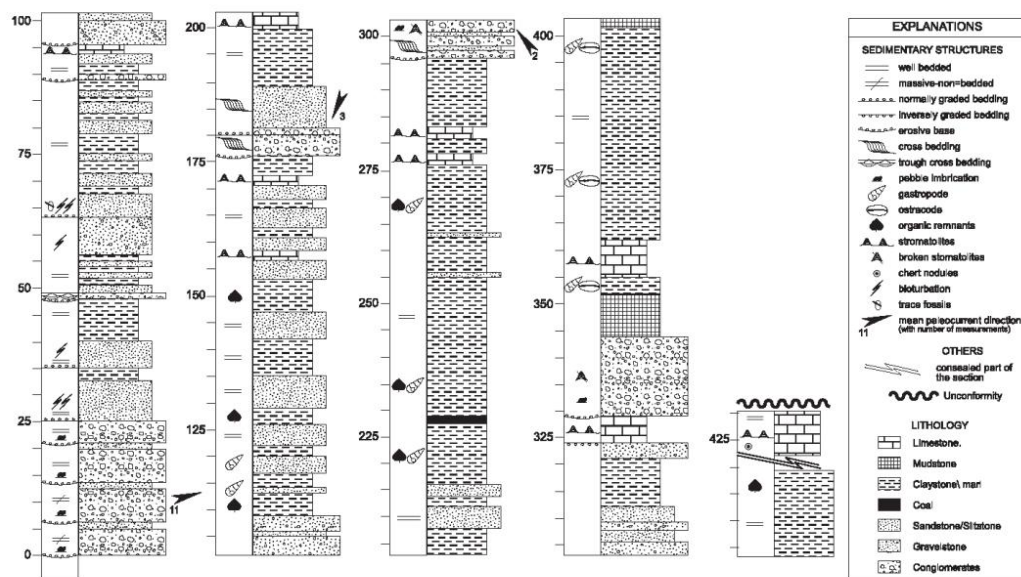


Fig. 9. Type-section of the Lower Altınapa Group.

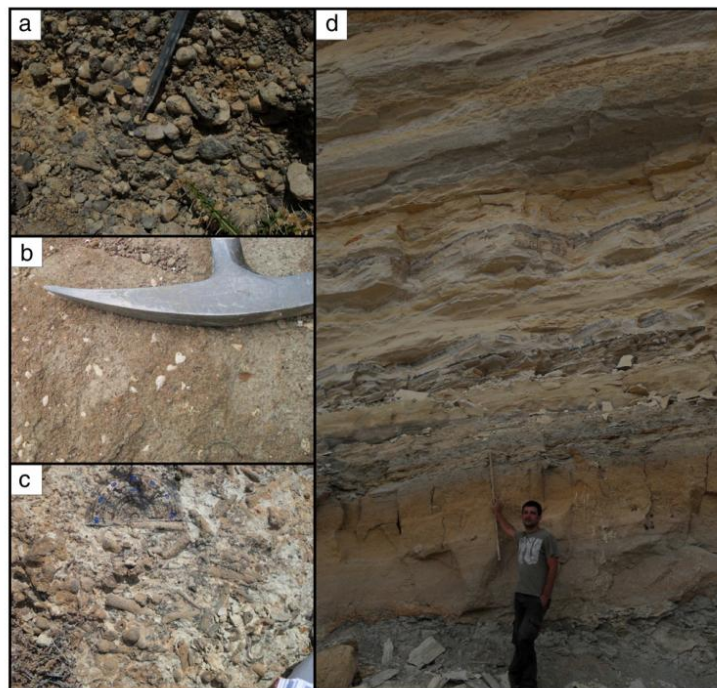


Fig. 10. Pictures showing typical facies of the Lower Altınapa Group: a) clast-supported, polymict conglomeratic units b) cross-bedded and bioturbated, fresh-water gastropods-bearing sandstones, c) well bedded fresh water stromatolitic limestone and d) alternation of siltstone, green-blue coal bearing claystone, marls.



Fig. 11. Picture depicting facies changes of Lower Altınapa Group from SW margin towards northeast into the basin center. The white line represents the Kızılören (normal) fault (ticks on the hanging-wall block). Note that coarse, poorly sorted, subangular coarse clastics dominate along the SW margin while they rapidly become finer-grained to marl-dominated towards NE (view to NW).

which is also adopted in this study. The Topraklı Formation is well exposed NW of the Ulumuhsine Village and it unconformably overlies pinkish tuffs and algal limestone belonging to the UAG (Figs. 12 and 14).

NW of Ulumuhsine, the formation is composed of a coarsening upward sequence of loosely cemented, unsorted and polymict, angular, pebble- to boulder-size (occasionally up to 80 cm diameter), matrix-supported conglomerates. Clasts originate from mostly limestones, sandstones, quartzites and cherts, i.e., lithologies that are abundant in the basement of the region. In addition, it reworks lacustrine limestone, dacite and andesite derived from Neogene units. The clasts are floating in a muddy/sandy matrix with iron-oxide cement. In addition, normally graded, polymict, sub-angular clast-supported

conglomerates were also observed in some levels. Sedimentary structures such as planar cross-bedding and pebble imbrications are common in these stratigraphic levels. Another common facies within this unit comprises alternations of mudstone and matrix-supported conglomerate. There are also well-developed channels and occasional concretions within the mudstones, both indicating alluvial plain deposition with paleosol horizons.

No fossils have been observed from the unit, so far, and its age can only be constrained by superposition. The Topraklı Formation covers all of the Neogene units in the basin and is in turn overlain by Quaternary alluvium.

Unsorted, as well as upward-coarsening, matrix-supported and boulder- to pebble-size conglomerates with angular pebbles suggest

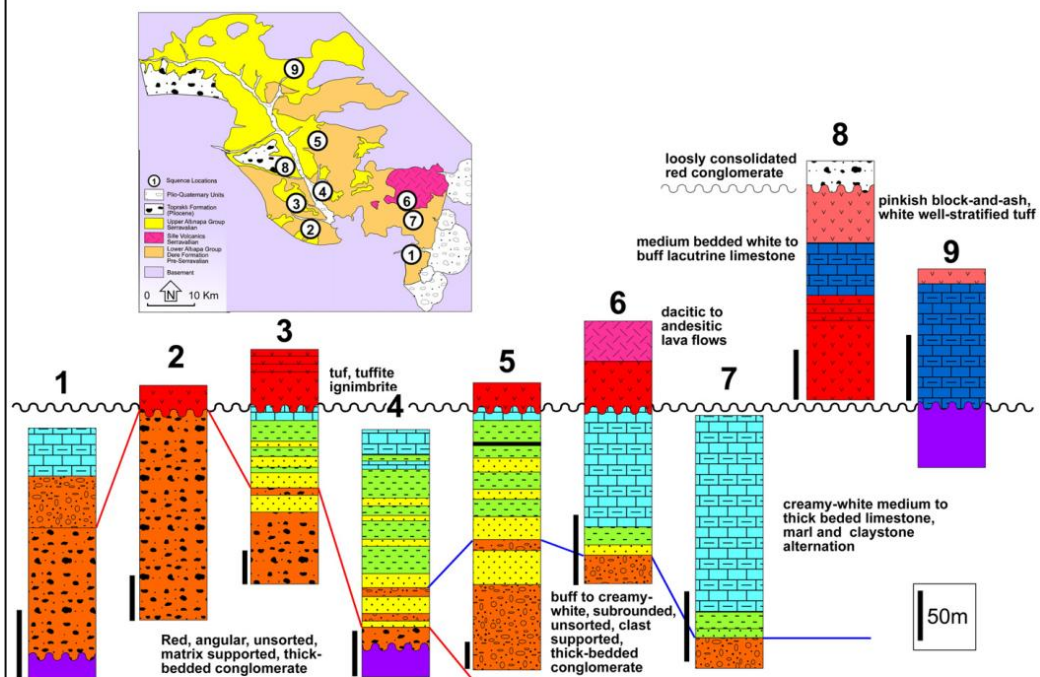


Fig. 12. Schematic illustration of the lithostratigraphy of the Altınapa Basin (not to scale). The section number is given on the geological map of the study area. Notice that grain size decreases from west to east. Vertical bars indicate the scales of each column independently.

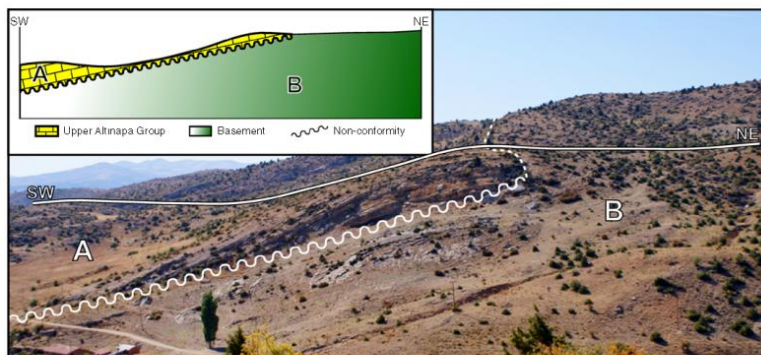


Fig. 13. Picture showing onlapping lacustrine algal limestones of the Upper Altınapa Group over the basement (location is 2 km north of Başarakavak, view to NW).

deposition in alluvial fans and continental debris flows. Additionally, sub-rounded, normally graded, grain-supported conglomerates showing pebble imbrications and erosional surfaces represent channelled fluvial stages within the alluvial fan deposition. Mudstones were most likely deposited by over concentrated currents, which define the flooding area and the distal part of the alluvial fan deposits. The caliche profiles in the mudstone suggest interruptions of sedimentation in a dry environment.

3. $^{40}\text{Ar}/^{39}\text{Ar}$ geochronology

Because previous age assignments rely on poorly dated endemic lacustrine faunas, we provide three $^{40}\text{Ar}/^{39}\text{Ar}$ ages from lavas and pumice horizons in the UAG (Fig. 4). One sample was taken from the lowermost lava we encountered (S3), one sample was taken from a gray tuff halfway the sequence (S2), and the third was collected from the uppermost pinkish tuffs (S1).

Bulk samples were crushed, washed and sieved. Grain size fractions of 1000–2000 μm (S1, S2) or 500–1000 μm (S3) were used for standard magnetic and heavy liquid separations. Final mineral fractions were separated by hand-picking under a microscope. The samples were wrapped in Al-foil packages and loaded in a 9 mm ID quartz vial. Between each set of 4 samples and at top and bottom positions, Fish Canyon Tuff sanidine (FCs) standard was used as neutron fluence monitor. The vial was irradiated for 10 h in the OSU Triga CLICIT facility, USA. After irradiation, samples and standards were loaded in 2 mm diameter holes of a copper tray and placed in an ultra-high vacuum extraction line. Single crystal $^{40}\text{Ar}/^{39}\text{Ar}$ fusion experiments were performed at

the Vrije Universiteit Amsterdam, The Netherlands using a Synrad 48–5 CO_2 laser and custom made beam delivery system. Samples were purified in an in-house designed sample clean up line and analyzed on a MAP215–50 noble gas mass spectrometer fitted with a Balzers SEV217 detector. Mass discrimination was monitored by 3 replicate runs of air pipettes every 12 unknowns and blanks were run every 3 unknowns.

Ages are calculated using the in-house developed ArArCalc software (Koppers, 2002) with Steiger and Jäger (1977) decay constants. Ages are calculated relative to the FCs of 28.198 ± 0.23 Ma (Kuiper et al., 2008); note that this study reports 28.201 Ma using decay constants of Min et al. (2000), which converts to 28.198 Ma using Steiger and Jäger (1977). Correction factors for neutron interference reactions are $(2.64 \pm 0.04) \times 10^{-4}$ for $(^{36}\text{Ar}/^{37}\text{Ar})_{\text{Ca}}$, $(6.73 \pm 0.08) \times 10^{-4}$ for $(^{39}\text{Ar}/^{37}\text{Ar})_{\text{Ca}}$, $(1.211 \pm 0.006) \times 10^{-2}$ for $(^{38}\text{Ar}/^{39}\text{Ar})_{\text{K}}$ and $(8.6 \pm 1.4) \times 10^{-4}$ for $(^{40}\text{Ar}/^{39}\text{Ar})_{\text{K}}$. The $^{40}\text{Ar}/^{36}\text{Ar}$ ratio of 295.5 of Nier (1950) is used in the calculations. Errors are reported at 2 sigma level. Outliers are identified by comparing MSWD with the T-student distributions. The summary of the $^{40}\text{Ar}/^{39}\text{Ar}$ results is given Table 1 and plateaus and isochrones are given in Fig. 17. Full analytical data are given in the Supplementary Data.

Sample S2 is the deepest level in the stratigraphy (Fig. 4). It does not yield a reliable weighted mean age. The sample is low on potassium and has low radiogenic ^{40}Ar yields. It most likely represents a glass fraction. The inverse isochron shows clear indications of excess argon and the inverse isochron age is 11.88 ± 0.11 Ma (± 0.26 Ma, full external error). K and/or Ar mobility can be an issue in glass fractions (Morgan et al., 2009) and this age is therefore considered to be

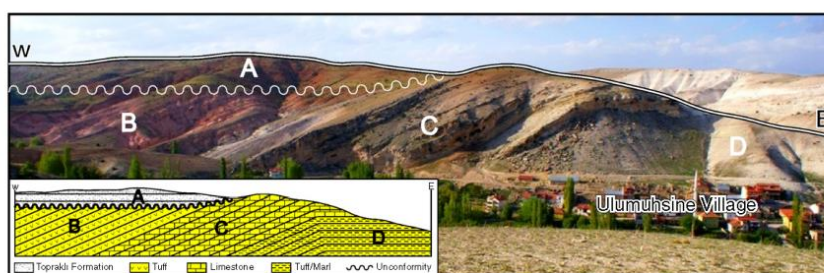


Fig. 14. Picture showing the angular unconformity between the Upper Altınapa Group (UAG) and overlying Topraklı formation near Ulumuhsine. The UAG consists of pinkish/white tuff, freshwater limestone (65 m) and marl/tuff alternation.

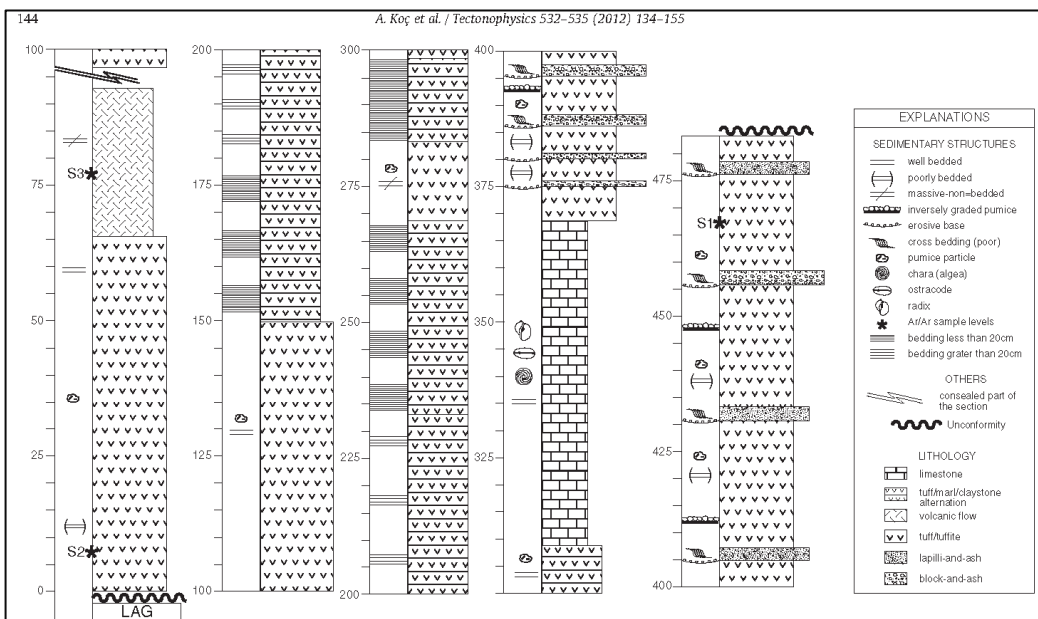


Fig. 15. Type-section of the Upper Altunapa Group around Ulumuhsine (see Fig. 5b for location of the section).

less reliable. However, its age is consistent with the stratigraphy with samples S3 and S1 being younger and stratigraphically higher in the section.

Sample S3 has a mixed population of grains based on K/Ca ratios. The four youngest grains with highest K/Ca ratio yield a weighted mean age of 11.67 ± 0.05 Ma (± 0.24 Ma full external error).

Sanidine of the highest sample S1 yields a weighted mean age of 11.61 ± 0.02 Ma (analytical error); or ± 0.24 Ma (full external error including standard age and decay constant uncertainties). The sample has high radiogenic $^{40}\text{Ar}^*$ contents and therefore data points cluster together on the isochrones. Although the $^{40}\text{Ar}/^{36}\text{Ar}$ atmospheric intercept on the inverse isochron deviates from the atmospheric intercept the weighted mean and isochron ages are similar.

4. Structural geology

The major structures which shaped the Altunapa Basin include large scale normal faults, numerous mesoscopic faults commonly

with no more than a few meters offset, and non-systematic open folds. Most of these structures were mapped using remote sensing techniques and subsequently verified in the field. Kinematic data were collected from mesoscopic faults for construction of paleostress configurations.

4.1. Remote sensing

The applied remote sensing techniques include processing and interpretation of satellite images and interpretation of stereographic aerial photographs of 1/40,000 scale, using mirror stereoscopes. The used satellite imagery includes Landsat TM and ETM⁺ and Terra-ASTER images. In addition, Quickbird images obtained from Google Earth were used for areas where higher resolution was required. All of these images were co-registered using 1/25,000 scale topographical maps and combined in a GIS medium together with previously obtained maps and a field database.

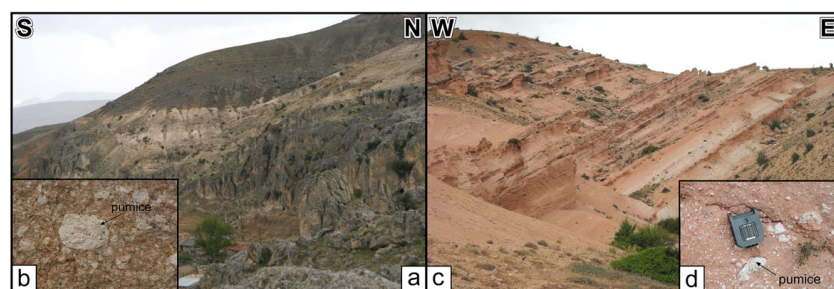


Fig. 16. Tuff facies of Upper Altunapa Group (UAG). a) The tuff facies at the bottom and b) their close up view. c) block and ash facies at the top of the UAG and d) their close up view.

Table 1

Summary of $^{40}\text{Ar}/^{39}\text{Ar}$ data. Full data tables are given in the appendix. Errors are reported with 2σ uncertainty and represent analytical error. Full external errors are reported between brackets. MSWD is Mean Square Weighted Deviate. N is the number of analysis included in the weighted mean age, between brackets the number of experiments excluded.

Irradiation ID	Location		Material	Weighted mean age	MSWD	N	Inverse isochron	$^{40}\text{Ar}/^{36}\text{Ar}$ intercept
	Long	Lat						
VU788-S1	32.24106	37.92545	Sanidine	$11.54 \pm 0.02(0.24)$	1.61	9(1)	$11.53 \pm 0.01(0.24)$	333 ± 25
VU788-S2	32.28291	37.92859	Glass	No reliable age	0.48	7(3)	$11.88 \pm 0.11(0.26)$	310.6 ± 2.3
VU788-S3	32.26722	37.92645	Feldspar	$11.67 \pm 0.05(0.24)$	1.14	4(5)	$11.70 \pm 0.03(0.24)$	276 ± 11

In addition to aerial photos and satellite images, 25x25 m resolution digital elevation models (DEMs) prepared from 1/25,000 scale topographical maps were used, together with 90x90 m (3 arc sec) resolution Shuttle Radar Topographical Mission (SRTM) data. These images and DEMs have different spatial resolutions, which is useful for detection and delineation of structures at different scales. In addition, the images were draped on the DEMs for 3D visualization in different directions, enhancing morphological expressions of structures in all directions. After the images were enhanced, lineaments were delineated manually on the images. Lineaments showing appreciable morphological expressions were labeled as faults. Digital elevation data and a resultant lineament map are shown in Fig. 18. In addition, a length-weighted rose diagram prepared from the trends of these structures (Fig. 18) displays two dominant directions (NE–SW and NW–SE) having approximately 60° acute angles.

4.2. Field observations

The major structures that shaped the Altınapa Basin are normal faults along at the margins of the basin. The basin stratigraphy is deformed along gentle to open folds and, in one locality, in a conspicuous 100 m scale monocline. In addition, numerous mesoscopic faults, which developed after and during sedimentation (Fig. 19) have pervasively affected the basin (Fig. 5).

Morphologically, the most prominent faults are identified at the margins of the basin (Fig. 5). Generally they are recognized as linear to curvilinear mountain fronts rising steeply at the contact of the basin fill units and basement rocks. Among these, the Kızılören Fault (KF) is inferred mainly on the basis of a thick accumulation of red clastics abutting against the basement rocks, although the main fault plane was not observed during field studies (Fig. 5). Nevertheless, the fault zone is characterized by smaller scale syn- and antithetic normal faults exposed along the sediment–basement contact.

The Mülâyim Fault (MF) is oriented NNW–SSE and dips to the NE. It controls the northwestern margin of the basin and separates gently dipping Plio–Quaternary Topraklı sediments from the carbonate basement units (Fig. 18). Along the fault, the basin fill units are characterized by unsorted, angular to sub-angular, boulder- to pebble-size (up to 1 m) sedimentary breccias and conglomerates. In Mülâyim village, adjacent to the fault, the basin fill units are almost horizontal.

The Tepeköy Fault Set (TFS) located at the northern margin of the basin comprises two ENE–WSW oriented conjugate normal faults. The northern branch of the fault set dips southwards while the southern branch dips northwards defining a graben around Tepeköy (Fig. 5). Both of the branches of the TFS extend beyond the present boundaries of the Altınapa Basin and are delimited in the SW by the Mülâyim Fault, which is almost perpendicular to the TFS. The south-dipping branch of the Tepeköy Fault delimits the northern boundary of the basin. The basement at this part of the basin comprises Paleozoic to Jurassic marbles and quartzites.

The Selahattin Fault (SF) is developed in the NW part of the study area and is oriented parallel to the TFS. It is also delimited by the Mülâyim Fault in the west. Along the SF the Topraklı Formation is juxtaposed with the basement units, which are composed mainly of Triassic carbonates. The eastward continuation of the fault within

the Upper Altınapa Group is uncertain. Morphologically, however, the fault can be followed eastward where it seems to link-up with one of the north-dipping branches of Başarakavak Fault Set (BFS) (Fig. 5).

The Başarakavak Fault Set (BFS) comprises a number of E–W striking faults with horst and graben morphology. Along the major faults of the BFS, basement and basin fill units are juxtaposed. Lateral continuity of the fault set within the basement is morphologically well expressed while within the basin towards the west the BFS is not exposed.

The southeastern boundary of the basin is delineated by the active (Ögütçü et al., 2010) Konya Fault which controls the northwestern boundary of the vast Konya Plain. The Konya fault is about 45 km long and shows an approximately NNE–SSW trend. It dips SE and separates the Neogene sedimentary fill of the Altınapa Basin in the foot-wall from the Quaternary alluvial sediments of the Konya Basin in the hanging wall. Well preserved fault planes with slip lines are exposed, and linear coalesced alluvial fan and apron systems developed within the Konya Basin, consistent with its ongoing activity as evident from the 11 September 2009 Sille Earthquake, ($M_w = 4.9$) along the fault. Finally, the eastern margin of the basin is characterized by onlap of lacustrine algal limestones of the UAG (Figs. 13 and 20), showing an asymmetric development of the basin.

The mainly E–W trending open folds that deform the stratigraphy of the Altınapa Basin are developed within both the Lower and Upper Altınapa groups. However, the dips of the limbs of these folds seem more gentle within the Upper Altınapa Group, with dips not exceeding 30°, whereas they are steeper within the Lower Altınapa Group, with dips up to 50° (Fig. 20). All of these folds form a series of anticlines and synclines parallel to the Tepeköy and Başarakavak Faults and almost perpendicular to the NNW–SSE trending basin bounding faults (Kızılören Fault). Their maximum observed wavelength is approximately 10 km and they developed in the hanging-walls of the normal faults. An exception to this general fold trend is formed by the Ulumuhsine Monocline, which strikes N15E, parallel to the Konya Fault and dips 30° W (Figs. 5, 14 and 20). This monocline, which is consistent with a buried blind normal fault at depth, deforms the UAG, but is unconformably covered by the Topraklı Formation.

5. Paleostress analysis

5.1. Data and method

In addition to the large-scale structural analysis, we carried out a detailed kinematic analysis from mesoscopic structures in order to unravel paleostress configurations during the development of the Altınapa Basin.

The paleostress configurations are reconstructed using Angelier's software to analyse fault slip data collected from exposed fault planes. Analysis of fault attitudes and their associated directions and sense of slip are used to infer principal stresses, a procedure also known as paleostress inversion (Angelier, 1990; 1994; Carey and Burinier, 1974; Etchecopar et al., 1981). Two assumptions are fundamental to these methods: 1) the bulk state of stress in a small area is uniform, and 2) the slip direction is parallel to the maximum resolved shear

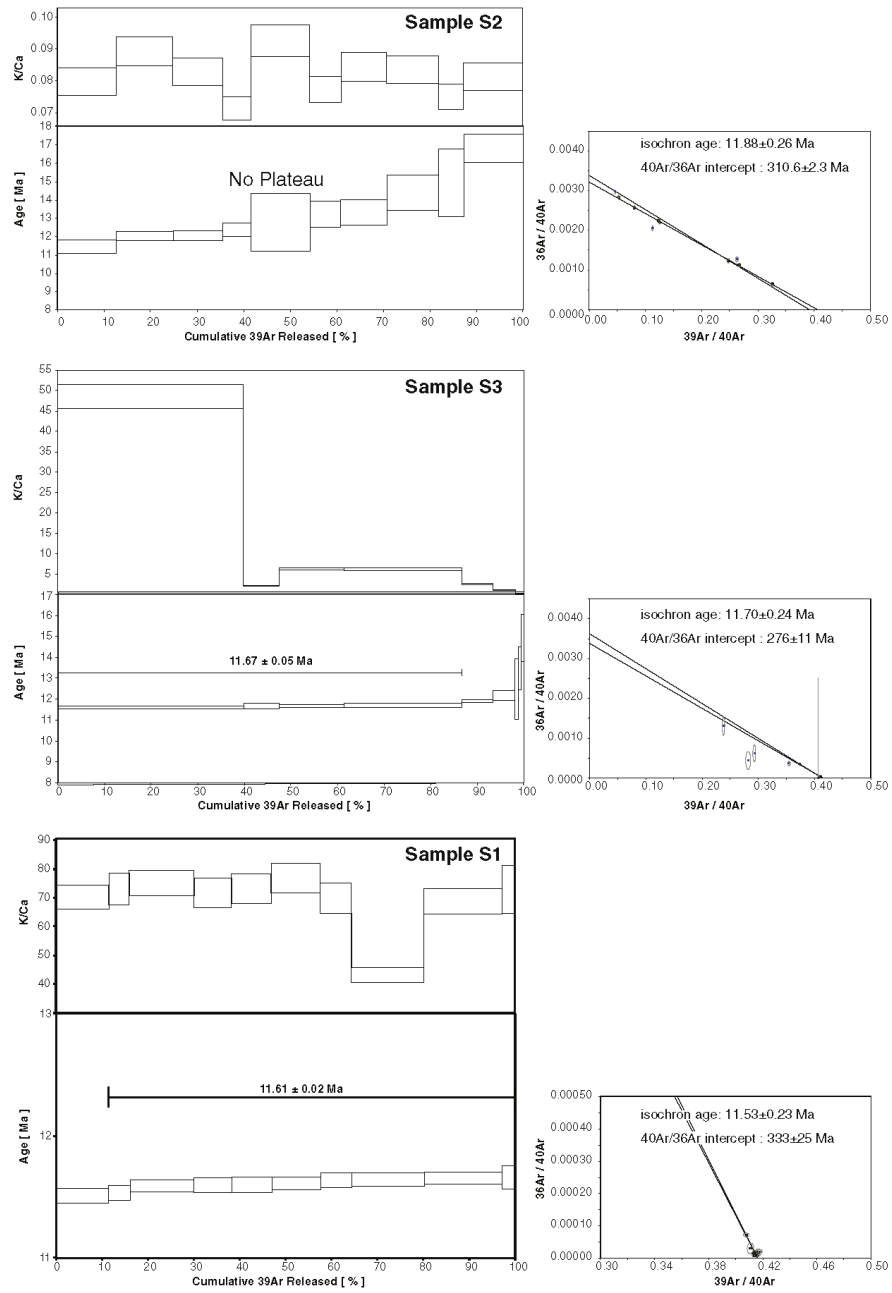


Fig. 17. Replicate single crystal fusion $^{40}\text{Ar}/^{39}\text{Ar}$ ages are plotted versus the % of ^{39}Ar released in each fusion analysis for the three lava samples from the Upper Altınapa Group. The width of the bars/steps represents the 2σ analytical error. On top the K/Ca ratio (gray area, width is 2σ error) is displayed. Weighted mean ages are given. The small insets show the inverse isochron diagrams.

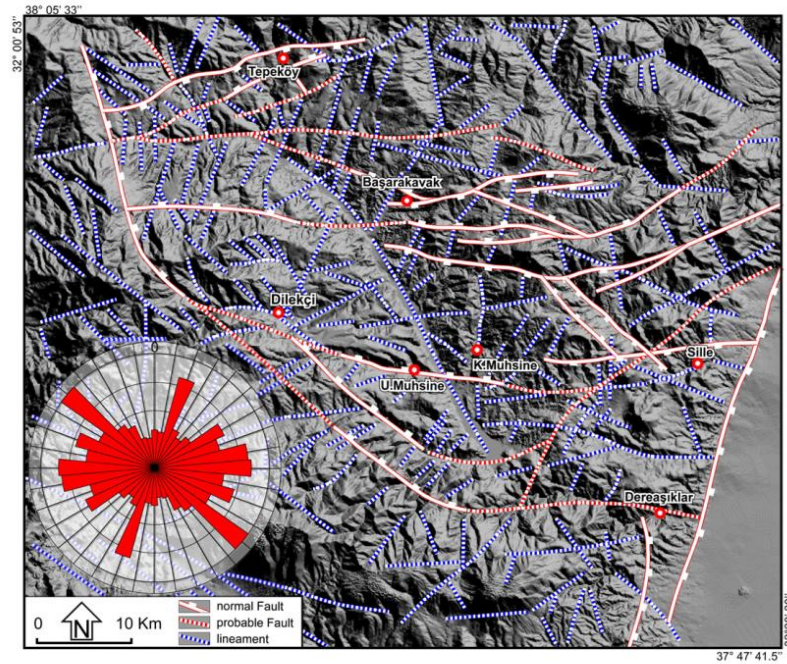


Fig. 18. Structural map of the Altınapa Basin, indicating faults and lineaments overlain on a 25 × 25m resolution digital elevation model. Rose diagram indicating orientations of both faults and lineaments.

stress on each fault plane. Paleostress analyses determine the best-fitting reduced stress tensor based on the given fault slip data, identifying the orientations of the three principal stress axes (σ_1 : maximum, σ_2 : intermediate and σ_3 : minimum) and the shape ratio of stress ellipsoid, $\Phi = (\sigma_2 - \sigma_3) / (\sigma_1 - \sigma_3)$ ranging between two extreme values of 0 and 1. The Φ ratio constrains all-possible cases between uniaxial ($\sigma_2 = \sigma_3$; $\Phi = 0$ or $\sigma_1 = \sigma_2$; $\Phi = 1$) to tri-axial stress configurations ($\sigma_1 > \sigma_2 > \sigma_3$; $\Phi = 0.5$) (Angelier, 1994).

From 29 sites, 377 fault-slip measurements (Fig. 21a), including direction and sense of relative movements were collected. Most of the data were collected from the infill of the Altınapa Basin, and from faults juxtaposing basement and basin-fill units. Strikes of the mesoscopic fault planes clustering around E–W and NE–SW directions (Fig. 21b) are consistent with the general trend of the major faults. Dips range between 45° and 90°. Inversion of the data was carried out on each site separately and 29 stress configurations are constructed (Fig. 21c and Table 2).

5.2. Spatial characteristics

In order to understand the type of deformation, the constructed paleostress orientations are analyzed for their regional consistency. Fig. 22 shows that σ_1 is generally oriented (sub-) vertically in all sites, whereas σ_2 and σ_3 do not show a consistent direction. Such distributions are characteristic for uniaxial stress conditions and result in stress permutation in regions where the magnitudes of σ_2 and σ_3 are close to or equal to each other (Homburg et al., 1997). The deformation that affected the Altınapa Basin is clearly extensional, as indicated by the vertical σ_1 , and consistent with normal fault activity along the major faults in the basin. The near equal σ_2 and σ_3 magnitudes

should produce Φ values approaching zero in the case of σ_1 magnitudes much greater than that of σ_2 . As seen in Fig. 22d and Table 2, the frequency distribution of Φ values are bimodal and has peak values at 0.15 and 0.35. In other words, in more than 20 sites Φ values are less than 0.5. This indicates that uniaxial stress conditions prevailed in the region.

In order to verify the compatibility of the constructed paleostress configurations relative to regional structures, the horizontal component of the minor principal stress is plotted on the map of Fig. 23. Apart from some strike-slip solutions (sites 4, 8, 15 and 19), most of the σ_3 directions are (near-) orthogonal to the dominant trends of the major structures (except for sites 3 and 6). This pattern implies unconstrained slip (somewhat similar to free fall of hanging-wall blocks along fault planes) along the major normal faults, as expected in uniaxial stress conditions. The sites with strike-slip solutions are indications of transfer faults and/or stress perturbations due to accommodation of local space problems.

5.3. Temporal relationships

In addition to spatial distribution of the paleostress directions, temporal changes of the paleostress configurations throughout the stratigraphy are very important to unravel any paleostress stratigraphy of the basin. In paleostress stratigraphy, the basement rocks potentially record the entire paleostress history during basin subsidence, whereas basin strata record paleostress tensors that were coeval with sedimentation. Structures developed in the upper most basin fill offer insight into only the youngest tectonism (Kleinspehn et al., 1989). Therefore, the younger events need to be extracted from the older ones, successively from younger to older. We therefore ordered

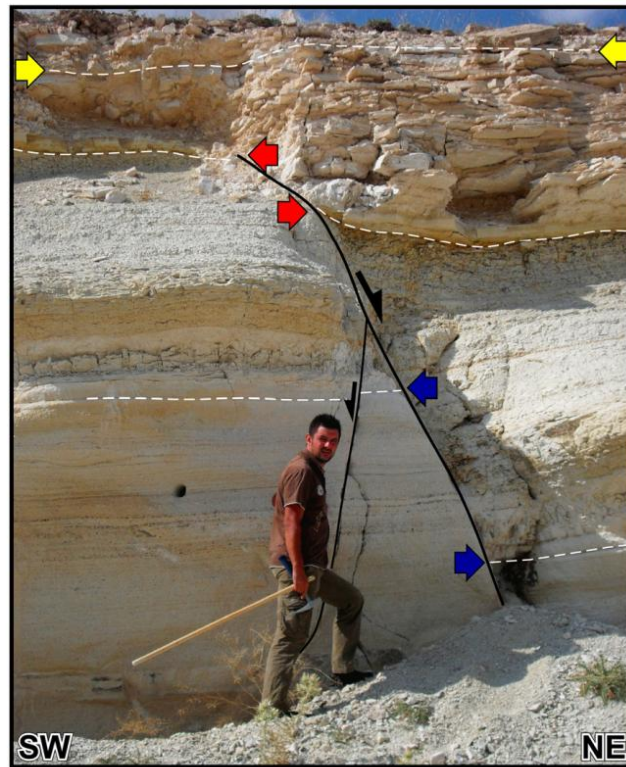


Fig. 19. Syn-sedimentary normal fault in the tuff units of Upper Altınapa Group.

our paleostress data according to the age of the rocks from which they were collected (Fig. 24), and according to cross-cutting relationships. The paleostress directions for the Lower and Upper Altınapa groups were plotted separately, and the resultant contour diagrams were compared. As seen in Figs. 22, 23 and 26, there is no notable difference between the measurements from the Lower and Upper Altınapa groups.

The youngest, still active extension direction in the Altınapa Basin is reflected by the Konya Fault, reflected by paleostress sites 10 and 15. This extension direction trends approximately E–W to NW–SE. This youngest tectonic regime is consistent with focal mechanism solutions of the Sille Earthquake (11 September 2009, $M_w = 4.9$, ETHZ) (Fig. 24). However, recent earthquakes along the Akşehir-Afyon Graben (AAG) to the north of the Altınapa Basin (Ergin et al., 2009; Taymaz et al., 2004) demonstrate extension directions ranging from N–S to NE–SW (Fig. 24), attesting to the fact that currently central Turkey has strongly varying σ_3 directions while σ_1 is (sub-) vertical. This is consistent with the paleostress patterns obtained throughout the stratigraphical successions of the Altınapa Basin.

6. Discussion

6.1. Altınapa Basin evolution

The Altınapa Basin developed unconformably on top of the Taurides fold-thrust belt which itself formed during subduction and

collision in late Cretaceous to perhaps Oligocene time. The onset of sedimentation in the basin predates 11.8 Ma, which is the oldest age we obtained from the UAG. The age of the onset of sedimentation remains unknown, but if sedimentation rates in the LAG were comparable to those in the UAG, the onset of sedimentation may also be of Middle Miocene age. However, UAG and LAG are divided by angular unconformity with an unknown stratigraphic hiatus, which means that LAG may also be older.

Subsidence was most likely related to extension, with a N–S to NE–SW dominant direction. The fining upwards sequence in the LAG, together with the unconformable contact with the overlying lacustrine UAG suggests that most of the accommodation space was formed during UAG deposition. The dominance of coarse clastic sedimentation along the southwestern fault-controlled margin, together with the onlap of the UAG over the northeastern basin margin suggests that initial subsidence was fault (NW–SE) controlled, and that this faulting gave rise to the development of a half-graben geometry to the basin.

The E–W trending open folds that affect the LAG more than the UAG are probably extension related since no compressional faults were observed in the basin. Similarly, all of the paleostress configurations indicate extension in the basin throughout its stratigraphy since Middle Miocene. The angular unconformity observed between the LAG and UAG indicates that some erosion occurred prior to UAG deposition. This angular unconformity may mark lake level fall or complete drought possibly due to climatic

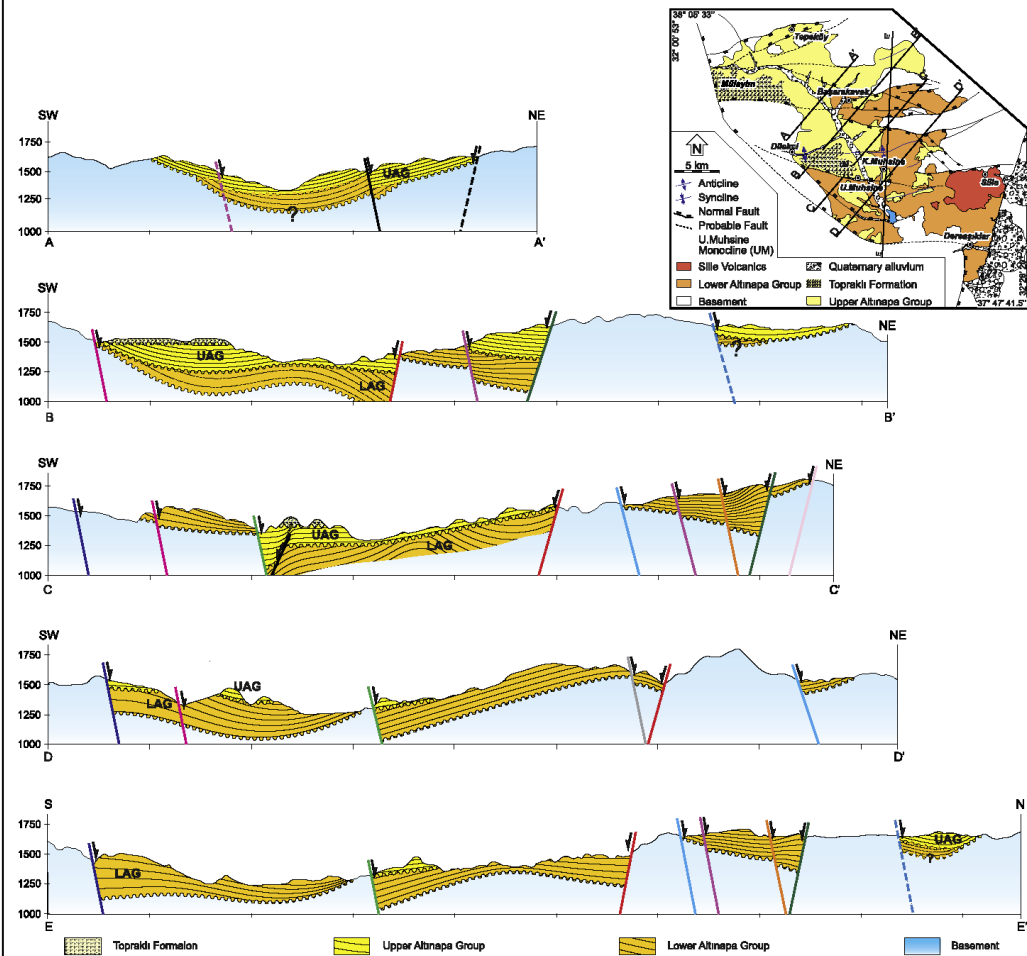


Fig. 20. Structural Cross-sections constructed from the geological map. Inset map shows the locations of the sections. Different colors for faults correspond to the same fault in different sections.

changes. Alternatively, the inception of volcanism in the vicinity of the Altınapa Basin may have led to local uplift and tilting of the LAG units. It seems unlikely that uplift was related to a local enhancement of relief, as the UAG is characterized by lacustrine deposition, and is fine-grained in nature. Our data show that since the Middle Miocene, the Altınapa Basin has been in a uniaxial extensional regime which is evidenced by spatially and temporally unconstrained extensional directions (Fig. 24).

6.2. Regional implications

Our structural and geochronological analysis of the Altınapa Basin provides evidence that extension to the north of the Tauride mountain range was already active since Middle Miocene time, and formed intramontane, continental basins on top of the late Cretaceous to Oligocene Taurides fold–thrust belt. To the south, west and southeast of the study area, sedimentation and extension in the Adana, Mut and

Manavgat basins appear to have started earlier, in the Early Miocene or locally perhaps in Late Oligocene time, and was marine in character (e.g. Burton-Ferguson et al., 2005; Çiner et al., 2008; Şafak et al., 2005). Our results may indicate that inception of Neogene extension started later in the north than in the south, consistent with the diachronous onset of sedimentation younging northwards from Cyprus (Bassant et al., 2005).

Miocene extension appears to be spatially restricted to the region north of the Cyprus subduction zone. To the east of the Adana Basin (Fig. 1), Middle Miocene and younger deformation has been dominated by N–S compression and strike-slip faulting related to westward Anatolian escape as a result of the Arabia–Europe collision (e.g., Faccenna et al., 2006; Hüsing et al., 2009; Kaymakci et al., 2010; Şengör et al., 2003), and to the west of the central Taurides, Middle–Late Miocene deformation was transpressional, related to vertical axis rotations of the Bey Dağları platform and Lycian Nappes at the eastern limit of the Aegean–west Anatolian orocline (Kissel and

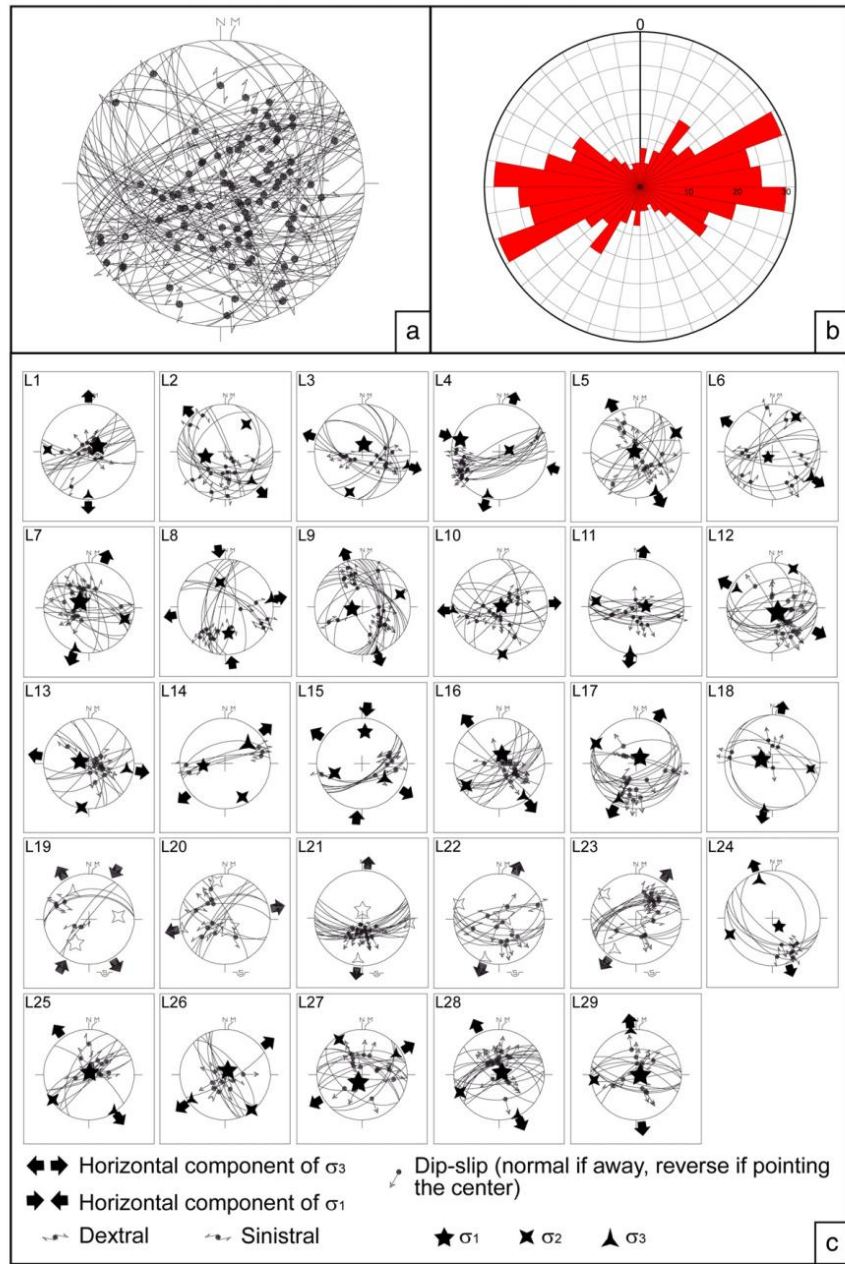


Fig. 21. (a) Stereoplot showing all of the collected fault slip measurements ($N=377$), (b) bidirectional rose diagram of fault strikes. Note that there are three distinct dominant directions. (c) Stereoplots showing constructed paleostress orientations, fault planes and slip lineations (lower hemisphere equal area projection).

Table 2
Locations and paleostress orientations for whole data.

Loc	Long	Lat	$\sigma_1(P/D^\circ)$	$\sigma_2(P/D^\circ)$	$\sigma_3(P/D^\circ)$	Φ	Mean ANG	Mean RUP	N
L1	32.16011	38.06960	71°/059°	16°/273°	10°/180°	0.112	37	73	13
L2	32.16214	38.06511	55°/257°	28°/037°	19°/138°	0.462	28	64	15
L3	32.10005	38.01244	77°/013°	13°/197°	01°/107°	0.276	18	42	13
L4	32.20648	37.95920	12°/287°	77°/081°	05°/195°	0.360	9	24	16
L5	32.31572	37.88673	87°/318°	01°/063°	03°/153°	0.449	18	46	15
L6	32.22815	37.98963	80°/226°	10°/033°	02°/123°	0.607	25	55	12
L7	32.25550	38.03066	71°/303°	18°/107°	05°/199°	0.142	22	46	16
L8	32.25891	38.03231	44°/173°	46°/348°	03°/081°	0.597	18	33	13
L9	32.40211	37.93452	73°/259°	17°/072°	02°/162°	0.330	25	49	20
L10	32.42253	37.87497	87°/066°	01°/176°	03°/266°	0.105	23	59	15
L11	32.38741	37.85167	74°/088°	16°/278°	03°/187°	0.513	25	59	14
L12	32.42282	37.87736	77°/128°	02°/029°	13°/298°	0.094	21	44	19
L13	32.39163	37.90838	74°/284°	02°/189°	16°/099°	0.330	25	51	12
L14	32.40954	37.85433	50°/265°	18°/152°	34°/050°	0.711	45	86	5
L15	32.42488	37.88497	30°/005°	36°/250°	39°/123°	0.734	33	55	8
L16	32.35526	37.95844	73°/017°	14°/236°	10°/143°	0.311	15	37	17
L17	32.33364	37.90951	77°/034°	02°/296°	13°/206°	0.352	16	47	16
L18	32.39194	37.85823	70°/285°	20°/099°	02°/190°	0.027	11	40	7
L19	32.42945	37.99422	39°/209°	35°/085°	31°/329°	0.462	30	62	5
L20	32.38742	37.89012	74°/157°	16°/348°	03°/257°	0.176	25	56	10
L21	32.34830	37.95438	76°/002°	01°/096°	14°/186°	0.264	11	22	18
L22	32.29146	37.89938	79°/053°	06°/291°	09°/200°	0.163	21	47	11
L23	32.28899	37.97180	68°/067°	11°/308°	19°/215°	0.206	13	39	16
L24	32.34778	37.96698	72°/141°	06°/249°	17°/341°	0.580	11	29	7
L25	32.28488	37.93799	86°/019°	03°/235°	03°/145°	0.396	28	69	10
L26	32.26213	38.00526	81°/033°	03°/143°	08°/233°	0.368	30	53	9
L27	32.27441	38.00479	75°/205°	08°/327°	13°/059°	0.192	15	39	14
L28	32.24566	37.92514	83°/053°	07°/246°	01°/155°	0.307	13	42	19
L29	32.34543	37.95603	82°/096°	07°/263°	02°/353°	0.136	16	47	12

σ_1 , σ_2 , σ_3 magnitude ratios of principle stresses; D/P, direction/plunge; Φ stress ratio; ANG, maximum allowed angular divergence RUP, maximum allowed quality value N, number of measurement for each site.

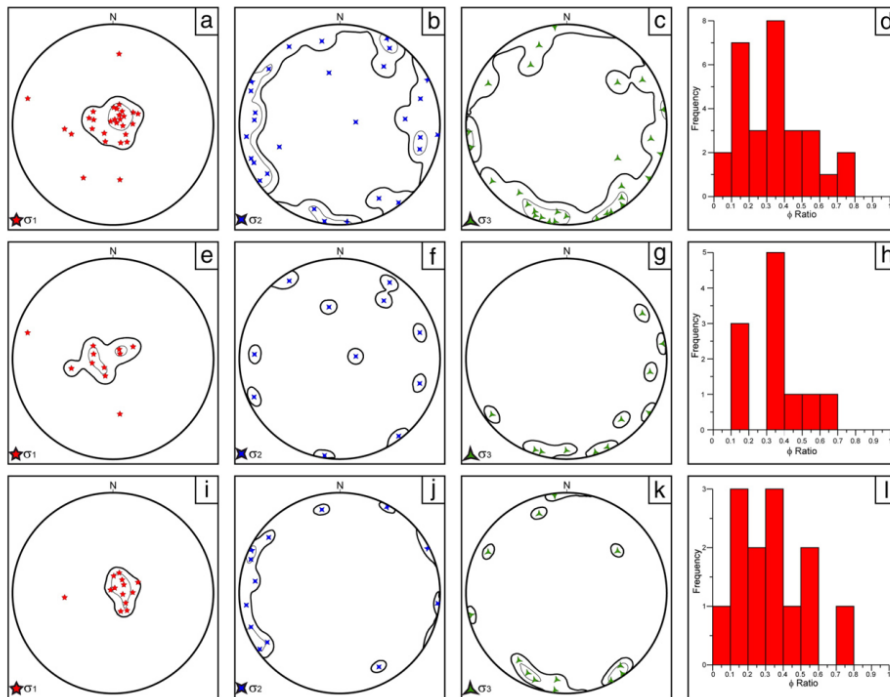


Fig. 22. Density diagrams for principal stress orientations and frequency distributions of Φ values. a–d) whole data, e–h) based on data from upper Altınapa Group, i–l) based on Lower Altınapa Group. Notice that the σ_1 is dominantly subvertical while σ_2 and σ_3 orientations are subhorizontal, with strongly varying directions indicating uniaxial stress conditions.

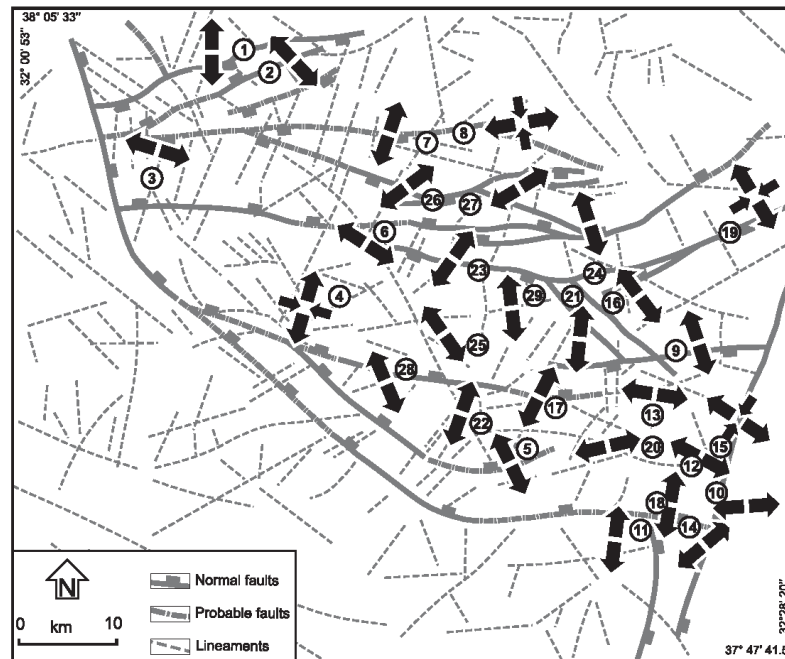


Fig. 23. (a) Major faults and lineament map of the study area. Arrows indicate horizontal component of the minor principal stress (σ_3) and numbers indicate the paleostress measurement sites which correspond to site numbers in Fig. 21c.

Poisson, 1987; Morris and Robertson, 1993; Poisson et al., 2003; van Hinsbergen, 2010; van Hinsbergen et al., 2010a,b). The spatial restriction of NE–SW to NW–SE extension to the region north of the Cyprus subduction zone suggests a direct relationship to the dynamics of the eastern Mediterranean subduction system, which has likely been in a state of relative southward trench retreat since at least Middle Miocene time (see also Over et al., 2004). Our analysis shows that not only the forearc, but also the volcanic arc region of the Cyprus subduction zone, to which the Altınapa Basin belongs, has been affected by this extension for at least the last ~12 Ma.

Finally, our analysis has an important implication for the evolution of southern Anatolian topography. In Middle to Late Miocene time, the Mut Basin, which has been uplifted since Late Miocene time to elevations up to 2 km, was marine (Cosentino et al., 2012), whereas the Altınapa Basin, currently at elevations around 1 km, was continental. No data are available to constrain the paleo-elevation of the Altınapa Basin during Middle Miocene sedimentation, but the fact that the Mut Basin lies presently at an about 1 km higher elevation than the Altınapa Basin demonstrates that the late Neogene history of the southern Turkey was characterized by strong differential uplift, with the southern Tauride mountain range uplifting at least 1 km more than the intramontane basins to their north. Cosentino et al. (2012) interpreted the uplift of the Taurides since the Late Miocene as a dynamic topographic effect, uplifting all of the Central Anatolian plateau. Although such dynamic topographic effects may have well played an important role, the major uplift difference between the Altınapa and Mut basins illustrates that at least half of the uplift of the southern Taurides resulted from regional tectonics rather than Anatolia-wide dynamic topography. The Tauride range as exposed today therefore likely represents a horst system, with regions to the north and

south showing smaller magnitudes of uplift than the range itself. We finally note that the modern topography of the Tauride range is thus a late Neogene phenomenon that is unrelated to the late Cretaceous to Oligocene folding and thrusting responsible for the dominant deformation within the range.

7. Conclusions

Our results demonstrate that the Altınapa Basin is an extensional basin, with a stratigraphy that can be subdivided in a Lower and Upper Altınapa Group. Volcanic deposits in the Upper Altınapa Group have been dated with $^{40}\text{Ar}/^{39}\text{Ar}$ geochronology, and demonstrate an age range of ~11.8–11.6 Ma. Extension-related subsidence, controlled along large basin-bounding faults, therefore started prior to 11.8 Ma. Paleostress analysis shows that σ_2 and σ_3 directions during and after deposition, up to and including the modern-day patterns, vary strongly and locally. A regional pattern of open, extension-related folds shows an approximately E–W trend and suggests that the dominant extension direction responsible for formation of the basin was ~N–S to NE–SW. These folds affect the Lower Altınapa Group more than the Upper Altınapa Group, between which an angular unconformity exists. This, together with the fact that the Lower Altınapa Group has a clear fining upward trend, suggests that the main basin forming phase predates 11.8 Ma. Our results are consistent with a regional pattern of NE–SW to NW–SE extension along the southern Taurides, which seems spatially coincident with the location of the Cyprus subduction zone.

The continental Middle Miocene sediments of the Altınapa Basin lie at present at an elevation of ~1 km, whereas partly contemporaneous marine deposits in the Mut Basin to the south, on top of the Tauride range, are elevated up to 2 km. This demonstrates that the southern

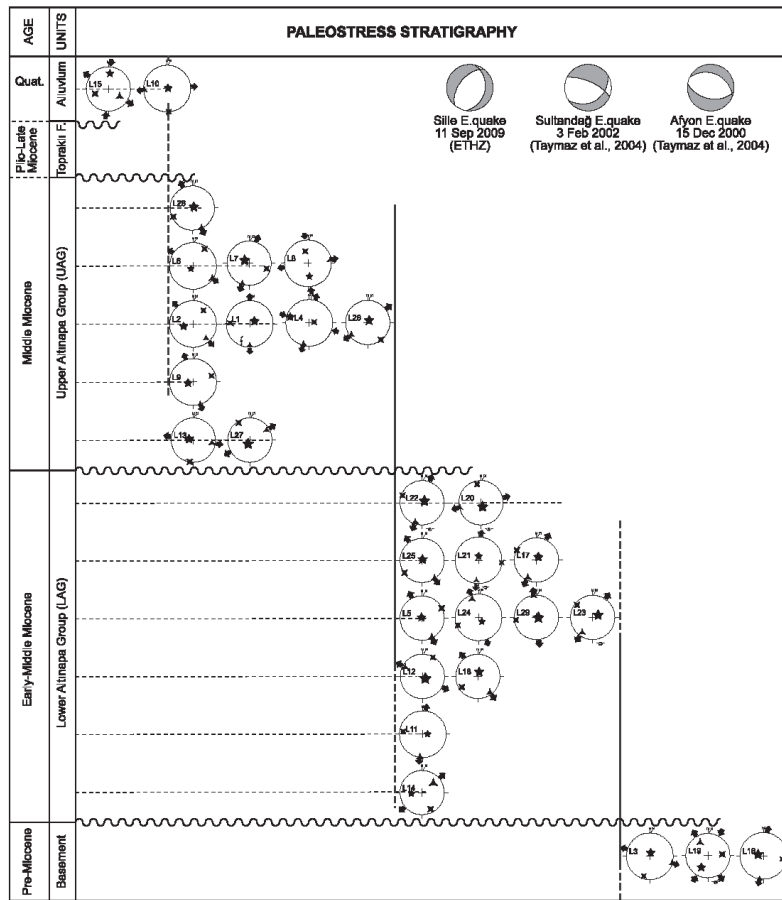


Fig. 24. Paleostress stratigraphy of the Apa Basin from the Middle Miocene to Recent. Arrows represent σ_3 directions. 1) 11 September 2009 Sille Earthquake ($M_w = 4.9$, ETHZ), 2) 15 December 2000 Afyon Earthquake ($M_s = 5.8$, Taymaz et al., 2004), 3) 03 February 2002 Sultandag Earthquake ($M_s = 6.4$, Taymaz et al., 2004). Note that the unconstrained nature of σ_3 directions and from Middle Miocene to Recent and variation of extension directions of recent earthquakes in the region.

Tauride range uplifted at least 1 km more than the flanking intramontane basins to the north, attesting to strong differential uplift in the late Neogene of southern Turkey. The high topography of the Tauride range is unrelated to the late Cretaceous to Oligocene thrusting that deformed the rocks in the range.

Acknowledgments

Research for this paper occurred within the context of the Netherlands Research School of Integrated Solid Earth Sciences (ISES) and was supported by ÖYP research fund of Turkish Government No: BAP-08-11-DPT.2002K120510 and DARIUS Programme. DJvH acknowledges financial support from Statoil (SPlates Model project). KK is funded by grant 814.01.004 of the Netherlands Organisation for Scientific Research. AK would like to thank Kemal Koç, Hasan Kocatepe, M. Onur Öztepe, Erhan Gülyüz, Murat Özkaptan, Mustafa

Y. Kaya, Kıvanç Yücel and Şule Gürboğa for their support during fieldworks in 2008 and 2009. Finally, we thank Domenico Cosentino and an anonymous reviewer for their valuable comments.

Appendix A. Supplementary data

Supplementary data to this article can be found online at doi:10.1016/j.tecto.2012.01.028.

References

- Alçicek, H., 2010. Stratigraphic correlation of the Neogene basins in southwestern Anatolia: regional palaeogeographical, palaeoclimatic and tectonic implications. *Palaeogeography, Palaeoclimatology, Palaeoecology* 291, 297–318.
- Altın, D., Yılmaz, İ.O., Özgül, N., Akar, N., Bayazitoglu, M., Gazıulusoy, Z.E., 1999. High-resolution sequence stratigraphic correlation in the Upper Jurassic (Kimmeridgian)–Upper Cretaceous (Cenomanian) peritidal carbonate deposits (Western Taurides, Turkey). *Geological Journal* 34, 139–158.

- Andrew, T., Robertson, A.H.F., 2002. The Beyşehir-Hoyran-Hadim nappes: genesis and emplacement of Mesozoic marginal and oceanic units of the northern Neotethys in southern Turkey. *Journal of the Geological Society of London* 159, 529–543.
- Angelier, J., 1990. Inversion of field data in fault tectonics to obtain the regional stress–III. A new rapid direct inversion method by analytical means. *Geophysical Journal International* 103, 363–376.
- Angelier, J., 1994. Fault slip analysis and paleostress reconstruction. In: Hancock, P.L. (Ed.), *Continental Deformation*. Pergamon Press, Oxford, pp. 53–101.
- Barrier, E., Vrielynck, B., 2008. MEBE Atlas of Paleotectonic maps of the Middle East. Commission for the Geological Map of the World.
- Bassant, P., van Buchem, F.S.P., Strasser, A., Görür, N., 2005. The stratigraphic architecture and evolution of the Burdigalian carbonate–siliciclastic sedimentary systems of the Mut Basin, Turkey. *Sedimentary Geology* 173, 187–232.
- Besang, C., Eckhart, F.J., Harre, W., Kreuzer, G., Müller, P., 1977. Radiometrische Alterbestimmung am neogenen Eruptivgesteinen der Türkei. *Geologisches Jahrbuch* 25, 3–36.
- Biryol, C.B., Beck, S.L., Zandt, G., Ozacar, A.A., 2011. Segmented African lithosphere beneath the Anatolian region inferred from teleseismic P-wave tomography. *Geophysical Journal International* 184, 1037–1057.
- Blumenthal, M.M., 1963. Le système structural du Taurus sud Anatolies. *Bull. Soc. Géol. Fr. Livre à Mémoire de Professor P. Fallot, Mémoire hors-série*, 1, pp. 611–662.
- Burton-Ferguson, R., Aksu, A.E., Calo, T.J., Hall, J., 2005. Seismic stratigraphy and structural evolution of the Adana Basin, eastern Mediterranean. *Marine Geology* 221, 189–222.
- Carey, E., Burinier, B., 1974. Analyse théorique et numérique d'un modèle mécanique élémentaire appliqué à l'étude d'une population de failles. *Comptes Rendus de l'Académie des Sciences Paris D279*, 891–894.
- Çiner, A., Karabiyikoglu, M., Monod, O., Deynoux, M., Tuzcu, S., 2008. Late Cenozoic sedimentary evolution of the Antalya Basin, Southern Turkey. *Turkish Journal of Earth Sciences* 17, 1–41.
- Cosentino, D., Schildgen, T.F., Cipollari, P., Faranda, C., Gliozzi, E., Hudáková, N., Lucifora, S., Strecker, M.R., 2012. Late Miocene surface uplift of the southern margin of the Central Anatolian Plateau, Central Taurides, Turkey. *Geological Society of America Bulletin* 124 (1–2), 133–145. doi:10.1130/B30466.1.
- Darbas, G., Nazik, A., 2010. Micropaleontology and paleoecology of the Neogene sediments in the Adana Basin (South of Turkey). *Journal of Asian Earth Sciences* 39, 136–147.
- Derman, A.S., Gürbüz, K., 2007. Nature, provenance and relationships of Early Miocene palaeovalley fills, northern Adana Basin, Turkey: their significance for sediment-bypassing on a carbonate shelf. *Turkish Journal of Earth Sciences* 16, 181–209.
- Doğan, A., 1975. Sızma–Ladik (Konya) Çıva Sahasının Jeolojisi ve Maden Yatakları Sorunlarının İncelenmesi. I.Ö. Fen Fakültesi Min. Pet. Kürsüsü, Yüksek Müh. Diploma Çalışması, İstanbul, 40.
- Eren, Y., 1992. Eldes–Gökçeyurt–Derbent (Konya kuzebatısı) Dolaylarında Kocaçaldag Yükselişinin Jeolojisi. S.Ü. Arastırma Fonu, Proje No: 88-026.
- Eren, Y., 1993. Eldes–Derbent–Tepekçi–Söğütözü Arasının Jeolojisi. PhD Thesis, S.Ü. Fen Bil. Enst. Konya, Turkey, 224.
- Eren, Y., 1996. Iğın–Sarayönü (Konya) güneyinde Bozdağlar Masifinin Yapısal Özellikleri. *Geological Bulletin of Turkey* 39, 49–64.
- Ergin, M., Aktar, M., Özalaybey, S., Tapırdamaz, M.C., Selvi, O., Tarancıoğlu, A., 2009. A high-resolution aftershock seismicity image of the 2002 Sultandagi–Çay earthquake (Mw=6.2). *Turkey Journal of Seismology* 13, 633–646.
- Eriş, K.K., Bassant, P., Ülgen, U.B., 2005. Tectono-stratigraphic evolution of an Early Miocene incised valley-fill (Derinçay Formation) in the Mut Basin, Southern Turkey. *Sedimentary Geology* 173, 151–185.
- Etchecopar, A., Vasseur, D., Daignières, M., 1981. An inverse problem in microtectonics for determination of stress tensors from faults striation analysis. *Journal of Structural Geology* 3, 51–65.
- Faccenna, C., Bellier, O., Martinod, J., Piromallo, C., Regard, V., 2006. Slab detachment beneath eastern Anatolia: a possible cause for the formation of the North Anatolian Fault. *Earth and Planetary Science Letters* 242, 85–97.
- Gans, C.R., Beck, S.L., Zandt, G., Biryol, C.B., Ozacar, A.A., 2009. Detecting the limit of slab break-off in central Turkey: new high-resolution Pn tomography results. *Geophysical Journal International* 179, 1566–1572.
- Göçer, E., Kırak, K., 1969. Kizilören Dolayının Jeolojisi. M.T.A. Rapor, 5204.
- Görmüş, M., 1984. Kizilören (Konya), Dolayının Jeolojisi İncelemesi. S.Ü. Fen Bil. Enst. M. Sc. Konya, Turkey, 67.
- Gül, M., 2007. Effects of antecedent topography on reefal carbonate deposition: Early–Middle Miocene of the Adana Basin, S Turkey. *Journal of Asian Earth Sciences* 31, 18–34.
- Homberg, C., Hu, J.-C., Angelier, J., Bergerat, F., Lacombe, O., 1997. Characterization of stress perturbations near major fault zones: insights from field studies (Jura Mountains) and numerical modelling. *Journal of Structural Geology* 19, 703–718.
- Hüsing, S.K., Zachariasse, W.J., van Hinsbergen, D.J.J., Krijgsman, W., Inceöz, M., Harzhauser, M., Mandic, O., Kroh, A., 2009. Oligo–Miocene foreland basin evolution in SE Anatolia: constraints on the closure of the eastern Tethys gateway. In: van Hinsbergen, D.J.J., Edwards, M.A., Govers, R. (Eds.), *Collision and Collapse at the Africa–Arabia–Eurasia subduction zone*. Geological Society, London, Special Publication, pp. 107–132.
- Janson, X., van Buchem, F.S.P., Dromart, G., Eichenseer, H.T., Dellamonicis, X., Boichard, R., Bonnaffé, F., Eberli, G.P., 2010. Architecture and facies differentiation within a Middle Miocene carbonate platform, Ermenek, Mut Basin, southern Turkey. In: van Buchem, F.S.P., Gerdas, K.D., Esteban, M. (Eds.), *Mesozoic and Cenozoic Carbonate Systems of the Mediterranean and the Middle East: Stratigraphic and Diagenetic Reference Models*. Geological Society, London, Special Publications, pp. 265–290.
- Karabiyikoglu, M., Tuzcu, S., Çiner, A., Deynoux, M., Örcen, S., Hakymez, A., 2005. Facies and environmental setting of the Miocene coral reefs in the late-orogenic fill of the Antalya Basin, western Taurides, Turkey: implications for tectonic control and sea-level changes. *Sedimentary Geology* 173, 345–371.
- Altıekin (Konya) civarının jeolojisi ve mineralojik-petrografik incelenmesi. MSc thesis, Selçuk University, Konya.
- Kaymakci, N., Özcelik, Y., White, S.H., van Dijk, P.M., 2009. Tectono-stratigraphy of the Çankiri Basin: late Cretaceous to early Miocene evolution of the Neotethyan suture zone in Turkey. In: van Hinsbergen, D.J.J., Edwards, M.A., Govers, R. (Eds.), *Collision and Collapse at the Africa–Arabia–Eurasia subduction zone*. Geological Society of London Special Publication, pp. 67–106.
- Kaymakci, N., Inceöz, M., Ertepinar, P., Koç, A., 2010. Late Cretaceous to Recent kinematics of SE Anatolia (Turkey). In: Sossou, M., Kaymakci, N., Stephenson, R.A., Bergerat, F., Stasenko, V. (Eds.), *Sedimentary basin tectonics from the Black Sea and Caucasus to the Arabian Platform*. Geological Society, London, Special Publications, pp. 409–435.
- Keller, J., Jung, D., Burgath, K., Wolff, F., 1977. Geologie und Petrologie des Neogenen Kalkalkalvulkanismus von Konya (Erenler Dagi, Alacadağ Massiv, Zentral Anatolien). *Geologisches Jahrbuch*, B 25, 37–117.
- Keskin, M., 2003. Magma generation by slab steepening and breakoff beneath a subduction–accretion complex: an alternative model for collision-related volcanism in Eastern Anatolia, Turkey. *Geophysical Research Letters* 30 (24), 8046. doi:10.1029/2003GL018019.
- Khair, K., Tsokas, G.N., 1999. Nature of the Levantine (eastern Mediterranean) crust from multiple-source Werner deconvolution of Bouguer gravity anomalies. *Journal of Geophysical Research* 104, 25469–25478.
- Kissel, C., Poisson, A., 1987. Étude paléomagnétique préliminaire des formations cénozoïques des Bey Dagları (Taurides occidentales, Turquie). *Comptes Rendus de l'Académie des Sciences Paris* 304 (8), 343–348 Série II.
- Kleinspehn, K.L., Pershing, J.C., Teysseir, C., 1989. Paleostress stratigraphy: a new technique for analyzing tectonic control on sedimentary-basin subsidence. *Geology* 17, 253–256.
- Koppers, A.A.P., 2002. ArArCALC-software for ⁴⁰Ar/³⁹Ar age calculations. *Computers & Geosciences* 28, 605–619.
- Kuiper, K.F., Deino, A.L., Hilgen, F.J., Krijgsman, W., Renne, P.R., Wijbrans, J.R., 2008. Synchronizing rock clocks of Earth history. *Science* 320, 500–504.
- Mackintosh, P., Robertson, A.H.F., 2009. Structural and sedimentary evidence from the northern margin of the Tauride platform in south central Turkey used to test alternative models of Tethys during Early Mesozoic time. *Tectonophysics* 473, 149–172.
- Meijers, M.J.M., Kaymakci, N., van Hinsbergen, D.J.J., Langereis, C.G., Stephenson, R.A., Hippolyte, J.-C., 2010. Late Cretaceous to Paleocene oroclinal bending in the Central Pontides (Turkey). *Tectonics* 29, TC4016. doi:10.1029/2009TC002620.
- Meijers, M.J.M., van Hinsbergen, D.J.J., Dekkers, M.J., Altiner, D., Kaymakci, N., Langereis, C.G., Stephenson, R.A., 2011. Pervasive Paleogene remagnetization of the central Taurides fold-and-thrust belt (southern Turkey) and implications for rotations in the Isparta Angle. *Geophysical Journal International* 184, 1090–1112.
- Min, K., Mundil, R., Renne, P.R., Ludwig, K.R., 2000. A test for systematic errors in ⁴⁰Ar/³⁹Ar geochronology through comparison with U/Pb analysis of a 1.1-Ga rhyolite. *Geochimica et Cosmochimica Acta* 64, 73–98.
- Morgan, L.E., Renne, P.R., Taylor, R.E., WoldeGabriel, G., 2009. Archaeological age constraints from extrusion ages of obsidian: examples from the Middle Awash, Ethiopia. *Quaternary Geochronology* 4, 193–203.
- Morris, A., Robertson, A.H.F., 1993. Miocene remagnetisation of carbonate platform and Antalya Complex units within the Isparta Angle, SW Turkey. *Tectonophysics* 220, 243–266.
- Niehoff, W., 1961. 1/100.000 ölçekli Akşehir 90/2 paftası, Iğın 91/1, 91/3 ve 91/4 paftaları üzerinde 1961 yaz mevsiminde yapılmış revizyon çalışmaları hakkında rapor. M.T.A. Rapor, 3387.
- Nier, A.O., 1950. A redetermination of the relative abundances of the isotopes of carbon, nitrogen, oxygen, argon, and potassium. *Physical Review* 77, 789.
- Öğütçü, Z., Horason, G., Kalafat, D., 2010. Investigation of microseismic activity sources in Konya and its vicinity, central Turkey. *Natural Hazards* 58 (1), 497–509. doi:10.1007/s11069-010-9683-6.
- Okay, A.L., Özgül, N., 1984. HP/LT metamorphism and the structure of the Alanya Massif, Southern Turkey: an allochthonous composite tectonic sheet. In: Dixon, J.E., Robertson, A.H.F. (Eds.), *The Geological Evolution of the Eastern Mediterranean*. Geological Society Special Publication, pp. 429–439.
- Okay, A.L., Satir, M., Maluski, H., Sıyako, M., Monié, P., Metzger, R., Akyüz, S., 1996. Paleo- and Neo-Tethyan events in northwestern Turkey: geologic and geochronologic constraints. In: Yin, A., Harrison, T.M. (Eds.), *The tectonic evolution of Asia*. Cambridge University Press, Cambridge, pp. 420–441.
- Okay, A.L., Zaitin, M., Cavazza, W., 2010. Apatite fission-track data for the Miocene Arabia–Eurasia collision. *Geology* 38, 35–38.
- Over, S., Özden, S., Ulugenc, U.C., 2004. Late Cenozoic stress distribution along the Misis Range in the Anatolian, Arabian, and African plate intersection region, SE Turkey. *Tectonics* 23, TC3008. doi:10.1029/2002TC001455.
- Özcan, A., Gönçioğlu, M.C., Turhan, N., Şentürk, K., Uysal, S., Isik, A., 1990. Konya–Kadinhanı–Iğın Dolayının Temel Jeolojisi. M.T.A. Rapor, 9535.
- Özer, E., Koc, H., Özsayar, T.Y., 2004. Stratigraphical evidence for the depression of the northern margin of the Menderes–Tauride Block (Turkey) during the Late Cretaceous. *Journal of Asian Earth Sciences* 22, 401–412.
- Özkan, A.M., 1998. Konya Batısındaki Neojen Çökelilerinin Stratigrafisi ve Sedimentolojisi. PhD Thesis, S.Ü. Fen Bil. Enst., Konya, Turkey, 208 pp.
- Özkan, A.M., Söğüt, A.R., 1999. Dilekçi (Konya batısı) çevresindeki Neojen çökelilerinin stratigrafisi. *Journal of Engineering Science* 5, 1131–1138.
- Poisson, A., Wernli, R., Sagular, E.K., Temiz, H., 2003. New data concerning the age of the Aksu Thrust in the south of the Aksu valley, Isparta Angle (SW Turkey): consequences for the Antalya Basin and the Eastern Mediterranean. *Geological Journal* 38, 311–327.

- Pourteau, A., Candan, O., Oberhänsli, R., 2010. High-pressure metasediments in central Turkey: constraints on the Neotethyan closure history. *Tectonics* 29, TC5004. doi:10.1029/2009TC002650.
- Ricou, L.E., Argyriadis, I., Marcoux, J., 1975. L'axe calcaire du Taurus, un alignement de fenêtres arabo-africaines sous des nappes radiolaritiques, ophiolitiques et métamorphiques. *Bulletin de la Société Géologique de France* 17, 1024–1043.
- Şafak, Ü., Kelling, G., Gökçen, N.S., Gürbüz, K., 2005. The mid-Cenozoic succession and evolution of the Mut basin, southern Turkey, and its regional significance. *Sedimentary Geology* 173, 121–150.
- Şengör, A.M.C., Yılmaz, Y., 1981. Tethyan evolution of Turkey: a plate tectonic approach. *Tectonophysics* 75, 181–241.
- Şengör, A.M.C., Özeren, S., Genç, T., Zor, E., 2003. East Anatolian high plateau as a mantle-supported, north-south shortened domal structure. *Geophysical Research Letters* 30 (24), 8045. doi:10.1029/2003GL017858.
- Steiger, R.H., Jäger, E., 1977. Subcommittee on geochemistry: convention on the use of decay constants in geo- and cosmochemistry. *Earth and Planetary Science Letters* 36, 359–362.
- Taymaz, T., Tan, O., Yolsal, S., 2004. Seismotectonics of western Turkey: a synthesis of source parameters and rupture histories of Recent earthquakes. *Eos Transactions AGU* 85, 47.
- Temel, A., Gündoğdu, M.N., Gourgau, A., 1998. Petrological and geochemical characteristics of Cenozoic high-K calcalkaline volcanism in Konya, Central Anatolia, Turkey. *Journal of Volcanology and Geothermal Research* 85, 327–354.
- Torsvik, T.H., Cocks, L.R.M., 2009. The Lower Palaeozoic palaeogeographical evolution of the northeastern and eastern peri-Gondwanan margin from Turkey to New Zealand. In: Bassett, M.G. (Ed.), *Early Palaeozoic Peri-Gondwana terranes: New insights from tectonics and biogeography*. Geological Society, London, Special Publications, pp. 3–21.
- van Hinsbergen, D.J.J., 2010. A key extensional metamorphic complex reviewed and restored: the Menderes Massif of western Turkey. *Earth-Science Reviews* 102, 60–76.
- van Hinsbergen, D.J.J., Dekkers, M.J., Bozkurt, E., Koopman, M., 2010a. Exhumation with a twist: paleomagnetic constraints on the evolution of the Menderes metamorphic core complex (western Turkey). *Tectonics* 29, TC3009. doi:10.1029/2009TC002596.
- van Hinsbergen, D.J.J., Dekkers, M.J., Koç, A., 2010b. Testing Miocene remagnetization of Bey Dağları: Timing and amount of Neogene rotations in SW Turkey. *Turkish Journal of Earth Sciences* 19, 123–156.
- van Hinsbergen, D.J.J., Kaymakci, N., Spakman, W., Torsvik, T.H., 2010c. Reconciling the geological history of western Turkey with plate circuits and mantle tomography. *Earth and Planetary Science Letters* 297, 674–686.
- Wiesner, K., 1968. Konya civa yatakları ve bunlar üzerindeki etütler. *M.T.A. Dergisi, Sayı* 70, pp. 178–213.
- Yağmurlu, F., 1991a. Stratigraphy and depositional environments of Yalvaç-Yarıkkaya Neogene basin, SW-Anatolia. *Geological Bulletin of Turkey* 34, 9–19.
- Yağmurlu, F., 1991b. Yalvaç-Yarıkkaya Neojen havzasının tektono-sedimanter özellikleri ve yapısal evrimi. *M.T.A. Dergisi, Sayı* 112, pp. 1–13.
- Yetiş, C., 1988. Reorganization of the Tertiary stratigraphy in the Adana basin, southern Turkey. *Newsletters in Stratigraphy* 20, 43–58.

CURRICULUM VITAE

PERSONEL INFORMATION

Surname, Name: Koç, Ayten
Nationality: Turkish (TC)
Date and Place of Birth: 4 October 1978
Marital Status: Single
Phone: +90 312 210 5743
Fax: +90 312 210 5750
e-mail: kayten@metu.edu.tr, i10.koc.geo@gmail.com

EDUCATION

Degree	Institution	Year of Graduation
MS	METU Geodetic and Geographic Information Technology	2005
BS	HÜ Hydrogeological Engineering	2001
High School	Fatsa High School, Fatsa-ORDU	1995

WORK EXPERIENCE

Year	Place	Enrollment
2006- Present	METU Department of Geological Engineering	Research Assistant
2002-2005	METU Department of Geodetic and Geographic Information Technology	Research Assistant

FOREIGN LANGUAGES

Advanced English

PUBLICATIONS

1. Koç, A. and Kaymakci, N. 2013. Kinematics of Sürgü Fault Zone (Malatya, Turkey): A remote sensing study. Journal of Geodynamics, 65, 292-307.

2. Koç, A., Kaymakci, N., van Hinsbergen, D.J.J., Kuiper, K.F. and Vissers, R.L.M, 2012. Tectono-sedimentary evolution and geochronology of the middle Miocene Altınapa basin, and implications for the late Cenozoic uplift history of the Taurides, southern Turkey, *Tectonophysics* 532–535, 134–155
3. Kaymakci, N., Inceöz, M., Ertepinar, P. and Koç, A. 2010. Late Cretaceous to recent kinematics of SE Anatolia (Turkey) In Sosson, M. Kaymakci, N., Stephenson, R., Starostenko, V. and Bergerat, F. (Eds.) *Sedimentary basin tectonics from the Black Sea and Caucasus to the Arabian Platform*. Geological Society London Special Issue No. 340, 409-435.
4. Hinsbergen, D.J.J.V., Dekkers, M. J., Koç, A (2010). Testing Miocene Remagnetization of Bey Dağları: Timing and Amount of Neogene Rotations in SW Turkey. *Turkish Journal of Earth Sciences*, 19/123-156.

HOBBIES

Rock Climbing, Running and Yoga

